

Dissertation zur Erlangung des Doktorgrades
der Fakultät für Chemie und Pharmazie
der Ludwig-Maximilians-Universität München

Correlation of structure and performance in
high temperature polymer electrolyte
membrane fuel cells

von
Christoph Heinzl
aus
Rosenheim
2014



Erklärung

Diese Dissertation wurde in Sinne von § 7 der Promotionsordnung vom 28. November 2011 von Frau Professor Dr. Christina Scheu betreut.

Eidesstattliche Versicherung

Diese Dissertation wurde eigenständig und ohne unerlaubte Hilfe erarbeitet.

München,

.....

(Unterschrift des Autors)

Dissertation eingereicht am 29.09.2014

1. Gutachterin: Prof. Dr. Christina Scheu

2. Gutachter: Prof. Dr. Konstantin Karaghiosoff

Mündliche Prüfung am 27.10.2014

Table of content

Table of content.....	I
List of abbreviations.....	VI
List of symbols.....	IX
List of figures.....	X
List of tables.....	XV
1 Introduction.....	1
1.1 Aim of the thesis.....	4
1.2 Chapter references	6
2 Theoretical background	8
2.1 Working principle of fuel cells	8
2.2 Types of fuel cells.....	10
2.3 Strengthening of PBI membranes for HT-PEMFC	11
2.4 Degradation of Pt catalysts in HT-PEMFC	13
2.5 Tungsten oxide as candidate for HT-PEMFC electrodes.....	13
2.6 Chapter references	15
3 Characterization methods.....	18
3.1 X-ray diffraction.....	18
3.2 Electron microscopy	19
3.2.1 Scanning electron microscopy	21
3.2.2 Focused ion beam microscopy	23
3.2.3 Transmission electron microscopy	25

3.3	Energy dispersive X-ray spectroscopy	29
3.4	Electron energy loss spectroscopy.....	31
3.5	Fuel cell characterization methods.....	32
3.5.1	Polarization curves.....	32
3.5.2	Cyclic voltammetry.....	34
3.5.3	Long term fuel cell test with continuous operation.....	35
3.5.4	Long term fuel cell test with start-stop cycle operation	35
3.6	Chapter references	37
4	Experimental details.....	38
4.1	Chemicals and substrates	38
4.2	Equipment	38
4.3	Analytical instruments.....	39
4.4	Sample preparation.....	40
4.4.1	SEM sample preparation	40
4.4.2	TEM sample preparation.....	40
4.5	Chapter references	44
5	Influence of the size and shape of silica nanoparticles on the properties and degradation of a PBI-based high temperature polymer electrolyte membrane.....	45
5.1	Introduction	45
5.2	Experimental	47
5.2.1	Preparation methods.....	47
5.2.2	Characterization methods.....	48
5.3	Results and discussion	50

5.3.1	Structural analysis	50
5.3.2	<i>Ex-situ</i> membrane properties	55
5.3.3	<i>In-situ</i> fuel cell testing and degradation analysis.....	59
5.4	Conclusion.....	63
5.5	Chapter references	65
6	Transmission electron microscopy study of silica reinforced polybenzimidazole membranes	67
6.1	Introduction	67
6.2	Experimental	69
6.2.1	Synthesis.....	69
6.2.2	Characterization methods.....	70
6.3	Results and discussion	72
6.3.1	<i>Ex-situ</i> membrane properties.....	72
6.3.2	<i>In-situ</i> membrane properties.....	73
6.3.3	Structural analysis	76
6.4	Conclusion.....	90
6.5	Chapter references	92
7	Tungsten materials as durable catalyst supports for fuel cell electrodes	94
7.1	Introduction	94
7.2	Experimental	97
7.2.1	Synthesis of WO _{xs}	97
7.2.2	Catalyst deposition	97
7.2.3	Determination of catalyst crystallite size and support structure.....	97

Table of content

7.2.4	Electrochemical characterization	98
7.2.5	Electrode and membrane-electrode-assembly preparation	99
7.2.6	<i>In-situ</i> test conditions	99
7.2.7	Thermogravimetric analysis	100
7.2.8	HT-PEM long term stack test	100
7.3	Results and discussion	100
7.3.1	Characterization of WC support material	100
7.3.2	Characterization of self-made WO _{xs}	101
7.3.3	Characterization of commercial WO _x	102
7.3.4	Catalyst deposition on tungsten based support materials	102
7.3.5	Potential cycling	105
7.3.6	CO-stripping	107
7.3.7	<i>In-situ</i> CV	108
7.3.8	TGA	110
7.3.9	XRD and electron microscopy analysis	111
7.3.10	HT-PEM fuel cell results	114
7.4	Conclusions	114
7.5	Chapter references	116
8	Insight into the degradation of HT-PEMFCs containing tungsten oxide catalyst support material for the anode	117
8.1	Introduction	117
8.2	Experimental	119
8.2.1	Synthesis	119

Table of content

8.2.2	Characterization methods.....	121
8.3	Results and Discussion	124
8.3.1	Structural Analysis.....	124
8.3.2	<i>In-situ</i> MEA properties	141
8.4	Summary and Conclusion	144
8.5	Chapter references	146
9	Conclusion	149
10	Appendix	154
11	Curriculum Vitae	156
12	List of Publications and Presentations	158
12.1	Scientific publications.....	158
12.2	Conference contributions.....	159

List of abbreviations

μm	Micrometer (10^{-6} m)
ADF	Annular dark field
BET	Brunauer-Emmett-Teller
BOL	Begin of life
BSE	Backscattered electrons
BF	Bright-field
CTF	Contrast transfer function
CV	Cyclic voltammetry
DF	Dark-field
DMAC	N,N-dimethylacetamide
ECA	Electrochemical active surface area
ED	Electron diffraction
EDS	Energy dispersive X-ray spectroscopy
EELS	Electron energy loss spectroscopy
EOL	End of life
eV	Electron volt ($1,60 \cdot 10^{-19}$ kg · m ² · s ⁻²)
FIB	Focused ion beam
FWHM	Full width at half maximum
GDE	Gas diffusion electrode
GDL	Gas diffusion layer
GPTMS	(3-glycidyloxypropyl)-trimethoxysilane
h	Hours
HAADF	High angle annular dark-field

HOR	Hydrogen oxidation reaction
HRTEM	High-resolution TEM
HSAC	High surface area carbon
HT-PEMFC	High temperature PEMFC
keV	Kilo electron volt
LT-PEMFC	Low temperature PEMFC
MEA	Membrane electrode assembly
min	Minutes
mm	Millimeter (10^{-3} m)
MPL	Micro porous layer
nm	Nanometer (10^{-9} m)
OCV	Open-circuit voltage
ORR	Oxygen reduction reaction
pA	Picoampere (10^{-12} A)
PBI	Polybenzimidazole
PC	Potential cycling
PEMFC	Polymer electrolyte membrane fuel cell
PTFE	Polytetrafluoroethylene
s	Seconds
SAD	Selected area diffraction
SE	Secondary electrons
SEM	Scanning electron microscopy
STEM	Scanning TEM
TEM	Transmission electron microscopy

List of abbreviations

TEOS	Tetraethoxy silane
TGA	Thermogravimetric analysis
XRD	X-ray diffraction

List of symbols

\AA	Ångstrom
c_A, c_B	Concentration of element A and B
C_s	Spherical aberration
d	Lattice plane distance
D_{XRD}	Domain size
h	Planck constant
hkl	Miller indices
K	Shape factor
k_{AB}	Cliff-Lorimer factor
m_0	Electron mass
n	Order of diffraction
p	Pressure or momentum
R	Distance
T	Temperature
u	Spatial frequency
V	Acceleration voltage
Z	Atomic number
$\Delta(2\theta)$	Line broadening at the half-maximum intensity
Δf	Defocus
θ	Bragg angle
λ	Wavelength
λL	Camera constant

List of figures

Figure 2.1: Schematic drawing of the main components of a PEMFC.....	8
Figure 2.2: Schematic of the working principle of a PEMFC.....	9
Figure 3.1: Schematic illustration of the Bragg relation.....	19
Figure 3.2: Scheme of the interaction of an electron beam with the specimen.	21
Figure 3.3: Schematic drawing of a SEM assembly and the electron path.....	23
Figure 3.4: Schematic drawing of a FIB microscope.....	24
Figure 3.5: Beam paths in a TEM for diffraction (left) and imaging mode (right).	26
Figure 3.6: Schematic drawing of the available detectors in STEM mode.	29
Figure 3.7: Schematic drawing of the excitation of an inner shell electron followed by relaxation and emission of a characteristic X-ray.....	30
Figure 3.8: EELS spectrum showing the zero loss peak and the element specific ionization edge of oxygen.....	32
Figure 3.9: Schematic drawing of a polarization curve.	33
Figure 3.10: Schematic drawing of an <i>in-situ</i> cyclic voltammogram.....	35
Figure 4.1: Schematic illustration of the preparation of a TEM cross-section.....	41
Figure 4.2: Schematic representation of the conventional sample preparation of a TEM lamella via FIB.	42
Figure 4.3: Schematic representation of the alternative sample preparation of a TEM lamella via FIB.	43
Figure 5.1: Sol-gel reaction of TEOS with GPTMS.....	47
Figure 5.2: STEM micrographs of membrane specimens.	51
Figure 5.3: Size distribution of the silica particles in the membranes.....	51

Figure 5.4: EDS spectra of 120% TEOS on a bright particle (black) and on a particle free region (gray).....	53
Figure 5.5: X-ray diffractograms of the samples.	55
Figure 5.6: TGA measurements of membrane samples.....	56
Figure 5.7: Stress-strain curves of membranes.....	57
Figure 5.8: Schematic drawing of the phosphoric acid (circles) uptake between the polymer chains (chains) at different silica contents (stars) and the same cross-linker content (strokes).	59
Figure 5.9: BOL polarization (solid lines) and power density (dashed lines) curves of the MEAs with 40%, 80% and 120% TEOS.	60
Figure 5.10: Start-stop-cycling of the MEAs with organic-inorganic composites.....	61
Figure 5.11: Polarization (solid lines) and power density (dashed lines) curves of 40% and 80% TEOS samples before (BOL) and after (EOL) cycling.	62
Figure 5.12: Long term fuel cell operation at constant current of the MEA.....	63
Figure 6.1: Stress-strain curves of membranes prepared at different temperatures.....	73
Figure 6.2: BOL polarization (solid lines) and power density (dashed lines) curves of the MEAs with membranes prepared at different temperatures.....	74
Figure 6.3. Start-stop-cycling behavior of the MEAs stirred at different temperatures...	75
Figure 6.4. Fuel cell operation under constant current conditions of MEAs with different preparation temperatures of the organic-inorganic composite membrane.	76
Figure 6.5. Comparison of the two investigated membranes.....	77
Figure 6.6. Schematic drawing of the silica particle distribution in the membranes.	78
Figure 6.7. Size distribution of the silica particles in the membranes.....	80
Figure 6.8. X-ray diffraction patterns of the membrane samples M I and M II.....	83
Figure 6.9. Elemental maps of sample M I acquired via EDS.....	86

Figure 6.10. EDS line scans of an ellipsoidal silica particle found in membrane M I.	88
Figure 6.11. Results of the EELS analysis of the different membrane areas.	89
Figure 7.1: CV curves of commercially available WC.....	100
Figure 7.2: CV curves of WC and self-made WO _{xs} without platinum.....	101
Figure 7.3: CV curves scans of commercial WO _x and self-made WO _{xs}	102
Figure 7.4: CV curves of Pt/WC and Pt/WO _{xs} after stabilization.	103
Figure 7.5: CV curves of Pt/WO _{xs} and WO _{xs} after stabilization.	104
Figure 7.6: CV curves of Pt/WC and Pt/WO _{xs}	104
Figure 7.7: Analysis scans of WO _x supported Pt catalyst.	105
Figure 7.8: Analysis scans of Pt loaded HSAC.	106
Figure 7.9: Comparison of H _{upd} charge loss of different supported Pt catalysts after 3600 cycles with upper reverse potentials of 1.1, 1.2 and 1.3 V.	107
Figure 7.10: CO-stripping result of Pt loaded WO _{xs} and Pt loaded HSAC.	108
Figure 7.11: In-situ CVs for HT-PEMFC of Pt/WC at different aging levels.	109
Figure 7.12: In-situ CVs of WO _x with (A) and without platinum (B) on the working electrode after 100 cycles.	110
Figure 7.13: TGA of WO _x , WO _{xs} , WC and HSAC.....	110
Figure 7.14: XRD patterns of Pt/WC, Pt/WO _x and Pt/WO _{xs}	112
Figure 7.15: (a) Secondary electron top view image shows the crystalline morphology of WO _x . (b) High-contrast TEM bright-field image of WO _x particles and related electron diffraction pattern (c).	112
Figure 7.16: TEM images of two representative areas of WO _x . 13 wt% Pt loaded WO _x (a) and detail with visible (111) lattice planes of Pt on WO _x (b).	113
Figure 7.17: TEM images of two representative areas of WO _{xs} . 13 wt% Pt loaded WO _{xs} (a) and detail of Pt on WO _{xs} (b).	113

Figure 7.18: 980 h test of a HT-PEM MEA in a 20-cell HT-PEMFC stack with methanol reformat on the anode at 160 °C.	114
Figure 8.1: Cross-sectional SEM micrograph of a ready-to-use MEA.....	125
Figure 8.2: SE images and correlated EDS line scans of the four MEA samples.....	128
Figure 8.3: SEM top view image of the ready-to-use WO _{3-x} anode.....	130
Figure 8.4: Comparison of the X-ray diffractograms of the investigated MEAs.....	131
Figure 8.5: Overview STEM micrograph of the anode area.	133
Figure 8.6: STEM images of WO _{3-x} based areas of: a) MEA I, b) MEA II, c) MEA III, d) MEA IV. In a) in addition an ED pattern of one grain is given.....	134
Figure 8.7: O-K EELS spectra of MEA I, MEA II, MEA III and MEA IV, taken in the interior of the WO _{3-x} grains.....	135
Figure 8.8: Pt catalyst structures at the interface region between anode and membrane of a) MEA I, b) MEA II, c) MEA III, d) MEA IV.....	136
Figure 8.9: Carbon based areas in the anode of a) MEA I, b) MEA II, c) MEA III, d) MEA IV.	139
Figure 8.10: STEM HAADF micrographs of the proton exchange membrane of: a) MEA I, b) MEA II, c) MEA III, d) MEA IV.	141
Figure 8.11: Polarization curves with synthetic reformat of MEAs with WO _{3-x} as catalyst support material on the anode after different fuel cell tests and in comparison to a HSAC based MEA.....	142
Figure 8.12: MEA II: nominal 600 h test at constant current density in a 50 cm ² single cell with pure hydrogen.....	143
Figure 8.13: Cell voltage during a nominal 2000 h stack test of MEAs with WO _{3-x} based anodes and HSAC based reference MEAs.....	144
Figure 10.1: TEM micrographs of a C based electrode before operation (a) and after 2000 h of operation (b).....	154

Figure 10.2: a) HRTEM micrograph of a Pt particle; b) schematic drawing of the particle with indexed facets.	154
Figure 10.3: SE image of a thinned FIB lamella.	155
Figure 10.4: HRTEM image of crystalline Pt particles on turbostratic carbon.....	155

List of tables

Table 2.1: Fuel cell types that are currently in use and development.	10
Table 4.1: Used chemicals and substrates.	38
Table 4.2: Equipment used for sample preparation.	38
Table 4.3: Analytical instruments used in this work.	39
Table 5.1: Average particle size, average equivalent spherical particle diameter and average particle density of the samples containing 40%, 80% and 120% TEOS as well as their respective standard deviations.	52
Table 5.2: Detected ratio of silicon to phosphor in atomic percent for the samples with 40%, 80% and 120% TEOS via overview EDS measurements.	54
Table 5.3: Extraction residue, liquid uptake and swelling of the membrane samples.	58
Table 6.1. Extraction residue, liquid uptake and swelling of the membrane samples.	73
Table 6.2. Average particle size, average equivalent spherical particle diameter and average particle density of the silica particles as well as the respective standard deviations. The data for M II is based on Ref. ^[18]	81
Table 6.3. Measured angles in the XRD data and calculated <i>d</i> -values for features a and b. Feature c could not be determined.	83
Table 6.4. Comparison of the average amount of Si to the amount of P measured by EDS in a window of 5 x5 μm^2	85
Table 8.1: Overview of the analyzed samples in this work and their mode of operation.	121
Table 8.2: Summary of the Pt catalyst particle size obtained by XRD and by TEM. The sign “-“ stands for not detected, the sign “*” for data which did not allow a quantitative size determination.	132

1 Introduction

The ever-growing energy consumption and the global environmental pollution combined with limited supplies of fossil fuels lead to increased demand for efficient and sustainable solutions for energy supply. Regenerative energy sources like solar energy or wind and water power have gained considerable attention in the last years and their further development is object of current research. A potential carrier for the energy generated by these regenerative sources is hydrogen which allows for a decentralized energy supply. The fuel cell technology offers an environmentally friendly and highly efficient way to convert the chemical energy of a fuel like hydrogen directly into electrical energy.^[1] The first fuel cell was developed in 1839 by Sir William Grove who generated energy using the reaction of hydrogen and oxygen to water.^[2] Nevertheless, other energy generators like the dynamoelectric machine seemed to be more promising and cheaper that time and the development of fuel cells was marginalized.^[3] In 1889 Ludwig Mond and Charles Langer postulated that the contact area of the applied gases, the electrolyte and the catalyst in a fuel cell should be maximized to reach good performance. They used Pt powder as catalyst, porous electrode materials and a liquid electrode to increase the contact area.^[4] Nevertheless, it took approximately another 100 years until fuel cells attracted considerable attention. The launch of Sputnik in 1957 and the following space race heavily influenced the development of fuel cells. The high energy density as well as the high efficiency combined with the small weight and size of a fuel cell made it the perfect candidate for space applications. In addition, the reaction product obtained during energy generation could be used by the astronauts as drinking water.^[5] The type of fuel cells used in these first applications were polymer electrolyte membrane fuel cells (PEMFC)^[4] and it is still the one which gains most interest in studies and developments today.^[6] One major concern in PEMFC is the fabrication of a chemical and mechanical stable polymer electrolyte membrane. In the late 1960s the company DuPONT was able to produce the first commercial fuel cell membrane named Nafion®. Due to its good long-term stability this membrane is still used in applications today.^[4,7]

Besides PEMFCs, a variety of fuel cell types exists which are tailored to different fields of application. They can be used as auxiliary power units in vehicles, as power generator in

mobile devices like notebooks or as stationary units to provide electricity and heat.^[8] The stationary systems for combined heat and power have been used in Japanese households for years and have recently started penetrating the European market.^[9] Nevertheless two major barriers to large-scale fuel cell commercialization remain: cost and durability. Regarding cost reduction, great progress was achieved in the last few years. The cost of running a complete fuel cell system was \$275/kW in 2002 and only seven years later in 2009 a price of \$61/kW was reached. This was achieved by using reduced loadings of the expensive catalyst Pt or by exchanging Pt with alloys (e.g. PtCo) or other catalysts like Ni.^[10] A further reduction of the costs to \$30/kW by 2015 would allow competition with conventional combustion engines.^[9] Improving the durability of fuel cells in long-term operation still remains challenging. After a thousand hours of operation most current fuel cells exhibit major performance decay. Even stronger degradation occurs when the fuel cell is operated under start-stop conditions.^[11] The materials used in fuel cells are exposed to acidic conditions, high temperatures, high electrochemical potentials, and abrupt changes in temperatures and potentials. Therefore the development of inexpensive and stable fuel cell components is still a challenging task.

On the basis of low temperature PEMFC (LT-PEMFC), fuel cells with operating temperatures above 100 °C were developed. The so-called high temperature PEMFC (HT-PEMFC) is operated between 150 °C and 200 °C and offers several advantages in contrast to the LT-PEMFC. First, the operation of HT-PEMFCs is simplified because no difficult additional water management is needed to humidify the fuel cell.^[12-14] Additionally, at higher temperatures the tolerance of the catalyst against catalyst poisoning from CO is increased and the cost- and time-intensive cleaning of the fuel with a reformer is not necessary before operation.^[15] Furthermore the increased temperatures lead to faster reaction kinetics on the electrodes and enhanced catalytic activity.^[16-18] Because of the higher temperatures new polymer electrolyte membranes based on thermally stable phosphoric acid doped polybenzimidazole (PBI) were developed.^[12,19,20]

Core components of a HT-PEMFC are the proton conductive polymer electrolyte membrane and the adjacent, catalyst loaded electrodes.^[6] These components account for nearly 50% of the fuel cell production costs.^[21] New materials and modifications of

conventional systems are investigated for membranes and electrodes. For example the mechanical stability and therefore the lifetime stability of membranes can be increased by incorporating silica nanofillers.^[22-24] The standard electrode material so far is high surface area carbon (HSAC) which suffers from severe degradation e.g. due to oxidation during fuel cell operation. The carbon electrodes can be replaced with novel materials like tungsten oxide which also has beneficial effects on the catalyzed reaction.^[25,26] Knowledge of the morphology of the fuel cell components is of great importance, since a high contact area between the catalyst, electrolyte and fuel is necessary for instance. Transmission electron microscopy (TEM) and related analytical techniques offer the possibility to analyze the microstructure of fuel cell electrodes and membranes. It allows the investigation of morphology, chemical composition and coordination of the systems with high spatial resolution.^[27] Several TEM studies of fuel cells are reported in literature, which mainly focus on the investigation of the catalyst loaded electrodes but some research was also done regarding fuel cell membranes. When it comes to the electrodes, the analysis of the catalyst particle distribution^[28] with different loadings^[29-33] or with ongoing fuel cell operation^[34-37] as well as new catalyst alloys^[38-41] are major fields of interest. Studies that focus on the fuel cell membranes mostly investigate the formation of catalyst bands in the membrane.^[35,42] Only few studies address the size and distribution of inorganic nanofillers (e.g. silica nanoparticles) in the membrane.^[23,43,44] In addition, most of the mentioned TEM studies on fuel cells deal with degradation processes occurring at the electrodes. As all degradation processes take place on small scales, TEM is a useful tool to analyze and understand them.^[32,45]

Although several studies about the degradation of the catalyst during fuel cell operation exist, detailed investigation of the structural changes of novel catalyst support materials like tungsten oxide due to degradation are still rare in literature.^[26] The influence of different operation times and modes on the electrode structure has yet to be analyzed. Only few TEM studies of polymer electrolyte membranes exist due to the difficult investigation of organic materials in TEM.^[46,47] The size, distribution and homogeneity of silica nanofillers in membranes are important data to interpret its resulting stability and performance but have not been quantitatively addressed yet.

The focus of this thesis is the detailed investigation of the structure of fuel cell components and their degradation using TEM and scanning electron microscopy (SEM)

and related analytical methods. Knowledge of the morphology, crystallinity and chemical composition of electrodes and membranes is a key issue to understand ongoing processes and optimize existing systems.

1.1 Aim of the thesis

The objective of this thesis is the investigation and optimization of novel materials for fuel cell applications. Different fuel cell membranes and electrodes are characterized via X-ray diffraction (XRD), SEM as well as TEM and its analytical techniques. Sample preparation strategies are developed in order to allow the investigation of very thin but stable samples with TEM. The organic polymers in particular proved very challenging and a new approach was needed. The morphology at the micro- and nanoscale, the crystallinity and the chemical composition of the components are analyzed. The results are then correlated to *in-situ* and *ex-situ* fuel cell tests that are performed by the collaboration partners at ELCOMAX GmbH. Besides determination of the chemical and mechanical stability and performance analysis, studying the degradation behavior of the proton exchange membranes and the catalyst loaded electrodes is a major focus of this thesis.

The incorporation of inorganic fillers into the organic membrane material positively influences the stability as well as the performance of this component. Different silica particle contents are generated in PBI based membranes by *in-situ* sol-gel reaction from the precursor tetraethoxy silane (TEOS) and cross-linked to the polymer chains. The size, shape and distribution of the silica nanoparticles are examined by TEM. The amorphous characteristics and the chemical composition of the silica particles are investigated using XRD as well as electron diffraction (ED) and energy dispersive X-ray spectroscopy (EDS) in TEM. The findings are described in Chapter 5.

Chapter 6 focuses on the influence of an additional heating step before membrane casting. Again, a PBI based proton exchange membrane with incorporated silica nanoparticles is analyzed with a focus on the homogeneity of the particles and their distribution within the membrane. The homogeneity and the morphology of the silica particles are investigated in detail by EDS line scans and maps in the scanning TEM (STEM) mode and electron energy loss spectroscopy (EELS) measurements.

The durability of fuel cell catalyst supports is of great importance for stable, long-term fuel cell operation. Tungsten carbide, tungsten oxide and self-synthesized tungsten oxide are investigated as possible candidates to replace standard HSAC as catalyst support materials. Cyclic voltammetry and XRD are used to investigate the new catalyst supports. The size and distribution of the catalyst nanoparticles on the electrode substrate are determined via TEM. The findings are discussed in Chapter 7.

A membrane electrode assembly (MEA) which utilizes a tungsten oxide based anode is tested under different operation modes and runtimes in single cells and fuel cell stacks in Chapter 8. Detailed TEM investigations of the anode before operation and after 600 h, 2000 h and 35 start-stop cycles are performed to gain insights regarding degradation. The redistribution of the elements in the anode depending on the operation mode is investigated by EDS line scans. Four different areas of the anode are analyzed with regard to degradation effects and the observed changes are correlated to fuel cell performance measurements.

1.2 Chapter references

- [1] Kurzweil, P. *Brennstoffzellentechnik - Grundlagen, Komponenten, Systeme, Anwendungen*; Springer: Wiesbaden, **2013**.
- [2] Grove, W. R. *Philos. Mag.* **1838**, *14*, 127.
- [3] Siemens, W. *Die dynamo-elektrische Maschine*; Springer Berlin: Heidelberg, **1891**.
- [4] Perry, M. L.; Fuller, T. F. *J. Electrochem. Soc.* **2002**, *149*, S59.
- [5] Winter, M.; Brodd, R. J. *Chem. Rev.* **2004**, *104*, 4245.
- [6] Chandan, A.; Hattenberger, M.; El-kharouf, A.; Du, S.; Dhir, A. et al. *J. Power Sources* **2013**, *231*, 264.
- [7] Asensio, J. A.; Sánchez, E. M.; Gómez-Romero, P. *Chem. Soc. Rev.* **2010**, *39*, 3210.
- [8] Reiche, A.; Haufe, S. *Chem. unserer Zeit* **2004**, *38*, 400.
- [9] Wang, Y.; Chen, K. S.; Mishler, J.; Cho, S. C.; Adroher, X. C. *Appl. Energy* **2011**, *88*, 981.
- [10] Schenk, A.; Grimmer, C.; Perchthaler, M.; Weinberger, S.; Pichler, B. et al. *J. Power Sources* **2014**, *266*, 313.
- [11] Borup, R.; Meyers, J.; Pivovar, B.; Kim, Y. S.; Mukundan, R. et al. *Chem. Rev.* **2007**, *107*, 3904.
- [12] Li, Q.; Jensen, J. O.; Savinell, R. F.; Bjerrum, N. J. *Prog. Polym. Sci.* **2009**, *34*, 449.
- [13] Li, Q.; He, R.; Jensen, J. O.; Bjerrum, N. J. *Chem. Mater.* **2003**, *15*, 4896.
- [14] Savadogo, O. *J. Power Sources* **2004**, *127*, 135.
- [15] Wang, C.-P.; Chu, H.-S.; Yan, Y.-Y.; Hsueh, K.-L. *J. Power Sources* **2007**, *170*, 235.
- [16] Zecevic, S. K.; Wainright, J. S.; Litt, M. H.; Gojkovic, S. L.; Savinell, R. F. *J. Electrochem. Soc.* **1997**, *144*, 2973.
- [17] Ma, Y. L.; Wainright, J. S.; Litt, M. H.; Savinell, R. F. *J. Electrochem. Soc.* **2004**, *151*, A8.
- [18] Korsgaard, A. R.; Refshauge, R.; Nielsen, M. P.; Bang, M.; Kær, S. K. *J. Power Sources* **2006**, *162*, 239.
- [19] Samms, S. R.; Wasmus, S.; Savinell, R. F. *J. Electrochem. Soc.* **1996**, *143*, 1225.
- [20] Wainright, J. S.; Wang, J. T.; Weng, D.; Savinell, R. F.; Litt, M. *J. Electrochem. Soc.* **1995**, *142*, L121.
- [21] Spendelow, J. S.; Papageorgopoulos, D. C. *Fuel Cells (Weinheim, Ger.)* **2011**, *11*, 775.
- [22] Ghosh, S.; Maity, S.; Jana, T. *J. Mater. Chem.* **2011**, *21*, 14897.
- [23] Suryani; Chang, Y.-N.; Lai, J.-Y.; Liu, Y.-L. *J. Membr. Sci.* **2012**, *403–404*, 1.
- [24] Wang, S.; Zhao, C.; Ma, W.; Zhang, N.; Zhang, Y. et al. *J. Mater. Chem. A* **2013**, *1*, 621.
- [25] Wickman, B.; Wesselmark, M.; Lagergren, C.; Lindbergh, G. *Electrochim. Acta* **2011**, *56*, 9496.

- [26] Antolini, E.; Gonzalez, E. R. *Appl. Catal. B* **2010**, 96, 245.
- [27] Williams, D. B.; Carter, C. B. *Transmission Electron Microscopy*; Springer US, **2009**.
- [28] Uchida, M.; Park, Y.-C.; Kakinuma, K.; Yano, H.; Tryk, D. A. et al. *Phys. Chem. Chem. Phys.* **2013**, 15, 11236.
- [29] Sattler, M. L.; Ross, P. N. *Ultramicroscopy* **1986**, 20, 21.
- [30] Aragane, J.; Murahashi, T.; Odaka, T. *J. Electrochem. Soc.* **1988**, 135, 844.
- [31] Zhang, X.; Chan, K.-Y. *J. Mater. Chem.* **2002**, 12, 1203.
- [32] Ferreira, P. J.; la O', G. J.; Shao-Horn, Y.; Morgan, D.; Makharia, R. et al. *J. Electrochem. Soc.* **2005**, 152, A2256.
- [33] Maillard, F.; Schreier, S.; Hanzlik, M.; Savinova, E. R.; Weinkauff, S. et al. *Phys. Chem. Chem. Phys.* **2005**, 7, 385.
- [34] Yasuda, K.; Taniguchi, A.; Akita, T.; Ioroi, T.; Siroma, Z. *Phys. Chem. Chem. Phys.* **2006**, 8, 746.
- [35] Kim, L.; Chung, C. G.; Sung, Y. W.; Chung, J. S. *J. Power Sources* **2008**, 183, 524.
- [36] Gyoten, H.; Hirayama, T.; Kondo, J.; Taomoto, A.; Aizawa, M. *Electrochemistry* **2011**, 79, 392.
- [37] Yoshida, K.; Bright, A.; Tanaka, N. *J. Electron Microsc.* **2012**, 61, 99.
- [38] Gontard, L. C.; Dunin-Borkowski, R. E.; Ozkaya, D. *J. Microsc. (Oxford, U. K.)* **2008**, 232, 248.
- [39] Wu, H.; Wexler, D.; Wang, G.; Liu, H. *J. Solid State Electrochem.* **2012**, 16, 1105.
- [40] Stephens, I. E. L.; Bondarenko, A. S.; Gronbjerg, U.; Rossmeisl, J.; Chorkendorff, I. *Energy Environ. Sci.* **2012**, 5, 6744.
- [41] Zhao, J.; Sarkar, A.; Manthiram, A. *Electrochim. Acta* **2010**, 55, 1756.
- [42] Xie, J.; Wood, D. L.; More, K. L.; Atanassov, P.; Borup, R. L. *J. Electrochem. Soc.* **2005**, 152, A1011.
- [43] Suryani; Liu, Y.-L. *J. Membr. Sci.* **2009**, 332, 121.
- [44] Linlin, M.; Mishra, A. K.; Kim, N. H.; Lee, J. H. *J. Membr. Sci.* **2012**, 411–412, 91.
- [45] Shao-Horn, Y.; Sheng, W. C.; Chen, S.; Ferreira, P. J.; Holby, E. F. et al. *Top. Catal.* **2007**, 46, 285.
- [46] Sezen, M.; Plank, H.; Fisslthaler, E.; Chernev, B.; Zankel, A. et al. *Phys. Chem. Chem. Phys.* **2011**, 13, 20235.
- [47] Michler, G. H. *Electron Microscopy of Polymers*; Springer-Verlag Berlin Heidelberg: Leipzig, Germany, **2008**.

2 Theoretical background

2.1 Working principle of fuel cells

A fuel cell is an electrochemical device that converts chemical energy of a fuel directly into electrical energy. Different types of fuel cells exist and they are distinguished by the used electrolyte and by their individual operating temperature. For a PEMFC for example the electrolyte is an insulating, proton conductive polymer electrolyte membrane. The core of a fuel cell system is the MEA. It consists of the electrolyte in the middle, the adjacent catalyst loaded anode and cathode electrodes and a gas diffusion layer (GDL) for each electrode. The anode and cathode usually consist of a microporous carbon catalyst support layer (MPL) that contains Pt nanoparticles with a high surface area.^[1,2] The GDL is composed of a macroporous carbon network and ensures homogeneous gas distribution and electric contact to the MPL. The combination of GDL and electron layer is called gas diffusion electrode (GDE). In order to reach an appropriate voltage, several MEAs are connected in series to a stack. Between the cells bipolar plates are introduced to supply the MEA with fuel and to remove the reaction products water and heat.^[3-7] The components of a PEMFC are illustrated in Figure 2.1.

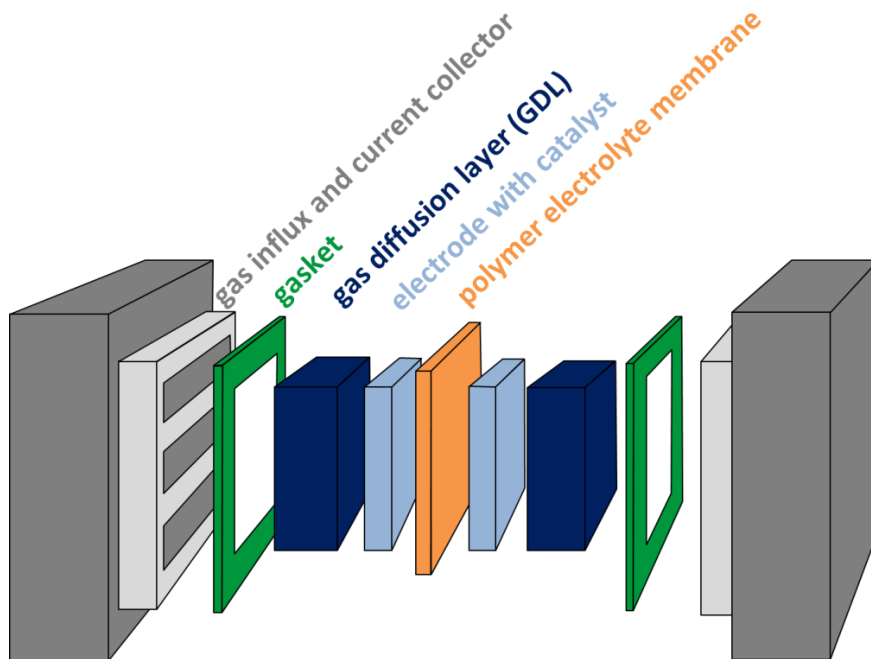


Figure 2.1: Schematic drawing of the main components of a PEMFC. The MEA in the middle consists of the polymer electrolyte membrane and the adjacent catalyst loaded electrodes with their GDLs.

In the following the working principle of fuel cells is described using the example of a PEMFC. The reaction that converts chemical into electrical energy occurs at the two interfaces between the electrodes and the electrolyte. At the anode hydrogen is oxidized to protons ($E^0 = 0 \text{ V}$) (2.1).



The electrons travel via an end-consumer to the cathode where oxygen from air is reduced. The protons formed at the anode can traverse the polymer electrolyte membrane to the cathode. At the cathode water is formed by the reaction of protons and oxide ions ($E^0 = 1.23 \text{ V}$) (2.2).



From the standard potentials E^0 of equations (2.1) and (2.2) an open circuit voltage of 1.23 V is obtained. Due to overpotentials at the electrodes the actual open circuit voltage is usually $\leq 1 \text{ V}$.^[4,8] Both the hydrogen oxidation reaction (HOR) and the oxygen reduction reaction (ORR) at the cathode are catalyzed by a catalyst (e.g. Pt nanoparticles). The membrane separates the oxidation and reduction processes and acts as electrical insulator.^[9] The working principle of a PEMFC is illustrated in Figure 2.2.

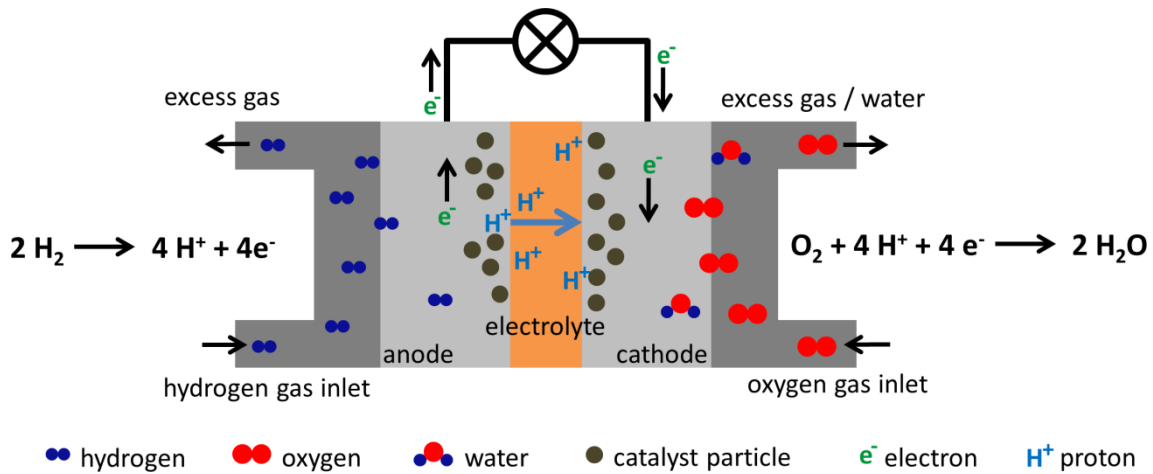


Figure 2.2: Schematic of the working principle of a PEMFC.

In the region of the porous electrode a three-phase interface is established among the reactants, the electrolyte and the catalyst. This area has to be filled with the respective gases (hydrogen or oxygen) and must have electric contact to the electrode and also to the electrolyte. Only when all three components are connected to each other the electrochemical reaction can take place. The absolute area of this three-phase interface

has a major impact on fuel cell performance. In fuel cells which contain a liquid electrolyte it is important to maintain a balance among the electrode, electrolyte and gaseous phases in the porous electrode structure. Otherwise the electrode may be flooded by the electrolyte and therefore block the transport of gaseous reactants to the reaction sites.^[10]

2.2 Types of fuel cells

As already mentioned, above several types of fuel cells exist and they can be classified by the used electrolyte and/or the operating temperature. Low-temperature fuel cells are the alkaline fuel cell (AFC), the LT- and the HT-PEMFC, the direct methanol fuel cell (DMFC) and the phosphoric acid fuel cell (PAFC). The molten carbonate fuel cell (MCFC) and the solid oxide fuel cell (SOFC) belong to the group of high-temperature fuel cells and are operated above 600 °C. Table 2.1 gives an overview of fuel cell types in the order of increasing operation temperature.^[2,10,11]

Table 2.1: Fuel cell types that are currently in use and development.

	Operating temperature / °C	Electrolyte	Charge carrier in the electrolyte
LT-PEMFC	50–90	Proton exchange membrane	H ⁺
AFC	60–90	Potassium hydroxide	OH ⁻
DMFC	80–150	Proton exchange membrane	H ⁺
HT-PEMFC	150–200	Proton exchange membrane	H ⁺
PAFC	160–220	Phosphoric acid	H ⁺
MCFC	600–800	Molten carbonate	CO ₃ ²⁻
SOFC	800–1000	Yttrium stabilized zirconia	O ²⁻

As explained above, PEMFCs use a proton exchange membrane as electrolyte. The most used membrane in LT-PEMFCs is Nafion® which is a sulfonated tetrafluorethylene based fluoropolymer and an excellent proton conductor.^[12] In a LT-PEMFC the only liquid is water which minimizes corrosion. Nevertheless, the water management plays a crucial role for the performance of the fuel cell. If the electrolyte dries out the membrane loses its proton conductivity and the fuel cell cannot operate. Therefore, humidification of the introduced gases and heat management is needed. Due to the lower temperatures and hence reduced reaction kinetics on the electrodes, the use of high catalyst loadings of

expensive noble metals like Pt is necessary. The catalyst is also vulnerable to CO poisoning at the rather low operating temperatures.^[13,14] Since the HT-PEMFC is operated at temperatures above 100 °C the electrolyte Nafion® is replaced by temperature and chemically stable polymers like PBI. Instead of water, phosphoric acid is introduced to ensure proton conductivity. In an AFC the electrolyte potassium hydroxide (concentration ~ 30 wt.-%) is retained in an asbestos matrix and several electrocatalysts like Ni, Ag, metal oxides and noble metals can be used. AFCs exhibit very high electrical efficiencies but they underlie restrictions concerning the used gases. Smallest impurities of the gases with CO₂ lead to decomposition of the electrolyte to carbonate ions and water. Therefore cost intensive pre-cleaning of the introduced oxygen is necessary.^[15] The DMFC is based on the technology of LT-PEMFC. Here, methanol is directly used as fuel and reforming is applied in DMFC. Its advantages are a high energy density and the possibility to use liquid fuel. DMFCs are suitable for devices that are turned on and off regularly.^[10,16] In a PAFC phosphoric acid concentrated to 100% in a silicon carbide matrix is used as electrolyte. Operating temperatures of up to 220 °C are possible which results in a high tolerance against CO and CO₂. Typically Pt is used as catalyst in this type of fuel cell.^[2] A combination of alkali carbonates in a ceramic matrix of LiAlO₂ is used as electrolyte in MCFCs. At operating temperatures of above 600 °C the alkali carbonates form a conductive salt and carbon ions provide ionic conduction. The advantage of MCFC is that Ni (anode) and NiO (cathode) are sufficient as catalysts. At this high temperature expensive noble metals are not required.^[17] The SOFC is operated at 800–1000 °C and uses solid, nonporous metal oxides like yttrium stabilized zirconia as electrolyte. Oxygen ions act as charge carriers. Like in MCFCs no noble metals are needed as catalysts and the fuel can be reformed internally. Nevertheless, the high operating temperatures also limit the application of SOFC since shutting down and starting up takes long time and effort.^[2,10,18]

2.3 Strengthening of PBI membranes for HT-PEMFC

With the introduction of HT-PEMFCs new membranes had to be found that meet the requirements of this type of fuel cell. Thermally stable phosphoric acid doped PBI membranes have proven to be ideal candidates for long-term fuel cell operation in HT-PEMFCs.^[19-21] PBI membranes are usually synthesized by casting a solution of PBI

powder in N,N-dimethylacetamide (DMAc). Afterwards, the prepared membrane is immersed in a phosphoric acid solution which leads to an immobilization of the acid in the polymer.^[22] With an increasing amount of phosphoric acid present in the membrane an improvement of the proton conductivity is possible but simultaneously the tensile strength of the membrane decreases.^[19] Different concepts have been developed to improve the mechanical properties of PBI membranes. To increase the strength, the formation of ionic and covalent networks or the incorporation of additional particles have been demonstrated to be successful.^[19,23] Different additives to the PBI have been investigated such as graphene^[24,25], carbon nanotubes^[26-28], clay^[29,30], silica- and phosphotungstic acid^[31-33] and silica nanoparticles which can be modified further with functional groups.^[34-41]

Silica nanoparticles can be incorporated in the membrane via an *in-situ* sol-gel synthesis.^[42,43] Chuang et al. synthesized silica nanoparticles *in-situ* using the precursor TEOS and connected them to the membrane using (3-isocyanatopropyl)triethoxysilane as linker. The resulting membrane exhibited an improved mechanical stability. The incorporated silica particles also have an influence on the proton conductivity of the membrane, although contradictory findings are reported in literature. Suryani et al. found that the proton conductivity increased due to incorporation of sulfonated silica nanoparticles. They concluded that a higher acid doping level is possible for the modified membrane and that new and faster proton conductive channels can form.^[34,35] On the other hand Chuang et al. observed a slight decrease in proton conductivity and they suggested that the silica particles inhibit the mobility of the protons within the membrane.^[37] It seems that the morphology, size and distribution of the silica nanoparticles are important and that differences in these quantities are responsible for the different results.

The mechanical properties get slightly worse at higher silica amounts as well as in the presence of phosphoric acid.^[37] The morphology of the silica nanoparticles can be controlled by additives and the reaction conditions.^[44] However, the resulting particle size, the morphology and the distribution of the particles has to be studied for new or modified membrane system again since its formation processes are not fully understood yet.^[45]

2.4 Degradation of Pt catalysts in HT-PEMFC

The most often used material for electrodes in HT-PEMFC is HSAC^[1] loaded with Pt nanoparticles.^[2] In order to enhance fuel cell efficiency effective and durable catalysts are necessary and this is an active area of research resulting in a large number of publications. On the same time, a reduction or replacement of Pt is desired because of its high costs and its limited natural resources.^[46,47] In addition, Pt is easily poisoned by CO or chlorides which can be inserted into the cell in the form of reactants or during synthesis.^[47] The distribution of the Pt particles and their available surface area has a large impact on fuel cell performance. A major degradation effect leading to a decrease in performance is the coalescence of Pt particles during operation. Smaller particles dissolve, they diffuse towards other particles and then agglomerate via Ostwald ripening.^[48-51] Another possibility is the migration of Pt particles and subsequent agglomeration.^[52,53] This type of degradation is well studied and huge effort is made to avoid it.

2.5 Tungsten oxide as candidate for HT-PEMFC electrodes

Besides the catalyst particles, also the catalyst support material can suffer from degradation with ongoing fuel cell operation.^[3,54] The turbostratic carbon used as catalyst support material can get oxidized which leads to a detachment of catalyst particles and therefore to a reduced efficiency. Although the oxidation of carbon is kinetically hindered to a great extent, high temperatures and potentials can still lead to carbon corrosion.^[55,56] A sign for carbon corrosion is a detectable amount of CO₂ in the exhaust gases.^[57] Due to this type of degradation non-carbon based materials are investigated as possible candidates to replace HSAC. Several requirements have to be fulfilled by an adequate electrode material. A high electrical conductivity is needed to ensure optimal transport of the electrons to the electrodes and away from them. Furthermore a stable anchoring of the catalyst to the electrode is important to prevent catalyst movement, agglomeration or loss. Besides a high corrosion resistance, a high surface area of the applied electrode material is beneficial to obtain good long-term efficiency. Alternatives to standard carbon material that are currently under investigation are electrodes based on e.g. titanium oxide, silicon oxide and tungsten oxide.^[58-60]

Tungsten is a transition element that can form a variety of oxides with different valence states (from -1 to $+6$). This flexibility makes tungsten suitable for photochromic, electrochromic, photocatalytic, gas sensor and fuel cell applications.^[61] Stoichiometric WO_3 is a $5d$ -transition-metal-oxide which exhibits a slightly distorted ABO_3 perovskite crystal structure. The W ions occupy the octahedral B cation sites and the A site is vacant.^[62,63] This monoclinic crystal structure is formed below 180°C .^[64] Stoichiometric WO_3 is an insulator due to the unoccupied $5d$ -orbitals of the W^{6+} .^[60,63] Since a high conductivity is vital for a fuel cell electrode material, tungsten suboxides WO_{3-x} are used.^[65] Due to oxygen vacancies pentavalent tungsten atoms are present in the WO_{3-x} which positively influences the electric conductivity of the material.^[65-68] In that case, the $5d$ -orbitals host delocalized electrons which makes WO_{3-x} an n -type semiconductor with a band gap of $2.6\text{--}2.8\text{ eV}$. Further advantages of this material are its high corrosion resistance, high melting point (1700°C), high tolerance against CO and excellent stability against the electrochemical conditions in a fuel cell. It can be used as catalyst, co-catalyst or catalyst support in fuel cell applications.^[58,60,68-71] Additionally, WO_{3-x} can also support the catalyst reaction due to hydrogen spill over when it is used as electrode material at the anode. The phenomenon of hydrogen spill over is related to the formation of tungsten bronzes as first described by Wöhler in 1824.^[72] During this process the protons, formed from hydrogen directly at the catalyst, can transfer to the support material WO_{3-x} and form oxyhydroxides as $\text{WO}_{3-x}(\text{OH})_y$. Hence the active catalyst sites can receive the next reactant faster. Via the Grotthuss mechanism the adsorbed protons can travel through the anode material to the electrolyte.^[73] This mechanism was proven by Tseung et al. in 1997.^[74]

2.6 Chapter references

- [1] Kaiser, J.; Simonov, P. A.; Zaikovskii, V. I.; Hartnig, C.; Jorissen, L. et al. *J. Appl. Electrochem.* **2007**, *37*, 1429.
- [2] Carrette, L.; Friedrich, K. A.; Stimming, U. *Fuel Cells* **2001**, *1*, 5.
- [3] Borup, R.; Meyers, J.; Pivovar, B.; Kim, Y. S.; Mukundan, R. et al. *Chem. Rev.* **2007**, *107*, 3904.
- [4] Kurzweil, P. *Brennstoffzellentechnik - Grundlagen, Komponenten, Systeme, Anwendungen*; Springer: Wiesbaden, **2013**.
- [5] Mehta, V.; Cooper, J. S. *J. Power Sources* **2003**, *114*, 32.
- [6] Chatenet, M.; Dubau, L.; Job, N.; Maillard, F. *Catal. Today* **2010**, *156*, 76.
- [7] Morozan, A.; Josselme, B.; Palacin, S. *Energy Environ. Sci.* **2011**, *4*, 1238.
- [8] Carrette, L.; Friedrich, K. A.; Stimming, U. *ChemPhysChem* **2000**, *1*, 162.
- [9] Chu, F.; Lin, B.; Qiu, B.; Si, Z.; Qiu, L. et al. *J. Mater. Chem.* **2012**, *22*, 18411.
- [10] *Fuel Cell Handbook*, EG&G technical services, 2000.
- [11] Dufour, A. U. *J. Power Sources* **1998**, *71*, 19.
- [12] Costamagna, P.; Srinivasan, S. *J. Power Sources* **2001**, *102*, 242.
- [13] Zhang, H.; Shen, P. K. *Chem. Soc. Rev.* **2012**, *41*, 2382.
- [14] Li, Q.; He, R.; Gao, J.-A.; Jensen, J. O.; Bjerrum, N. J. *J. Electrochem. Soc.* **2003**, *150*, A1599.
- [15] Kohnke, H.-J. *Chem. Ing. Tech.* **2011**, *83*, 2027.
- [16] Baldauf, M.; Preidel, W. *J. Power Sources* **1999**, *84*, 161.
- [17] Farooque, M.; Maru, H. C. *J. Power Sources* **2006**, *160*, 827.
- [18] Landes, H. *Chem.-Ing.-Tech.* **1995**, *67*, 1310.
- [19] Li, Q.; Jensen, J. O.; Savinell, R. F.; Bjerrum, N. J. *Prog. Polym. Sci.* **2009**, *34*, 449.
- [20] Samms, S. R.; Wasmus, S.; Savinell, R. F. *J. Electrochem. Soc.* **1996**, *143*, 1225.
- [21] Wainright, J. S.; Wang, J. T.; Weng, D.; Savinell, R. F.; Litt, M. *J. Electrochem. Soc.* **1995**, *142*, L121.
- [22] Ma, Y. L.; Wainright, J. S.; Litt, M. H.; Savinell, R. F. *J. Electrochem. Soc.* **2004**, *151*, A8.
- [23] Asensio, J. A.; Sánchez, E. M.; Gómez-Romero, P. *Chem. Soc. Rev.* **2010**, *39*, 3210.
- [24] Wang, Y.; Shi, Z.; Fang, J.; Xu, H.; Yin, J. *Carbon* **2011**, *49*, 1199.
- [25] Wang, Y.; Shi, Z.; Fang, J.; Xu, H.; Ma, X. et al. *J. Mater. Chem.* **2011**, *21*, 505.
- [26] Suryani; Chang, C.-M.; Liu, Y.-L.; Lee, Y. M. *J. Mater. Chem.* **2011**, *21*, 7480.
- [27] Fujigaya, T.; Okamoto, M.; Nakashima, N. *Carbon* **2009**, *47*, 3227.
- [28] Kannan, R.; Kagalwala, H. N.; Chaudhari, H. D.; Kharul, U. K.; Kurungot, S. et al. *J. Mater. Chem.* **2011**, *21*, 7223.

- [29] Chuang, S.-W.; Hsu, S. L.-C.; Hsu, C.-L. *J. Power Sources* **2007**, *168*, 172.
- [30] Ghosh, S.; Sannigrahi, A.; Maity, S.; Jana, T. *J. Phys. Chem. C* **2011**, *115*, 11474.
- [31] He, R.; Li, Q.; Xiao, G.; Bjerrum, N. J. *J. Membr. Sci.* **2003**, *226*, 169.
- [32] Staiti, P. *Mater. Lett.* **2001**, *47*, 241.
- [33] Staiti, P.; Minutoli, M.; Hocevar, S. *J. Power Sources* **2000**, *90*, 231.
- [34] Suryani; Liu, Y.-L. *J. Membr. Sci.* **2009**, *332*, 121.
- [35] Suryani; Chang, Y.-N.; Lai, J.-Y.; Liu, Y.-L. *J. Membr. Sci.* **2012**, *403–404*, 1.
- [36] Ghosh, S.; Maity, S.; Jana, T. *J. Mater. Chem.* **2011**, *21*, 14897.
- [37] Chuang, S.-W.; Hsu, S. L.-C.; Liu, Y.-H. *J. Membr. Sci.* **2007**, *305*, 353.
- [38] Mustarelli, P.; Quartarone, E.; Grandi, S.; Carollo, A.; Magistris, A. *Adv. Mater.* **2008**, *20*, 1339.
- [39] Yu, Y.; Xin, H. L.; Hovden, R.; Wang, D.; Rus, E. D. et al. *Nano Lett.* **2012**, *12*, 4417.
- [40] Pu, H.; Liu, L.; Chang, Z.; Yuan, J. *Electrochim. Acta* **2009**, *54*, 7536.
- [41] Sadeghi, M.; Semsarzadeh, M. A.; Moadel, H. *J. Membr. Sci.* **2009**, *331*, 21.
- [42] Hench, L. L.; West, J. K. *Chem. Rev.* **1990**, *90*, 33.
- [43] Alberti, G.; Casciola, M. *Annu. Rev. Mater. Res.* **2003**, *33*, 129.
- [44] Colicchio, I.; Keul, H.; Sanders, D.; Simon, U.; Weirich, T. E. et al. *Fuel Cells* **2006**, *6*, 225.
- [45] Alzina, C.; Sbirrazzuoli, N.; Mija, A. *J. Phys. Chem. C* **2011**, *115*, 22789.
- [46] Christian, J. B.; Smith, S. P. E.; Whittingham, M. S.; Abruña, H. D. *Electrochem. Commun.* **2007**, *9*, 2128.
- [47] Ehteshami, S. M. M.; Chan, S. H. *Electrochim. Acta* **2013**, *93*, 334.
- [48] Yoshida, K.; Bright, A.; Tanaka, N. *J. Electron Microsc.* **2012**, *61*, 99.
- [49] Shao-Horn, Y.; Ferreira, P.; la O', G. J.; Morgan, D.; Gasteiger, H. A. et al. *ECS Trans.* **2006**, *1*, 185.
- [50] Schulze, M.; Wagner, N.; Kaz, T.; Friedrich, K. A. *Electrochim. Acta* **2007**, *52*, 2328.
- [51] Mayrhofer, K. J. J.; Meier, J. C.; Ashton, S. J.; Wiberg, G. K. H.; Kraus, F. et al. *Electrochem. Commun.* **2008**, *10*, 1144.
- [52] Vielstich, W.; Gasteiger, H.; Lamm, A. *Handbook of Fuel Cells, Fundamentals, Technology and Applications*; Volume 2, John Wiley & Sons: New York, **2003**.
- [53] Wilson, M. S.; Garzon, F. H.; Sickafus, K. E.; Gottesfeld, S. *J. Electrochem. Soc.* **1993**, *140*, 2872.
- [54] Jensen, J. O.; Li, Q.; Pan, C.; Bjerrum, N. J.; Rudbeck, H. C. et al. In *18th World Hydrogen Energy Conference 2010*; Stolten, D., Grube, T., Eds.; Forschungszentrum Jülich GmbH, Zentralbibliothek: Essen, 2010, p 115.
- [55] Meier, J. C.; Galeano, C.; Katsounaros, I.; Topalov, A. A.; Kostka, A. et al. *ACS Catalysis* **2012**, *2*, 832.

- [56] Meier, J. C.; Katsounaros, I.; Galeano, C.; Bongard, H. J.; Topalov, A. A. et al. *Energy Environ. Sci.* **2012**, 5, 9319.
- [57] Matthew, M.; Emin Caglan, K.; Veziroglu, N. T. *Polymer Electrolyte Fuel Cell Degradation*; Academic Press: Boston, **2012**.
- [58] Sharma, S.; Pollet, B. G. *J. Power Sources* **2012**, 208, 96.
- [59] Winter, M.; Brodd, R. J. *Chem. Rev.* **2004**, 104, 4245.
- [60] Ye, Y.; Joo, J.; Lim, B.; Lee, J. *Chemistry – A European Journal* **2012**, 18, 2797.
- [61] Chhina, H.; Campbell, S.; Kesler, O. J. *Electrochem. Soc.* **2007**, 154, B533.
- [62] Salje, E.; Viswanathan, K. *Acta Crystallographica Section A* **1975**, 31, 356.
- [63] Reich, S.; Tsabba, Y. *Eur. Phys. J. B* **1999**, 9, 1.
- [64] Tanisaki, S. *J. Phys. Soc. Jpn.* **1960**, 15, 573.
- [65] Guo, C.; Yin, S.; Yan, M.; Kobayashi, M.; Kakihana, M. et al. *Inorg. Chem.* **2012**, 51, 4763.
- [66] He, T.; Yao, J. *J. Mater. Chem.* **2007**, 17, 4547.
- [67] Viswanathan, K.; Brandt, K.; Salje, E. J. *Solid State Chem.* **1981**, 36, 45.
- [68] Pickering, R.; Tilley, R. J. D. *J. Solid State Chem.* **1976**, 16, 247.
- [69] Lebedeva, N. P.; Rosca, V.; Janssen, G. J. M. *Electrochim. Acta* **2010**, 55, 7659.
- [70] Lassner, E.; Schubert, W.-D. *Tungsten: Properties, Chemistry, Technology of the Element, Alloys and Chemical Compounds*; Springer-Verlag: Berlin, **1999**.
- [71] Song, Y.; Yang, Y.; Medforth, C. J.; Pereira, E.; Singh, A. K. et al. *J. Am. Chem. Soc.* **2003**, 126, 635.
- [72] Wöhler, F. *Annalen der Physik* **1824**, 78, 345.
- [73] Nalbadjan, V. B.; Trubnikov, I. L.; Bukun, N. G.; Medvedev, B. S. *Inorganic Mater* **1986**, 22, 836.
- [74] Tseung, A. C. C.; Chen, K. Y. *Catal. Today* **1997**, 38, 439.

3 Characterization methods

3.1 X-ray diffraction

XRD is a common technique to obtain quantitative and qualitative information concerning the crystal structure of a material. With its help it is possible to determine lattice parameters, particle sizes and phase compositions of the analyzed material.

X-rays are generated in a high vacuum tube by acceleration of a focused electron beam which is then directed towards an anode material (such as Cu or Co). The electron beam excites inner shell electrons of the anode material to unoccupied states. When these electrons relax back to their ground state X-rays can be emitted or Auger electrons are released which are characteristic for each material. In addition, a fraction of the incident electrons is slowed down in the Coulomb field of the atomic nucleus which leads to the so-called *bremsstrahlung*. By using several metal filters, a collimator and a monochromator a monochromatic X-ray beam without *bremsstrahlung* can be achieved (for example Cu $K\alpha$ radiation). The so generated X-rays possess wavelengths between 0.1 Å and 100 Å.

A part of the X-rays is scattered at the electron cloud of the individual sample atoms located at different lattice planes. At certain Bragg angles constructive interference between several scattered waves occurs. The scattered waves remain in phase when the path length difference of each wave is equal to an integer number of the wavelength (see Figure 3.1). The Bragg equation (3.1) gives the relation of the lattice plane distance to the scattering angle.

$$n\lambda = 2d_{hkl} \sin \theta \quad (3.1)$$

Here, n is a positive integer corresponding to the order of diffraction, λ is the wavelength of the X-rays, d_{hkl} is the lattice plane distance of the analyzed sample with the Miller indices hkl and θ is the scattering angle.^[1,2]

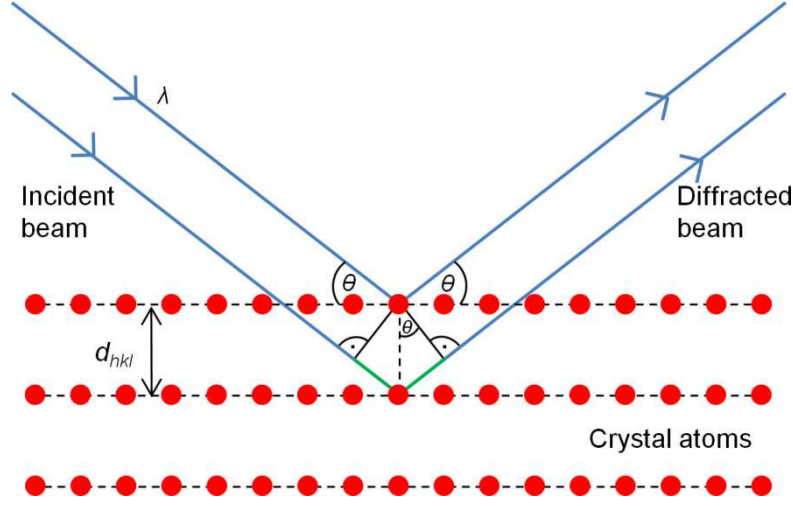


Figure 3.1: Schematic illustration of the Bragg relation. Two X-rays (blue) with the wavelength λ are scattered at an angle θ by parallel atomic lattice planes (red) with a distance d_{hkl} . The path difference is marked in green. Modified from Williams and Carter.^[3]

Depending on the crystallinity of the material different diffraction patterns are obtained. XRD patterns of crystalline materials show sharp diffraction peaks with a defined distribution regarding their position and intensity. This is because of the regular, periodic arrangement of atoms in such materials. For amorphous materials exhibiting no long-range ordering only broad diffraction peaks can be observed.

By measuring the broadening of the diffraction peaks the average crystallite size (D_{XRD}) of e.g. crystalline nanoparticles can be calculated via the Scherrer equation (3.2).^[4]

$$D_{XRD} = \frac{K\lambda}{\Delta(2\theta) \cos\theta} \quad (3.2)$$

K is the shape factor (0.9 for spherical shape), λ is the X-ray wavelength in nm, $\Delta(2\theta)$ is the peak broadening at full width at half maximum (FWHM) in radians and θ is the Bragg angle.

3.2 Electron microscopy

Electron microscopy is a powerful tool that is commonly used to investigate the micro- and nanostructure of materials. In contrast to a light microscope, accelerated electrons are used as source of illumination in electron microscopes. The idea of electron microscopy was proposed shortly after the discovery of the wave-particle dualism by Louis de Broglie in 1924. In general, the resolution of a microscope is limited by

diffraction effects and the wavelength of the illumination source (Rayleigh criterion). Hence, the substantially shorter wavelength of electrons compared to visible light and their wave-like characteristics allow atomic resolution and ED. The term electron microscopy was first used in 1932 by Knoll and Ruska who also built one of the first TEMs.

Each type of electron microscope utilizes an electron gun that generates a beam of electrons accelerated by an electric field. The kinetic energy of the electrons is equal to the potential energy (equation (3.3)):

$$\frac{m_0 v^2}{2} = eV \quad (3.3)$$

where e is the elementary charge, V is the acceleration voltage and m_0 is the electron mass. The momentum p of the electrons can be calculated as shown in equation (3.4):

$$p = m_0 v = \sqrt{2m_0 eV} \quad (3.4)$$

Via the de Broglie equation the wavelength of the electrons can finally be related to the acceleration voltage of the electron microscope (equation (3.5)):

$$\lambda = \frac{h}{p} = \frac{h}{m_0 v} = \frac{h}{\sqrt{2m_0 eV}} \quad (3.5)$$

where h is Planck's constant. This calculation is valid for SEMs but since most TEMs are operated above 100 kV the velocity of the electrons becomes greater than half the speed of light. Therefore a relativistic approach has to be used to calculate the wavelength in these cases. In a typical TEM wavelengths shorter than 0.03 Å can be reached. Nevertheless, the resolution of an electron microscope is way larger due to lens aberrations as explained later.

Another advantage of electron microscopes versus light microscopes is the fact that electrons as an ionizing radiation can interact with matter in various ways. The generation of these secondary signals can be used to gather information about e.g. the morphology and chemical composition of the sample. Electron microscopes are usually operated at high vacuum to prevent interaction of the electron beam with gas molecules in the column. Figure 3.2 illustrates the signals generated due to interaction of an electron beam with a sample.

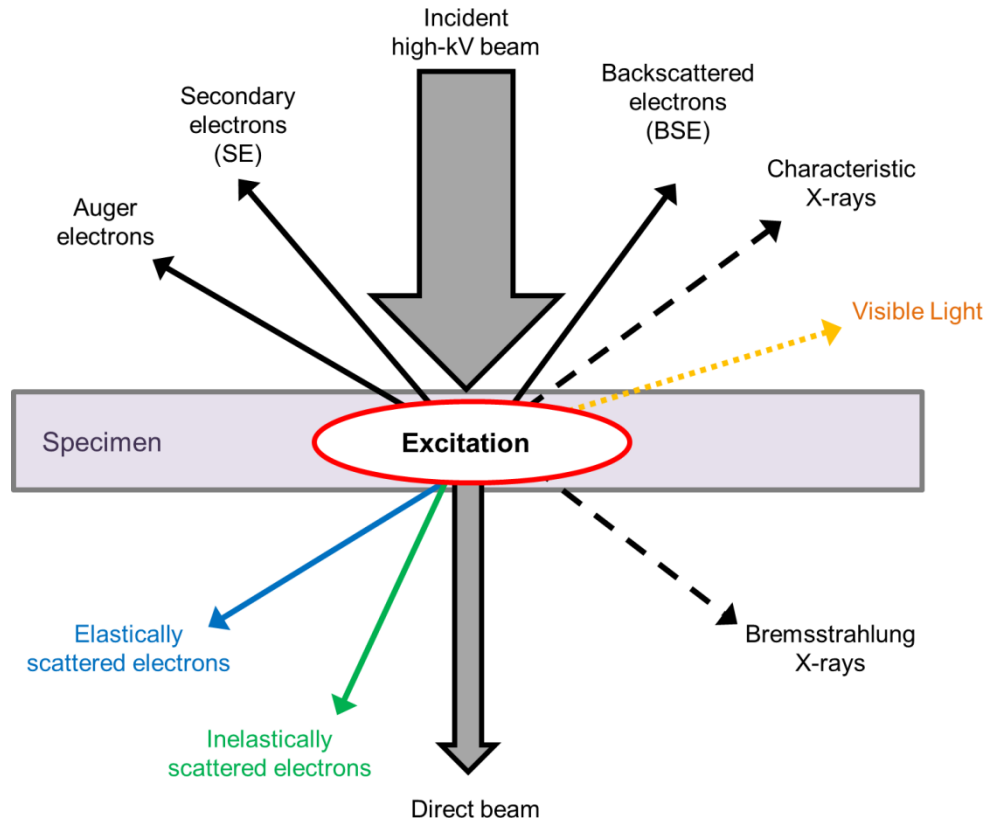


Figure 3.2: Scheme of the interaction of an electron beam with the specimen. Several signals which can be utilized for analysis are generated in this process. Modified from Williams and Carter.^[3]

Secondary electrons (SE) and backscattered electrons (BSE) are used for imaging in SEM. The imaging in TEM is based on elastically scattered and inelastically scattered electrons which are transmitted through the sample. The generated characteristic X-rays and Auger electrons can be utilized for analytical measurements giving information on the elemental composition. The energy loss of the transmitted inelastically scattered electrons is required for EELS.

In summary in electron microscopy, the generated signals allow imaging, diffraction investigations and additional analytical methods. The following chapters will go into more detail on the utilization of the different signals and on the mentioned techniques.^[3,5]

3.2.1 Scanning electron microscopy

SEM is commonly used to analyze the surface morphology of a bulk sample or to investigate cross-sections of layered structures. In a SEM an accelerated electron beam is scanned over a specimen. The generated signals of each sample point, which are

separated in SE and BSE, are detected and an image of the sample surface topography or composition can be formed. Although the resolution of an SEM is inferior to a TEM, resolutions better than 1 nm can be achieved. In contrary to micrographs obtained from TEM, the images in SEM provide a high depth of field which gives an intuitively understandable three dimensional impression of the sample surface. The investigated samples have to be conductive or otherwise charging effects due to electron trapping can occur. To avoid this disturbance samples are usually coated with thin layers of a conductive material e.g. graphite or gold before measurement. Different types of electron guns are available to generate an electron beam in a SEM. In thermionic guns a tungsten wire or a lanthanum hexaboride crystal are heated up and thus emit electrons. Other emitters are thermally assisted field emitters (Schottky emitters) and cold field emitters. By applying an electrical field at the sharp tip of the field emitter the potential barrier is reduced and electrons can tunnel from the cathode into the vacuum. In the case of thermally assisted field emitters additional heating is provided to raise the electrons energy. The advantages of field emitters are the high intensity and the narrow energy distribution of the generated electron beam. The emitted electrons are accelerated in a SEM to energies between 1 keV and 30 keV by applying an electric field between the cathode and the anode. A condenser lens system and the objective lens demagnify the electron beam to a diameter of 2–10 nm when hitting the sample. With help of scanning coils the electron beam is scanned across the sample. SE have energies of few eV and are collected by an Everhart-Thornley detector. Since they arise from the upper ~50 nm of the sample surface they are used to study the morphology of the sample. BSE on the other hand have energies of several keV close to the energy of the incident electron beam. These electrons are quasi-elastically scattered by the specimen and their intensity strongly depends on the atomic number of the investigated material. Therefore BSE are most commonly used to visualize the elemental composition of the sample. The detection of BSE is realized with dedicated BSE detectors based on semiconductor devices.^[5,6] A schematic illustration of a SEM showing its main components is given in Figure 3.3.

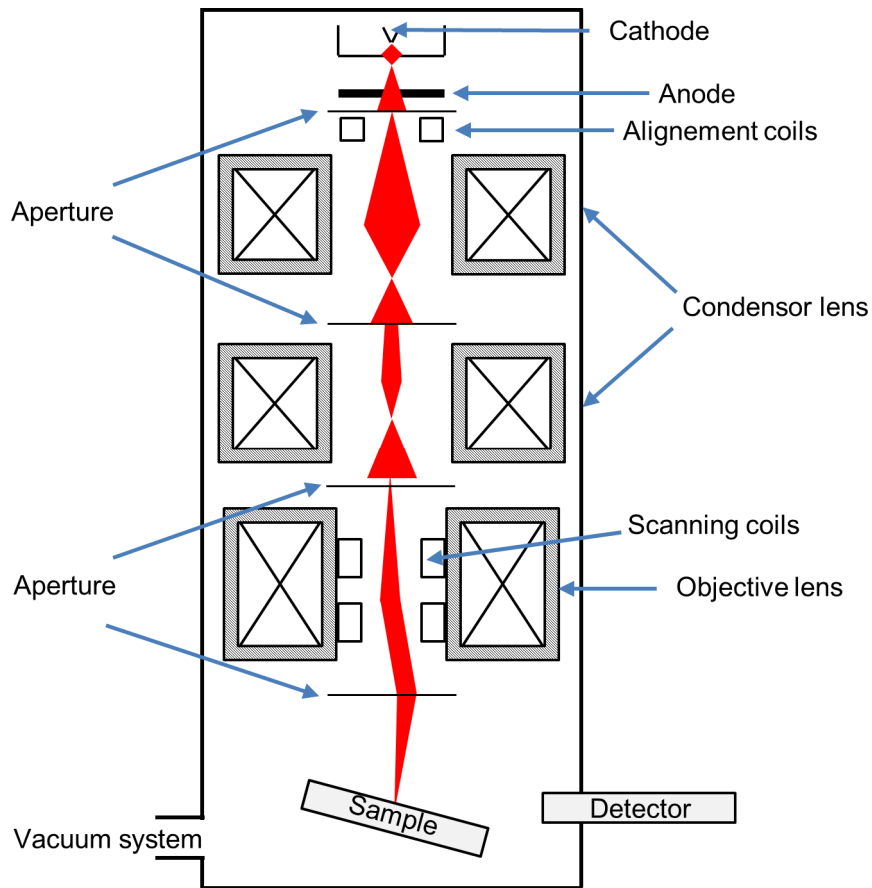


Figure 3.3: Schematic drawing of a SEM assembly and the electron path. Modified from Brandon and Kaplan.^[6]

3.2.2 Focused ion beam microscopy

Focused ion beam (FIB) microscopy is similar to SEM with regards to setup and basic imaging as can be seen in Figure 3.4. It is a powerful tool that allows the precise milling of specimens so that for example high quality TEM samples or defined nanostructures for semiconductor devices can be achieved.^[7] Instead of electrons, accelerated ions (e.g. gallium or helium) are used to image and manipulate the sample. In general an electron and ion beam column can be implemented in one system to enable both processes at the same time. An ion gun is built of a tungsten needle that is covered with liquid gallium which forms a so-called Taylor cone. A strong electric field is applied at the small tip which causes ionization and finally emission of the ions, a process called field evaporation. The ions are accelerated by an electric field to energies of 1–50 keV. The beam is focused via electrostatic lenses and scanned over the sample like in a SEM. When the ion beam hits the sample at lower beam currents secondary ions and SE are generated which can be used for imaging. The imaging contrast depends on the

orientation of the investigated crystals. If a sample is oriented in a particular zone axis the incoming ion beam is penetrating deeper into the crystal (channeling effect). During this process SE are generated but since they cannot escape from the sample the regarding crystal appears darker. As mentioned above, the great advantage of a FIB is the nanometer precise sputtering and milling of material (micro machining). That way it is possible to choose the exact area that should be prepared for TEM investigations. At higher beam currents sample atoms can easily be removed due to inelastic interaction with the ion beam. Before the milling a protection layer of e.g. C or Pt is deposited at the desired sample area to avoid damage of the surface structure of the specimen. After the rough cutting of the sample it is polished by using very low beam currents until electron transparency is reached.^[6,8] Depending on the type of TEM sample preparation the thinned lamella is transferred to a TEM grid or the thinned stripe of material is fixed in a folding grid. The two mentioned sample preparation strategies are described in detail in 4.4.2.

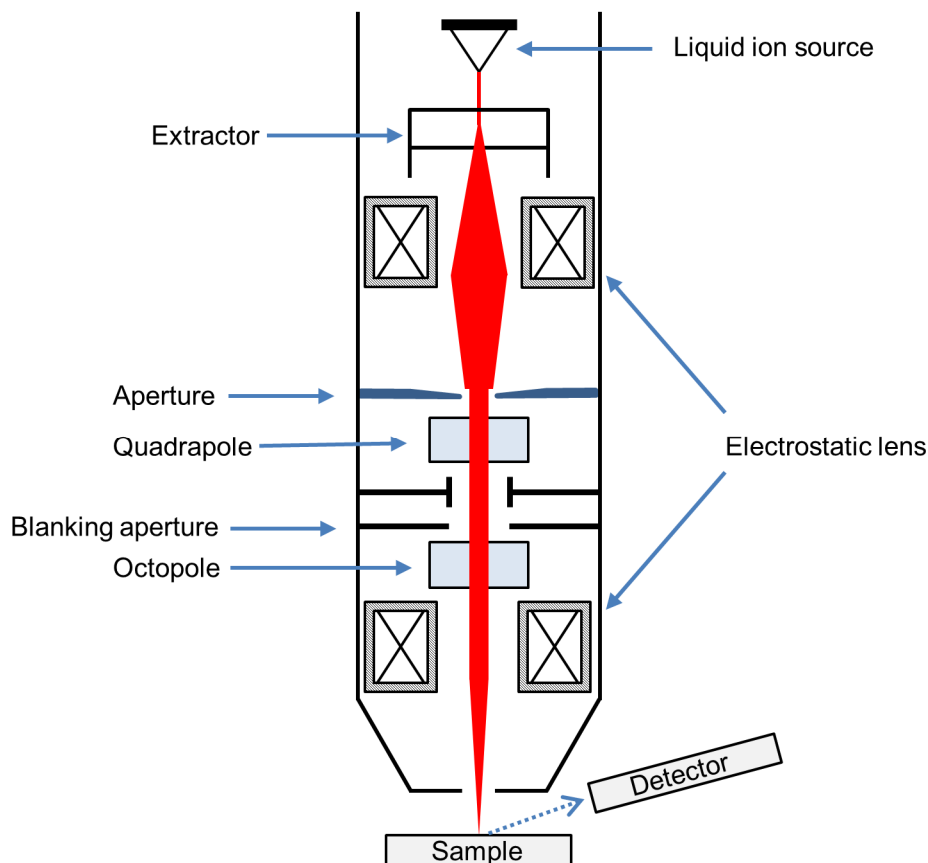


Figure 3.4: Schematic drawing of a FIB microscope. Modified from Brandon and Kaplan.^[6]

3.2.3 Transmission electron microscopy

In TEM, electrons are transmitted through a thin sample and the interaction of the electrons with the sample is used to form an image and gain analytical information on it. The resolution of a standard TEM/STEM lies in the sub-nanometer regime (see chapter 3.2) and in addition it allows the accomplishment of several analytical measurements. The setup of a TEM/STEM is similar to a SEM (see Figure 3.3) with the main difference that only electrons that are transmitted through the electron transparent sample are detected. The electron beam can be generated by different electron guns as described in chapter 3.2.1. TEMs are operated at an acceleration voltage ranging from 80–300 kV depending on the studied material. Just like in SEM the focusing and deflection of the beam is realized via electromagnetic lenses. Usually a TEM consists of three sets of lenses and corresponding apertures. The condenser lens system focuses the electron beam on the specimen and regulates the intensity and the convergence of the beam. It can be operated such that an illumination with a parallel or a convergent electron beam is possible. The objective lens system forms the first intermediate image or diffraction pattern of the sample and is located in close distance to the specimen. The specimen itself is inserted via a special sample holder and usually has a diameter of 3 mm and a thickness of less than 100 nm. The ED pattern of the specimen is created in the back focal plane of the objective lens. Via the objective aperture inserted in this back focal plane a selected part of the transmitted electrons can be blocked in order to enhance the contrast of the resulting image (explained in more detail later). The following selected area diffraction (SAD) aperture which is placed in the first image plane below the objective lens allows to choose a specific sample area. The intermediate and projection lens system magnifies the intermediate image generated by the objective lens. The resulting image or diffraction pattern can be detected via a fluorescent screen or a charge coupled device camera. One advantage of a TEM is the ability to switch between imaging and diffraction mode. This can be achieved by changing the strength of the intermediate lens so that the back focal plane of the objective lens is projected on the screen. Figure 3.5 shows the beam paths in the lens system below the specimen in the case of diffraction and imaging.

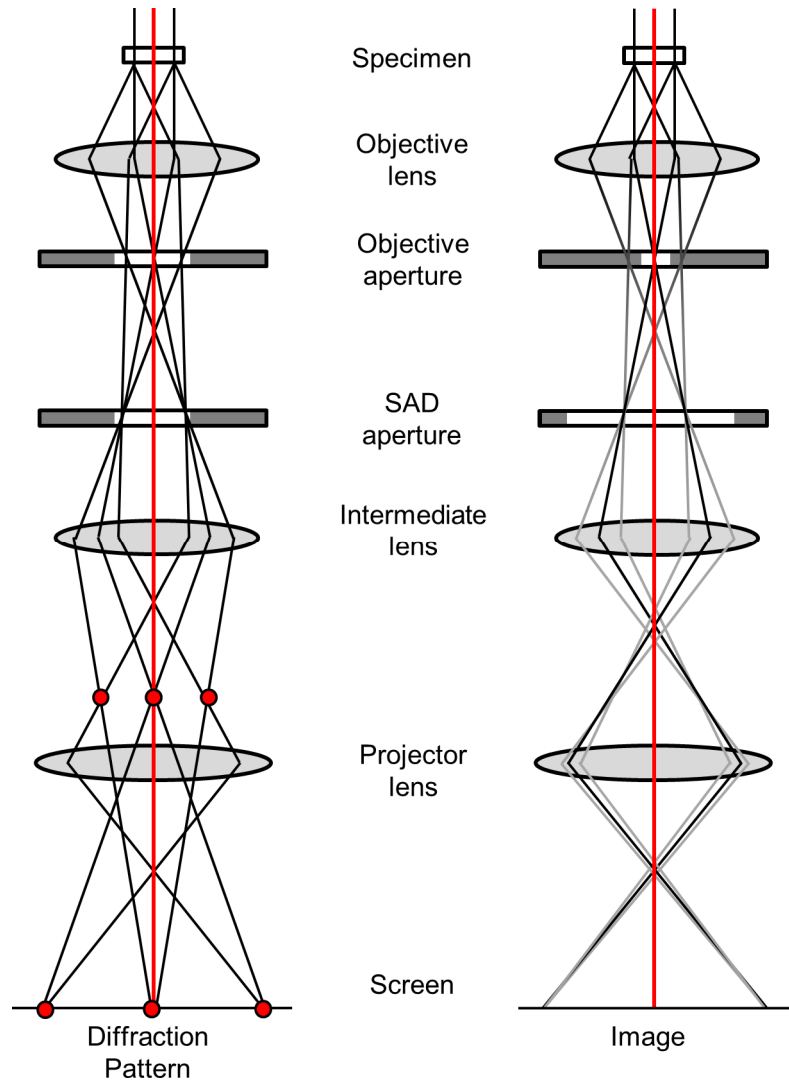


Figure 3.5: Beam paths in a TEM for diffraction (left) and imaging mode (right). Modified from Brandon and Kaplan.^[6]

Different lens aberrations like spherical aberration, chromatic aberration and astigmatism together with the diffractions limit the resolution of a TEM. While astigmatism can be corrected in each TEM, additional correctors have to be implemented to eliminate the spherical and chromatic aberrations. By doing so, the resolution of a TEM can be enhanced to $< 1 \text{ \AA}$. In addition, the implementation of a monochromator can reduce the energy width of the primary beam to $\sim 0.1 \text{ eV}$ which is of interest for EELS measurements with high energy resolution.^[3,5]

Electron diffraction

Just like in XRD (see chapter 3.1) diffracted electrons can interfere constructively and lead to spots in ED patterns. Since the wavelength of electrons in a TEM is much smaller

than the radiation used in XRD, a much larger Ewald sphere occurs and several reflections can be observed in the pattern. The lattice spacings d_{hkl} of a material can be calculated for a known camera constant (see equation (3.6)).

$$\lambda L = R d_{hkl} \quad (3.6)$$

The camera constant λL can be determined by measuring a standard sample like a Si single crystal. R is the distance between the primary beam and the investigated diffraction spot and can be measured in the diffraction pattern. A specific area of the specimen can be selected for diffraction by inserting a SAD aperture.^[2,3]

Conventional TEM

The most common imaging mode in conventional TEM is the bright-field (BF) imaging. Hereby, the objective aperture is positioned around the primary beam. The electrons that are scattered by the specimen are blocked. Areas exhibiting stronger scattering appear darker. On the contrary only electrons scattered in a preferred direction can be used for imaging in dark-field (DF) mode. Either the aperture is placed at the position of a scattered beam or the beam is tilted in a way that the diffracted beam is oriented parallel to the optical axis. In this mode only the specimen areas that scatter the beam in a certain direction appear bright. Diffraction contrast arises when the sample is oriented such that the Bragg condition is fulfilled, meaning that crystalline specimen regions appear darker in BF images. Besides the diffraction contrast the mass-thickness contrast plays an important role in conventional TEM. Regions of the specimen that are thicker or have a larger atomic number scatter electrons more strongly and also appear darker in BF images.^[3]

High resolution TEM

High resolution TEM (HRTEM) is used to study the specimen at the atomic scale. When a crystalline specimen is tilted in zone axis its lattice planes become visible. The objective aperture is removed in this mode, so that all scattered and unscattered electrons contribute to the image. Using aberration-correcting optics and a monochromated high-brightness source resolutions of 0.05 Å can be realized in HRTEM.^[9] Nevertheless, unlike in STEM, the interpretation of the obtained HRTEM images is not intuitive and more difficult. Therefore, simulations have to be performed in order to be able to assign the gathered signals to atomic columns. The parallel electron beam which is used in HRTEM

is treated as a plane wave. In general the phase and the amplitude of this plane wave is shifted when it passes through the specimen due to interactions with the Coulomb potential of the atoms. The so-called exit wave which is the electron wave that leaves the sample is influenced by the atomic arrangement, the chemical composition and the thickness of the specimen. For thin samples it is assumed that, the amplitude of the electron wave stays constant and only the phase changes (“weak-phase object”). Due to defocussing and lens aberrations the different wave vectors of the exit wave experience different phase shifts. The simplified contrast transfer function (CTF) (3.7) for a weak phase object describes the influence of defocus and spherical aberration on the phase of the exit wave.

$$\chi(u) = \pi\Delta f\lambda u^2 + \frac{1}{2}\pi C_s\lambda^3 u^4 \quad (3.7)$$

Δf is the defocus, λ is the wavelength, u is the spatial frequency and C_s is the spherical aberration coefficient. Whenever the function passes zero, the contrast in the resulting image is reversed. The instrumental resolution limit is defined as the first zero-crossing of the CTF at the highest possible spatial frequency. The corresponding defocus value is called Scherzer defocus.^[2,3]

Scanning TEM

In STEM mode the specimen is scanned by a convergent electron beam (probe) and the transmitted electrons are detected. The beam is deflected with two pairs of scan coils in such a way that the beam is always parallel to the optical axis when it is scanned across the specimen. For each scanned position the scattered signal is measured and an image is formed point by point. Three different detectors which are placed around the optical axis can be used depending on the scattering angle θ of the transmitted electrons. A BF detector is applied for electrons that are scattered in forward direction ($\theta < 10$ – 25 mrad). For larger scattering angles ($25 < \theta < 50$ mrad) annular dark-field (ADF) and finally high angle annular dark-field (HAADF) detectors ($\theta > 75$ mrad) are used. The HAADF signal is proportional to the scattering cross section of the incoherent, elastically scattered electrons. This Rutherford cross section is directly proportional to the atomic number squared. This allows an intuitive interpretation of HAADF STEM images regarding the distinction of heavier and lighter elements in the specimen.

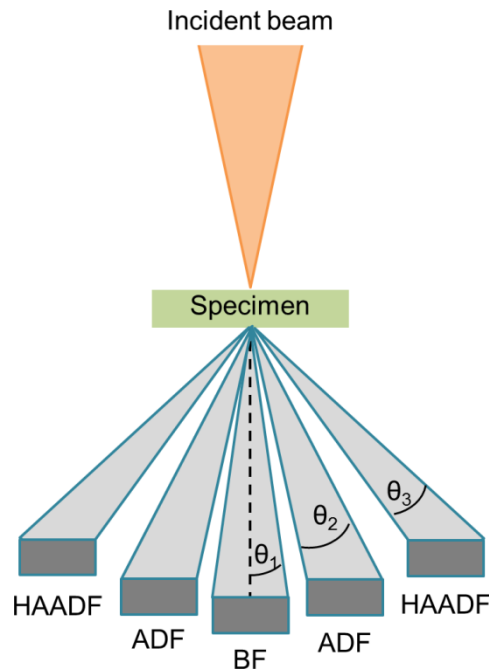


Figure 3.6: Schematic drawing of the available detectors in STEM mode. Modified from Williams and Carter.^[3]

Due to the image formation, STEM images are not affected by aberrations of the imaging lenses but depend on the quality of the condenser system. The resolution in a STEM image depends on the size of the formed probe. By implementing a probe corrector in the condenser lens system resolutions of < 0.1 nm can be achieved. A great advantage of STEM is the possibility to obtain analytical signals, like EDS and EELS, with a high spatial resolution while simultaneously acquiring a HAADF image.^[3,10]

3.3 Energy dispersive X-ray spectroscopy

EDS can be used in SEM and TEM to investigate the chemical composition of a sample. The process leading to the emission of characteristic X-rays is visualized in Figure 3.7. A high energy electron beam hits the sample and eventually knocks out an inner-shell electron of an atom. Since this state is unstable, an electron from an outer shell with a higher energy can be transferred to the inner shell to fill the hole. The energy difference between the two shells can either be released as an X-ray or lead to the emission of an Auger electron. Since this energy difference and therefore the X-ray wavelength are characteristic for each element, EDS can be used for qualitative analysis.

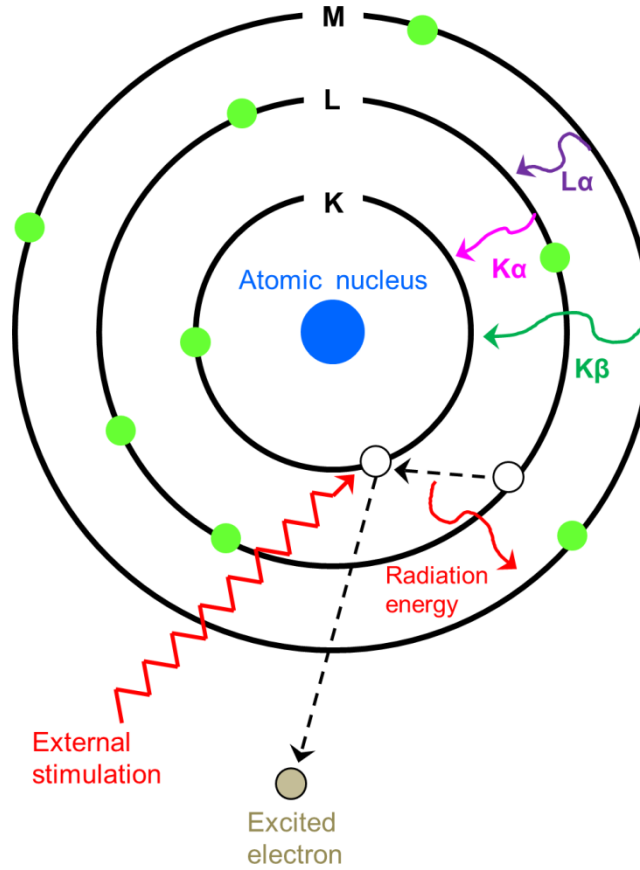


Figure 3.7: Schematic drawing of the excitation of an inner shell electron followed by relaxation and emission of a characteristic X-ray. Modified from Williams and Carter.^[3]

The emitted X-rays are named depending on the electron shell from which the electron is excited (K, L, M) and depending on the electron shell from which the electron comes to fill the state (α , β , γ). EDS is preferably used for elements with an atomic number $Z > 13$ because the low energy X-rays associated with light elements can easily be absorbed by the sample itself or the detector window. In addition to the emission of characteristic X-rays, a part of the electrons are decelerated by the Coulomb field of the atomic nucleus. This process leads to the generation of *bremsstrahlung* which forms the background of an EDS spectrum. Before performing quantitative EDS analysis, the background has to be subtracted from the spectrum which can be done via Kramer's equation. Finally the area under the peaks is measured and the concentration ratio of the contained elements can be calculated with the Cliff-Lorimer equation (3.8).

$$\frac{c_A}{c_B} = k_{AB} \frac{I_A}{I_B} \quad (3.8)$$

The concentration ratio c_A and c_B is proportional to the intensity ratio I_A and I_B of the elements A and B . The Cliff-Lorimer factor k_{AB} depends on the analyzed elements and measurement parameters like high voltage and detector efficiency.^[3,5,6]

3.4 Electron energy loss spectroscopy

EELS is a versatile technique to investigate a number of properties of a material (e.g. chemical composition, electronic properties, coordination) with high spatial and energy resolution. In a TEM, electrons pass through the sample and loose a certain amount of energy due to inelastic scattering events with electrons from the material. The inelastically scattered electrons are energy-dispersively separated by a magnetic prism and finally detected as a function of their energy loss. In Figure 3.8 an EELS spectrum is shown which can be classified in three regions. At 0 eV the most intense peak, called the zero loss peak, is formed by the transmitted electrons that did not undergo inelastic scattering processes. Electrons with very small energy losses due to excitation of phonons are also part of the zero loss peak. The low loss region which contains excitation of plasmons as well as inter and intra band transitions reaches up to an energy loss of 50 eV. This area can be used for band gap investigations or to determine the thickness of the sample. At energy losses higher than 50 eV characteristic ionization edges can be detected in the so called-core loss region. The energy of the primary electrons can be transferred to inner shell electrons of the sample that are excited into empty states above the Fermi level. The onset and the shape of the edge give information about structural and chemical properties of the investigated specimen. The edge fine structure for example is determined by the density of states and acts as a fingerprint for coordination and valence state. In addition, EELS is used best to detect lighter elements and is therefore a complementary method to EDS.

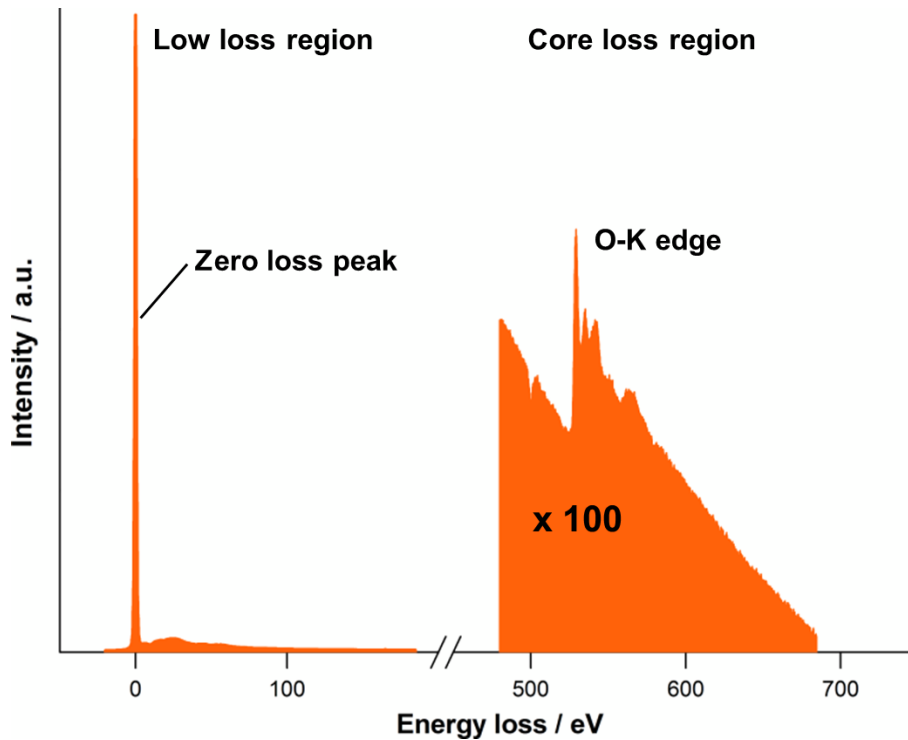


Figure 3.8: EELS spectrum showing the zero loss peak and the element specific ionization edge of oxygen.

EELS spectra also hold quantitative information and allow the determination of the chemical composition of the sample. First, the background has to be modeled via a power-law function and is subtracted. Then a scattering cross-section has to be determined theoretically or experimentally depending on the measurement parameters and the specimen properties.^[3,11]

3.5 Fuel cell characterization methods

In the following chapter the fuel cell characterization methods most commonly used in this work are presented. All of the mentioned measurements were performed at ELCOMAX GmbH, Munich by Tanja Ossiander and Markus Perchthaler.

3.5.1 Polarization curves

The standard electrochemical technique for the characterization of fuel cells is the acquisition of polarization curves. It allows obtaining information on performance losses in the cell or stacking under operating conditions. Hereby, the cell voltage is recorded in dependency of the current during operation (see Figure 3.9).

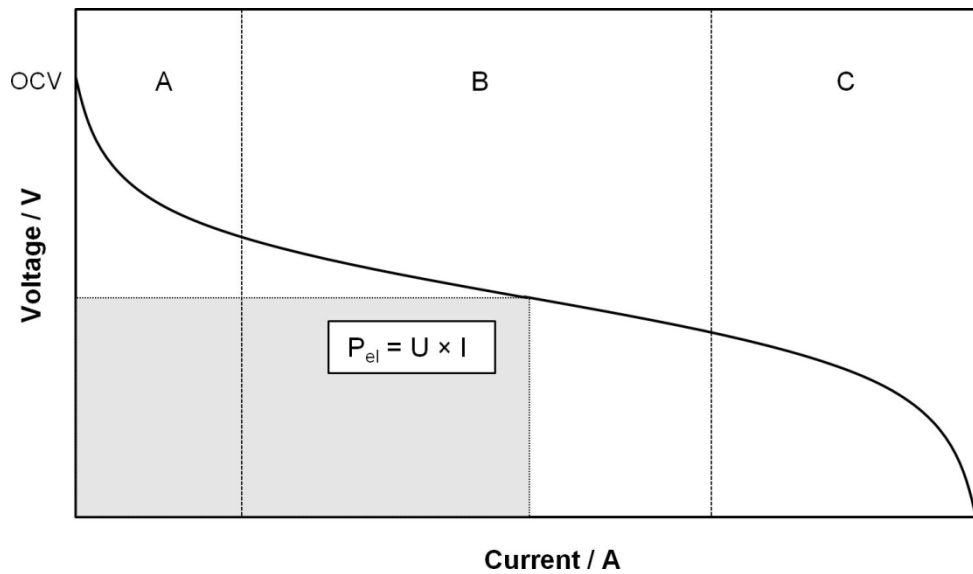


Figure 3.9: Schematic drawing of a polarization curve which can be divided into three regions corresponding to different voltage losses. The multiplication of voltage and current gives the electrical power at each data point.

When no electric load is applied, the corresponding voltage provided by a fuel cell is called the open-circuit voltage (OCV). The measured OCV is always lower than the theoretical thermodynamic voltage, mainly due to fuel cross-over from the anode to the cathode.

The shape of the curve is influenced by several processes that are related to voltage losses during operation. The difference between measured and thermodynamic voltage is called overpotential which is an important factor for the performance of fuel cells. The polarization curve can be divided into three different regions that give information on different types of voltage losses. The first region (see Figure 3.9 A) is influenced by kinetic-related activation losses. Due to the charge-transfer kinetics of the O_2 reduction and H_2 oxidation rates at the electrode surfaces the working potential is reduced in the low current density region. The second region (see Figure 3.9 B) corresponds to so-called ohmic losses. These originate from electric contact resistance among the fuel cell components and the proton resistance of the proton-conducting membrane. The working potential shows a linear behavior with increasing current density. At high current density values (see Figure 3.9 C) the transfer speed of reactants and products is slower than the reaction rate which leads to a severe decrease of the working potential. Therefore, the third region is called mass transport loss region.^[12,13]

All polarization curves were measured using a single cell setup with an active area of 50 cm² and a serpentine channel flow field structure on anode and cathode. Mass flow controllers regulated the reactants flow rates. Electrical heating cartridges controlled the cell temperature at 160 °C.

3.5.2 Cyclic voltammetry

With cyclic voltammetry qualitative information about the rates of reaction and reactant diffusion in a fuel cell system can be obtained. It is often used to examine the electrochemical active surface area (ECA) of the catalyst. This method can be performed *ex-situ* for the catalyst only and *in-situ* for the MEA of a fuel cell. The potential is scanned at a working electrode and the resulting current is monitored via a counter electrode. In the conducted experiments the anode is fueled with hydrogen. Therefore, it acts as the counter electrode and as a pseudo reference electrode. For the determination of the active catalyst surface at the cathode (working electrode), a triangular voltage is applied and the resulting current is measured. Assuming carbon based fuel cell electrodes with Pt catalyst, the potential is cycled between 0 V and 1.23 V. At the anodic half cycle at positive current values surface oxidation reactions like H desorption and Pt oxidation take place (see Figure 3.10). In contrast at negative current values surface reduction reactions (Pt-O reduction, H adsorption) can be observed. The shape of the cyclic voltammogram is dependent on the type of used electrode, the ECA of the catalyst and impurities on the surfaces. The ECA of the catalyst can be calculated by measuring the area under the peak which corresponds to the H desorption. The amount of electrons which is needed to oxidize the Pt equals the amount of desorbed H atoms and is therefore also equal to the number of free adsorption places on the Pt surface.^[12,13]

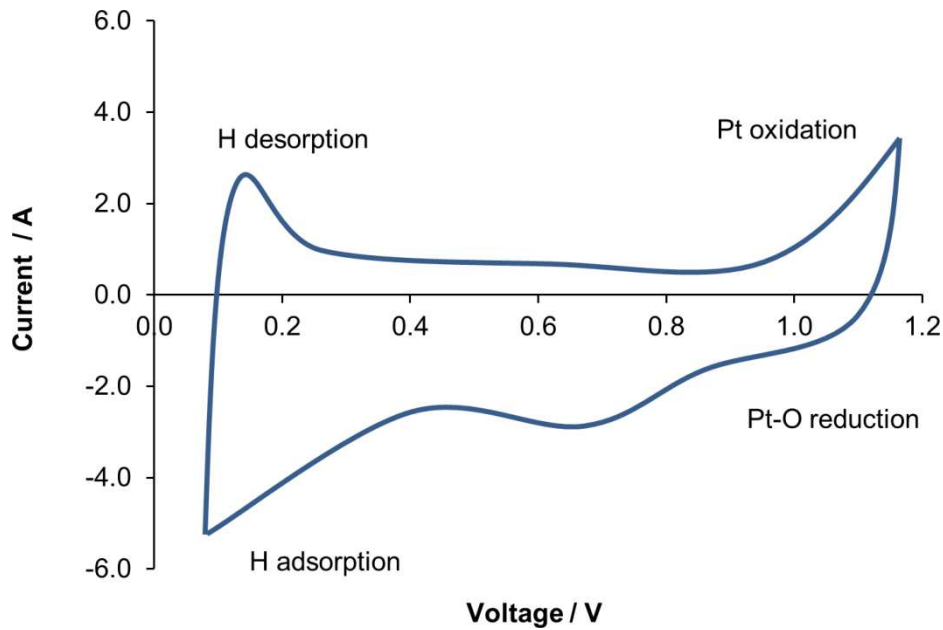


Figure 3.10: Schematic drawing of an *in-situ* cyclic voltammogram. Several characteristic regions are labeled.

3.5.3 Long term fuel cell test with continuous operation

Long term fuel cell degradation measurements were performed under constant load in an assembled fuel cell stack. In these experiments the voltage is monitored as a function of time. A 20 cell stack with an active surface of 153 cm^2 was used. The measurements were done under a constant load of 0.2 A cm^{-2} and at a temperature of 160°C . The stack was fueled with reformed methanol on the anode side and air on the cathode side.

3.5.4 Long term fuel cell test with start-stop cycle operation

The start-stop cycle operation for fuel cells is usually performed to examine the long term stability of fuel cell materials. The cyclic heating and cooling as well as the periodical load change lead to a high electrochemical and thermal stress for the fuel cell material. This allows for investigation of the reliability of the system when it comes to regular shutdowns as well as the degradation stability in general.^[14]

A 50 cm^2 single cell was heated up to 80°C . At this temperature, the cathode was purged with dry air for 5 min. Then the cell was heated to 120°C . At this temperature, the anode was purged with nitrogen plus the hydrogen and air gases were switched on. While the cell was heated up to 160°C , current was drawn at 0.25 A cm^{-2} . As soon as a temperature of 160°C was reached, the current was increased to 0.5 A cm^{-2} and then

held for 4 h. In the stop phase, the current was decreased to 0.25 A cm^{-2} while cooling the cell to 120°C . The current was switched off when the temperature was reached. Afterwards, the anode was purged with nitrogen and the cell cooled down to room temperature for 4 h. This procedure was repeated for several cycles.

3.6 Chapter references

- [1] Massa, W. *Kristallstrukturbestimmung*; 7 ed.; Vieweg+Teubner Verlag: Wiesbaden, **2011**.
- [2] Fultz, B.; Howe, J. M. *Transmission Electron Microscopy and Diffractometry of Materials*; 3 ed.; Springer Verlag: Berlin, **2008**.
- [3] Williams, D. B.; Carter, C. B. *Transmission Electron Microscopy*; Springer US, **2009**.
- [4] Scherrer, P. *Nachrichten von der Gesellschaft der Wissenschaften zu Göttingen, Mathematisch-Physikalische Klasse* **1918**, 1918, 98.
- [5] Goodhew, P. J.; Humphreys, F. J.; Beanland, R. *Electron microscopy and analysis*; Taylor & Francis: London; New York, **2001**.
- [6] Brandon, D. G.; Kaplan, W. D. *Microstructural characterization of materials*; 2 ed.; Wiley-VCH Verlag: Weinheim, **2008**.
- [7] Steve, R.; Robert, P. *Journal of Micromechanics and Microengineering* **2001**, 11, 287.
- [8] Baram, M.; Kaplan, W. D. *Journal of microscopy* **2008**, 232, 395.
- [9] Kisielowski, C.; Freitag, B.; Bischoff, M.; van Lin, H.; Lazar, S. et al. *Microsc. Microanal.* **2008**, 14, 469.
- [10] Pennycook, S. J.; Nellist, P. D. *Scanning Transmission Electron Microscopy*; 1 ed.; Springer: New York, **2011**.
- [11] Brydson, R. *Electron Energy Loss Spectroscopy*; 1 ed.; Taylor & Francis, **2001**.
- [12] Wang, H.; Yuan, X.-Z.; Li, H. *PEM Fuel Cell Diagnostic Tools*; CRC Press Taylor & Francis Group: Boca Raton, FL, **2012**.
- [13] Kurzweil, P. *Brennstoffzellentechnik - Grundlagen, Komponenten, Systeme, Anwendungen*; Springer: Wiesbaden, **2013**.
- [14] Hartnig, C.; Schmidt, T. J. *J. Power Sources* **2011**, 196, 5564.

4 Experimental details

In the following chapter the used chemicals and substrates as well as the used equipment and microscopes are listed. Furthermore the sample preparation of SEM and TEM samples is described.

4.1 Chemicals and substrates

In Table 4.1 the used chemicals and substrates are summarized.

Table 4.1: Used chemicals and substrates.

Name	Chemical formula	Purity	Supplier
Acetone	C_3H_6O	Pure	BRENNTAG
Ethanol	C_2H_6O	$\geq 99.9\%$	MERCK
Isopropyl alcohol	C_3H_8O	$\geq 99.9\%$	FLUKA-ANALYTICAL
Silver conductive lacquer	-	-	ACHESON
G1 Epoxy	-	-	GATAN
Aluminum substrate	Al	-	CONRAD ELECTRONIC
Brass substrate	$CuZn_x$	-	CONRAD ELECTRONIC
Silicon substrate	Si	-	SILCHEM

4.2 Equipment

The equipment used for sample preparation is summarized in Table 4.2.

Table 4.2: Equipment used for sample preparation.

Equipment	Short description
Diamond wire saw	Precision Vertical Diamond Wire Saw, Model 3242 from WELL
Disc grinder	Model 623 from GATAN, grinding paper with 40 μm and 5 μm grain size
Dimple grinder	Model 656 from GATAN, diamond paste with 3 μm and 0.25 μm (for polishing)
Ion polishing system	Precision ion polishing system (PIPS) from GATAN equipped with a cold stage controller from GATAN
Light microscope	Optical Technology from OPTTECH
Thickness gauge	Model 12.5 mm-0.001 / .5"-0.0005 from KÄFER

4.3 Analytical instruments

The microscopes and X-ray diffractometers used in this work are listed in Table 4.3.

Table 4.3: Analytical instruments used in this work.

Method	Instrument	Short description
XRD	D8 Discovery from BRUKER	Using Cu-K α radiation ($\lambda=1.54 \text{ \AA}$)
	Seifert THETA/THETA from GE INSPECTION TECHNOLOGIES (operated in Düsseldorf)	equipped with a Meteor OD detector, using Co-K α radiation ($\lambda=1.79 \text{ \AA}$)
SEM	JSM-6500F from JEOL	Equipped with an EDS spectrometer from OXFORD INSTRUMENTS INCA ENERGY
FIB	NVision 40 from ZEISS (operated in Garching)	Dual focused ion beam and scanning electron microscope; SEM used at 2.5 keV; FIB used at 30 keV and 1.5 pA
	Helios NanoLab 600i from FEI (operated in Düsseldorf)	Dual focused ion beam and scanning electron microscope
TEM	JEM 2011 from JEOL	Operated at 200 keV acceleration voltage; equipped with an EDS spectrometer from EDAX
	Titan from FEI	S/TEM operated at 80–300 keV; equipped with an EDS spectrometer from EDAX, a HAADF detector from FISCHIONE INSTRUMENTS (model 3000) and a Tridiem energy filter from GATAN

The XRD measurements were performed by Tina Reuther at the LMU Munich and by Benjamin Breitbach at the MPIE Düsseldorf.

The preparation of TEM samples via FIB was performed at the Walter-Schottky Institute of the TU Munich by Ramona Hoffmann and Sonja Matich. In addition, Tristan Harzer and Katharina Hengge prepared TEM lamellae at the MPIE in Düsseldorf.

4.4 Sample preparation

4.4.1 SEM sample preparation

For basic investigations of sample surfaces a 0.5×0.5 cm piece of the samples was cut with a scalpel and then glued onto a cylindrical SEM sample holder using conductive silver lacquer. Cross-sectional SEM samples were prepared by molding the rotated sample in resin and subsequent grinding until the desired sample area was uncovered of the resin at the top.

A thin layer of carbon was sputtered on all samples to prevent charging effects during investigation of the sample surface.

4.4.2 TEM sample preparation

As a rule of thumb samples have to be thinner than about 100 nm in order to analyze them in a TEM. In this work different sample preparation strategies were applied to reach this small sample thickness.

Standard TEM samples

To investigate shape and crystallinity of individual components the dropping method is a useful and quick way to prepare TEM samples. The sample powder was suspended in a solvent and ultrasonicated so that larger features broke apart and electron transparency was ensured. Afterwards, one drop of the suspension was dropped onto a 3 mm in diameter TEM grid (usually copper) coated with an amorphous holey carbon film. The solvent was evaporated at room temperature and the sample material remained on the grid.

Cross-sectional TEM samples

The preparation of cross-sectional TEM samples was performed following the method reported by Strecker et al.^[1] In this work it was primarily used for the preparation of membrane samples. The procedure for this method is illustrated in Figure 4.1. A small piece of specimen material (see Figure 4.1 a)) was glued between two wafers (aluminum, brass or silicon) by using a two-component glue (G1 Epoxy : hardener = 10 : 1). The formed “sandwich” was then cut with a diamond wire saw in a way that it fitted into a brass tube with an internal diameter of 2.0 mm (see

Figure 4.1 b)). The “sandwich” was glued into the brass tube (see Figure 4.1 c)) using again a two-component glue (G1 Epoxy : hardener = 10 : 1). A specimen slice with a thickness of approximately 200 μm was cut off the tube with the diamond wire saw (see Figure 4.1 d)). Afterwards the slice was thinned via manual disc grinding to a thickness of about 50 μm (see Figure 4.1 e)). In the next step two dimples were grinded into the thinned specimen disk to further reduce the thickness in its center to about 15 μm (see Figure 4.1 f)). The final thinning was performed by a precision ion polisher. Two argon ion beams with an energy of 3 keV were directed at the specimen center with an angle of 5° . Due to the ion bombardment a wedge shape with a small hole in the middle of the specimen was formed. During the Ar ion bombardment the sample was cooled with liquid nitrogen to prevent damage due to heat (see Figure 4.1 g)). The wedge right next to the hole in the specimen is thin enough for TEM investigation.

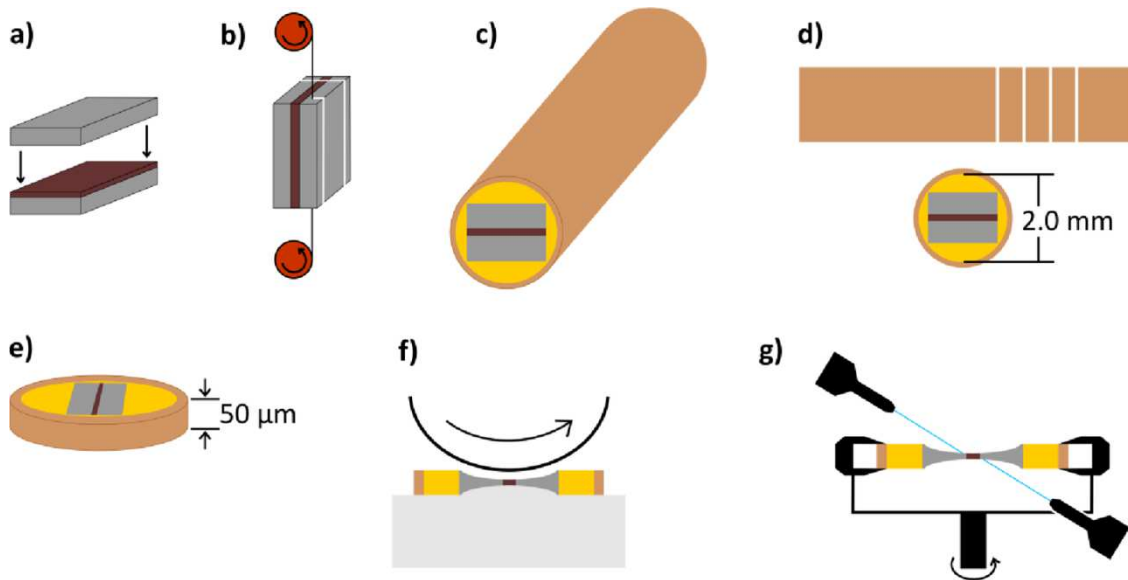


Figure 4.1: Schematic illustration of the preparation of a TEM cross-sectional specimen: a) gluing of a metal wafer (grey) and specimen material (brown) forming a “sandwich”; b) cutting of the “sandwich” with a diamond wire saw; c) brass tube with seated “sandwich” and embedded in glue; d) cutting of specimen slices with the diamond wire saw; e) reducing the thickness of the specimen slice via disc grinding leads to a sample thickness of about 50 μm ; f) grinding of two dimples with a dimple grinder for further specimen thinning; g) final preparation of the specimen slice with help of an ion polishing system. Figure courtesy of Stephan Gleich.^[2]

TEM sample preparation with FIB

Two different preparation routes for TEM samples via FIB have been used in this work. For the first method a surface region of the sample ($20\ \mu\text{m} \times 2\ \mu\text{m}$) containing the

desired features (see Figure 4.2 a)) is sputtered with a 400–800 nm thick, protective carbon layer (see Figure 4.2 b)). Subsequently, the material at the long sides of the specimen area is removed by a focused beam of gallium ions, starting at a distance of 10 μm at an angle of 20° (see Figure 4.2 c)). The free-standing lamella has a size of $2 \times 20 \times 5 \mu\text{m}$ and is cut out of the sample material (see Figure 4.2 d)). Before cutting the lamella loose, it is fixed to a manipulator needle by depositing carbon with a gas-injector system (see Figure 4.2 e)). The remaining connection of the lamella to the sample is cut (see Figure 4.2 f)) and the lamella is transported to a 3 mm half-ring Cu TEM grid (see Figure 4.2 g)). It is glued to the grid with carbon and the manipulator is cut off with the ion beam (see Figure 4.2 h)). Finally, the lamella is further thinned and polished at low beam currents until electron transparency is reached (see Figure 4.2 i)).

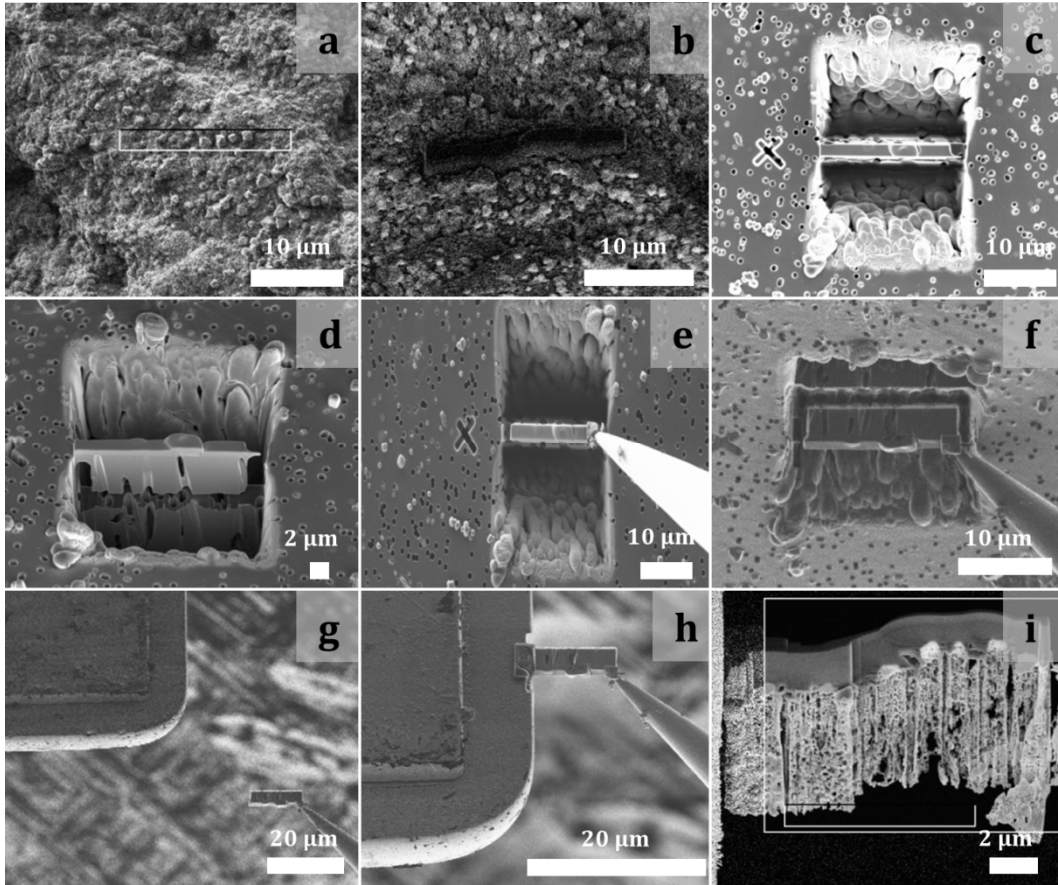


Figure 4.2: Schematic representation of the conventional sample preparation of a TEM lamella via FIB. Figure courtesy of Katharina Hengge.^[3]

Part of the investigation in this work focused on the interface of anode and membrane of the fuel cells. Since this interface is located about 20 μm below the sample surface a different preparation strategy was used. The MEA was glued cathode side down onto an

aluminum substrate. The carbon GDL and micro porous layer (MPL) were removed and the sample was cut in stripes with a thickness of about 150 μm (see Figure 4.3 a)). A 20 μm long sample area in the center of the stripe was chosen and thinned until electron transparency was reached (see Figure 4.3 b)). The thinning was performed by going towards the interesting sample area at high beam currents (45 nA, 27 nA, 13 nA). The closer the beam got to the region of interest the more the ion beam current was reduced. By doing so, damaging of the sample and incorporation of gallium into the sample was reduced (see Figure 4.3 c) and d)). The thinned area remained in the 150 μm long sample stripe and the stripe was transferred to a folding Cu TEM grid. Some of the Cu stripes were removed so that the thinned sample area was free-standing and could be analyzed in the TEM.

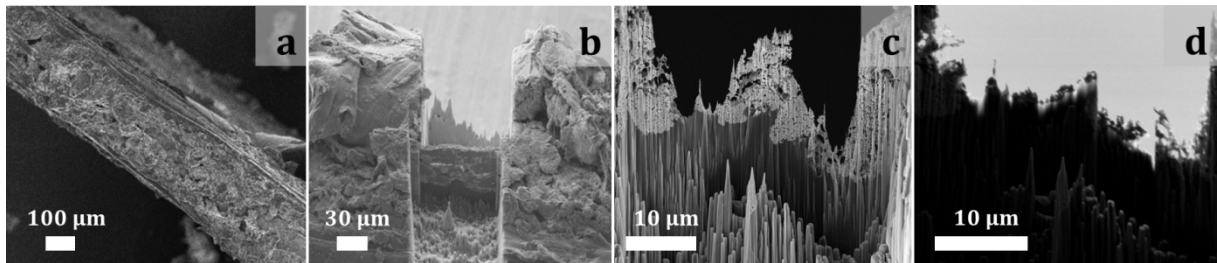


Figure 4.3: Schematic representation of the alternative sample preparation of a TEM lamella via FIB.

4.5 Chapter references

- [1] Strecker, A.; Salzberger, U.; Mayer, J. *Prakt. Metall.* **1993**, *30*, 482.
- [2] Gleich, S. Master Thesis, 2013.
- [3] Hengge, K. Master Thesis, 2013.

5 Influence of the size and shape of silica nanoparticles on the properties and degradation of a PBI-based high temperature polymer electrolyte membrane

This chapter is based on the following publication:

Tanja Ossiander*, Christoph Heinzl*, Stephan Gleich, Frank Schönberger, Petra Völk, Marina Welsch, Christina Scheu *Journal of Membrane Science* **2014**, 454, 12–19.

* These authors contributed equally.

5.1 Introduction

Polymer electrolyte membrane fuel cells (PEMFC) have gained considerable attention in fuel cell applications over the last several years.^[1] The limitation of low temperature PEMFC membranes like Nafion® leads the main focus of future development on membranes which can be operated at temperatures above 100 °C.^[2,3] Savinell et al. presented phosphoric acid doped polybenzimidazole (PBI) for fuel cell operation from 150 °C to 200 °C without humidification.^[4-6] These high temperature PEMFCs (HT-PEMFC) benefit from faster reaction kinetics on the electrodes, increased catalytic activity and simplified heat management.^[7-10] In spite of these advantages, the lifetime of HT-PEMFC still remains the major concern.^[11] Striving for the goals of performance, lifetime and cost on the membrane side, different approaches for ruggedized membranes have been reported in literature.^[12-15] Besides ionic and covalent cross-linking, the third main concept is the application of organic-inorganic composite membranes.

The incorporation of inorganic nanofillers in the polymer matrix is often realized by an in-situ sol-gel creation of the particles during membrane casting.^[16-21] This method prohibits silica nanoparticle agglomeration and therefore enables higher inorganic contents.^[22] Chuang et al. prepared silica nanoparticles in-situ from tetraethoxy silane

(TEOS) with (3-isocyanatopropyl)triethoxysilane as a cross-linker by sol-gel technique.^[23] The procedure is driven by a combination of hydrolysis and condensation reactions. The resulting silica particles are surrounded by silanole end groups and cross-linked to the polymer chains.^[24] By using the sol-gel technique the size, shape and amount of particles are controlled by the concentration and type of additives as well as the reaction parameters such as temperature or time.^[22,23,25,26] The smaller the resulting particles are, the more surface sites are available which can interact with the polymer chains and therefore influence the membrane properties.^[1] The membrane benefits in various ways such as better retention for liquids, higher mechanical and thermal stability and lower gas permeability.^[4,23,27,28] In some cases even better proton conductivity was gained.^[4,29,30] Originally various different combinations of inorganic fillers and polymer materials were tested and reviewed for low temperature PEMFCs and direct methanol fuel cells.^[20,22,31] It turned out that silica nanoparticles play an outstanding role because of their high pore volume and thermal stability.^[21,32] These particles were also incorporated in phosphoric acid doped PBI-membranes for HT-PEMFC.^[24,33-35] This general concept of organic-inorganic composite membranes addresses the weaknesses of PBI-based membranes by improving the mechanical stability in doped status plus reducing the phosphoric acid loss during operation.^[21] While the mechanical strength of these membranes is reported to be increased, the proton conductivity is frequently too low.^[21] Lifetime analysis of phosphoric acid PBI-based HT-PEMFC have been reported previously.^[36] Since the publications in the field of organic-inorganic PBI-based composite membranes concentrate mainly on ex-situ membrane properties, the important question of these materials' long term stability still remains open.

In this work, silica nanoparticles are formed from TEOS by in-situ sol-gel procedure and cross-linked to the PBI polymer chains with (3-glycidyloxypropyl)-trimethoxysilane (GPTMS) (see Figure 5.1). The influence of three different TEOS contents on the size, shape and distribution of the nanoparticles are investigated by transmission electron microscopy (TEM). By applying local energy dispersive X-ray spectroscopy (EDS) measurements at nanometer regime and electron diffraction the observed particles were proven to be amorphous silica. Their influences on the thermal, chemical and mechanical properties are studied using thermogravimetric analysis (TGA), solvent

extraction analysis and stress-strain measurements. Besides in-situ performance testing, the main goal of this work is to prove lifetime and cycle stability of the developed silica stabilized PBI-membrane electrode assemblies (MEA) in long-term fuel cell operation.

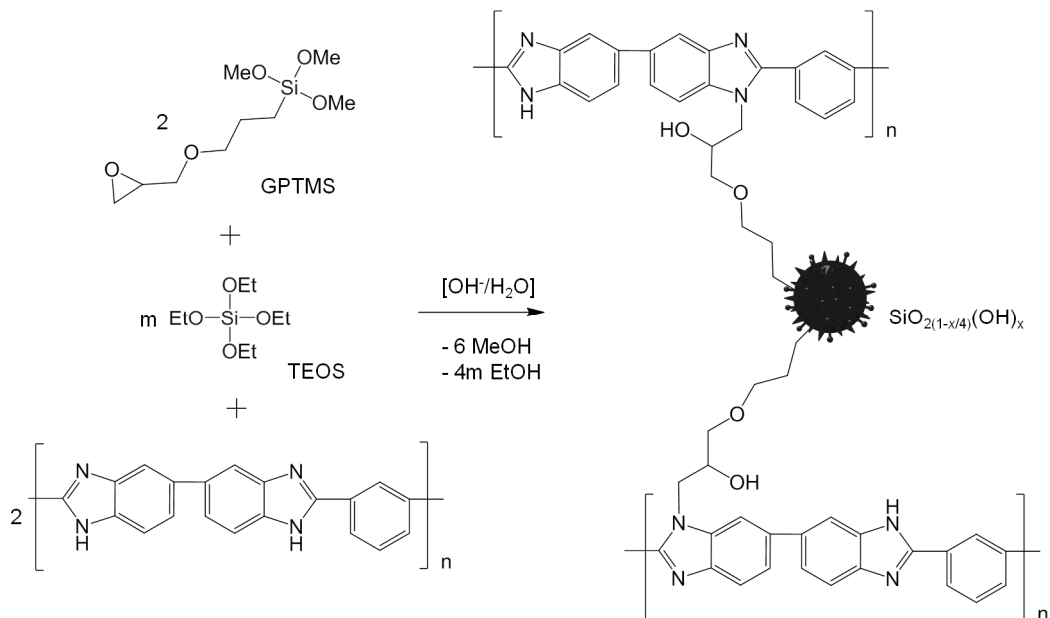


Figure 5.1: Sol-gel reaction of TEOS with GPTMS. The cross-linking of the particles is based on an epoxide ring opening reaction of GPTMS with the imidazole groups of the PBI.

5.2 Experimental

5.2.1 Preparation methods

Membrane and MEA preparation

Three different membranes with TEOS contents of 40, 80 and 120 wt% of the polymer PBI were prepared. PBI was dissolved in N,N-dimethylacetamide (DMAc, Merck) and stirred for 3 h at 200 °C under pressure. The solution was filtered over a 20 µm filter and added in a glass reactor. A solution of TEOS (Alpha Aesar) and GPTMS (Alpha Aesar) in DMAc was added to the PBI solution under stirring. To the resulting viscous solution, potassium hydroxide (Sigma Aldrich) is added. The reaction product was filtrated over a 20 µm filter and coated on a carrier foil.

The HT-PEM MEAs are manufactured by doping the gas diffusion electrodes with phosphoric acid and hot-pressing them with the membrane.

5.2.2 Characterization methods

5.2.2.1 Ex-situ membrane testing

Thermal properties

The thermal stability of the membrane samples was determined by TGA on a Perkin-Elmer TGA 4000. About 10 mg of the material was filled into the crucible. All measurements were recorded with a heating rate of $10\text{ }^{\circ}\text{C min}^{-1}$ in the temperature range between 40 and $600\text{ }^{\circ}\text{C}$ under nitrogen atmosphere.

Chemical stability

The membrane chemical stability was tested by extraction in DMAc. Pieces in the size of $3 \times 3\text{ cm}^2$ were dried in the oven over night at $150\text{ }^{\circ}\text{C}$ before their weight was measured. After this, the membrane was put into a round bottom flask and covered with DMAc. The solvent was heated up to $130\text{ }^{\circ}\text{C}$ for 1 h. After cooling the solution to room temperature, within 1 h, the samples were taken out of the flask. The extracted samples were dried over night at $150\text{ }^{\circ}\text{C}$ and weighted afterwards. The extraction residue was calculated.

Swelling ratio and liquid uptake

The swelling behavior and liquid uptake of the membranes were measured by immersing $2.5 \times 3\text{ cm}^2$ pieces in phosphoric acid for 30 min at $130\text{ }^{\circ}\text{C}$. The weight and dimensional changes between the dry and the doped membrane were recorded. Liquid uptake and swelling ratios were calculated as percentage weight increase and dimensional growth.

Mechanical properties

The mechanical properties of the samples were determined by acquiring stress-strain curves on a *BT1-FR0.5TN.D14/500 N Zwicki* from Zwick. Membrane pieces ($1 \times 15\text{ cm}^2$) were punched out of the membrane. The average thickness of every sample was evaluated with a thickness gauge from *Sylvac*. All measurements were carried out at room temperature.

Morphology and chemical composition analysis

The morphology as well as the chemical composition of the silica structures incorporated in the membrane was examined via TEM. The samples were prepared in a

way based on the standard cross-sectional TEM sample preparation as described by Strecker et al.^[37] The membrane was glued between two spacers (aluminum or brass) and this sandwich was glued into a brass tube with an outer diameter of 3 mm. After slicing thin discs (200 μm) off this tube with a diamond saw, these slices were thinned by using a grinder and dimpler from GATAN. Electron transparency was reached by further thinning the samples with a beam of argon ions (precision ion polishing system from GATAN; 3 keV, 5°, double mode). The used TEM was a FEI Titan 80–300 (S)TEM equipped with an EDAX detector for EDS measurements. Although the Titan can be operated between 80 and 300 kV, the measurements were mostly done at 80 kV to reduce beam damage effects like knock-on damage. The microscope is also equipped with a high angle annular dark-field (HAADF) detector from Fischione Instruments (Model 3000) which allows for scanning TEM (STEM) imaging.

Statistical particle evaluation

To evaluate the size distribution of the particles and to determine the membrane area covered by silica, the area of several hundred particles was measured in each sample with help of the program ImageJ.^[38] A band-pass filter was applied on micrographs to enhance the contrast between particles and substrate. In the next step, the threshold of intensity was defined filtering out the background and leaving only the particles. The size and number of particles were determined and subsequently the equivalent spherical diameter as well as the particle density was calculated.

Crystallinity analysis

X-ray diffraction (XRD) patterns were obtained on a Bruker D8 Discovery diffractometer with $\text{CuK}\alpha$ radiation ($\lambda = 1.54 \text{ \AA}$) to investigate the crystal structure of the membranes and the incorporated silica. The 2θ range was chosen from 10° to 50° with a scanning rate of 0.05°/s.

5.2.2.2 MEA testing

Electrochemical behavior

The electrochemical behavior of the MEAs was studied using begin of beginning-of-life (BOL) polarization curves. A single cell setup with an active area of 50 cm^2 and a serpentine channel flow field structure on anode and cathode was used. Reactants flow

rates were measured and controlled using mass flow controllers. Cell temperature was 160 °C and controlled by electrical heating cartridges.

Cycle stability

Start-stop cycle tests were done to investigate the stability of the MEAs under cycled fuel cell operation. A 50 cm² single cell was heated up to 80 °C. At this temperature, the cathode was purged with dry air for 5 min. Then the cell was heated to 120 °C. At this temperature, the anode was purged with nitrogen plus the hydrogen and air gases were switched on. While the cell was heated up to 160 °C, current was drawn at 0.25 A/cm². As soon as 160 °C was reached, the current was increased to 0.5 A/cm² and then held for 4 h. In the stop phase, the current was decreased to 0.25 A/cm² while cooling the cell to 120 °C. The current was switched off when the temperature was reached. Afterwards, the anode was purged with nitrogen and the cell cooled down to room temperature for 4 h. This procedure was repeated for several cycles.

Degradation at long term operation under constant load

Long term operation under constant load was conducted at a current density of 0.2 A/cm² at 160 °C. The stack was fueled with reformed methanol on the anode side with a stoichiometry of 1.4 and air on the cathode side with a stoichiometry of 2.0.

5.3 Results and discussion

5.3.1 Structural analysis

The TEM investigation of the membrane samples containing 40%, 80% and 120% of TEOS and a constant amount of 10% GPTMS reveals the successful formation of silica particles during the in-situ sol-gel reaction. Figure 5.2 shows HAADF STEM micrographs of the three different systems. The intensity in these images is proportional to the atomic number squared. Therefore, the obtained silica structures appear bright in the micrographs. The inhomogeneous brightness and the channel-like structure of the gray appearing membrane matrix arise from the sample preparation. The observed silica structures in all samples are amorphous. Neither via electron diffraction nor via high resolution TEM could any evidence of crystallinity be found.

While the sample with a content of 40% TEOS shows elongated large silica particles, the other two membranes contain relatively round-shaped silica particles. When comparing the membrane containing 80% TEOS with the 120% TEOS sample it can be seen that the size of the silica particles gets smaller but their amount rises. Overall, it can be observed that the sizes of the well dispersed silica particles in the membranes decrease at higher concentrations of introduced TEOS.

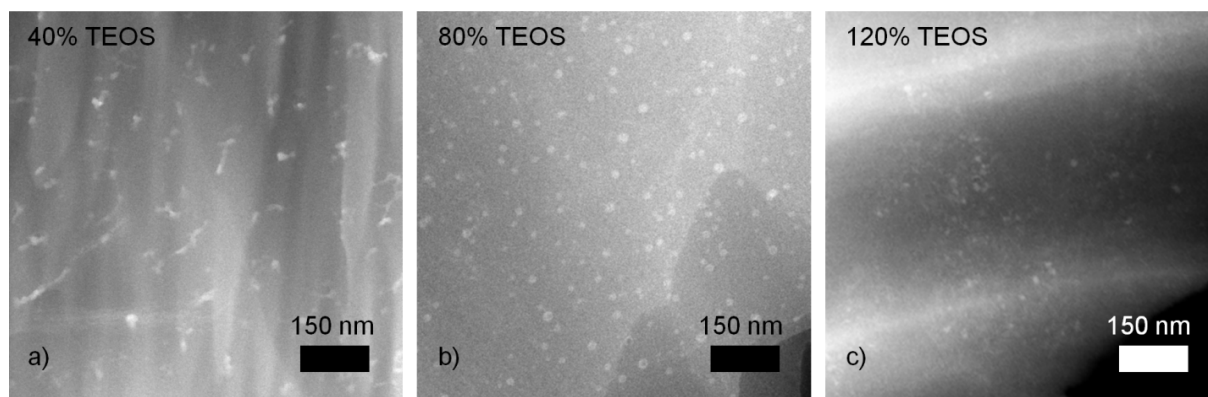


Figure 5.2: STEM micrographs of membrane specimens with an amount of TEOS of 40% (a), 80% (b) and 120% (c) reveal incorporated bright appearing particles with different sizes and distributions.

The statistical size distribution of the silica particles in the samples 40%, 80% and 120% TEOS is illustrated in Figure 5.3.

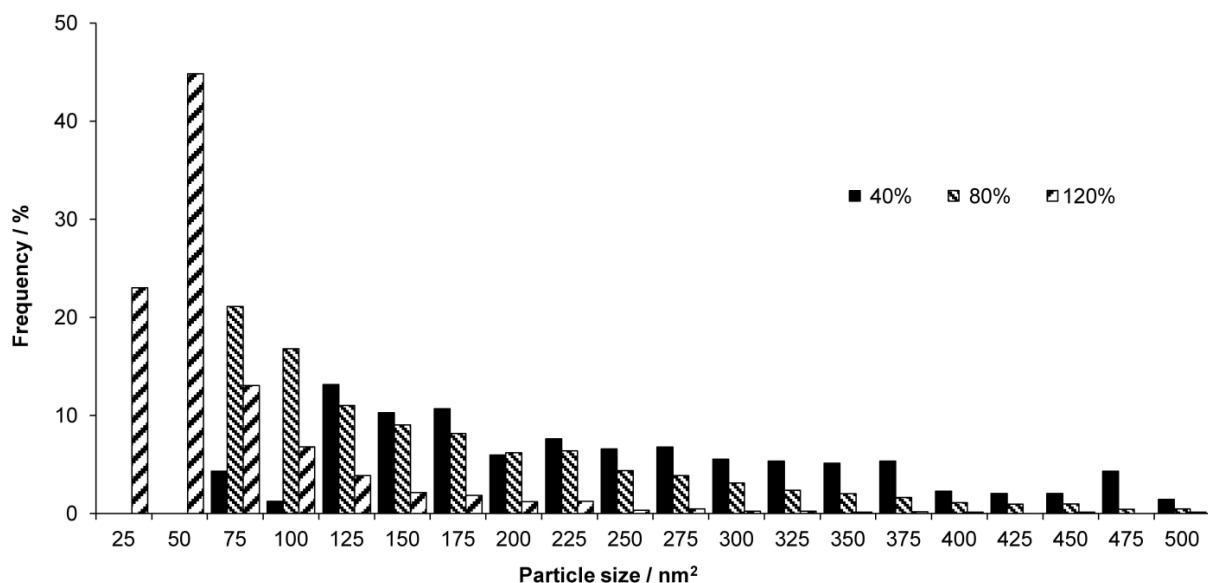


Figure 5.3: Size distribution of the silica particles in the membranes with different contents of TEOS.

5 Influence of the size and shape of silica nanoparticles on the properties and degradation of a PBI-based high temperature polymer electrolyte membrane

The silica particle sizes in the sample containing 40% TEOS are distributed over a large range and show no preferred size. More than half of the evaluated particles exhibit a size larger than 100 nm² and smaller than 400 nm². For reasons of vivid representation, the shown histogram was cut off at a particle size of 500 nm². Nevertheless, only about 10% of the counted silica particles of the sample 40% TEOS are larger than 500 nm² and their size distribution above 500 nm² linearly decreases to a maximum particle size of about 800 nm². The silica particles in the 80% TEOS membranes are in generally smaller than those of the sample containing 40% TEOS but they are also distributed over a wide size range up to several hundred nm². When it comes to the sample with 120% TEOS, the size distribution of the particles is rather narrow and the particles are again smaller in size. Less than 7% of the measured particles in the 120% TEOS membrane inherit a size larger than 150 nm². For a better overview the average particle size and the average particle density with their respective standard deviations were calculated and are summarized in Table 5.1. The particle density was determined by dividing the total area of all particles in a micrograph by the whole area of the micrograph. Furthermore, an average equivalent spherical diameter, assuming spherical particles, is given which simplifies the estimation and comparison of the particle sizes of each specimen.

Table 5.1: Average particle size, average equivalent spherical particle diameter and average particle density of the samples containing 40%, 80% and 120% TEOS as well as their respective standard deviations.

TEOS (%)	average particle size (nm ²)	average equivalent spherical particle diameter (nm)	average particle density (%)
40	293 ± 201	18 ± 6	3 ± 1
80	162 ± 107	14 ± 4	3 ± 1
120	56 ± 56	8 ± 3	6 ± 1

As already implied, the average particle size decreases with higher concentrations of TEOS from 293 ± 201 nm² (40% TEOS) over 162 ± 107 nm² (80% TEOS) to 56 ± 56 nm² (120% TEOS). The high standard deviation arises from the existence of a few large silica particles and the broad size distribution in every sample. The average equivalent

spherical particle diameter follows the tendency of the average particle size. Regarding the particle density an inverse behavior can be observed. The higher the amount of introduced TEOS the higher the density and the smaller the size of the particles is.

In order to verify that the bright structures in STEM micrographs are silica, EDS measurements were performed on both, the bright particles and particle-free regions of the membranes. In Figure 5.4 two EDS spectra measured on 120% TEOS are shown exemplarily. The black colored spectrum was measured on a bright particle and the gray spectrum was measured on a particle-free region.

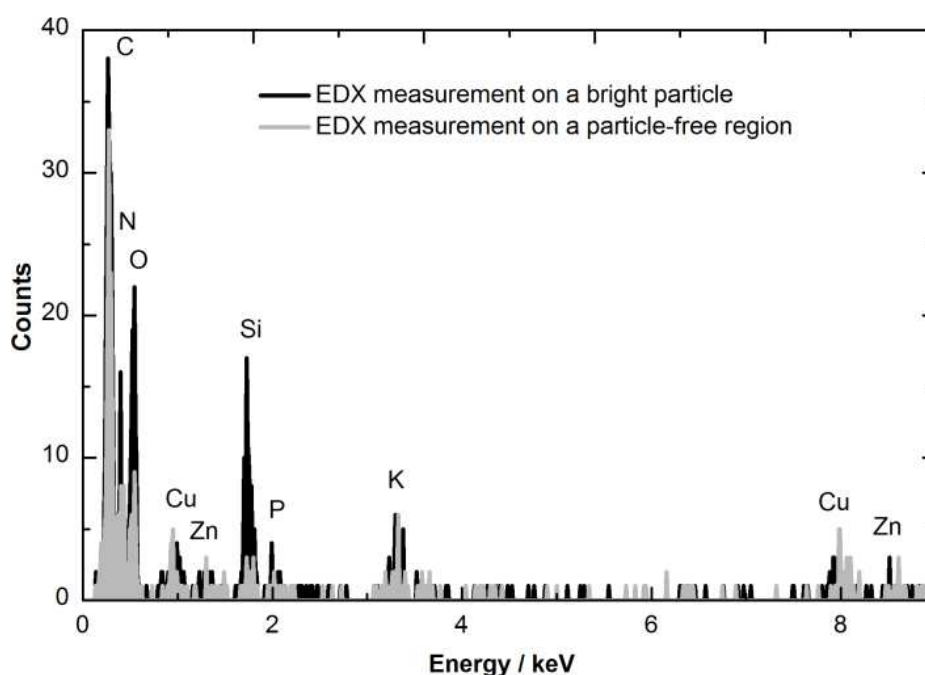


Figure 5.4: EDS spectra of 120% TEOS on a bright particle (black) and on a particle free region (gray).

PBI is composed of carbon and nitrogen. A dialkylphosphate softener which is equally distributed within the membrane contains phosphor and oxygen and an added catalyst is made up of potassium. The elements copper and zinc originate from the used brass tube and wafer for the specimen preparation. The data clearly shows a higher silicon and oxygen proportion for the bright particle indicating that the particles consist of silica.

In addition to measurements over only a few nm², several EDS overview measurements over an area of 5 × 5 μm² have been conducted on all samples. In Table 5.2 the amount of

silicon is compared to the amount of phosphor which is present in each of the membranes in equal quantity as well as in uniform distribution.

Table 5.2: Detected ratio of silicon to phosphor in atomic percent for the samples with 40%, 80% and 120% TEOS via overview EDS measurements.

TEOS (%)	Si (at%)	P (at%)
40	71 ± 5	29 ± 5
80	74 ± 4	26 ± 4
120	77 ± 3	23 ± 3

The silicon to phosphor rate increases from 40% over 80% to 120% TEOS content which correlates with the silica precursor concentration. Thus, it appears that if a higher amount of TEOS is used, a higher amount of silica is indeed incorporated into the membrane.

XRD measurements were performed to reveal possible structural changes in the polymer matrix due to the presence of silica particles. In Figure 5.5 the X-ray diffraction patterns of the three membrane specimens with 40%, 80% and 120% TEOS are illustrated. Additionally, the pattern of a PBI membrane which was not treated with TEOS (0% TEOS) is shown by way of comparison. At a 2θ value of about 21.0° a broad reflection can be identified in all samples. This value for the amorphous PBI membrane is in rough agreement with literature.^[39] The full width at half maximum (FWHM) Δ was measured for each broad reflection. All of the broad diffraction peaks of 40% TEOS ($\Delta = 9.154^\circ$), 80% TEOS ($\Delta = 8.290^\circ$) and 120% TEOS ($\Delta = 8.485^\circ$) exhibit a larger FWHM than the one of 0% TEOS ($\Delta = 7.128^\circ$). A possible explanation for this observation is an increasing disorder in the polymer matrix because of the existence of silica particles. A high disorder leads to a less defined stacking of the PBI chains resulting in a broader reflection. The reflection width of the membranes incorporated with silica particles also varies but no obvious trend can be detected between the size or the amount of silica precursor and the FWHM of the respective reflections.

No discrete, sharp reflexes were observed during the measurements indicating that none of the parts of the membrane or the silica particles are crystalline.

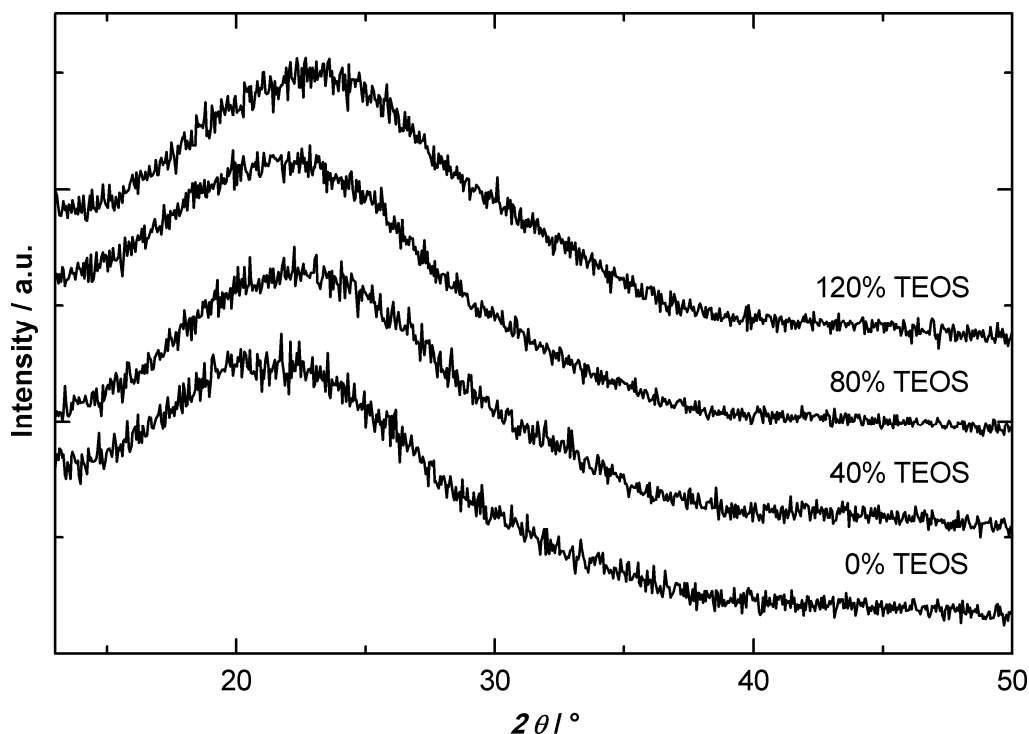


Figure 5.5: X-ray diffractograms of the samples containing 40%, 80% and 120% TEOS. A PBI membrane without incorporated silica particles (0% TEOS) is also shown. For a better comparison the diffraction patterns are normalized as well as displaced along the y-axis.

5.3.2 *Ex-situ* membrane properties

5.3.2.1 Thermal stability

The thermal behavior of all three composites with 40%, 80% and 120% TEOS was investigated in comparison to a pure PBI membrane via thermogravimetric analysis up to 600 °C (see Figure 5.6). The TEOS contents have no influence on the mass loss of the samples. With the boiling point of TEOS being at 168 °C, all precursor molecules have reacted to silanole surrounded silica particles during membrane preparation.^[40]

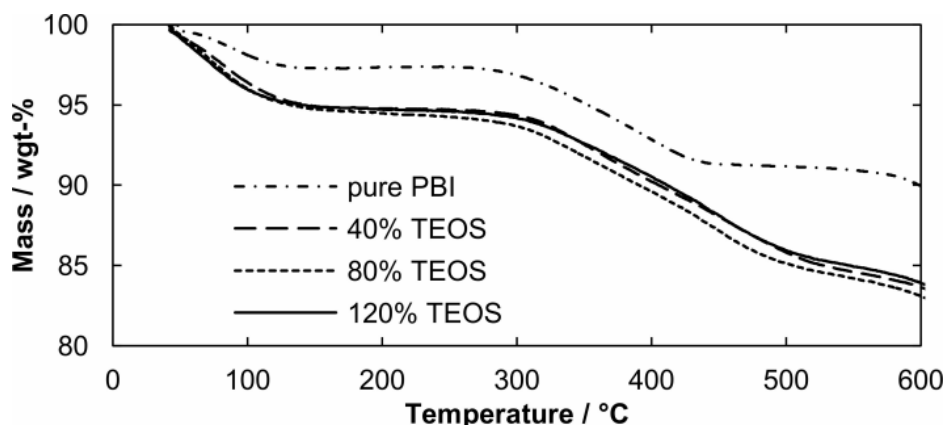


Figure 5.6: TGA measurements of membrane samples with 40%, 80% and 120% TEOS content in comparison to a pure PBI membrane.

The first mass loss until 150 °C is due to absorbed water in the membranes and traces of the solvent. As organic-inorganic membranes have higher water binding capacity, they lose more weight in this temperature range than the pure PBI membrane. Between 300 and 500 °C a constant weight loss of 9% for the samples containing silica was observed. As the boiling point of GPTMS is at 260 °C, this mass loss results mainly from DMAc evaporation.^[41] Altogether, the examined samples are thermally stable up to 300 °C, which qualifies all three membranes for high temperature fuel cell operation. This is in agreement to the results previously reported for related membrane compositions.^[24,27,42] These materials also showed no differences in thermal stability at different silica contents. Respecting the effects of the different pre-treatments and additives, their curve behavior was also similar.

5.3.2.2 Mechanical stability

Stress-strain curves of the different materials were measured to test the mechanical stability of the samples with 40%, 80% and 120% TEOS as well as a pure PBI membrane (Figure 5.7). Based on the different sizes, shapes and distributions of the silica particles in the three membranes, a difference in the mechanical stability is observed. Incorporation of inorganic particles in the membrane enhances the strength in comparison to pure PBI significantly.

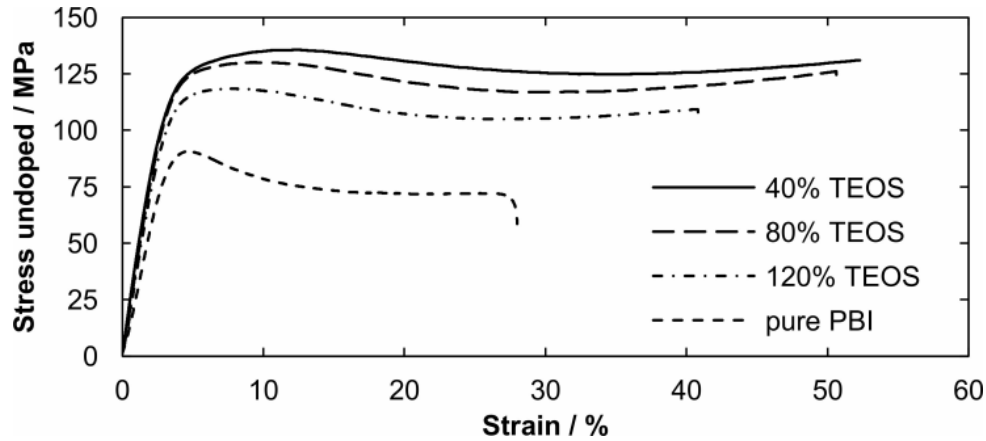


Figure 5.7: Stress-strain curves of membranes with 40%, 80% and 120% TEOS content in comparison to a pure PBI membrane.

The membrane with 40% TEOS content gives the best mechanical stability. By adding additional silica, the mechanical strength of the materials is reduced. Young's modulus decreases from 4500 to 2800 MPa and the yield stress from 136 to 119 MPa. Furthermore, the ultimate strain is reduced from 52% to 42% by raising the TEOS content in the membranes.

The elongated, large particles in the membrane with 40% TEOS enhance the strength and Young's modulus without leading to cracks in the material. The elastic deformation of these membranes is improved, compared to membranes without TEOS, as the particles block the unfolding process of the polymer chains to a certain extent.^[20] The higher amount and smaller particle size at higher silica contents does not hinder the unfolding of the polymer chains as much as bigger particles. This results in lower elastic deformation and therefore lower yield strength and Young's modulus.^[20] The slight differences in ultimate strain of the samples with different TEOS contents are also affected by the different particle morphologies. In the membrane with 40% TEOS, a small amount of large particles is bound to the polymer chains via the cross-linker GPTMS. On the other hand, in membranes with high silica contents the same amount of small particles can be bound to the polymer. This results in nearly equal plastic deformation and values of ultimate strain. Assuming a higher amount of separate unbound particles in the material with 120% TEOS, its plastic deformation is smaller than in membranes with lower silica contents. Even in the three membranes' preparation, the 120% TEOS content showed a much higher brittleness than the other

samples. In related membrane compositions with lower TEOS contents, a comparable reduction in strength was observed in literature while increasing the TEOS contents.^[24]

5.3.2.3 Chemical stability

For testing the chemical stability of the 40%, 80% and 120% TEOS samples, the extraction residue in DMAc was measured. In addition, the amount of liquid uptake and the swelling in plane plus thickness in phosphoric acid were determined (Table 5.3).

Table 5.3: Extraction residue, liquid uptake and swelling of the membrane samples.

Inorganic content [%]	Extraction residue [%]	Liquid uptake [wt%]	Swelling in plane [%]	Swelling in thickness [%]
Pure PBI	0	490	72	96
40	98	430	113	81
80	99	410	116	79
120	100	430	107	79

While a membrane of pure PBI dissolves in hot DMAc, the incorporation of inorganic particles in the membrane results in high extraction residues of 98–100%. In coincidence with previous works, all membranes containing TEOS exhibit equally good chemical stability in the solvent.^[24] In phosphoric acid, the incorporation of 40% TEOS leads to a slight reduction in liquid uptake from 490 wt% to 430 wt% in comparison to the pure PBI. The swelling in thickness is reduced from 96% to 81%, whereas the swelling in plane is rising from 72% to 113%. Comparing different inorganic contents of 40%, 80% and 120% TEOS, the liquid uptake behavior and the swelling parameters are not affected by the amount of used TEOS. The phosphoric acid uptake in membranes with different TEOS contents is schematically shown in Figure 5.8. The swelling and acid uptake of the material is mainly influenced by the chambers size, which are formed by cross-linking the inorganic particles with the polymer chains. These chambers can take up phosphoric acid to a certain extent. Smaller, highly distributed particles at higher silica contents have the same degree of cross-linking and therefore the same liquid uptake behavior as the samples with larger particles. It seems, that smaller particles

between the cross-linkers either result in smaller chambers with an enhanced acid uptake through the unbound silica particles or the size of the chambers is independent from the particle size inbetween. Both options are visualized in Figure 5.8 schematically.

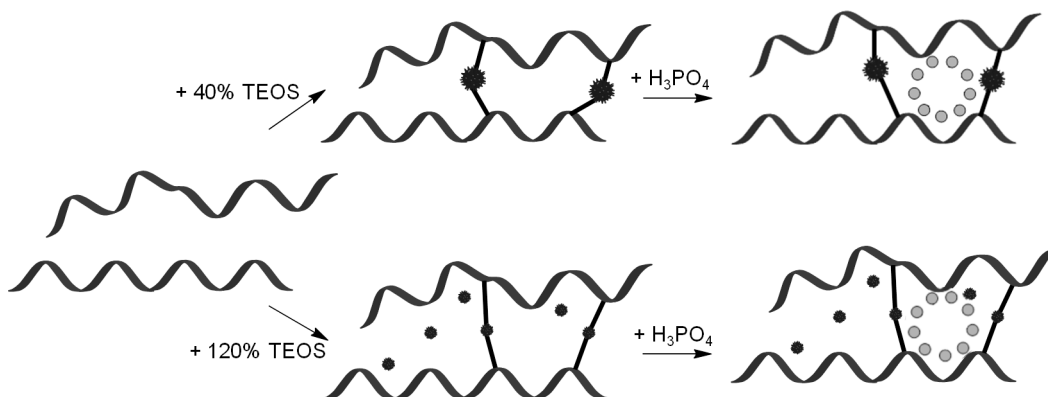


Figure 5.8: Schematic drawing of the phosphoric acid (circles) uptake between the polymer chains (chains) at different silica contents (stars) and the same cross-linker content (strokes).

The results show the importance of the created inorganic structure for gaining an adequate chemical stability. On the other hand, different particle distributions and sizes do not affect the liquid uptake and swelling behavior of the membranes significantly. To verify whether the distribution of phosphoric acid within the membrane or the final MEA is changed by different silica contents, *in-situ* testing was carried out.

5.3.3 *In-situ* fuel cell testing and degradation analysis

5.3.3.1 Polarization curves

The polarization curves in Figure 5.9 show the same performance behavior of the samples with different TEOS contents. A variation of the phosphoric acid contents in the MEAs proved that the ideal doping level is the same for all samples. Therefore, the different particle structures do not change the BOL performance and power density curves in the whole current density range. All samples show very good open-circuit voltage values at 0 A cm^{-2} , indicating that no short circuits or electrical losses are present.

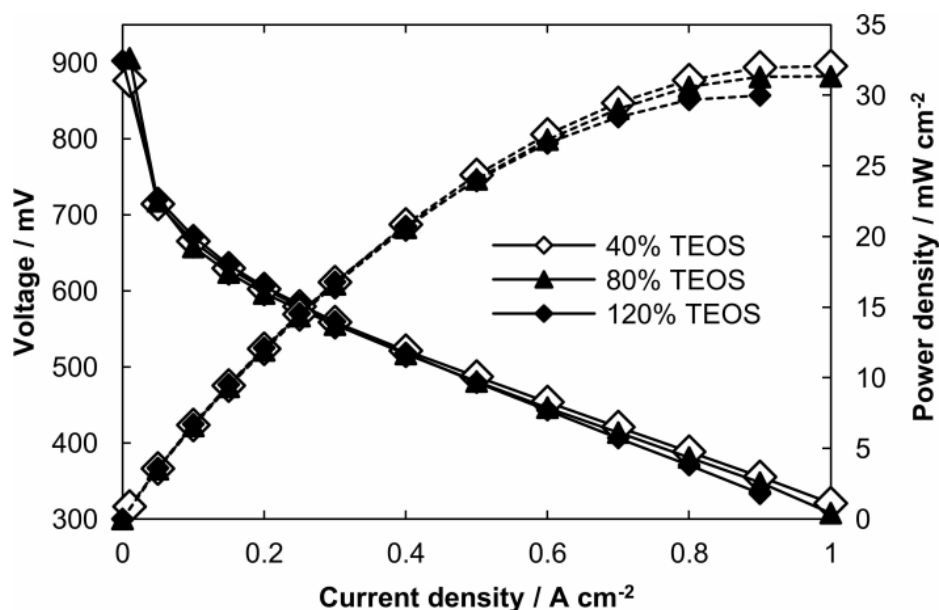


Figure 5.9: BOL polarization (solid lines) and power density (dashed lines) curves of the MEAs with 40%, 80% and 120% TEOS.

5.3.3.2 Start-Stop-Cycling and degradation effects

The long-term degradation behavior of the post cured membranes was simulated in MEAs under fuel cell conditions via start-stop-cycling. This method is often used for the simulation of accelerated lifetime tests in HT-PEMFC.^[43] The results of the samples with 40% and 80% TEOS content are shown in Figure 5.10. As mentioned before, the membrane with 120% TEOS content was very brittle and therefore not suited for MEA production. The graph demonstrates the higher cycle stability of the membrane with lower TEOS content. This MEA starts at a 50 mV lower BOL voltage, but as its degradation with 0.05 mV per cycle is much less, its performance surpasses the MEA with 80% TEOS content after 230 h of operation.

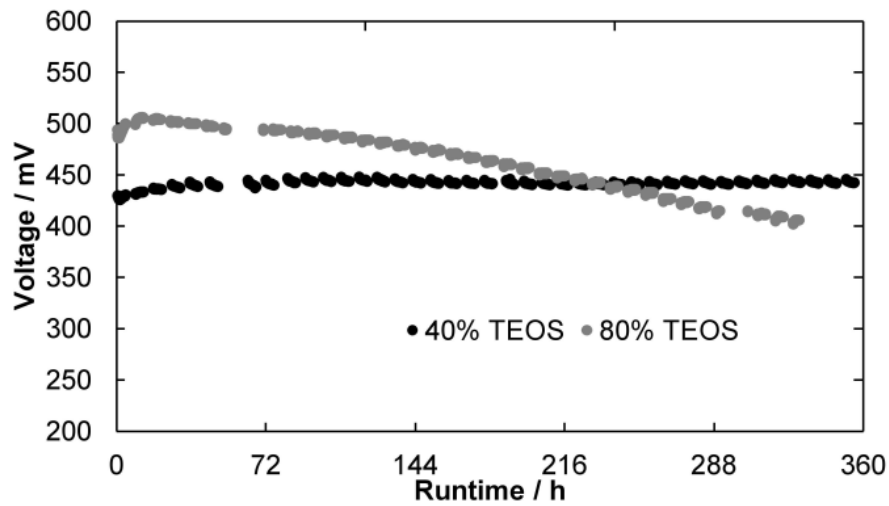


Figure 5.10: Start-stop-cycling of the MEAs with organic-inorganic composites with 40% and 80% TEOS content.

To identify the reason for the higher degradation rate in the MEA with 80% TEOS content, the cycled MEAs were characterized after operation (end of life, EOL). The polarization and power density curves before and after the testing are shown in Figure 5.11. While the performance of the MEA with 40% TEOS content remains unchanged at low current densities, the polarization curve of the MEA with the higher content is reduced during operation. The reduced performance occurs mainly at low current densities. The loss in open-circuit voltage indicates the formation of short circuits during cycling.

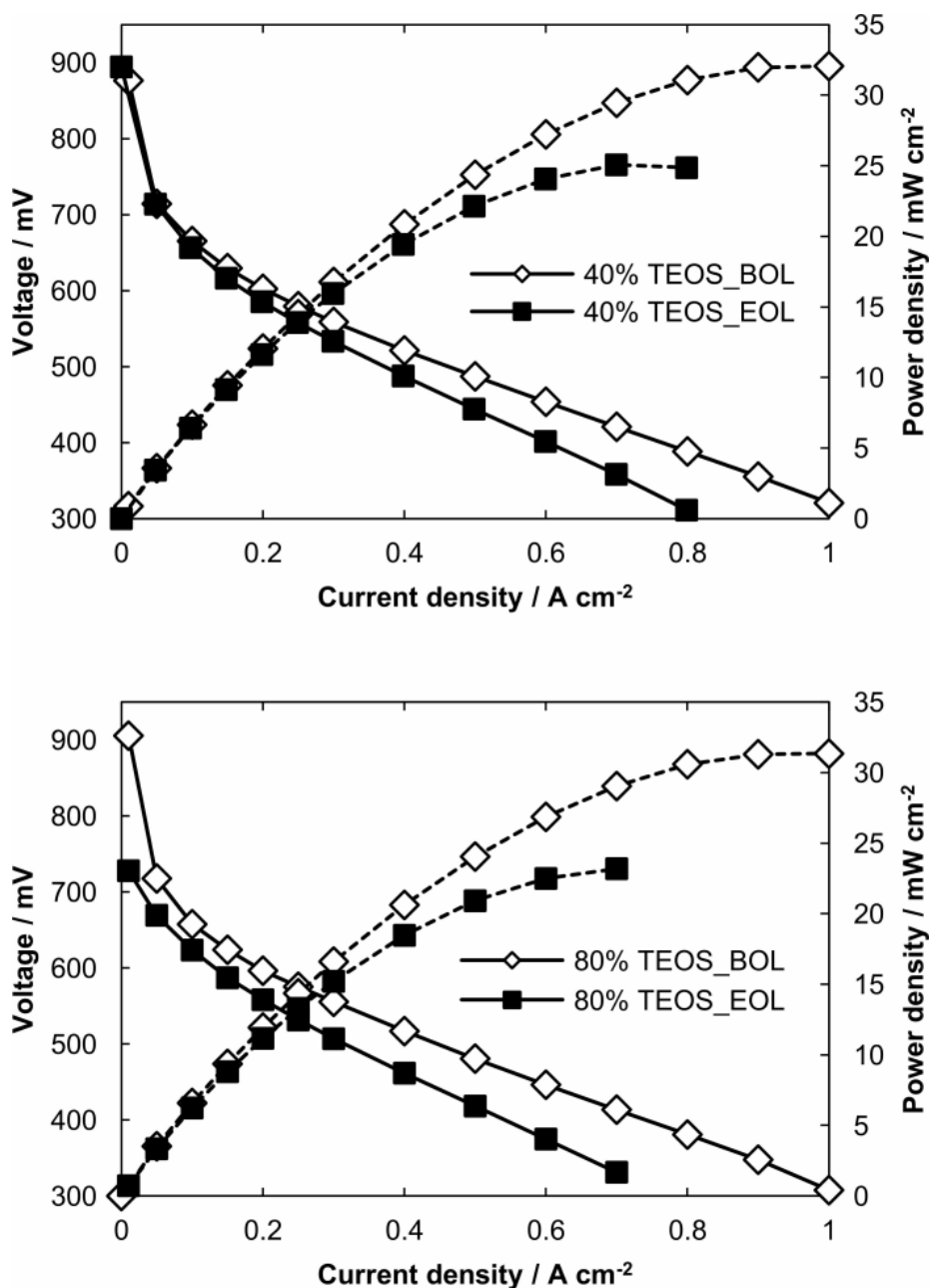


Figure 5.11: Polarization (solid lines) and power density (dashed lines) curves of 40% and 80% TEOS samples before (BOL) and after (EOL) cycling.

Short cut localization tests proved that the MEA with 80% TEOS content formed several electrical and gas short circuits in fuel cell operation. These results explain the high cycle degradation of the material. The increased formation of short circuits in MEAs and the brittleness of the membrane at higher TEOS contents lead to the assumption that lower silica contents are more beneficial for fuel cell operation.

5.3.3.3 Long-term fuel cell operation

In order to prove the benefits of the developed organic-inorganic composite membrane composition with 40% TEOS content, a MEA using this membrane is compared with a pure PBI membrane under long term fuel cell operation over 1300 h (Figure 5.12). The MEA made out of pure PBI starts at a lower voltage and shows a higher degradation rate during operation. By incorporating the fibrous silica particles and cross-linking them to the polymer, a better performance and durability are gained.

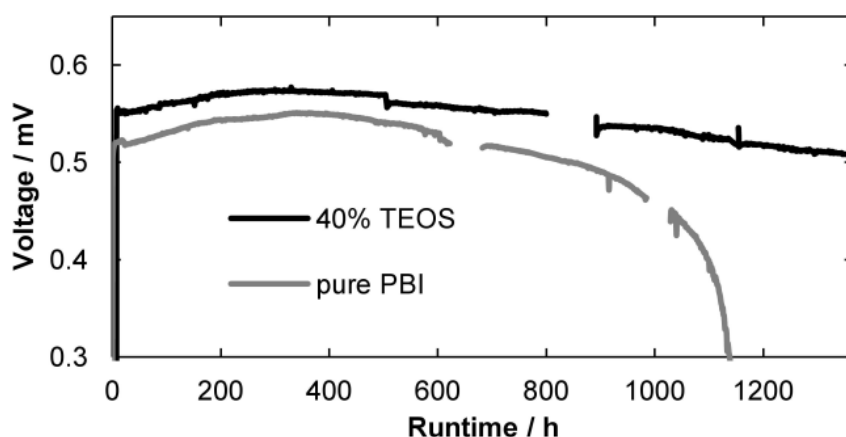


Figure 5.12: Long term fuel cell operation at constant current of the MEA with 40% TEOS content in comparison with a pure PBI membrane.

5.4 Conclusion

By in-situ sol-gel reaction PBI-based membranes with 40%, 80% and 120% of the inorganic silica precursor TEOS was produced. The particles were bound to the polymer PBI by adding a constant amount of 10% GPTMS as a cross-linking agent. Structural analysis by STEM, EDS and XRD proved the formation of amorphous silica particles in the membrane. Their shape, size and distribution were shown to be highly affected by the precursor content. Whereas lower silica contents lead to few large, fibrous particles, adding higher TEOS contents resulted in small, highly distributed particles of spherical shape. By TEM and statistical methods the distribution of the inorganic particles was analyzed.

Ex-situ membrane characterization showed an unaffected thermal stability at different silica contents. The best mechanical stability was observed with a small amount of

fibrous silica particles resulting from a low TEOS content of 40%. Even though the incorporation of silica particles did not result in a higher acid uptake, it did influence the efficiency of acid distribution in the MEA and therefore led to an improved performance. The cross-linking of differently sized inorganic particles to the polymer gave an overall high *ex-situ* chemical stability of the membrane.

Whereas the beginning of life polarization curves of all samples were the same, the cycling behavior of the MEA with 80% TEOS showed a much higher degradation per cycle than the sample with 40% TEOS due to the formation of electrical short circuits. At high silica contents the membranes had a lower mechanical stability and started to get brittle. The higher amount of smaller particles accelerated the formation of short circuits and gas leakages in cycle testing. In comparison to the MEA with pure PBI, the developed membrane with large, fibrous inorganic particles showed an enhanced durability in constant operation.

Altogether the optimized phosphoric acid distribution and mechanical stability of the organic-inorganic composite membrane with few fibrous particles from 40% TEOS content led to a higher performance and degradation rate in constant and cycled fuel cell operation.

5.5 Chapter references

- [1] Asensio, J. A.; Sánchez, E. M.; Gómez-Romero, P. *Chem. Soc. Rev.* **2010**, 39, 3210.
- [2] Li, Q.; Hjuler, H. A.; Bjerrum, N. J. *Electrochim. Acta* **2000**, 45, 4219.
- [3] Gottesfeld, S.; Zawodzinski, T. A. In *Adv. Electrochem. Sci. Eng.*; Wiley-VCH Verlag GmbH: 2008, p 195.
- [4] Li, Q.; Jensen, J. O.; Savinell, R. F.; Bjerrum, N. J. *Prog. Polym. Sci.* **2009**, 34, 449.
- [5] Li, Q.; He, R.; Jensen, J. O.; Bjerrum, N. J. *Chem. Mater.* **2003**, 15, 4896.
- [6] Savadogo, O. *J. Power Sources* **2004**, 127, 135.
- [7] Zecevic, S. K.; Wainright, J. S.; Litt, M. H.; Gojkovic, S. L.; Savinell, R. F. *J. Electrochem. Soc.* **1997**, 144, 2973.
- [8] Ma, Y.-L.; Wainright, J. S.; Litt, M. H.; Savinell, R. F. *J. Electrochem. Soc.* **2004**, 151, A8.
- [9] Wang, C.-P.; Chu, H.-S.; Yan, Y.-Y.; Hsueh, K.-L. *J. Power Sources* **2007**, 170, 235.
- [10] Korsgaard, A. R.; Refshauge, R.; Nielsen, M. P.; Bang, M.; Kær, S. K. *J. Power Sources* **2006**, 162, 239.
- [11] Jensen, J. O.; Li, Q.; Pan, C.; Bjerrum, N. J.; Rudbeck, H. C. et al. In *18th World Hydrogen Energy Conference 2010*; Stolten, D., Grube, T., Eds.; Forschungszentrum Jülich GmbH, Zentralbibliothek: Essen, 2010, p 115.
- [12] Bose, S.; Kuila, T.; Nguyen, T. X. H.; Kim, N. H.; Lau, K.-t. et al. *Prog. Polym. Sci.* **2011**, 36, 813.
- [13] Zhang, J.; Xie, Z.; Zhang, J.; Tang, Y.; Song, C. et al. *J. Power Sources* **2006**, 160, 872.
- [14] Mader, J.; Xiao, L.; Schmidt, T.; Benicewicz, B. In *Fuel Cells II*; Scherer, G., Ed.; Springer Berlin Heidelberg: 2008; Vol. 216, p 63.
- [15] Borup, R.; Meyers, J.; Pivovar, B.; Kim, Y. S.; Mukundan, R. et al. *Chem. Rev.* **2007**, 107, 3904.
- [16] Jones, D. J.; Rozière, J. In *Handbook of Fuel Cells*; John Wiley & Sons, Ltd: 2010.
- [17] Schnecko, H. *Die Angew. Makromol. Chem.* **1979**, 76, 1.
- [18] Ogoshi, T.; Chujo, Y. *Compos. Interfaces* **2005**, 11, 539.
- [19] Herring, A. M. *J. Macromol. Sci. Part C* **2006**, 46, 245.
- [20] Alberti, G.; Casciola, M. *Annu. Rev. Mater. Res.* **2003**, 33, 129.
- [21] Ghosh, S.; Maity, S.; Jana, T. *J. Mater. Chem.* **2011**, 21, 14897.
- [22] Jones, D.; Rozière, J. In *Fuel Cells I*; Scherer, G. G., Ed.; Springer Berlin Heidelberg: 2008; Vol. 215, p 219.
- [23] Chuang, S.-W.; Hsu, S. L.-C.; Liu, Y.-H. *J. Membr. Sci.* **2007**, 305, 353.
- [24] Wang, S.; Zhao, C.; Ma, W.; Zhang, N.; Zhang, Y. et al. *J. Mater. Chem. A* **2013**, 1, 621.

- [25] Colicchio, I.; Keul, H.; Sanders, D.; Simon, U.; Weirich, T. E. et al. *Fuel Cells* **2006**, 6, 225.
- [26] Alzina, C.; Sbirrazzuoli, N.; Mija, A. *J. Phys. Chem. C* **2011**, 115, 22789.
- [27] Suryani; Liu, Y.-L. *J. Membr. Sci.* **2009**, 332, 121.
- [28] Quartarone, E.; Mustarelli, P.; Carollo, A.; Grandi, S.; Magistris, A. et al. *Fuel Cells* **2009**, 9, 231.
- [29] Alberti, G.; Casciola, M.; Pica, M.; Tarpanelli, T.; Sganappa, M. *Fuel Cells* **2005**, 5, 366.
- [30] He, R.; Li, Q.; Xiao, G.; Bjerrum, N. J. *J. Membr. Sci.* **2003**, 226, 169.
- [31] Kumar, B.; Fellner, J. P. *J. Power Sources* **2003**, 123, 132.
- [32] Namazi, H.; Ahmadi, H. *J. Power Sources* **2011**, 196, 2573.
- [33] Kurdakova, V.; Quartarone, E.; Mustarelli, P.; Magistris, A.; Caponetti, E. et al. *J. Power Sources* **2010**, 195, 7765.
- [34] Suryani; Chang, Y.-N.; Lai, J.-Y.; Liu, Y.-L. *J. Membr. Sci.* **2012**, 403–404, 1.
- [35] Linlin, M.; Mishra, A. K.; Kim, N. H.; Lee, J. H. *J. Membr. Sci.* **2012**, 411–412, 91.
- [36] Quartarone, E.; Mustarelli, P. *Energy Environ. Sci.* **2012**, 5, 6436.
- [37] Strecker, A.; Salzberger, U.; Mayer, J. *Prakt. Metall.* **1993**, 30, 482.
- [38] Schneider, C. A.; Rasband, W. S.; Eliceiri, K. W. *Nat. Methods* **2012**, 9, 671.
- [39] Sadeghi, M.; Semsarzadeh, M. A.; Moadel, H. *J. Membr. Sci.* **2009**, 331, 21.
- [40] Patel, S.; Bandyopadhyay, A.; Vijayabaskar, V.; Bhowmick, A. K. *J. Mater. Sci.* **2006**, 41, 927.
- [41] Sanchez, R.; Todoli, J.-L.; Lienemann, C.-P.; Mermet, J.-M. *J. Anal. At. Spectrom.* **2009**, 24, 391.
- [42] Chu, F.; Lin, B.; Qiu, B.; Si, Z.; Qiu, L. et al. *J. Mater. Chem.* **2012**, 22, 18411.
- [43] Hartnig, C.; Schmidt, T. J. *J. Power Sources* **2011**, 196, 5564.

6 Transmission electron microscopy study of silica reinforced polybenzimidazole membranes

This chapter is based on the following publication:

Christoph Heinzl, Tanja Osslander, Stephan Gleich, Christina Scheu *Journal of Membrane Science* (accepted).

6.1 Introduction

The development and optimization of proton exchange membrane fuel cells (PEMFC) as promising systems for efficient, environmentally friendly energy conversion has gained considerable attention in research over the last several years.^[1] One research focus is the introduction of new membrane types, which can be operated above 100 °C and thereby overcome the limitations of commonly used Nafion® membranes. By operating at higher temperatures (150 °C to 200 °C) the high temperature PEMFC (HT-PEMFC) exhibits features like an increased CO tolerance, an increased electrocatalytic activity, simplified water management and in addition no need for a complex thermal management system.^[2] The most widely used material for HT-PEMFC membranes is polybenzimidazole (poly(2,2'-*m*-phenylene-5,5'-bibenzimidazole), PBI).^[3-5] It combines advantageous properties like high thermal and mechanical stability as well as low gas permeability with a high CO tolerance.^[3] The long-term stability of the phosphoric acid doped PBI-based membranes under fuel cell operation conditions is a crucial prerequisite for the development of stable and efficient HT-PEMFCs. In this regard, leaching of the phosphoric acid and low proton conductivity are some of the known challenges of PBI-based membranes. Different strategies were applied to improve the stability and the properties of these kinds of membranes for the use in HT-PEMFC. By modifying the polymer structure to adjust the basicity of PBI a higher proton conductivity was obtained.^[6] To enhance the mechanical strength and oxidative stability of PBI-based membranes the preparation of hyperbranched and cross-linked PBI was reported to be a successful approach.^[7,8] Another promising method is the incorporation of inorganic nanofillers in the polymer matrix to form organic-inorganic composite

membranes. Pure or functionalized silica particles introduced in PBI-based membranes enhanced their mechanical stability and improved their acid retention capability and therefore their proton conductivity.^[9-16] These positive effects were also observed for silica doped Nafion® membranes.^[17] The incorporation is often realized by an *in-situ* sol-gel reaction of the particles during membrane casting.^[18] By doing so, the agglomeration of the silica particles is prevented. Saxena et al. reported that control over the spacing between silica domains can be achieved by applying polyethylene glycol of different molecular weight during synthesis.^[11] In order to maintain a high conductivity the formation of percolation pathways at the interface between the polar and nonpolar domains in the functionalized membrane is important.^[19]

Altogether control over the size and distribution of the incorporated inorganic particles is crucial for the development of efficient HT-PEMFC membranes. Most of the applied analysis methods in literature focus on *ex-situ* and *in-situ* techniques which give an averaged behavior of the membrane properties. Regarding the electrodes of HT-PEMFC detailed electron microscopic analytical work was performed.^[20,21] In case of membranes only basic scanning electron microscopy and transmission electron microscopy (TEM) measurements were mostly conducted to get information on the size and agglomeration behavior of the introduced particles.^[9,10,12-14,17,21] Detailed studies of the distribution of the occurring elements via analytical measurements such as energy dispersive X-ray spectroscopy (EDS) and electron energy-loss spectroscopy (EELS) are rare. The electron microscopical analysis of organic materials such as the PBI-based membrane is challenging due to several reasons.^[22] The interaction of electrons with organic matter results in inelastic scattering processes which cause ionization and break chemical bonds. In addition, the sample suffers from mass loss, fading of crystallinity and heat generation.^[23] Thus, polymers decompose and damage quickly under electron bombardment.

In our recent work^[18] we showed that silica nanoparticles embedded in a PBI-based membrane significantly enhance the chemical and mechanical stability as well as the performance of the resulting membrane electrode assemblies (MEA). We found that a certain amount of silica doping gave the best results and that larger silica nanoparticles seemed to have a beneficial influence on the MEA performance. In the present work the

influence of an additional heating step during the membrane synthesis on the size, distribution and composition of the embedded silica particles is investigated. We also demonstrate that TEM is a well-suited method to obtain local information on the size, distribution and composition of silica nanoparticles in a PBI-based membrane as well as to study possible segregation phenomena which might occur at the particle/polymer interface. The applied techniques include high-angle annular dark-field (HAADF) imaging in the scanning TEM (STEM) mode for the determination of the sizes and distribution of the silica particles in the membrane as well as EDS and EELS for the chemical composition analyses. In addition, the chemical and mechanical properties of the membranes are studied. The cycle stability as well as the long-term fuel cell operation stability was examined to investigate the suitability of the newly synthesized silica stabilized PBI-membrane electrode assemblies in HT-PEMFC applications.

6.2 Experimental

6.2.1 Synthesis

Membrane and MEA preparation

Two different membranes based on the polymer PBI were prepared. First, PBI was dissolved under pressure by stirring in N,N-dimethylacetamide (DMAc, Merck) over 3 h at 200 °C. After filtering using a 20 µm filter, the product was mixed with a solution of tetraethoxy silane (TEOS, Alpha Aesar) and (3-glycidyloxypropyl)-trimethoxysilane (GPTMS, Alpha Aesar) in DMAc. Potassium hydroxide (Sigma Aldrich) was added to the resulting viscous solution. Stirring at 70 °C, filtration and coating on a carrier foil resulted in membrane M I. For comparison we used a membrane which had been studied in our previous work and which was stirred at room temperature while all other parameters were the same.^[18] This reference membrane is labeled M II in the following. For both membranes an amount of 40% TEOS with regard to the PBI was introduced. The membrane thickness was ~50 µm. By the chosen synthesis procedure the silica nanoparticles are cross-linked via GPTMS to the PBI chains of the membrane. In order to fabricate HT-PEM MEAs, the membranes were hot-pressed with phosphoric acid doped gas diffusion electrodes as described elsewhere.^[24]

6.2.2 Characterization methods

6.2.2.1 *Ex-situ* membrane testing

Chemical stability

Chemical stability of the two membranes was tested by extraction in the solvent DMAc. Samples were dried overnight at 150 °C in the oven to obtain the basic weight. The membrane pieces were covered with DMAc in a round bottom flask and heated to 130 °C for one hour. Within one additional hour the solution was cooled to room temperature. The extracted samples were dried at 150 °C over night, weighted and the extraction residue was calculated.

Swelling ratio and liquid uptake

Swelling behavior and liquid uptake were determined as percentage weight increase and dimensional growth by immersing the samples in phosphoric acid at 130 °C for 30 min. The changes in weight and dimension between the undoped and phosphoric acid doped membranes were measured.

Mechanical properties

Stress-strain curves of the samples where measured on a *BT1-FR0.5TN.D14/500 N Zwicki* from *Zwick* at room temperature. The average thickness of the membrane pieces was evaluated with a thickness gauge from Sylvac.

Morphology and chemical composition analysis

In-depth investigations of the silica particles in the membrane regarding their morphology as well as their chemical composition were performed by TEM based techniques. Cross-sectional TEM samples were prepared using the procedure reported by Strecker.^[25] By glueing a piece of the membrane between two spacers (aluminium or brass) a sandwich was obtained which was subsequently glued into a brass tube with an outer diameter of 3 mm. Thin discs (200 µm) were sliced off this tube with a diamond saw and thinned using a grinder and dimpler from GATAN. Further thinning of the samples with a beam of argon ions (using a precision ion polishing system from GATAN; 3 keV, 5°, double mode) was performed until electron transparency was achieved. For all TEM investigations a FEI Titan 80-300 (S)TEM equipped with an EDAX detector for EDS measurements was used. The Titan was operated at 80 kV and at 300 kV. Beam damage

of the membrane material could be minimized by keeping the accumulated electron dose lower than $\sim 10^5$ e/nm². This was achieved by carefully choosing the spot size, the condenser aperture and the acquisition time. An attached HAADF detector from Fischione Instruments (Model 3000) was used for STEM imaging. EELS measurements were performed in STEM mode with a Gatan Tridiem image filter. The full width at half maximum (FWHM) of the zero loss peak was around 0.9 eV. We used a 2 mm entrance aperture and a dispersion of 0.1 eV per channel leading to a satisfying energy resolution and a good signal to noise ratio. The camera length was varied between 128 mm and 196 mm leading to collector angles of 13.5 mrad and 9.3 mrad respectively.

Statistical particle evaluation

For statistical analysis, an area of several hundred silica particles was measured in each sample and analyzed with help of the program ImageJ^[26] to evaluate the size distribution of the particles and to determine the membrane area covered by silica. By applying a band-pass filter the contrast between particles and the PBI-based matrix was enhanced. A threshold of brightness value was defined to filter out the background and to allow for analyzing only the particles. After the determination of the size and number of the particles, the equivalent spherical diameter as well as the particle density was calculated.

Crystallinity analysis

X-ray diffraction (XRD) patterns were taken on a Seifert THETA/THETA-diffractometer (GE Inspection Technologies) equipped with a Meteor OD detector, using Co-K α radiation ($\lambda = 1.79$ Å) to investigate the crystallinity of the membranes and the incorporated silica on a global scale. A 2θ detection range of 10°–70°, a step size of $2\theta = 0.05^\circ$ and an acquisition time of 10 s/(2θ -step) were used. In addition, selected area electron diffraction (SAD) studies were performed in the TEM to obtain information on the crystallinity on a local scale. For these investigations a SAD aperture with a diameter of approximately 170 nm was used to select the region of interest.

6.2.2.2 MEA testing

Electrochemical behavior

Beginning-of-life (BOL) polarization curves were measured using a single cell setup with an active area of 50 cm² and a serpentine channel flow field structure on anode and cathode. Mass flow controllers regulated the reactants flow rates. Electrical heating cartridges controlled the cell temperature at 160 °C.

Cycle stability

The start-stop-cycle stability of a 50 cm² single cell was investigated under cycled fuel cell operation. The cell was heated up to 80 °C and purged with air for 5 minutes on the cathode. After heating the cell to a temperature of 120 °C, the anode was purged with nitrogen. Under hydrogen and air, the cell was heated up to 160 °C. At this temperature, current was drawn at 0.5 A/cm² and held for 4 h. In the stop phase, the current was decreased to 0.25 A/cm² while cooling the cell to 120 °C. Current was switched off and the anode was purged with nitrogen. Afterwards, the cell was cooled to room temperature. This procedure was repeated for several cycles.

Degradation at long-term operation under constant load

Long-term operation under constant load was conducted at a current density of 0.2 A/cm² at 160 °C. On the anode side, the stack was fuelled with reformed methanol (stoichiometry 1.4) and on the cathode side with air (stoichiometry 2.0).

6.3 Results and discussion

6.3.1 *Ex-situ* membrane properties

The membrane prepared at 70 °C (M I) was characterized *ex-situ* by several techniques including chemical and mechanical stability. The data are compared to the ones of membrane M II which was prepared at room temperature.^[18]

The chemical stability of the membrane samples in the solvent DMAc turned out to be similar for both membranes and amount to 98% (see Table 6.1). On the other hand liquid uptake and swelling of these samples are influenced by the temperature applied during processing. Higher temperatures during the sol-gel reaction lead to a membrane

exhibiting a higher liquid uptake. While swelling in plane of both membranes gave similar results, at room temperature prepared membrane samples expanded less in thickness.

Table 6.1. Extraction residue, liquid uptake and swelling of the membrane samples.

Sample	Extraction residue [%]	Liquid uptake [wt%]	Swelling in plane [%]	Swelling in thickness [%]
M I	98 ± 1	500 ± 20	110 ± 1	101 ± 3
M II	98 ± 0	430 ± 13	113 ± 2	81 ± 2

Stress-strain curves of the two membranes were measured in order to determine the mechanical properties of the different membranes. Figure 6.1 shows that the membranes prepared at higher temperatures have a higher yield stress of 160 MPa (compared to 135 MPa^[18]) whereas the ultimate strain of the samples was reduced from 52 % to 43 %. The Young's modulus of both samples is equivalent in the range of 4500 MPa.

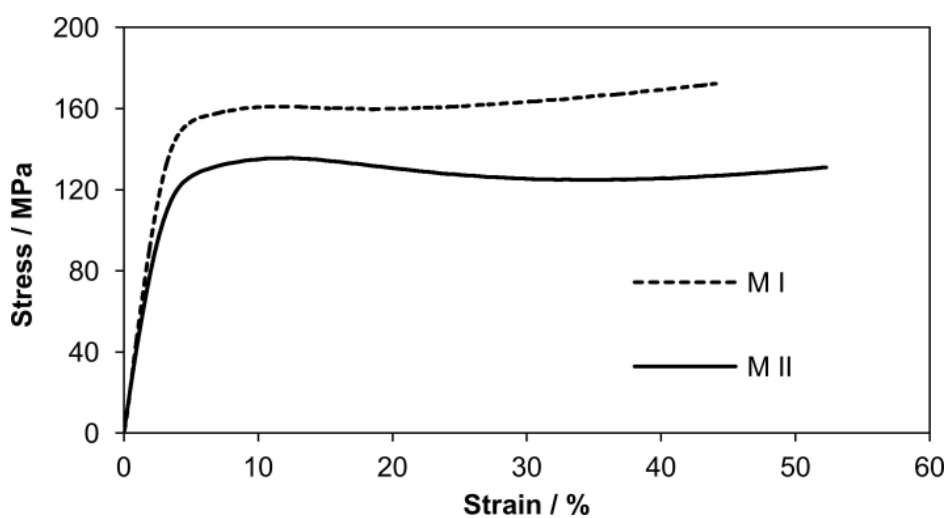


Figure 6.1: Stress-strain curves of membranes prepared at different temperatures. Data for M II is taken from Ref.^[18].

Thus, the manufacturing temperature apparently affects the membrane structure resulting in an enhanced strength of the membrane during stress-strain testing as well as an enhanced liquid uptake and difference in swelling.

6.3.2 *In-situ* membrane properties

The two membranes M I and M II were also characterized *in-situ* by analyzing polarization curves, start-stop cycles and long-term fuel cell operation tests.

The polarization curves in Figure 6.2 show the voltage of the MEAs in dependency of current density. An equivalent ideal phosphoric acid doping level was determined for both samples. Even though the good open-circuit voltage values at 0 A cm^{-2} indicate that no short circuits and electrical losses are present, the performance of the MEA of the membrane prepared at higher temperature is far lower than the one prepared at room temperature.

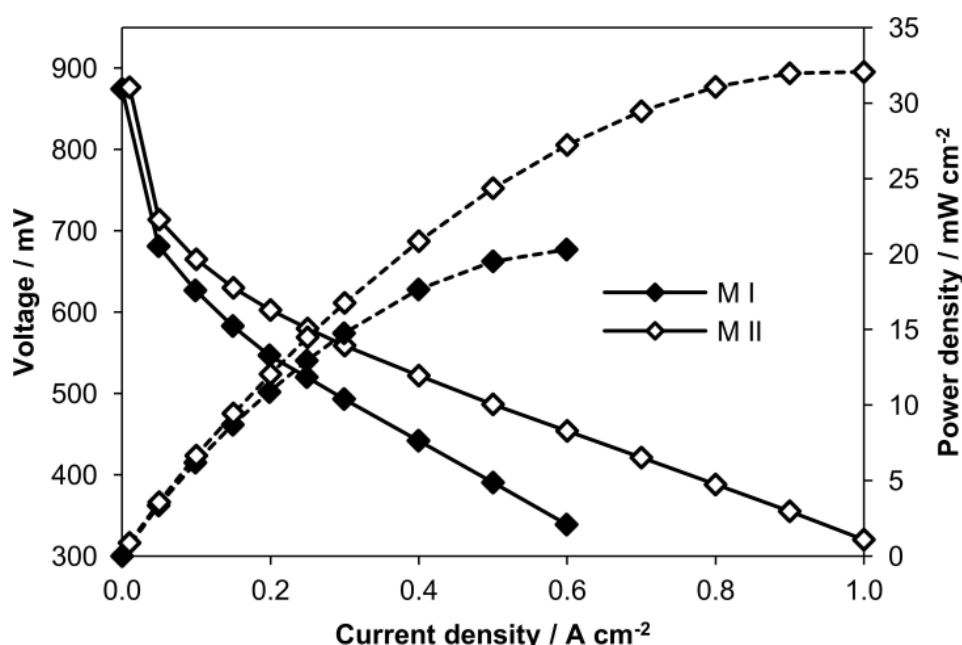


Figure 6.2: BOL polarization (solid lines) and power density (dashed lines) curves of the MEAs with membranes prepared at different temperatures. Data for M II taken from Ref.^[18].

Accelerated stress tests of the membranes in MEAs were done via start-stop-cycling under fuel cell conditions over 240 h (see Figure 6.3). Both samples have good cycling stability. But the membrane M II that was prepared at room temperature results in a higher performance of the corresponding MEA at the end of the test. Therefore, lower preparation temperature lead to an enhanced cycle stability of the MEA. The explanation of these findings will be addressed later (see section 6.3.3.1).

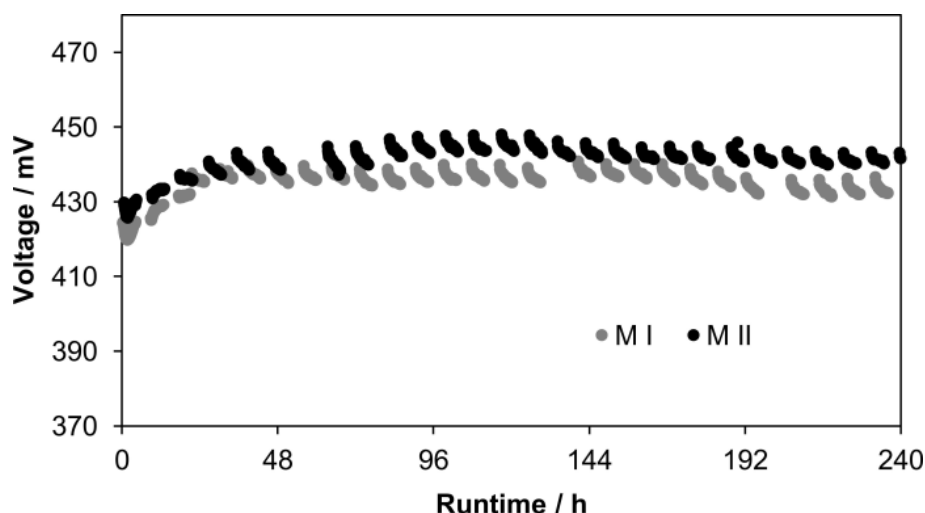


Figure 6.3. Start-stop-cycling behavior of the MEAs stirred at different temperatures. Data for M II is taken from Ref.^[18].

Long-term testing under constant current conditions of the two different MEAs is shown in Figure 6.4. The MEA constructed using M II does result in a higher performance and slightly lower degradation rate over 1300 h. In contrast to the above shown *ex-situ* data, the higher preparation temperature of the membranes which apparently affects the membrane structure is not beneficial for the MEAs performance under constant current and cycling conditions. Consequently, structural and chemical analyses of the two membranes M I and M II by various TEM methods are crucial to understand the results of the *in-situ* as well as the *ex-situ* membrane measurements.

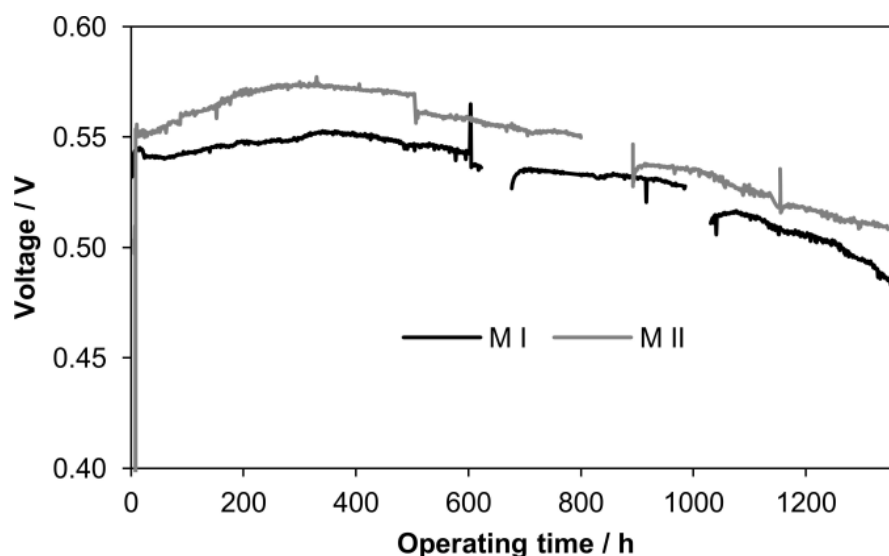


Figure 6.4. Fuel cell operation under constant current conditions of MEAs with different preparation temperatures of the organic-inorganic composite membrane. Each graph is based on three measurements. Data for M II is taken from Ref.^[18].

6.3.3 Structural analysis

6.3.3.1 Morphology

The two synthesized membranes were analyzed in-depth with several TEM based methods in order to explain their observed *ex-situ* and *in-situ* characteristics shown above. In Figure 6.5 a comparison of the two membrane systems is presented. The top row a) – c) presents the microstructure of membrane M I, which underwent an additional heat treatment at 70 °C during synthesis, and the bottom row d) – f) presents that of membrane M II, synthesized without additional heating. In both samples the successful formation of particles during the *in-situ* sol-gel reaction can be observed. Since the shown micrographs were recorded with the HAADF detector in STEM mode, the obtained bright contrast of the particles indicates that they consist of heavier elements compared to the membrane. This is due to the fact that the intensity is roughly proportional to the atomic number squared in this image mode.^[27] As will be shown below, these particles are silica particles which form during the membrane synthesis. The channel-like structure and the irregular brightness of the grey appearing membrane matrix arise from an inhomogeneous argon ion thinning process during the TEM sample preparation resulting in thickness variations.

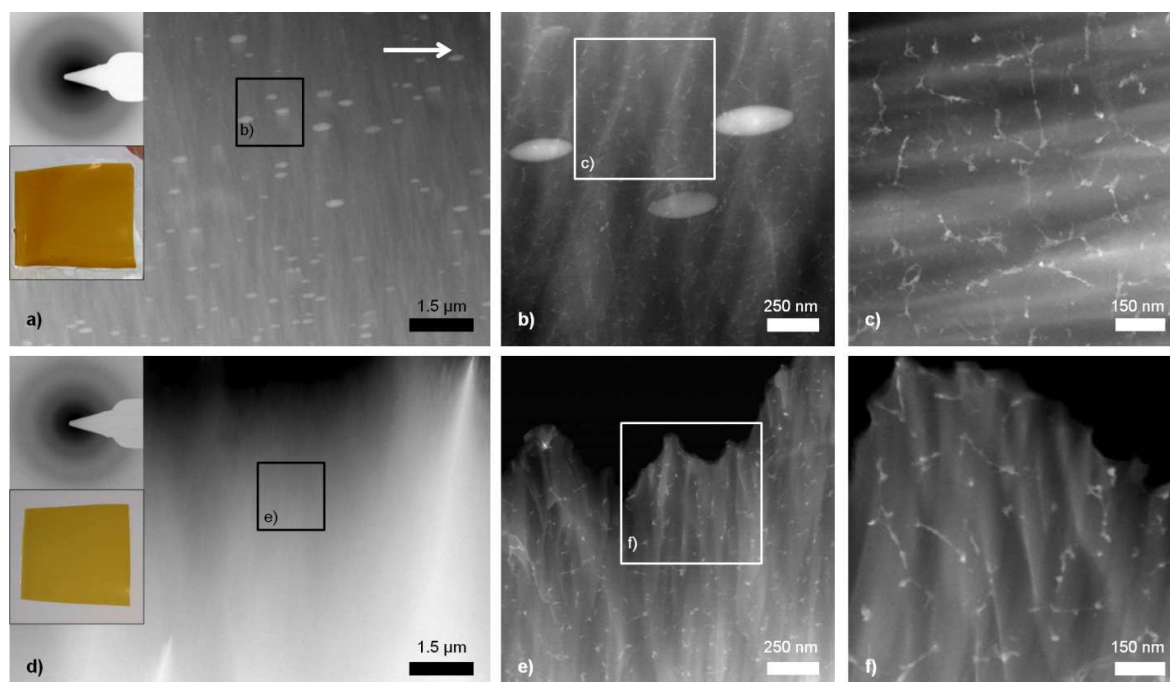


Figure 6.5. Comparison of the two investigated membranes. The top row shows the microstructural features of membrane M I (synthesized at 70 °C), the bottom row presents the one of the conventional membrane M II (synthesized at room temperature). (a, b, c) STEM micrographs of membrane M I with increasing magnifications. The insets in (a) show an electron diffraction pattern of the sample as well as a photograph of it; (d, e, f) STEM micrographs of membrane M II. Again, the insets in (d) show an electron diffraction pattern of this sample as well as a photograph of it. The white arrow in (a) corresponds to the pulling direction during processing.

Figure 6.5 a) and b) show that membrane M I which was synthesized at 70 °C comprises large ellipsoidal particles (up to few hundred nanometers in diameter). All of these particles are elongated in membrane pulling direction and are homogeneously dispersed in the membrane. When going to higher magnifications such as in Figure 6.5 b) and c) additional smaller, bright appearing agglomerates of nanoparticles are visible. These worm-like arranged structures exhibit no preferred orientation in the membrane. In membrane M II which was casted at room temperature no large ellipsoidal particles could be found (d)). However, at higher magnification bright, worm-like nano agglomerates are also present in this membrane. The size and distribution of these agglomerates strongly resemble those found in membrane M I. The quantitative analysis of the particle size distribution will be addressed later.

The electron diffraction patterns of the two membranes shown as insets in Figure 6.5 a) and d) expose the amorphous character of the organic membranes as well as the

inorganic silica structures. In both electron diffraction patterns two diffuse rings indicative for an amorphous material are observed. They can be correlated to interatomic distances of 1.2 Å and 2.0 Å, respectively, and are the same for both samples. Photographs of each membrane are shown as insets in Figure 6.5 a) and d). Membrane M I is opaque and darker, brownish in color in comparison to the clean yellow color of membrane M II. Most likely the larger ellipsoidal silica particles in membrane M I scatter light strongly and therefore lead to an opaque appearance.

Figure 6.6 shows schematic drawings of both membranes to further illustrate the distribution of the particles. As seen in the STEM micrographs in Figure 6.5, membrane M I exhibits both types of particles whereas in membrane M II only the smaller elongated silica particles are observed. All of the large, ellipsoidal particles are oriented parallel to the horizontal plane of the membrane. The arrow in the inset illustrates the membrane pulling orientation.

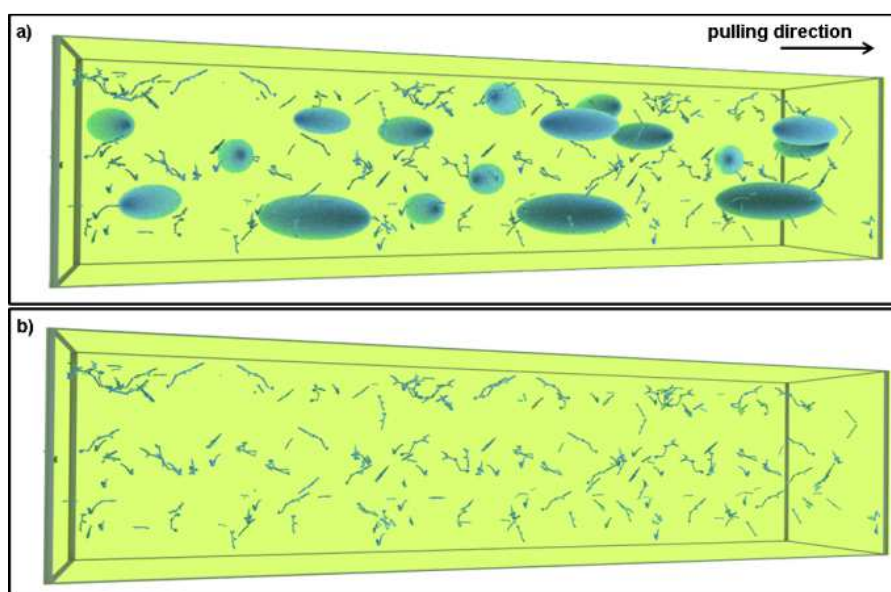


Figure 6.6. Schematic drawing of the silica particle (blue) distribution in the membranes (green). Large, ellipsoidal and smaller, elongated silica particles are present in M I (a). In M II (b) only the small worm-like nano agglomerates can be observed.

The small, elongated silica nanoparticles, present in both membranes, form during the beginning of the synthesis, when both sample solutions are stirred at room temperature. Due to the higher temperature applied for the second stirring procedure in case of membrane M I the formation of larger silica particles is favored. We assume that for this

membrane, in some regions the small silica particles congregate and/or that TEOS which has not formed silica particles so far starts to react. The morphology and orientation of the large ellipsoidal particles can be explained as followed. The coating of the final membrane is realized via a doctor blade process. The silica particles have already formed before, however they are most likely not present as rigid, perfect aligned SiO_2 . Instead the merging of the TEOS molecules via condensation leads to an inhomogeneous flexible network. Some of the large silica particles are large enough to be affected by the constraints during the doctor blade process. Therefore, they become compressed and align in a preferred orientation resulting in an ellipsoidal shape. The elongated silica particles which are present in both membranes are too small to be affected and remain distributed with no preferred orientation.

The orientation of the larger particles in plane within the membrane M I are potentially the reason for the enhancement of the liquid uptake in thickness (see 6.3.1). Furthermore, the large ellipsoidal particles in the membrane enhance the strength during stress-strain testing (see 6.3.1). Due to a blocking mechanism the unfolding of the polymer chains during the elastic deformation of the material is prolonged.^[18,27] However, it seems that the larger particles influence the phosphoric acid distribution within the membrane which is not beneficial for its proton conductivity and therefore performance (see Figure 6.2). Most likely the large particles hinder the formation of proton channels through the membrane. In addition, the microstructure of M II containing only smaller, elongated particles, which can be achieved with lower preparation temperature, leads to an enhanced cycle stability of the MEA and to a slightly better long-term cycling stability.

6.3.3.2 Statistical particles size evaluation

By measuring the size of several hundred silica particles in each sample statistical information can be obtained. In Figure 6.7 a histogram illustrates the particle size distribution of the silica particles in the membranes. For comparison the equivalent spherical particle diameter is used which assumes spherical particles and therefore simplifies the real microstructure. The size of the worm-like silica nano agglomerates in membrane M II shows a narrow distribution.^[18] The equivalent spherical particle diameter reaches from 10 nm to a maximum of 40 nm. No larger silica particles were

found in this sample. For membrane M I the two types of observed silica particles are discussed independently. The ellipsoidal, large silica particles show an overall broad size distribution and can be separated in two distribution functions. About 30 % of the particles exhibit an equivalent spherical particle diameter in the regime of 25 nm to 50 nm. The remaining 70 % have sizes of 70 nm up to a maximum of 360 nm. Since only approximately 1 % of the particles have a diameter larger than 300 nm, the histogram is cut off at this maximum value. The smaller, elongated silica particles show similar behavior regarding equivalent spherical particle diameter distribution as those of membrane M II. These particles also lie within the size range of 10 nm to 40 nm. Only 0.5 % of the particles are larger, having sizes up to a maximum value of 80 nm. Since the morphology as well as the size distribution of the small, worm-like particles is similar in both membranes we assume that these particles are formed via a similar reaction mechanism.

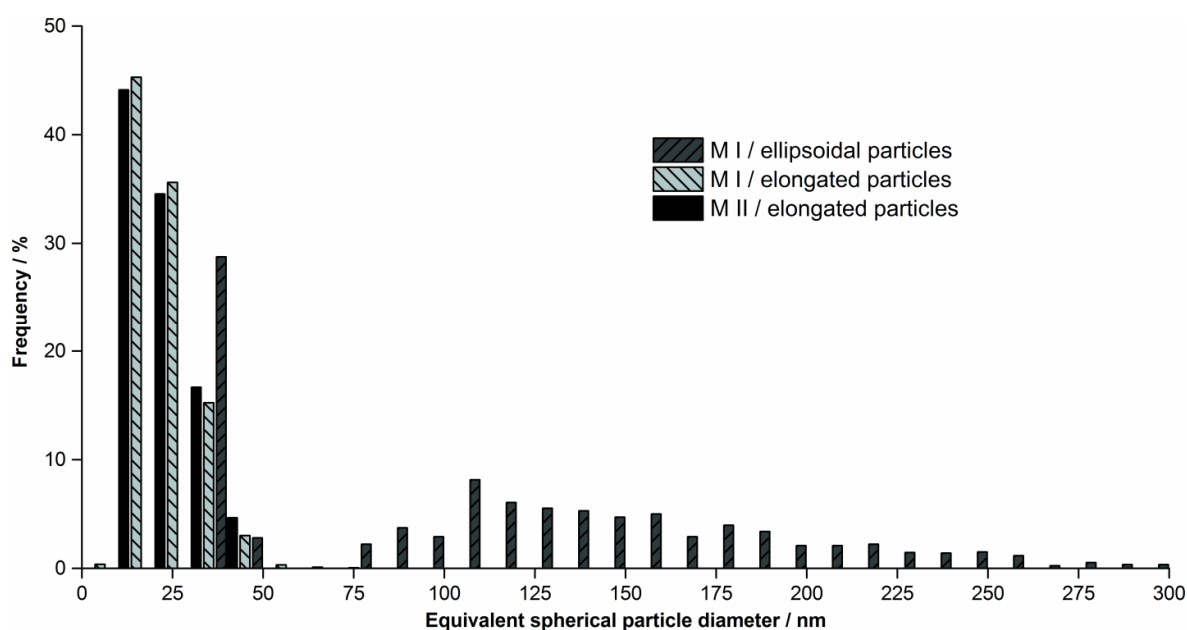


Figure 6.7. Size distribution of the silica particles in the membranes which had been synthesized at different temperature. Membrane M I was prepared at 70 °C, membrane M II at room temperature (data for M II taken from Ref.^[18]).

The results of the statistical particle size evaluation are summarized in Table 6.2. Aside from the average equivalent spherical particle diameter, the average particle size and the average particle density were calculated with their respective standard deviations.

To determine the particle density the total area covered by all particles in a micrograph was divided by the whole area of the micrograph.

Table 6.2. Average particle size, average equivalent spherical particle diameter and average particle density of the silica particles as well as the respective standard deviations. The data for M II is based on Ref.^[18].

Sample (type of particle)		Average particle size / nm ²	Average equivalent spherical particle diameter / nm	Average particle density / %
M I (ellipsoidal particles)	Small	1034 ± 157	36 ± 3	1.6 ± 0.5
	Large	20595 ± 15658	153 ± 54	
M I (elongated particles)		458 ± 368	23 ± 9	4.0 ± 0.8
M II (elongated particles)		472 ± 357	23 ± 9	4.0 ± 0.6

As shown in the histogram (Figure 6.7), the average equivalent spherical diameter of the elongated particles is similar in both membranes and is about 23 ± 9 nm. Consequently, also their occupied size in nm² is about the same. It is interesting to note that also the particle density has similar values of 4.0 ± 0.8 % when only the small particles are assumed. Regarding the large ellipsoidal particles in membrane M I two size ranges can be distinguished. The smaller ones have an average spherical particle diameter of 36 ± 3 nm and the larger ones 153 ± 54 nm. The particle density of this type of particles is lower (1.6 ± 0.5 %) than for the small, elongated particles. Since the size difference of the two types of particles in membrane M I is large, they cannot be evaluated simultaneously using one micrograph taken at one specific magnification. An alternative route was developed in order to obtain statistically relevant values for the particle density of both types combined. The smaller particles can only be observed at high magnifications. However, only few large particles are present in the same micrograph as can be seen for example in Figure 6.5 b). Hundreds of particles have to be taken into account to achieve representative results. Therefore, we normalized the measurement areas for the discussed elongated particles and calculated a normalized average particle

density. In a second step the same procedure was performed for the large particles, but using images taken at lower magnifications. Then the results were combined.

The total particle density obtained in this way is 5.6 ± 1.3 % and is larger than the silica particle density of M II (4.0 ± 0.6 %). The overview EDS measurements (shown later) indicate that the total amount of Si is similar in both membranes. This would imply that the amount of Si which has not reacted to form silica particles is higher in membrane M II or that small particles are present in this membrane which have a size below the resolution limit in our micrographs.

Overall, we can state that membrane M II contains only small, elongated particles whereas M I has additional large, ellipsoidal particles.

6.3.3.3 Crystallinity

XRD measurements were performed to determine the crystallinity of the polymer and the particles on a global scale. Figure 6.8 shows the X-ray diffraction patterns of the membranes M I and M II. For comparison a pure PBI membrane without silica particles (standard membrane) is also displayed. The diffuse peak present in all samples at a 2θ value of about 24.0° is typical for amorphous PBI and in rough agreement with the data published in literature.^[12] For each broad reflection the FWHM Δ was measured. The standard membrane has the smallest FWHM ($\Delta = 15.9^\circ$), followed by membrane M II ($\Delta = 16.6^\circ$) which contains only the smaller elongated silica particles. The largest value for the FWHM was obtained for membrane M I ($\Delta = 16.8^\circ$) in which also large ellipsoidal silica particles are present. These results indicate that the incorporation of silica particles in the PBI-based membrane leads to a slightly increased disorder of the polymer matrix compared to the standard, particle free membrane. A less defined stacking of the PBI chains is responsible for the broader peaks in the XRD pattern of the silica reinforced membranes. In addition, the results indicate that larger particles further promote the disordering of the polymer chains.

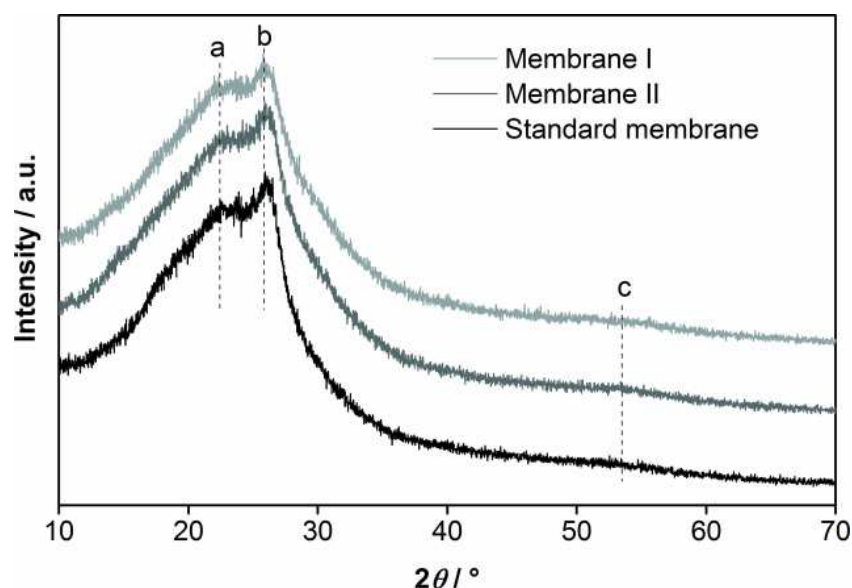


Figure 6.8. X-ray diffraction patterns of the membrane samples M I and M II. A standard PBI membrane without incorporated silica particles is also shown. For a better comparison the diffraction patterns are normalized as well as displaced along the y-axis. The most prominent features are labeled with a, b and c.

Three distinctive features can be observed in all diffractograms. Features a and b are located in the broad reflection discussed earlier and feature c is a weak, broad signal at a 2θ of about 53° . Feature c can also be found in literature^[28]. Table 6.3 summarizes the measured angles and the calculated d -spacings of the XRD measurements.

Table 6.3. Measured angles in the XRD data and calculated d -values for features a and b. Feature c could not be determined.

Sample	Feature a		Feature b	
	angle [$^\circ 2\theta$]	d [\AA]	angle [$^\circ 2\theta$]	d [\AA]
M I	22.17	4.65	25.90	3.99
M II / Standard membrane	22.75	4.54	26.20	3.95

Membrane M II and the standard membrane without silica particles have peaks at identical 2θ values in the XRD pattern. The peaks in the diffractogram of M I are shifted to smaller angles and therefore correspond to slightly larger d -values. However, the difference between the obtained d -values is small when considering the large error associated with the diffuse peak in our XRD measurements. Since the signal of feature c is too broad and shallow, no d -values were calculated. Nevertheless, a 2θ value of about

53° corresponds to a d -value of 2.0 Å which was also determined from the electron diffraction pattern (see Figure 6.5). The large d -values of features a and b in the XRD could not be detected in the electron diffraction patterns because of the high intensity of the direct electron beam. It is likely that the signals gathered in electron diffraction ($d = 2.0$ Å and $d = 1.2$ Å) represent high order diffraction ($n = 2, 3$) of the main signal of PBI at about 4.0 Å. All presented values originate from near-order phenomena. In summary the insertion of silica particles into the membrane did not strongly alter its crystallinity i.e. it remains non-crystalline. The silica particles themselves are amorphous as no reflexes attributable to crystalline silica are visible in the XRD pattern.

6.3.3.4 Elemental composition analysis

EDS measurements were performed to determine the overall amount of introduced silicon and to analyze the particles in more detail. The EDS data reveal the presences of C, N, O, Si, P, Cl, Cu and Zn. The detected elements C and N can be attributed to the PBI membrane. Si and O are visible due to the presence of silica particles. P originates from a dialkylphosphate softener. Cl is present in all samples as minor contamination. In addition, Cu and Zn were detected which originate from the used brass tube for the TEM specimen preparation. For quantitative analysis we used only Si and P. The reason for this is that the fluorescence quantum yield of the elements C, N and O is rather small and that the corresponding characteristic, low energy X-rays are easily absorbed in the detector or in the sample. Accordingly, the quantification of these elements can only be considered as a rough estimate and is therefore not considered here.

In Table 6.4 the detected amount of silicon is associated with the amount of phosphor which is present in both membranes in equal quantity as well as in uniform distribution, as will be shown below. Several 5 x 5 μm² large areas were measured to compare the overall amount of silicon. The quantification was performed using the standard Cliff-Lorimer equation.^[27]

Table 6.4. Comparison of the average amount of Si to the amount of P measured by EDS in a window of 5 x5 μm^2 .

membrane	Si / atomic%	P / atomic%
M I	72 \pm 3	28 \pm 3
M II	71 \pm 5	29 \pm 5

The data show that, independent of the synthesis temperature, the same amount of silicon is introduced into the membrane when the same amount of precursor (TEOS) is used.

The different regions of interest of the membranes were analyzed in more detail via EDS measurements performed on the nanoscale. By applying small measuring windows only the region of interest of the membranes was taken into account. Three distinctive regions were investigated: the pure membrane without silica particles, the elongated worm-like silica nano agglomerates and the larger ellipsoidal silica particles. In order to get statistic relevant data more than ten measurements were performed for each region of interest. One has to consider that the investigated TEM samples still have a thickness of several tens of nanometers and that the X-ray signals emerge from the whole sample volume illuminated by the electron beam. Therefore, when measuring on the small, elongated silica particles, the surrounding matrix (in particular below the particle) is also contributing to the signal. Instead of quantitative values only trends were obtained because of the mentioned difficulties. For example, the homogeneous distribution of P was verified on all samples and the measurement areas of bright particles showed increased amounts of Si and O, which proves that the bright structures are silica particles.

In addition, EDS elemental maps were used to analyze and illustrate the distribution of the elements, in particular in and close to the silica particles. With this method the distribution of the different elements of a defined sample area can be visualized. Figure 6.9 shows two elemental maps of the elements C, O and Si of membrane M I exemplarily. In Figure 6.9 a) an area containing two ellipsoidal silica particles is analyzed with a scanning step size of 20 nm and a measuring time of several seconds for each acquisition

point. It can be seen that the elements Si and O dominate at the position of the bright particles. The element C can be found mostly on the pure membrane while its concentration is much lower at the area of the bright particles. Other elements like P, Cl and K are not shown here because their intensity is too weak for elemental mapping at the chosen conditions. Nevertheless, it is possible to analyze the small elongated silica particles via EDS mapping as well. In Figure 6.9 b) the elemental maps for such a particle are shown. Here the scanning step size is 5 nm for each acquisition point. The observed noise in the maps of Si and O is stronger than for the large particles in a), as a smaller amount of Si and O atoms generates less X-rays. Also the investigated TEM sample thickness is much larger than the size of these particles and therefore the surrounding polymer matrix (in direction of the incident beam) is strongly contributing. Nonetheless, the shape of the silica particle can be recognized in the Si and O maps. In addition, we were able to prove that silica is enriched in the bright structures.

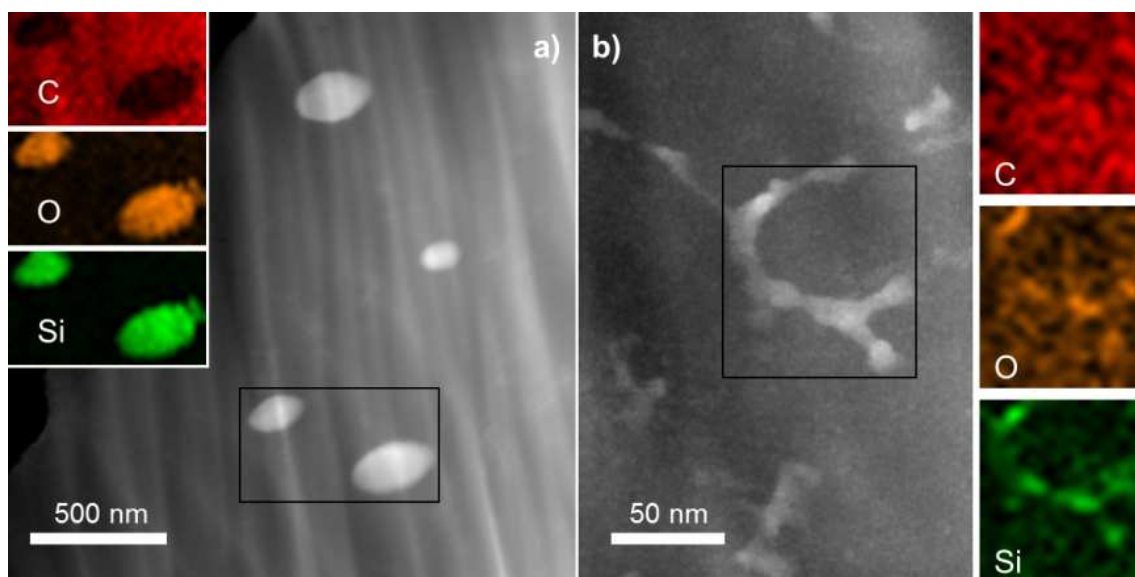


Figure 6.9. Elemental maps of sample M I acquired via EDS. Both large (a) and small (b) silica particles can be detected. The K_{α} signal for the elements C, O and Si is displayed as insets. Please note the different scale bars in the images.

In a next step we examined the interface between silica particles and the matrix with regard to enrichment of specific elements. Therefore, EDS line scans were performed. In Figure 6.10 a) a HAADF STEM micrograph of a large, ellipsoidal particle, which was analyzed in two perpendicular directions, is shown exemplarily. Another feature, which can be observed in this micrograph, is the superposition of different particles in the

projection direction (for this effect see also the schematic representation in Figure 6.6). Some of the small, elongated particles appear to lie on top of the large ellipsoidal silica particle. Since TEM gives a two dimensional projection of a three dimensional object this can easily occur. The elemental composition of the particle in vertical direction is shown in Figure 6.10 b). Every 2 nm an EDS signal was collected for 5 s. It can clearly be seen that the intensity of the signal for Si and O strongly rises once the beam is scanned over the bright appearing particle. The continuous increase in intensity for these signals can be explained by an increase of particle thickness. When the electron beam is positioned adjacent to the particle, the signal intensity for Si and O drops. An inverse behavior can be observed for the C signal. N is distributed homogeneously over the scanning range. Other elements like P, Cl and K are likewise present at all scanned sample positions in very low concentrations (< 1 atomic %). In horizontal direction (c, d) similar results were found for all given elements. With these EDS line scan measurements we were able to prove not only that the particles consist of Si and O but also that they have a homogeneous elemental composition and are free of any kind of contamination. In addition, we did not find an enrichment of other elements such as P or Cl at the interface between the particles and the polymer matrix.

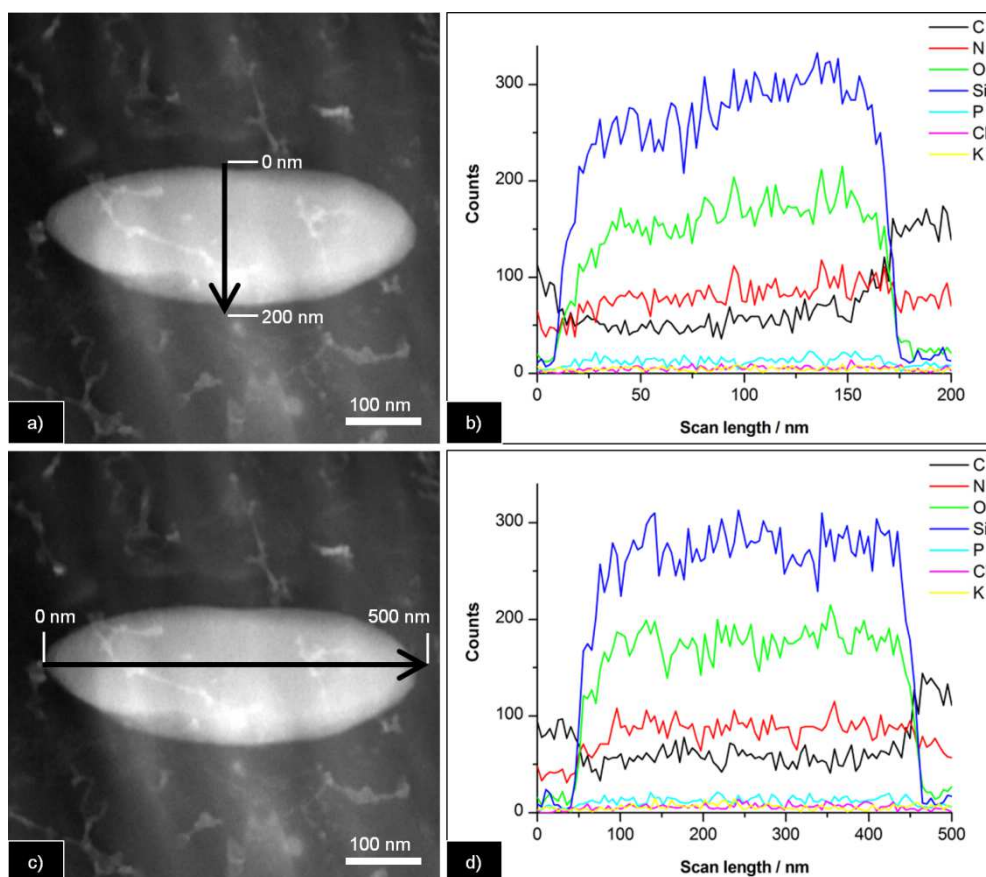


Figure 6.10. EDS line scans of an ellipsoidal silica particle found in membrane M I. The particle was scanned parallel to its short axis (a) and to its long axis (c). The corresponding elemental distributions are shown in (b) for the vertical scan and in (d) for the horizontal one.

6.3.3.5 EELS investigation

By examining the membranes via EELS we can determine the local chemistry, the bonding behavior, the valence state and the nearest-neighbor coordination. In Figure 6.11 the results of the EELS measurements are summarized. We analyzed the characteristic, element specific edges of Si, O, C and N at different sample positions which have an edge onset of 105 eV for Si-L_{2,3}, 539 eV for O-K, 283 eV for C-K and about 400 eV for N-K. The measured values are in good accordance with literature.^[29-32] This approach enables the detection of possible deviations of the composition, phase and bonding situation of different shaped silica particles in the two membranes.

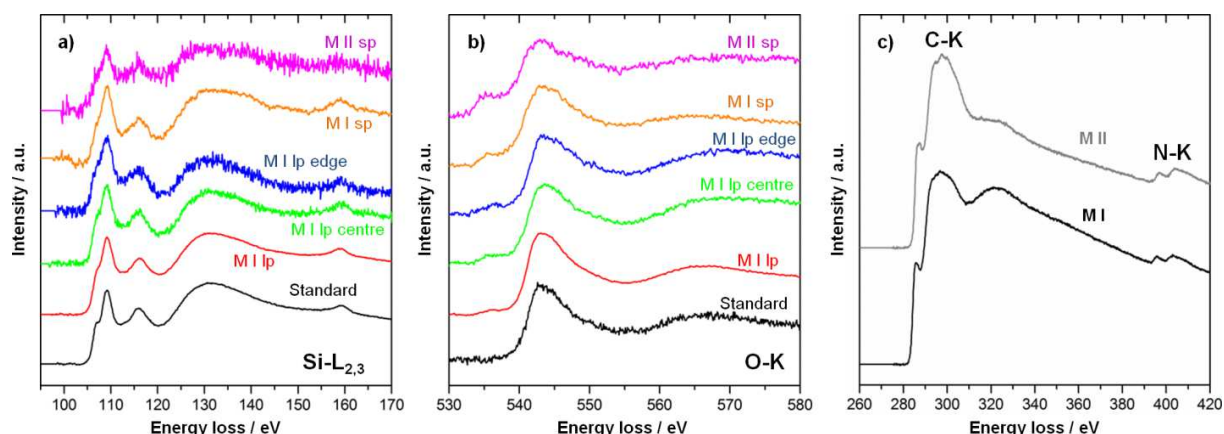


Figure 6.11. Results of the EELS analysis of the different membrane areas. Four different characteristic edges are shown: the Si-L_{2,3} edge (a), the O-K edge (b) and the C-K and N-K edges (c). The samples are labeled in the following way: lp stands for large (ellipsoidal) particle, sp stands for small (elongated) particle. For comparison the EELS spectra of an amorphous silica particle were added in (a) and (b).

The different silica particles were analyzed regarding their Si-L_{2,3} edges shown in Figure 6.11 a) and their corresponding O-K edge shown in b). The spectra of an amorphous silicon oxide standard sample were added for comparison. For both Si and O five different areas were investigated. The spectra of an ellipsoidal large silica particle shown in red exhibit very similar features compared to the amorphous silica standard. The center of a large particle and the corresponding particle/matrix interface were also analyzed via EELS to examine possible differences in composition or bonding situation. Both spectra of Si and O are again similar to the standard. Hence the ellipsoidal particles are apparently built of homogeneous, amorphous silicon oxide. In addition, the EELS spectra of the small elongated particles of membranes M I and M II are shown in Figure 6.11 a) and b). Since the EELS spectra possess similar features as the standard material we can assume that the smaller elongated silica particles, present in both membranes, also consist of pure amorphous silicon oxide. The only difference between some of the spectra is the signal to noise ratio. The spectra of the small particles in M II exhibit stronger noise which can be attributed to the fact that a much lower number of atoms contribute to the signal. In principle, the signal to noise ratio can be improved by using longer acquisition times, but the sample suffered from beam damage during the measurement. This can also be seen from the pre-peak in the O-K EELS spectrum at an energy loss of about 535 eV. This pre-peak originates from atomic oxygen and is a sign

for the decomposition of the sample.^[33] In Figure 6.11 c) the C-K edge and the N-K edge of the two membranes M I and M II are shown. The spectra were taken on a particle-free region to analyze possible differences of the membranes. The C-K edge which has the characteristic appearance of amorphous carbon as well as the N-K edge which also originates from the PBI is similar for both membranes. The higher intensity of the peak at ~320 eV of the C-K edge of membrane M I can be attributed to multiple scattering events which are related to the larger thickness of the TEM sample.

6.4 Conclusion

Organic-inorganic PBI-based composite membranes were synthesized by incorporation of silica particles via an *in-situ* sol-gel reaction. The binding of the particles to the polymer PBI was achieved by the use of a linker (GPTMS). The influence of an additional heating step during synthesis on the morphology of the silica particles as well as the resulting fuel cell performance was investigated. The detailed structural analysis of the membrane was performed by using several electron microscopy based methods like STEM, EDS and EELS. The size, shape and distribution of the silica particles were studied. In addition, the crystallinity of the samples was analyzed via XRD. The introduction of silica nanoparticles did not change the overall crystallinity of the samples but the disorder of the polymer chains was slightly increased. By applying EDS maps the position and distribution of the silica particles was visualized. The additional heating step heavily influenced the morphology and the size of the resulting silica particles. This was analyzed in detail by a statistical particle size evaluation. The synthesis without additional heating led to a network consisting of small, elongated silica particles, whereas in case of the heated membrane in addition particles with a size five times larger and an ellipsoidal morphology were found. The homogeneity and amorphous character of the silica particles was proven by EDS line scans and EELS measurements.

The membranes containing the large, ellipsoidal silica particles have a higher liquid uptake and also a higher mechanical stability. MEAs of both membranes were assembled and analyzed *in-situ* via polarization curves, start-stop-cycling and long-term fuel cell operation. Here the results show that the large, ellipsoidal silica particles are not

beneficial for the fuel cell performance. It seems that the silica particles obtained via an additional heating step are too large and therefore hinder the formation of proton channels through the membrane. Further studies have to be carried out to determine the optimal size and distribution of silica nanoparticles in a PBI-based membrane which combine excellent ex-situ properties and performance.

6.5 Chapter references

- [1] Steele, B. C.; Heinzl, A. *Nature* **2001**, 414, 345.
- [2] Bose, S.; Kuila, T.; Nguyen, T. X. H.; Kim, N. H.; Lau, K.-t. et al. *Prog. Polym. Sci.* **2011**, 36, 813.
- [3] Li, Q.; He, R.; Jensen, J. O.; Bjerrum, N. J. *Fuel Cells (Weinheim, Ger.)* **2004**, 4, 147.
- [4] Asensio, J. A.; Sánchez, E. M.; Gómez-Romero, P. *Chem. Soc. Rev.* **2010**, 39, 3210.
- [5] Zhang, H.; Shen, P. K. *Chem. Soc. Rev.* **2012**, 41, 2382.
- [6] Carollo, A.; Quartarone, E.; Tomasi, C.; Mustarelli, P.; Belotti, F. et al. *J. Power Sources* **2006**, 160, 175.
- [7] Xu, H.; Chen, K.; Guo, X.; Fang, J.; Yin, J. *J. Membr. Sci.* **2007**, 288, 255.
- [8] Li, Q.; Pan, C.; Jensen, J. O.; Noye, P.; Bjerrum, N. J. *Chem. Mater.* **2007**, 19, 350.
- [9] Patel, S.; Bandyopadhyay, A.; Vijayabaskar, V.; Bhowmick, A. K. *J. Mater. Sci.* **2006**, 41, 927.
- [10] Chuang, S.-W.; Hsu, S. L.-C.; Liu, Y.-H. *J. Membr. Sci.* **2007**, 305, 353.
- [11] Saxena, A.; Tripathi, B. P.; Shahi, V. K. *J. Phys. Chem. B* **2007**, 111, 12454.
- [12] Sadeghi, M.; Semsarzadeh, M. A.; Moadel, H. *J. Membr. Sci.* **2009**, 331, 21.
- [13] Suryani; Liu, Y.-L. *J. Membr. Sci.* **2009**, 332, 121.
- [14] Ghosh, S.; Maity, S.; Jana, T. *J. Mater. Chem.* **2011**, 21, 14897.
- [15] Quartarone, E.; Magistris, A.; Mustarelli, P.; Grandi, S.; Carollo, A. et al. *Fuel Cells* **2009**, 9, 349.
- [16] Suryani; Chang, Y.-N.; Lai, J.-Y.; Liu, Y.-L. *J. Membr. Sci.* **2012**, 403–404, 1.
- [17] Tang, H. L.; Pan, M. *J. Phys. Chem. C* **2008**, 112, 11556.
- [18] Ossiander, T.; Heinzl, C.; Gleich, S.; Schönberger, F.; Völk, P. et al. *J. Membr. Sci.* **2014**, 454, 12.
- [19] Di, N. V.; Piga, M.; Giffin, G. A.; Quartarone, E.; Righetti, P. et al. *Phys. Chem. Chem. Phys.* **2011**, 13, 12146.
- [20] Wang, H.; Yuan, X.-Z.; Li, H. *PEM Fuel Cell Diagnostic Tools*; CRC Press Taylor & Francis Group: Boca Raton, FL, **2012**.
- [21] Perchthaler, M.; Ossiander, T.; Juhart, V.; Mitzel, J.; Heinzl, C. et al. *J. Power Sources* **2013**, 243, 472.
- [22] Sezen, M.; Plank, H.; Fisslthaler, E.; Chernev, B.; Zankel, A. et al. *Phys. Chem. Chem. Phys.* **2011**, 13, 20235.
- [23] Michler, G. H. *Electron Microscopy of Polymers*; Springer-Verlag Berlin Heidelberg: Leipzig, Germany, **2008**.
- [24] Ossiander, T.; Perchthaler, M.; Heinzl, C.; Scheu, C. *J. Power Sources* **2014**, 267, 323.

- [25] Strecker, A.; Salzberger, U.; Mayer, J. *Prakt. Metall.* **1993**, *30*, 482.
- [26] Schneider, C. A.; Rasband, W. S.; Eliceiri, K. W. *Nat. Methods* **2012**, *9*, 671.
- [27] Williams, D. B.; Carter, C. B. *Transmission Electron Microscopy*; Springer US, **2009**.
- [28] Han, J. Y.; Lee, J. Y.; Kim, H.-J.; Kim, M.-H.; Han, S. G. et al. *J. Appl. Polym. Sci.* **2014**, *131*, 40521.
- [29] Garvie, B. *Am. Mineral.* **1999**, *84*, 946.
- [30] Lieske, N.; Hezel, R. *Thin Solid Films* **1979**, *61*, 217.
- [31] Kimoto, K.; Kobayashi, K.; Aoyama, T.; Mitsui, Y. *Micron* **1999**, *30*, 121.
- [32] Dennenwaldt, T.; Sedlmaier, S. J.; Binek, A.; Schnick, W.; Scheu, C. *J. Phys. Chem. C* **2014**, *118*, 8416.
- [33] Jiang, N.; Spence, J. C. H. *Ultramicroscopy* **2006**, *106*, 215.

7 Tungsten materials as durable catalyst supports for fuel cell electrodes

This chapter is based on the following publication:

Markus Perchthaler, Tanja Ossiander, Viktorija Juhart, Jens Mitzel, Christoph Heinzl, Christina Scheu, Viktor Hacker *Journal of Power Sources* **2013**, 243, 472–480.

7.1 Introduction

The corrosion of today's widely used high surface area carbon blacks is one of the main reasons of performance degradation in fuel cells, especially under start-stop conditions and high electrochemical potentials on anode and cathode. Because of high potentials and temperatures the carbon catalyst support oxidizes to CO₂, which can be detected in the anode and cathode off-gas.^[1] A lot of effort was put in the development of more stable carbon compounds as catalyst support material, especially with a more graphitic structure, e.g. carbon nanotubes or carbon nanofibers. These structured carbon materials show lower carbon corrosion rates^[2-4], but they cannot prevent carbon oxidation.

Due to this non-carbon materials with high corrosion resistance and high stability under acidic fuel cell conditions are in the focus of interest of research groups worldwide in order to substitute conventional electrode material. However there are several factors which are important for catalyst support materials such as high surface area, porosity, electrical conductivity, electrochemical stability and surface functional groups.^[5] These mentioned parameters have to be fulfilled for any successful application.

Tungsten Oxides (WO_x) are compounds with very high melting points of 1700 °C and very low vapor pressure.^[6] WO_x is formed by the reaction of metallic tungsten with oxygen to form stoichiometric tungsten trioxide (WO₃) and lower non stoichiometric oxides WO_x, with 2 < x < 3.^[7] WO_{2 < x < 3} is an *n*-type semiconductor with a band gap of about 2.6–2.8 eV.^[8] It has a high conductivity which arises from a donor level formed by oxygen-vacancy defects. This leads to the decrease in the resistivity from 1 Ω cm for WO₂

to a minimum of $0.1 \Omega \text{ cm}$ for $\text{WO}_{2.75}$ ^[8], which is sufficient for the use in fuel cell electrodes.

Hobbs and Tseung^[9] observed that the rate for hydrogen oxidation in acidic solution increases by the use of Polytetrafluoroethylene (PTFE) bonded Pt supported on WO_3 . They explained this behavior with hydrogen that spills over onto the surface of the hydrogen tungsten bronze (H_xWO_3), freeing these Pt sites for further chemisorptions of hydrogen. This spill-over mechanism of hydrogen between WO_3 and Pt has been suggested as being responsible for the increased activity for the Oxygen Reduction Reaction (ORR).^[10] On the other hand Ota et al.^[11] claimed that the observed enhancement of the ORR activity is due to reduced PtO_2 formation. This leads to a higher oxide free Pt-surface area, which is more active for the ORR. Further works on the topic of the relationship between structure and activity of Pt on different synthesized WO_3 support material were done by Shim et al.^[12] and Kulesza and Faulkner^[13]. They showed that Pt loaded WO_3 nanorods are more stable compared to WO_3 bulk when cycling is conducted between -0.2 and 1.0 V in $2 \text{ N H}_2\text{SO}_4$ for several times.

As discussed before WO_3 shows a considerable high proton transfer due to the formation of WO_3 hydrates. This is a very attractive property for fuel cell catalyst supports^[14] since this has a beneficial impact on the number of three phase reaction zones, where the catalyst is in contact with an electron conducting support and a proton conducting electrolyte.

In contrast to WO_x , WC was also evaluated as possible material for fuel cell catalyst supports and even catalyst material for the hydrogen oxidation reaction (HOR). Nikolov and Vitanov^[15,16] investigated the corrosion resistance of WC in H_2SO_4 and the changes in catalytic activity during corrosion. They discovered that the amount of oxides linearly increases with time, suggesting that during corrosion the catalyst surface was not passivated. In contrast to these findings, Brady et al.^[17] reported passivation of WC based catalysts. Depending on the surface stoichiometric ratio of W:C, with higher W content, surface passivation to WO_3 in H_2SO_4 occurs. This causes a loss of electrocatalytic activity of WC for the HOR.

Chhina et al.^[18] claimed that the stability of WC under electrochemical oxidizing conditions is higher compared to High Surface Area Carbons (HSAC). Meng and Shen^[19]

^{21]} studied the effect of the addition of Pt onto WC. They observed a ten times larger activity for the ORR of Pt-W₂C/C than that of Pt/C in an alkali medium and proposed a synergy between W₂C and Pt. In acidic media Santos et al.^[22] found that the use of Pt on W₂C as catalyst support material leads to a remarkable enhancement of the ORR activity compared to Pt on carbon, although both catalysts follow the four electron mechanism. Another idea from Shao et al.^[23] to get a higher stability of the catalyst support material is to coat the commercial available carbon based catalyst supports with an electrochemical process with phase pure WC and Pt. They achieved a two fold increase of the corrosion resistivity compared to not coated carbon based support materials.

The major drawback of commercial available WC and W₂C is the low Brunauer-Emmett-Teller (BET) surface area (2.1 m² g⁻¹) compared to HSAC (about 250 m² g⁻¹), which hinders their implementation in fuel cells. Ganesan and Lee^[24] synthesized platinum particles on WO₃ nanoparticles with controlled oxidation of W₂C microspheres by calcination at 773 K in O₂ atmosphere for 3 h. Zhu et al.^[25] recently showed that the electrochemical stability of WC is dependent on the specific surface area. The higher the specific surface area, the more WC is prone to get oxidized to WO₃ under oxidizing electrochemical conditions (>0.7 V). They also measured very low ORR activity values, which they explained by a high contact resistance between the catalyst and catalyst support. When WC is oxidized it forms an insulating WO₃ layer. This layer blocks the electron transfer between the catalyst and catalyst support, and according to that the contact resistance increases significantly.^[26]

In this study we evaluate the characteristics of WC, self-made WO_{xs} and commercial available WO_x for the use as electrode material in high-temperature proton exchange (HT-PEM) fuel cells. Electrodes are fabricated with and without platinum and their electrochemical properties are investigated and compared to each other.

The materials are evaluated in *in-situ* experiments in HT-PEM fuel cells and *ex-situ* with Cyclic Voltammetry (CV), Potential Cycling (PC), CO-Stripping, Thermogravimetric Analysis (TGA), X-ray diffraction (XRD) and electron microscopy investigations. The resulting degradation effects, the formation of WO_x and tungsten bronzes and the influence of the catalyst support on the CO oxidation behavior are discussed. Finally a 980 h long term test at constant load in a HT-PEM fuel cell stack was done and no degradation was observed.

7.2 Experimental

7.2.1 Synthesis of WO_{xs}

Commercial available WC (WC CRC 010u, Wolfram Bergbau und Hütten AG) with a BET surface area of $2.71 \text{ m}^2 \text{ g}^{-1}$ and a grain size of 0.47 μm were oxidized in order to obtain a surface oxidized WO_{xs} species.

For this, the raw WC powder (3 g) is dispersed in 50 ml of a mixture (3:2) of HNO_3 (65wt%, BDH Prolabo, AnalaR Normapur) and H_2SO_4 (98wt%, MERCK KGAA, EMSURE) and heated under reflux for 6 h. After this treatment the resulting green powders are washed several times with deionized water until a neutral pH value was obtained.

7.2.2 Catalyst deposition

The deposition of platinum catalyst on the different catalyst supports is realized via electroless deposition methods. WO_x , WO_{xs} , WC and for comparison HSAC based catalyst supports (0.5 g) are ultrasonicated in a three neck round bottom flask in 30 ml of ethylene glycol and 10 ml deionized water. The deposition of the Pt precursor was done according to the procedure described elsewhere.^[26] A platinum loading of 13wt% on tungsten and HSAC based powders is obtained and confirmed via elemental and Energy-Dispersive X-ray (EDS) measurements.

7.2.3 Determination of catalyst crystallite size and support structure

To investigate the general morphology and to determine the overall chemical composition of the Pt loaded and unloaded electrode materials a JEOL JSM-6500F scanning electron microscope operated at 4.0 kV and equipped with an energy-dispersive X-ray detector from Oxford Instruments (Inca Energy) was used. Using the implemented JEOL standard detector, secondary electron (SE) images were acquired. SEM top view samples were prepared using conventional preparation techniques. Transmission electron microscopy (TEM) investigations were accomplished by using a FEI Titan 80e300 (S)TEM microscope equipped with a Gatan Tridiem image filter and an EDAX EDS detector for analytical measurements. Standard TEM samples were obtained by suspending the powders in ethanol (100%) followed by ultrasonication for 10 min and placing it on a holey carbon coated copper grid. The Titan was operated at 300 kV for all measurements.

7.2.4 Electrochemical characterization

7.2.4.1 *Ex-situ* cyclic voltammetry

The electrochemical measurements are performed in a PTFE cell, using a working electrode with a glassy carbon substrate (2.01 cm² geometrical surface area) and a potentiostat (Ivium) in a conventional three-electrode setup with an aqueous 0.1 N HClO₄ solution. The electrolyte is prepared using deionized water (>17.8 MΩ) and 1 N HClO₄ (BDH Prolabo). A chlorine free saturated Hg/Hg₂SO₄ electrode (Radiometer) was used as reference electrode, and a glassy carbon electrode (Radiometer) as counter electrode. All potentials are given to the reversible hydrogen potential.

The catalysts or the catalyst supports are ultrasonically suspended in isopropanol/water. Then an appropriate amount of 42 μg cm⁻² catalyst support or 7 μg cm⁻² Pt for catalyst loaded support material are pipetted on the glassy carbon surface and are dried at room temperature to get a uniform film on the glassy carbon electrode.

After immersion into the nitrogen saturated electrolyte the catalyst is treated by potential cycling between 50 and 1100 mV with 500 mV s⁻¹ until a stable CV is recorded. The scanning speed in all analysis measurements is set to 50 mV s⁻¹. The analysis scan is performed between 50 mV and 1100 mV.

7.2.4.2 Potential cycling

PC experiments are done by cycling the catalyst 3600 times at a scan rate of 500 mV s⁻¹ between 50 mV and 1100 mV, followed by an analysis scan. Then they are cycled 3600 times between 50 mV and 1200 mV, followed by an analysis scan, and finally 3600 times between 50 mV and 1300 mV followed by an analysis scan. The decrease of the charge in the analysis scans between 50 mV and 400 mV is compared to the starting value and the relative loss is calculated.

7.2.4.3 CO-stripping

For supported catalysts the electrochemical active surface area (ECA) and the CO-oxidation behavior is measured in an electrochemical cell. The same cell as in the CV measurements is used. The electrolyte is purged for 90 s with a flow of CO (100 mL min⁻¹) at an adsorption potential of 50 mV to obtain a CO monolayer on the

catalyst. At this potential the catalyst is blocked very fast with CO. After that the electrolyte is purged with nitrogen for 18 min in order to remove any excess CO from the electrolyte.

The working electrode is then cycled between 50 mV and 1100 mV to get information about the CO-desorption charge, the ECA and the onset potential of the CO oxidation. The ECA is calculated according to equation (7.1).

$$ECA(m^2g^{-1}) = \frac{Q_{CO}}{420 \times 10^{-6} C cm^{-2} \times M} \times 1000 \quad (7.1)$$

Q_{CO} is the charge for the CO oxidation on Pt, $420 \times 10^{-6} C cm^{-2}$ is the charge required for the oxidation of a monolayer of adsorbed CO on $1 cm^2$ of Pt surface and M is the Pt loading of the electrode.

7.2.5 Electrode and membrane-electrode-assembly preparation

For *in-situ* tests of the supported catalysts Membrane Electrode Assemblies (MEAs) are prepared and evaluated by *in-situ* CV tests and *in-situ* CO-stripping. The catalyst support is applied on a wet proofed carbon based gas diffusion layer via a doctor blade process.

The catalyst support slurry consists of PTFE dispersion (Dyneon™, TF 5035 PTFE), used as hydrophobic reagent and binder, deionized water and isopropanol (gradient grade, Merck). The applied slurry is dried at 170 °C. Then the catalyst is deposited on the catalyst support layer via an electroless deposition method. The HT-PEM MEAs are manufactured by doping the catalyst layer with phosphoric acid and hot pressing them with a membrane based on polybenzimidazole (PBI).

7.2.6 *In-situ* test conditions

CVs are recorded in a $50 cm^2$ HT-PEM single cell at cell temperatures of 160 °C with humidified nitrogen with a relative humidity of 6% at ambient pressure. The gas flows are $131 mL min^{-1}$ for H_2 and $100 mL min^{-1}$ for N_2 . The electrochemical measurements are carried out with an electrochemical workstation (Zahner IM6) and a power potentiostat (Zahner PP240). CVs were recorded between 52 mV and 1200 mV with a sweep rate of $50 mV s^{-1}$ and three cycles per measurement.

7.2.7 Thermogravimetric analysis

The catalyst support materials are characterized by a thermogravimetric analysis system. The heating rate is set to $10\text{ }^{\circ}\text{C min}^{-1}$ starting from $40\text{ }^{\circ}\text{C}$ to $450\text{ }^{\circ}\text{C}$ under air atmosphere. The weight change of the sample (starting weight approx. 10 mg) is recorded.

7.2.8 HT-PEM long term stack test

The HT-PEM MEAs were tested in a 20-cell stack at a constant current of 0.2 A cm^{-2} . As anode gas reformed methanol with 1.2 vol% CO, 76 H₂ and 22.8% CO₂ was used. The cell potential over the time is recorded.

7.3 Results and discussion

7.3.1 Characterization of WC support material

The commercially available WC powders were used as reference and starting material for the WO_x synthesis. In Figure 7.1 the CV analysis before and after 100 cycles between 52 mV and 1100 mV are shown.

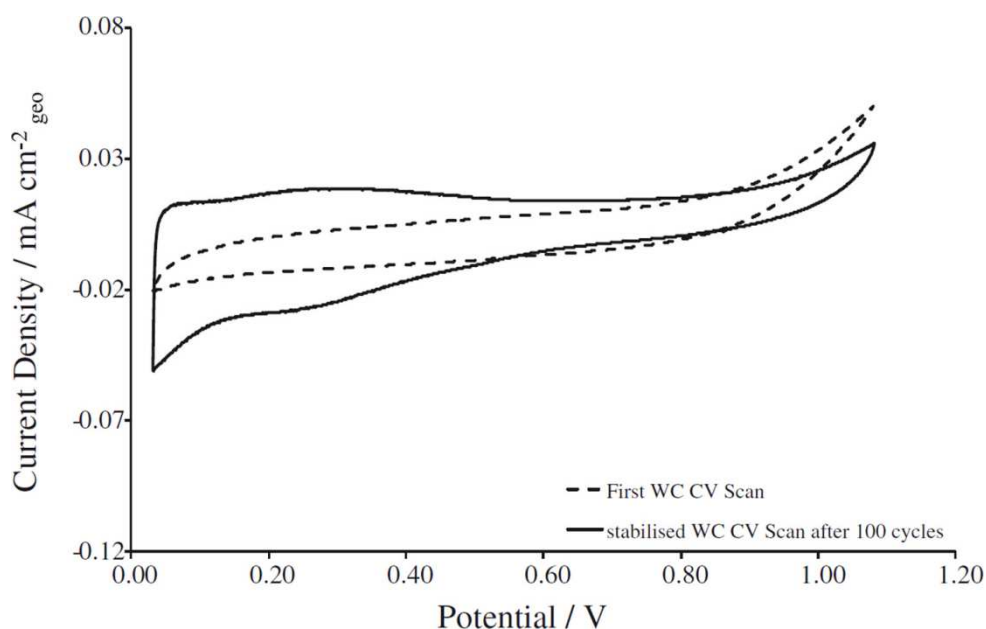


Figure 7.1: CV curves of commercially available WC in 0.1 N HClO₄ at room temperature and sweep rates of 0.05 V s^{-1} and a loading of 42 mg cm^{-2} before and after stabilization of the CV.

The first scan shows a significant oxidation current starting at about 0.9 V. This can be attributed to the oxidation of WC and formation of surface oxides. After 100 scans with a sweep rate of 0.5 V s^{-1} the CVs are stabilized and the oxidation currents at potentials higher than 0.9 V are decreased. In addition to that, at lower potentials the shape of the CV changed significantly. After most of the surface is oxidized, WC shows a muted peak between 0.7 and 0.8 V. The surface oxidation of WC- WO_x can be identified with the peak area at low potentials between 0.052 V and 0.4 V in the oxidation and reduction direction of the CV.^[12,13] This shape can be assigned to the intercalation of protons into the support material. The applied electrochemical pre-treatment of WC in acidic media and the applied potentials are comparable to the conditions in an operating fuel cell.

7.3.2 Characterization of self-made WO_{xs}

For the characterization of self-made WO_{xs} , *ex-situ* CVs of the prepared samples were recorded. The stabilized CV curves after 100 cycles of each material are shown in Figure 7.2.

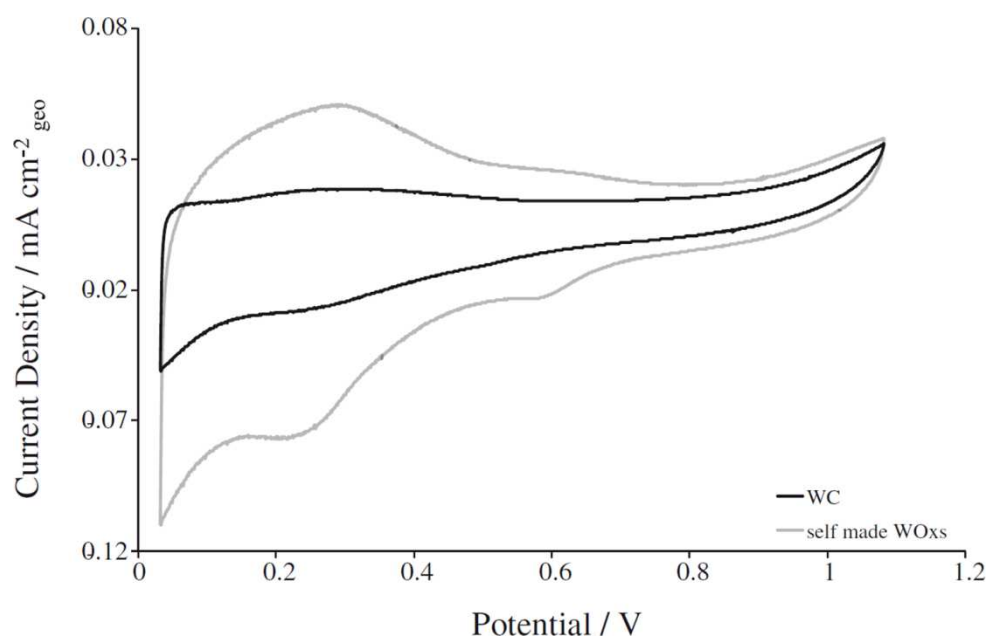


Figure 7.2: CV curves of WC and self-made WO_{xs} without platinum in 0.1 N HClO_4 at room temperature, sweep rates of 0.05 V s^{-1} and a loading of 42 mg cm^{-2} after 100 potential cycles with 0.5 V s^{-1} .

The synthesis of WO_{xs} leads to a more pronounced peak in the potential range which is characteristic for WO_x compared to the WC sample after 100 electrochemical potential cycles. Starting from the same WC material the chemical oxidation leads to a higher level

of amorphous or nanoparticulate WO_x as observed in literature.^[26] Bearing in mind that mechanical detachment of catalyst from the catalyst support material is a main degradation factor in fuel cell electrodes, the use of WC, which is prone to get oxidized on the surface, is not suitable as support material for fuel cell electrodes.

7.3.3 Characterization of commercial WO_x

The CV curve of commercially available WO_x ($\text{WO}_3\text{-XY-JM}$, Wolfram Bergbau und Hütten AG) with a BET surface area of $\sim 5 \text{ m}^2 \text{ g}^{-1}$ is compared to self-made WO_{xs} (Figure 7.3).

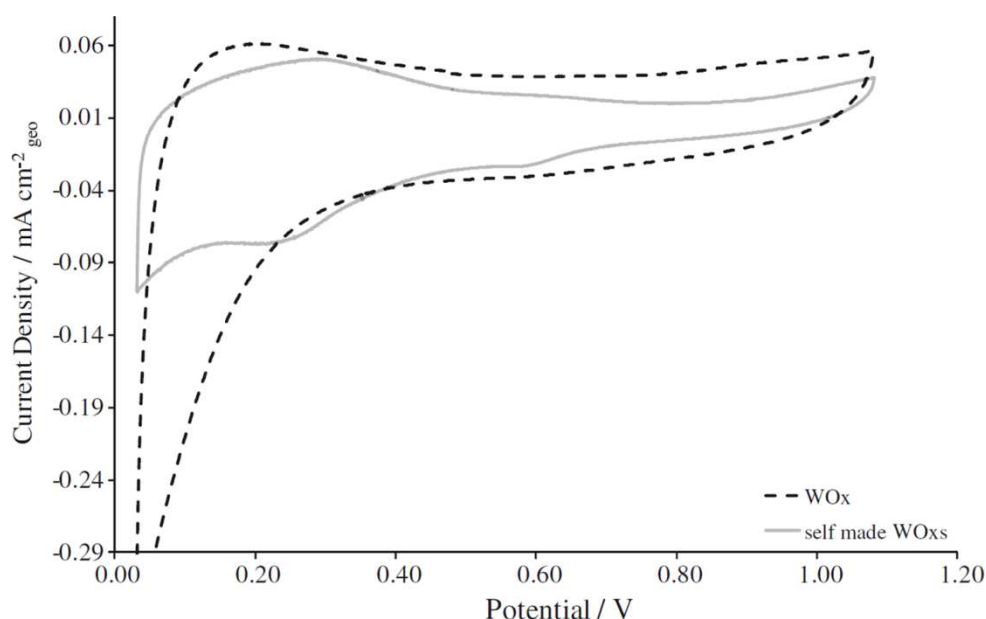


Figure 7.3: CV curves scans of commercial WO_x and self-made WO_{xs} in 0.1 N HClO_4 at room temperature, sweep rates of 50 mV s^{-1} and a loading of 42 mg cm^{-2} .

The commercial WO_x shows a more pronounced current in the WO_x designated low potential region in the oxidation direction, which is comparable to results shown in Figure 7.2.

For commercially available WO_x the hydrogen oxidation current increases dramatically compared to WC or WO_{xs} materials. This indicates that the activity of the WO_x samples toward the formation of hydrogen is higher compared to WC or WO_{xs} samples. The BET surface areas of the two samples are comparable within an order of magnitude.

7.3.4 Catalyst deposition on tungsten based support materials

The CV curves of WO_{xs} and WC catalyst support material after platinum deposition are given in Figure 7.4. They possess very different characteristics in the voltammetric

profile compared to each other. This is in accordance with the results of the non catalyst loaded supports (see Figure 7.2). The self-made Pt/WO_{xs} shows a more pronounced peak area in the WO_x characteristic low potential region compared to Pt/WC, which can be attributed to the formation of tungsten bronzes (compare equation (7.2)):

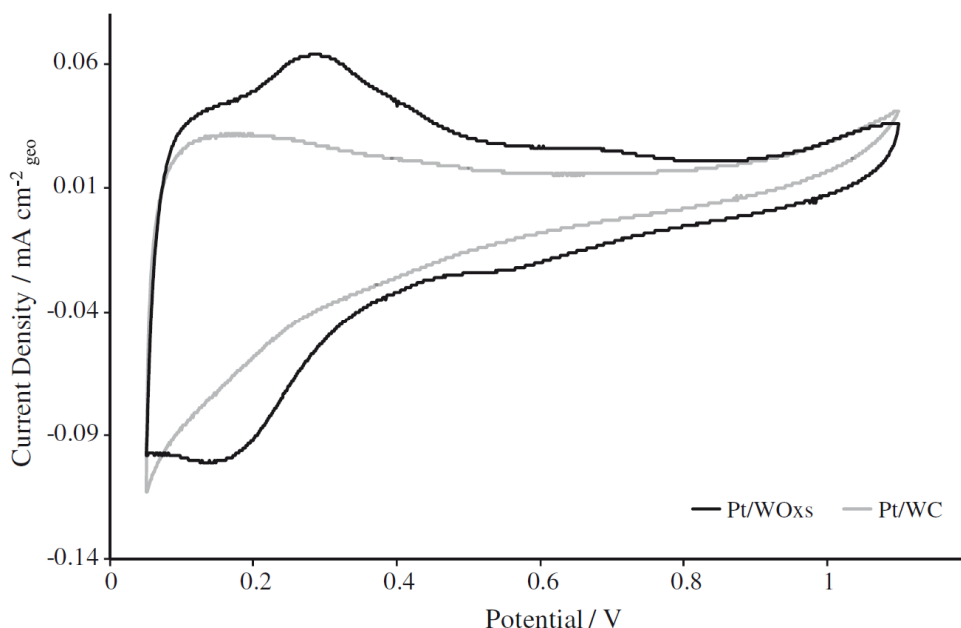
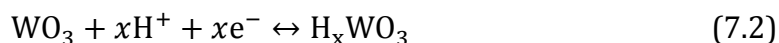


Figure 7.4: CV curves of Pt/WC and Pt/WO_{xs} after stabilization with a sweep rate of 0.05 V s⁻¹ in 0.1 N HClO₄.

The CV curve of the Pt/WC sample in Figure 7.4 shows the analysis scan after 100 stabilization cycles, where the H_{upd} region gets more pronounced (compare Figure 7.1). The Pt/WO_{xs} sample shows a characteristic WO_x behavior in the low potential region even in the first CV cycle.

In Figure 7.5 the analysis scans of Pt/WO_{xs} and WO_{xs} are shown. The H_{upd} region of Pt/WO_x shows the same characteristics of Pt in the H_{upd} region. Below 0.4 V several processes occur: hydrogen underpotential deposition (H_{upd}) and desorption, formation of tungsten bronzes and formation and decomposition of substoichiometric tungsten oxides. So it is not possible to distinguish between these superimposing factors occurring in the low potential region.^[27]

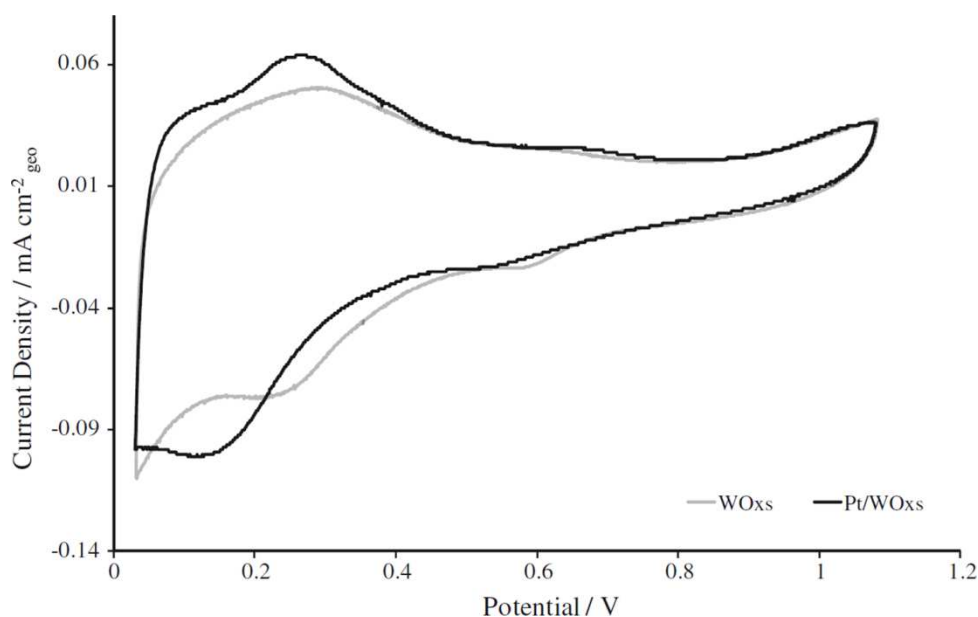


Figure 7.5: CV curves of Pt/WO_{xs} and WO_{xs} after stabilization with a sweep rate of 50 mV s⁻¹ in 0.1 N HClO₄.

The formation of oxides on the surface of WC is confirmed by the results of the electrochemical characterization of WO_x. The CV curves of the commercial available WO_x, where Pt is deposited via the same in-house procedure, reveals the same shape compared to self-made WO_{xs}. The CV measurements of Pt/WO_x and Pt/WC are displayed in Figure 7.6.

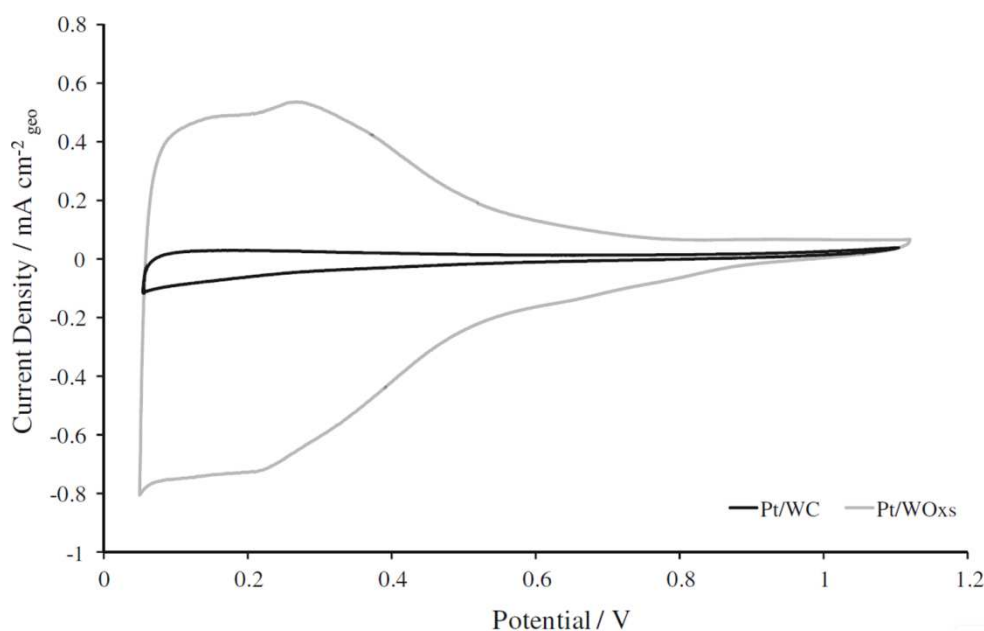


Figure 7.6: CV curves of Pt/WC and Pt/WO_{xs} with a sweep rate of 0.05 V s⁻¹ in 0.1 N HClO₄.

The peak in the low potential region in the case of Pt/WO_x is more than one magnitude higher than for the Pt/WC. The CV shape of Pt/WO_{xs} is similar to the CV shape of WO_x. Another difference is the double layer charge capacity (C_{dl}) in the region of about 0.6 V, which is much higher in the case of Pt/WO_x, which indicates a higher surface area of WO_x compared to WC.

7.3.5 Potential cycling

Potential Cycling (PC) experiments were done in order to get information on the stability of the platinum loaded tungsten based support material and compared to measurements on Pt loaded HSAC. The results are shown in Figure 7.7, Figure 7.8 and are summarized in Figure 7.9. The decrease of the H_{upd} charge (Figure 7.7) of Pt/WO_{xs} can be attributed to the loss of active platinum sites. The C_{dl} , which can be seen at 0.6 V, is not changing, so the surface area and the amount of tungsten based support material is not changing significantly and no loss of support material can be observed. The loss of charge in the low potential region can be attributed to Pt-agglomeration or Pt-dissolution.

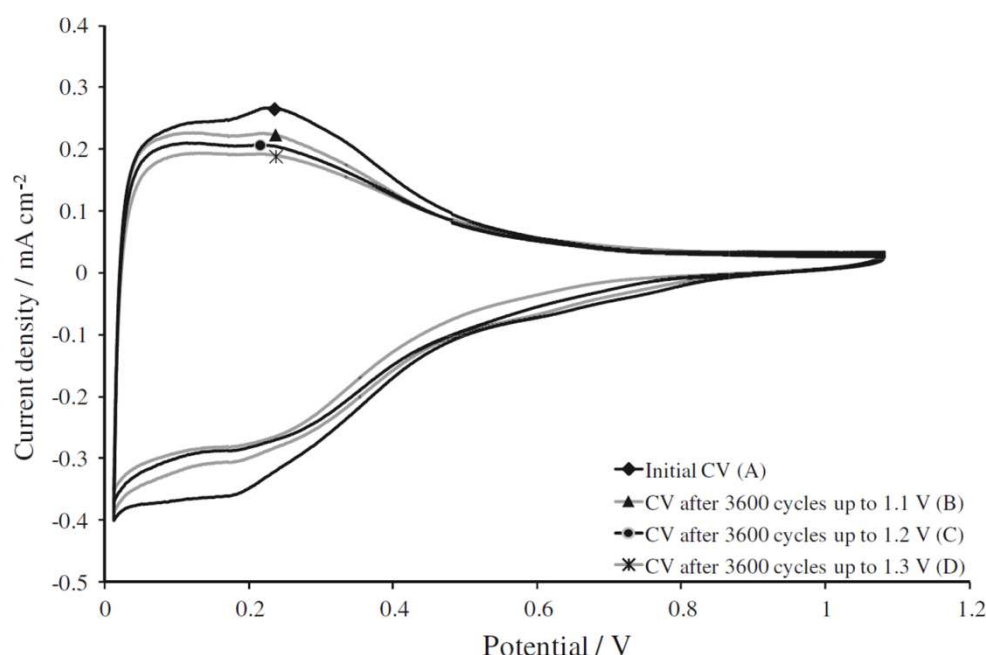


Figure 7.7: Analysis scans of WO_x supported Pt catalyst. (A) Initial analysis scan of Pt/WO_x, (B) after 3600 cycles up to 1.1 V, (C) after 3600 consecutive cycles up to 1.2 V and (D) after 3600 consecutive cycles up to 1.3 V.

In Figure 7.8 the CV scans of a PC experiment with Pt/HSAC are shown. The decrease of the H_{upd} charge (between 0.052 and 0.3 V) is much higher compared to WO_x, especially

when the electrode is cycled up to potentials of 1.3 V, where almost the whole H_{upd} charge is lost after the PC.

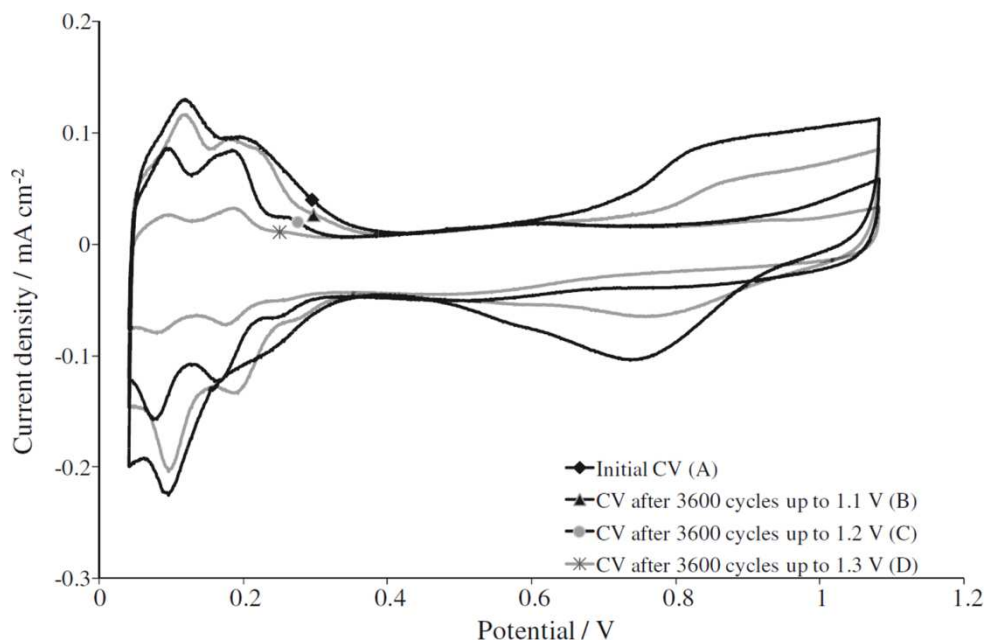


Figure 7.8: Analysis scans of Pt loaded HSAC. (A) Initial analysis scan of Pt loaded HSAC, (B) after 3600 cycles up to 1.1 V, (C) after 3600 consecutive cycles up to 1.2 V and (D) after 3600 consecutive cycles up to 1.3 V with a sweep rate of 0.05 V s^{-1} in 0.1 N HClO_4 .

In Figure 7.9 the results of the PC experiments are summarized. Depending on the upper reverse potential the remaining H_{upd} charge in the low Potential region is calculated and compared to the starting value. The Pt loaded WO_{xs} catalyst supports showed a much higher remaining H_{upd} especially at potentials up to 1.3 V, indicating a higher stability of the catalyst and catalyst support system (compare Figure 7.7).

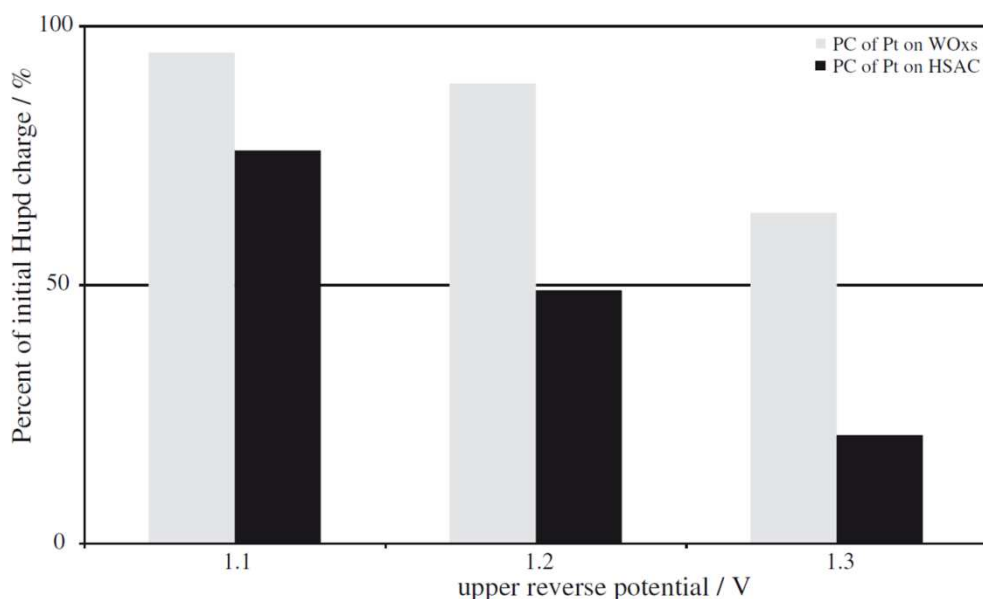


Figure 7.9: Comparison of H_{upd} charge loss of different supported Pt catalysts after 3600 cycles with upper reverse potentials of 1.1, 1.2 and 1.3 V.

7.3.6 CO-stripping

The CV curves after the adsorption of a CO monolayer were recorded in order to determine the CO-oxidation behavior of Pt on different catalyst support materials, as shown in Figure 7.10. In the first scan the CO-oxidation behavior from Pt on WO_{xS} is different from the CO-oxidation behavior from Pt on carbon. The CO-oxidation peak of tungsten based supports at 0.8 V is much smaller compared to Pt on HSAC, but therefore a broader peak at lower potentials appears. In Figure 7.10 a clear CO oxidation of Pt loaded WO_{xS} between 0.6 and 0.8 V is observed. It is significantly smaller than the maxima for Pt on HSAC. The calculated ECA from the CO-stripping experiments of WO_{xS} based catalyst support is only 8 m² g⁻¹ Pt.

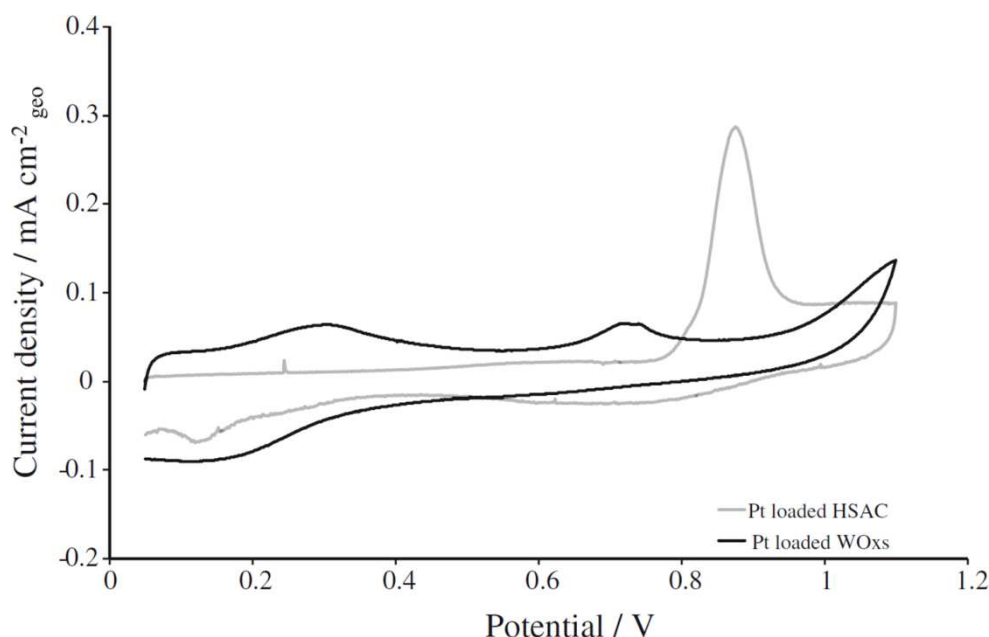


Figure 7.10: CO-stripping result of Pt loaded WO_x s and Pt loaded HSAC with a sweep rate of 0.05 V s^{-1} in 0.1 N HClO_4 .

7.3.7 *In-situ* CV

PBI based MEAs were produced according to the procedure described in Section 2.5 in order to get information about the stability and performance of tungsten based catalyst support materials. On the working electrode WC, home-made WO_{xs} or WO_x with and without platinum were used. A Pt/HSAC electrode was used as reference electrode.

The *in-situ* CV for HT-PEM of a Pt/WC working electrode is presented in Figure 7.11. The initial CV (A) shows a different shape in contrast to the peaks after 100 cycles between 0.052 V and 1.2 V (B). The region in the range of 0.052–0.4 V shows similarities to the character of WO_x . The cathodic oxidation region ($>0.7 \text{ V}$) stabilizes after gradually diminishing (C), which is due to the electrooxidation of WC- WO_x . The WO_x formation on the WC support in the range between 0.052 V and 0.4 V pretends an increase in the H_{upd} charge, when platinum loaded WC is used.

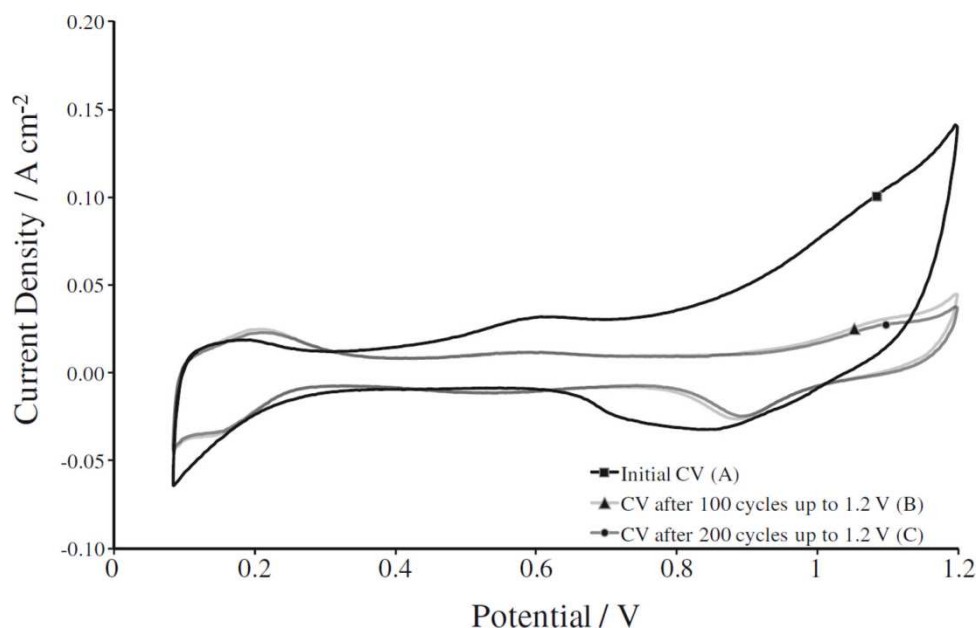


Figure 7.11: In-situ CVs for HT-PEMFC of Pt/WC at different aging levels. (A) Initial scan, (B) after 100 cycles between 0.052 V and 1.2 V (C) after 100 consecutive cycles between 0.052 V and 1.2 V.

The *in-situ* CVs after 100 cycles of WO_x -based working electrodes with (A) and without (B) platinum are shown in Figure 7.12. The cathodic peak at 0.3 V in the WO_x and Pt/WO_{xs} working electrode can be attributed to the intercalation of protons and forming hydrogen tungsten bronzes (H_xWO_3). The difference between Pt/WO_{xs} and WO_x in the low potential region (<0.4 V) can be attributed to H_2 formation and its re-oxidation at the platinum catalyst.

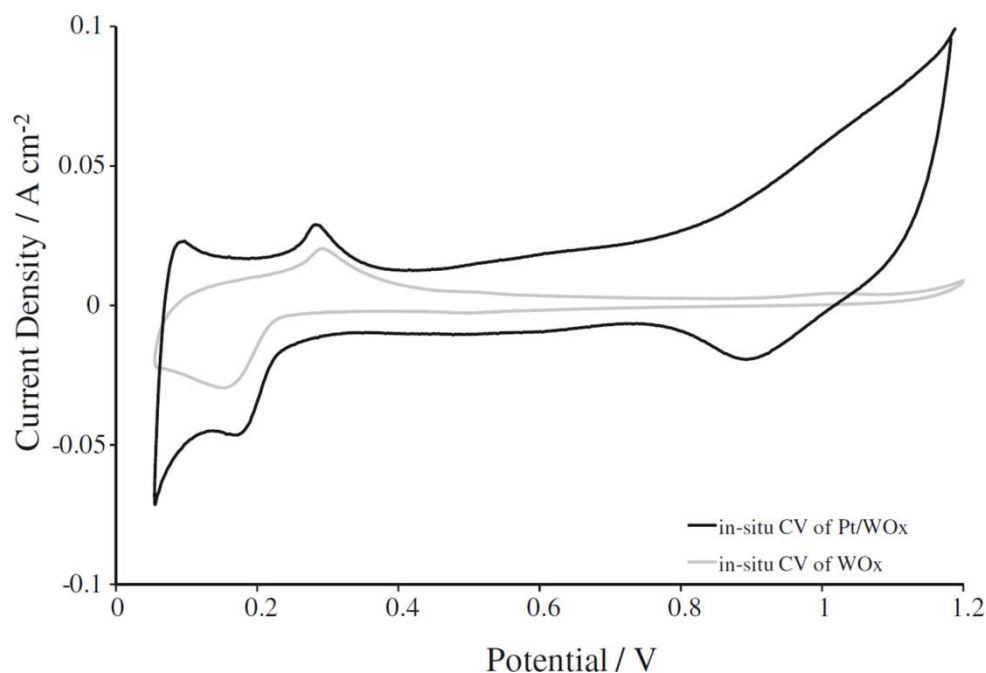


Figure 7.12: In-situ CVs of WO_x with (A) and without platinum (B) on the working electrode after 100 cycles between 0.052 V and 1.2 V with a sweep rate of 0.050 V s^{-1} in 0.1 N HClO_4 .

7.3.8 TGA

The TGA measurements in air of WO_{xs} , WC and WO_x were done to get information about the stability of tungsten based support materials and are presented in Figure 7.13.

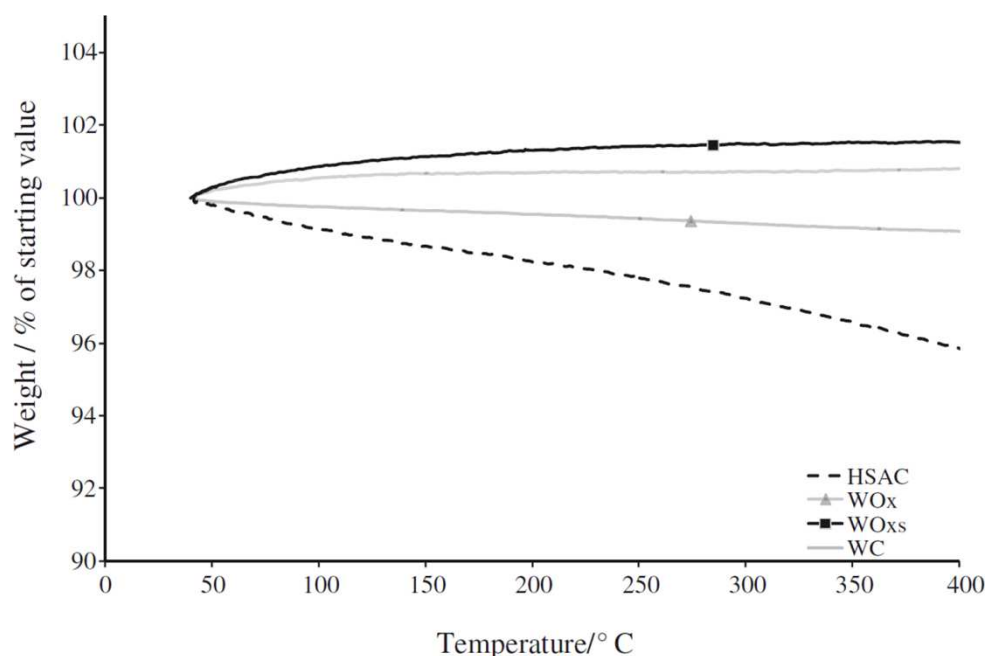


Figure 7.13: TGA of WO_x , WO_{xs} , WC and HSAC from 40°C to 400°C at a scan rate of 10°C s^{-1} under air atmosphere.

Commercial WC possesses a stable behavior up to 400 °C under air atmosphere. In contrast to that stable behavior, the commercial WO_x shows a linear decrease of weight. The self-made WO_{xs} revealed a weight gain up to 400 °C. When compared to today's widely used HSAC support materials, the weight loss of the tungsten based materials is insignificant up to 400 °C.

The different behavior of WO_{xs} and WO_x at temperatures up to 250 °C occurs due to incomplete oxidation of WC in the synthesis of WO_{xs}. This can explain a weight gain of 2% for WC. In contrast to that, the commercial available WO_x powders are losing about 1% of the initial weight up to 250 °C, which can be explained by impurities in the fabrication process.

7.3.9 XRD and electron microscopy analysis

The XRD patterns for Pt loaded tungsten based catalyst support materials are given in Figure 7.14. The diffractogram of the pre-treated WC shows the characteristic reflections for Pt-fcc and hexagonal WC. The procedure to synthesize Pt on self-made WO_{xs} leads to a similar, but not equal, XRD pattern compared to Pt on WO_x, which is in accordance with the *ex-situ* and *in-situ* CV results and the TGA measurement. The intensity as well as the number of reflections is changed in these two patterns indicating a change in symmetry. In all patterns, the WC, WO_x and WO_{xs} signals possess a high diffraction intensity, in contrast to the platinum signals at 39.7° and 63.5° 2θ which are rather small. In addition, the observed reflections of Pt are broad due to the small size of the Pt particles. This finding is in good accordance to the results of the HR-TEM measurements shown later.

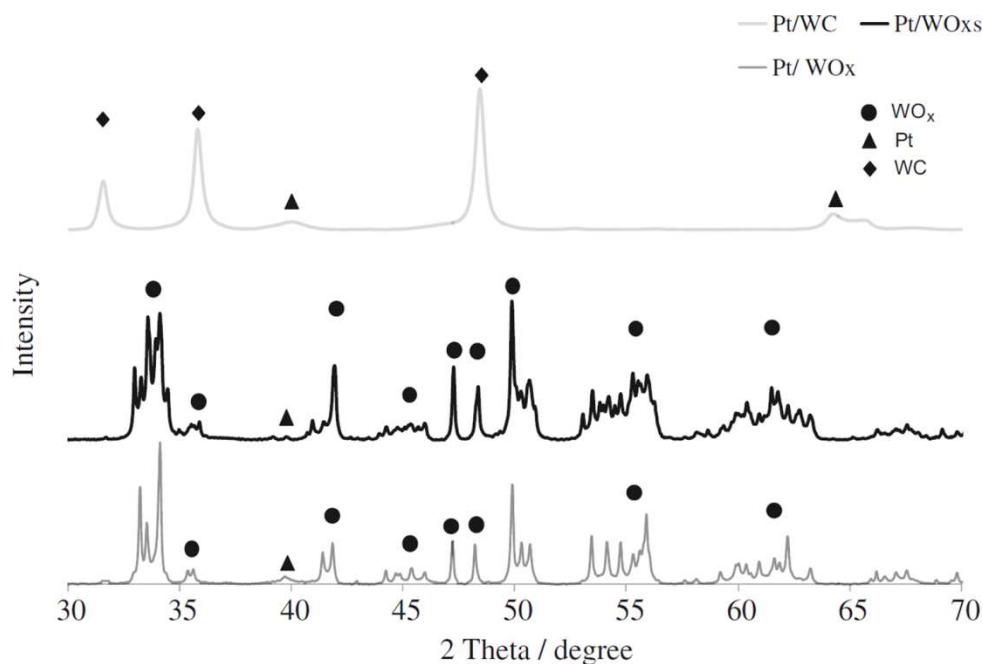


Figure 7.14: XRD patterns of Pt/WC, Pt/WO_x and Pt/WO_{xs}.

Electron microscopy investigations were performed in order to get information on the size of the WO_x and Pt particles as well as the platinum distribution on WO_x. As an example Figure 7.15 shows SEM and TEM images of untreated WO_x particles without platinum. The size of the connected WO_x particles ranges from 0.1 mm to 0.8 mm. With the aid of EDS measurements performed in the SEM a loading of 13wt% of Pt on WO_x was confirmed. The high-contrast TEM bright-field image (b) and electron diffraction pattern (c), shown as insets in Figure 7.15 clarify the high crystallinity of the WO_x particles.

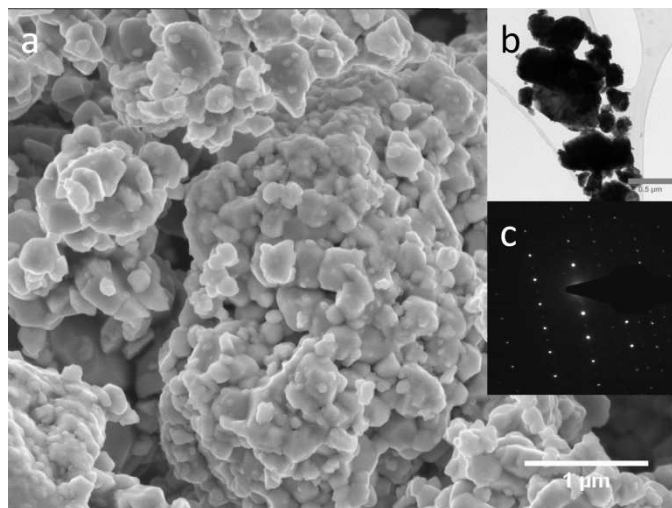


Figure 7.15: (a) Secondary electron top view image shows the crystalline morphology of WO_x . (b) High-contrast TEM bright-field image of WO_x particles and related electron diffraction pattern (c).

The catalyst particles are randomly distributed on the surface of the WO_x particles as visible in Figure 7.16. The morphology of the WO_x particles is not very uniform. Nevertheless, the diameter of the platinum particles can be estimated from the high resolution micrograph (Figure 7.16). It displays the characteristic Pt-interatomic distances of small spherical platinum particles in a (111) lattice plane configuration and reveals a Pt crystal size of about 3–4 nm.

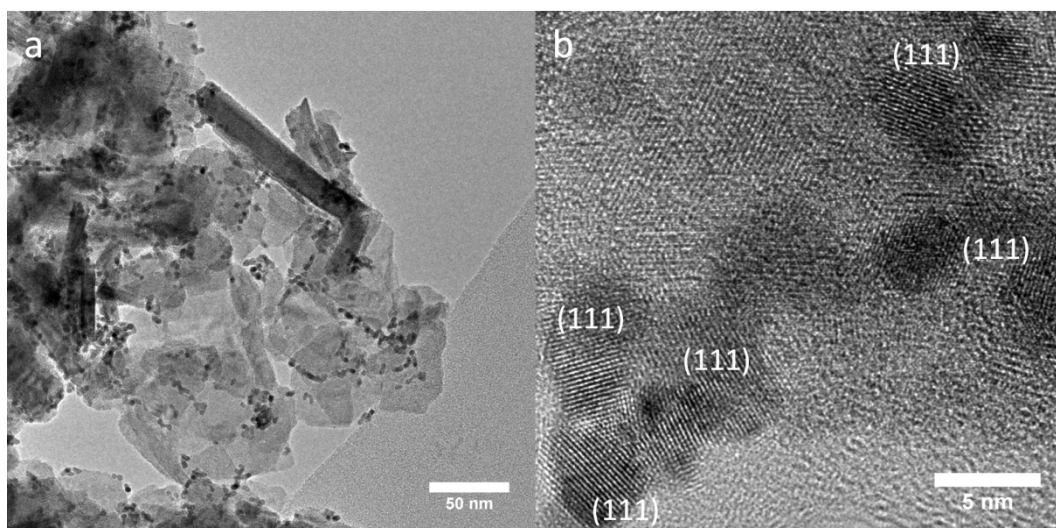


Figure 7.16: TEM images of two representative areas of WO_x . 13 wt% Pt loaded WO_x (a) and detail with visible (111) lattice planes of Pt on WO_x (b).

In Figure 7.17 the Pt loaded WO_{xs} support materials are shown. The platinum distribution and the particle sizes of WO_{xs} are in the same range as in the WO_x samples.

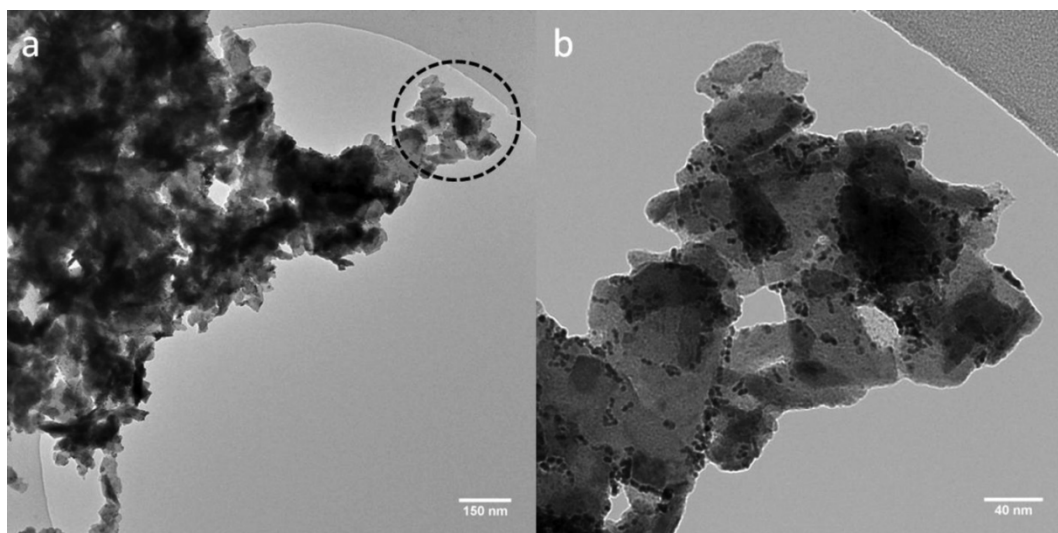


Figure 7.17: TEM images of two representative areas of WO_x , 13 wt% Pt loaded WO_x (a) and detail of Pt on WO_x (b).

7.3.10 HT-PEM fuel cell results

The catalyst support material was used as anode support in HTPEM fuel cells. The WO_x -based anode was doped with phosphoric acid and pressed with a standard HSAC-cathode.

In Figure 7.18 the results of a HT-PEM MEA test for 980 h with a WO_x based anode are shown. After a conditioning time of about 500 h with rising cell potential, a stable cell potential until 980 h was obtained.

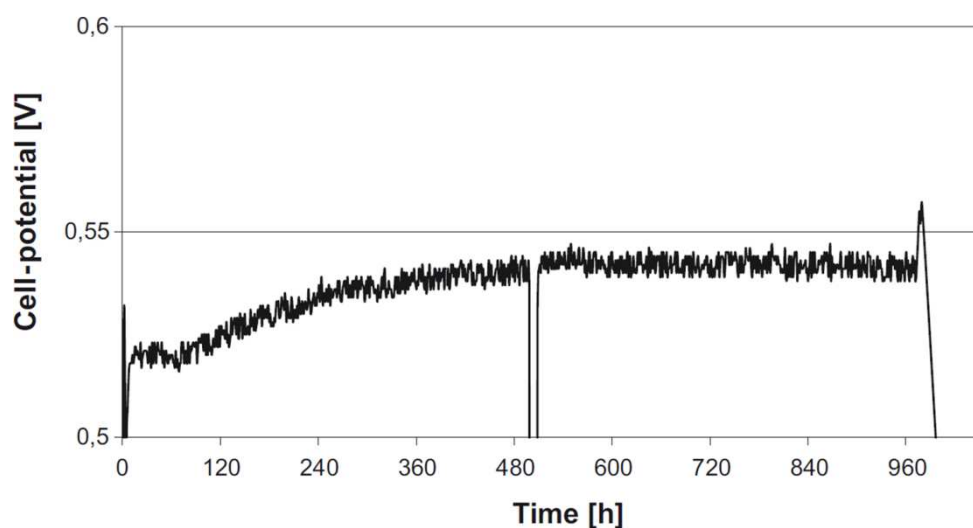


Figure 7.18: 980 h test of a HT-PEM MEA in a 20-cell HT-PEMFC stack with methanol reformat on the anode at 160 °C and 0.2 A cm^{-2} current density at ambient pressure.

7.4 Conclusions

Self-made WO_{xs} , commercial available WC and commercial available WO_x were evaluated as a catalyst support material for HTPEM fuel cells. The self-made WO_{xs} was compared to the starting material WC and commercial available WO_x . The electrochemical and chemical characteristics were determined via *ex-situ* CV, PC, TGA, SEM and TEM and *in-situ* CV and PC measurements. The chemical and electrochemical treatment and high electrochemical potentials are leading to a formation of WO_x on the surface of WC. WO_x formed during the PC leads to the formation of hydrogen tungsten bronzes and to the oxidation and reduction of sub-stoichiometric oxides. The loss or the oxidation/reduction of catalyst support material can be identified from the C_{dl} at potentials in the cathodic scan direction in the region higher than 0.7 V. WO_x and WO_{xs} were used as catalyst support material for further investigations because WC gets oxidized to WO_x under fuel cell conditions.

XRD investigations showed that the self-made WO_{xs} is formed under oxidizing acidic conditions. The commercially available WO_x shows the same electrochemical characteristics compared to the self-made WO_{xs} . The onset potential of the CO oxidation is shifted to more negative values. This effect arises from a hydrogen spillover on the surface of WO_x , which liberates the active Pt sites from contaminants.

HT-PEM in-situ experiments with WC based MEAs show a comparable formation of WO_x (or hydrogen tungsten bronzes), which was confirmed with measurements of MEAs with a WO_x working electrode without Pt.

In-situ measurements show that the deposition procedure of platinum on WO_x support results in a partial reduction of WO_x , which can be re-oxidized under fuel cell conditions. WO_x -based support materials have a high chemical stability up to more than 450 °C under air. The electrochemical stability under oxidizing conditions is higher compared to Pt/HSAC. TEM measurements showed that platinum particles have an average diameter of 3–4 nm and are uniformly dispersed on the tungsten based support material. A 980 h test with reformed methanol on the anode in a PBI based HT-PEM MEA at 0.2 A cm⁻² was done. After a conditioning time of 500 h a stable cell potential for 480 h was achieved and no degradation rate was observed. This test showed that WO_x can be used as catalyst support material for the anode in HT-PEM fuel cells.

7.5 Chapter references

- [1] Baumgartner, W. R.; Parz, P.; Fraser, S. D.; Wallnöfer, E.; Hacker, V. *J. Power Sources* **2008**, *182*, 413.
- [2] Wallnöfer, E.; Perchthaler, M.; Hacker, V.; Squadrito, G. *J. Power Sources* **2009**, *188*, 192.
- [3] Planeix, J. M.; Coustel, N.; Coq, B.; Brotons, V.; Kumbhar, P. S. et al. *J. Am. Chem. Soc.* **1994**, *116*, 7935.
- [4] Park, C.; Baker, R. T. K. *J. Phys. Chem. B* **1998**, *102*, 5168.
- [5] Sharma, S.; Pollet, B. G. *J. Power Sources* **2012**, *208*, 96.
- [6] Lessner, E.; Schubert, W. D. *Tungsten: Properties, Chemistry, Technology of the Element, Alloys and Chemical Compounds*; Kluwer Academic: NY, **1999**.
- [7] Hobbs, B. S. *J. Electrochem. Soc.* **1975**, *122*, 1174.
- [8] Butler, M. A. *J. Appl. Phys.* **1977**, *48*, 1914.
- [9] Hobbs, B. S.; Tseung, A. C. C. *Nature* **1969**, *222*, 556.
- [10] Huang, Y. J.; Dai, H. H.; Li, W. S.; Li, G. L.; Shu, D. et al. *J. Power Sources* **2008**, *184*, 348.
- [11] Ota, K.; Ishihara, A.; Mitsushima, S.; Lee, K.; Suzuki, Y. et al. *J. New Mater. Electrochem. Syst.* **2005**, *8*, 25.
- [12] Shim, J.; Lee, C.-R.; Lee, H.-K.; Lee, J.-S.; Cairns, E. J. *J. Power Sources* **2001**, *102*, 172.
- [13] Kulesza, P. J. *J. Electrochem. Soc.* **1989**, *136*, 707.
- [14] Antolini, E.; Gonzalez, E. R. *Appl. Catal. B* **2010**, *96*, 245.
- [15] Nikolov, I.; Vitanov, T. *J. Power Sources* **1980**, *5*, 273.
- [16] Nikolov, I.; Vitanov, T. *J. Power Sources* **1980**, *5*, 283.
- [17] Brady, C. D. A.; Rees, E. J.; Burstein, G. T. *J. Power Sources* **2008**, *179*, 17.
- [18] Chhina, H.; Campbell, S.; Kesler, O. *J. Electrochem. Soc.* **2007**, *154*, B533.
- [19] Meng, H.; Shen, P. K. *Chem Commun (Camb)* **2005**, 4408.
- [20] Meng, H.; Shen, P. K. *Electrochem. Commun.* **2006**, *8*, 588.
- [21] Meng, H.; Shen, P. K. *J. Phys. Chem. B* **2005**, *109*, 22705.
- [22] Santos, L. G. R. A.; Freitas, K. S.; Ticianelli, E. A. *J. Solid State Electrochem.* **2007**, *11*, 1541.
- [23] Shao, M.; Merzougui, B.; Shoemaker, K.; Stolar, L.; Protsailo, L. et al. *J. Power Sources* **2011**, *196*, 7426.
- [24] Ganesan, R.; Lee, J. S. *J. Power Sources* **2006**, *157*, 217.
- [25] Zhu, W.; Ignaszak, A.; Song, C.; Baker, R.; Hui, R. et al. *Electrochim. Acta* **2012**, *61*, 198.
- [26] Wu, F.; Liu, Y.; Wu, C. *J. Mater. Sci. Technol.* **2010**, *26*, 705.
- [27] Martín, A. J.; Chaparro, A. M.; Daza, L. *J. Power Sources* **2011**, *196*, 4187.

8 Insight into the degradation of HT-PEMFCs containing tungsten oxide catalyst support material for the anode

This chapter is based on the following publication:

Christoph Heinzl, Katharina A. Hengge, Markus Perchthaler, Viktor Hacker, Christina Scheu *Journal of The Electrochemical Society* (accepted).

8.1 Introduction

With the ongoing increase of energy demand, the advancing sensibility for the environment and the slow but steady running out of natural resources like oil, coal or natural gas there is an urgent need for new, nonpolluting energy sources.^[1] Among the wide field of feasible solutions like wind power, solar cells, etc. also fuel cells are an interesting alternative. Fuel cells enable the conversion of chemical energy of a fuel into electrical energy with an efficiency of up to 60%.^[2] Generally the wide variety of fuel cells can be divided into six classes which differ from each other in fuel, operating temperature and material.^[3,4] In the present work we investigated high temperature proton exchange membrane fuel cells (HT-PEMFCs). These are operated at elevated temperatures in the range of 100–200 °C, taking advantage of an improved water management, a decrease of catalyst poisoning^[5,6] as well as a significant increase of the oxygen reduction reaction kinetics which is one of the limiting factors in the performance of the HT-PEMFCs.^[7-10] Associated with the increased operating temperature the produced thermal heat can as well be utilized by an end-consumer, leading to a theoretical total maximum efficiency of 90% of the operating fuel cell system.^[11,12]

The major drawback in fuel cell applications are degradation processes that take place with ongoing fuel cell operation times. Though these processes happen at the nanoscale, a macroscopic loss of active surface area and thereafter a decrease in fuel cell efficiency can be observed. The most common used catalyst support material up to now is high

surface area carbon (HSAC), coated with Pt nanoparticles. However, investigations render that HSAC is not the optimum catalyst support material for long-term and start-stop operation modes, especially at elevated temperatures, due to its susceptibility for degradation.^[13-16] HSAC is subjected to oxidation during fuel cell operation. The formed CO adsorbs to the surface of the catalyst where it blocks catalytic active sites.^[17] Further degradation mechanisms like dissolution^[18-25], Ostwald ripening^[26-28], agglomeration^[29,30] and particle detachment affect the Pt catalyst.^[31,32]

Tungsten oxide as a catalyst support exhibits several advantages over HSAC which have an impact on fuel cell performance. It has a high melting temperature of up to 1470 °C^[33], a good corrosion resistance as well as an exceptional stability in electrochemical cells. Its outstanding CO tolerance^[34] renders tungsten oxide a promising material to replace HSAC. However, it is important to use a tungsten suboxide (WO_{3-x}) rather than stoichiometric WO_3 . The latter one is an insulator due to unoccupied 5d-orbitals whereas WO_{3-x} contains W^{5+} ions next to W^{6+} ions so electron conductivity is ensured.^[35] The resistivity is ranging from 1 Ωcm for WO_2 to a minimum value of 0.1 Ωcm for $\text{WO}_{2.75}$.^[36]

Beside electron conductivity also proton conductivity belongs to the attributes a suitable catalyst support should have. Tungsten oxide is capable of hydrogen spill over, a phenomenon that was first reported by F. Wöhler in 1824.^[37] Hydrogen spillover defines the process during which previously oxidized protons are transferred from the catalyst to the support material, setting active catalytic sites free comparatively fast while forming oxyhydroxides. In the case where tungsten oxide is the support material, $\text{WO}_{3-x}(\text{OH})_y$ is formed. The presence of water enables the adsorbed protons to travel through the anode material via the Grotthuss mechanism.^[38,39] Due to the insertion of protons into the tungsten oxide material also the electrical conductivity is changed. Thus by exposing the material to different atmospheres the electrical and proton conductivity can be controlled.^[40] Due to these reasons WO_{3-x} is a promising material for application as fuel cell electrode material.^[41] In preliminary tests we had used WO_{3-x} as support material at both, the anode as well as the cathode side. The performance of the resulting fuel cells was lacking behind the performance of a cell using a standard HSAC support. Therefore, in the present work we used WO_{3-x} only as anode support material. Due to

the hydrogen spillover mechanism and the good electrical conductivity, which are both important quantities at the anode side, we expect an optimized fuel cell characteristic and lower degradation for this assembly.

The addressed degradation processes mentioned above take place on small scales and therefore electron microscopy is a useful tool to analyze and understand the related phenomena.^[18,42] Some of the reported degradation analysis via electron microscopy is done using the so called identical location transmission electron microscopy (TEM) method.^[43,44] Here, exactly the same position of an electrode on a TEM grid is analyzed before and after operation. The operation is designed as to simulate realistic conditions of fuel cell operation but is performed on a sample consisting of Pt decorated HSAC particles which represent an electrode in a cell. In our work we present detailed TEM analysis of real HT-PEMFC stacks with a WO_{3-x} based anode before and after different modes of operation. These include continuous operation as well as start-stop cycles which are designed to reach high anode and cathode potentials according to the mechanism postulated by Reiser et al..^[45]

Due to our employed focused ion beam (FIB) microscopy sample preparation strategy we are able to analyze large sample areas at specific regions of interest and obtain satisfying statistics. The morphology as well as the chemical composition and distribution of elements are investigated via electron microscopy based techniques like scanning electron microscopy (SEM), energy dispersive X-ray spectroscopy (EDS), TEM and electron energy loss spectroscopy (EELS). In addition *in-situ* membrane electrode assembly (MEA) testing is performed to investigate the suitability of the WO_{3-x} based anode material in HT-PEMFC applications.

8.2 Experimental

8.2.1 Synthesis

8.2.1.1 Synthesis of WO_{3-x}

Commercially available WC raw powders with a surface area of $2.71 \text{ m}^2 \text{ g}^{-1}$ and a grain size of $0.47 \mu\text{m}$ were surface modified via harsh chemical oxidation. For this, 3 g of WC powder was dispersed in a 50 ml mixture (3:2) of HNO_3 (65 wt%, BDH Prolabo, AnalaR

Normapur) and H_2SO_4 (98 wt%, MERCK KGAA, EMSURE) and heat treated under reflux for 6 h. The obtained green powders were washed several times with deionized water until a neutral pH was detected.^[41]

8.2.1.2 Anode preparation

500 mg of WO_{3-x} and HSAC based catalyst supports were ultrasonicated in a mixture of 30 ml ethylene glycol and 10 ml deionized water. The Pt catalyst was then deposited on these substrates via different electroless deposition techniques. The Pt precursor required for this was prepared by a procedure described elsewhere.^[46] The amount of Pt was kept constant which results in different thicknesses for support layers based on WO_{3-x} or HSAC. The loading was 13 wt% Pt. This value was confirmed via elemental and EDS measurements.

8.2.1.3 Membrane electrode assembly

For *in-situ* tests MEAs were prepared using WO_{3-x} based catalyst support materials on the anode side and a HSAC material on the cathode side. Additionally, an MEA with HSAC on both electrodes was fabricated as a standard. The catalyst support materials were deposited on a wet proofed carbon based gas diffusion layer via a doctor blade process. The ink contained polytetrafluorethylene dispersion (Dyneon™, TF 5035 PTFE) as hydrophobic reagent and binder, deionized water, isopropanol (gradient grade, Merck) and the catalyst material. The applied slurry was dried at 170 °C. For the preparation of MEAs phosphoric acid was added to the catalyst layer and then hot pressed with a membrane based on polybenzimidazole (PBI) as described elsewhere.^[47]

8.2.1.4 Investigated samples

Table 8.1 summarizes the samples investigated in this work and gives the modes of operation. Altogether, four MEA samples were analyzed in this work regarding their morphology and chemical composition on the nanoscale as well as their electrochemical behavior. One MEA was studied before operation (MEA I), two after nominal 600 h (MEA II) and nominal 2000 h (MEA III) of continuous operation respectively and one after periodical start-up and shut-down cycles (MEA IV). In all cases the same electrodes and membrane were used for the fabrication of the MEA. It is important to note that the real testing times of the stacks was usually slightly lower than these

nominal values due to shut-downs of the testing devices. The two continuous operation modes differed in the type of supplied fuel and number of cells. For the nominal 600 h continuous operation mode a single cell test with pure hydrogen and for the nominal 2000 h continuous operation mode a stack test with reformed methanol were performed. This is related to standard in-house procedures, in which the nominal 600 h continuous operation mode is used as a pre-test before the nominal 2000 h continuous operation stack test is started. While the differences in fuel and number of cells tested do have an influence on the *in-situ* fuel cell characteristics as can be seen later, the overall morphology and elemental distribution should not be affected strongly. For comparison, the morphology of the ready-to-use WO_{3-x} anode was investigated.

Table 8.1: Overview of the analyzed samples in this work and their mode of operation.

Sample	Operating mode
MEA I	Ready-to-use
MEA II	Continuous operation for nominal 600 h
MEA III	Continuous operation for nominal 2000 h
MEA IV	Start-stop operation for 35 cycles
WO_{3-x} anode	Ready-to-use

8.2.2 Characterization methods

8.2.2.1 Structural and chemical analysis

SEM

The general morphology of the WO_{3-x} based electrode and the resulting MEAs was studied by using a JEOL JSM-6500F SEM operated at 25.0 kV. Secondary electron (SE) micrographs were obtained by using the JEOL standard detector. The distribution of the chemical components was analyzed via EDS line scans which were acquired with an EDS detector from Oxford Instruments (Inca Energy). The overall chemical composition of the MEAs was determined by quantitative EDS analysis, which was performed on a JEOL JSM-6490 operated at 15.0 kV and equipped with a standard EDAX detector. SEM top view samples of the anode were prepared by using conventional preparation techniques. For cross-sectional samples, the MEAs were embedded in resin and grinded until a smooth sample surface was reached.

Crystallinity analysis

To investigate the crystallinity of the electrodes on a global scale, X-ray diffraction (XRD) patterns were taken on a Seifert THETA/THETA-diffractometer (GE Inspection Technologies) equipped with a Meteor OD detector, using Co-K α radiation ($\lambda=1.79$ Å). A 2θ detection range of 10–120°, a step size of $2\theta = 0.05^\circ$ and an acquisition time of 40 s per 2θ -step were used. Prior to the investigation, the gas diffusion layer and the micro porous carbon were removed with a scalpel from the MEA so that the anode was freestanding. The broadening of the peaks was measured and an average crystallite size of the Pt catalyst particles (D_{XRD}) was calculated using the Scherrer equation (8.1).^[48]

$$D_{XRD} = \frac{K\lambda}{\Delta(2\theta) \cos\theta} \quad (8.1)$$

K is the shape factor which is 0.9 for spherical particles, λ is the X-ray wavelength in nm (here Co-K α), $\Delta(2\theta)$ is the peak broadening at full width at half maximum (FWHM) in radians and θ is the Bragg angle. The Scherrer equation was applied to obtain statistical information on the average size of the catalyst in the MEA before and after operation.

To obtain information on the crystallinity on a local scale selected area electron diffraction (ED) studies were performed in the TEM. The region of interest was selected by using a selected area diffraction aperture with a diameter of approximately 170 nm.

TEM

To obtain information on the nanoscale concerning the morphology, chemical composition and crystal structure different TEM based techniques were applied. Site-specific TEM samples were prepared by FIB sectioning since conventional cross-sectional sample preparation failed. A ZeissNVision40 FIB microscope with an integrated SEM and an FEI Helios NanoLab 600i also with an integrated SEM were used for TEM lamellae preparation. Besides the conventional lift-out technique an additional FIB preparation method was used, which allowed to fabricate larger (up to 40 μm) than average sized FIB lamellae. For this method, the MEA was glued, cathode side down, on an aluminum spacer. At the anode side the gas diffusion layer and the micro porous carbon layer were removed with a scalpel. 150 μm broad stripes of the MEA were then sliced off with a diamond wire saw from GATAN. This stripe was then thinned in the FIB. A size of 20-40 μm was chosen which was reduced in thickness until electron

transparency was achieved (< 100 nm). Afterwards the stripe was fixed in a special folding TEM grid (Plano). The sample exhibits a higher stability than usual, free standing FIB lamellae, due to the presence of the stabilizing stripe.

All TEM investigations were performed with an FEI Titan 80-300 (S)TEM equipped with an EDAX detector for EDS measurements. The Titan was operated at 300 kV. Scanning TEM (STEM) imaging was achieved by using the attached high angle annular dark-field (HAADF) detector from Fischione Instruments (Model 3000). A Gatan Tridiem image filter was utilized for EELS measurements in STEM mode. The FWHM of the zero loss peak was around 0.9 eV. By using a 2 mm entrance aperture and a dispersion of 0.1 eV per channel we were able to achieve satisfying energy resolution and a good signal to noise ratio. The camera length was 77 mm leading to a collector angle of 20.6 mrad.

8.2.2.2 MEA testing

Polarization curves

To record polarization curves, a single cell setup with an active area of 50 cm^2 and a serpentine channel flow field structure was chosen. The flow rates of the reactants were controlled using mass flow controllers. The cell temperature was fixed at $160\text{ }^\circ\text{C}$ with the help of electrical heating cartridges and the stoichiometries of the fuel were kept constant at 1.4 for hydrogen (3.0, Westfalen AG) or synthetic reformat (76% H_2 , 1.2% CO and 22.8% CO_2 , Westfalen AG) and 2.0 for air, respectively.

Cycle stability

The cycling was done according to the strategies developed by Reiser et al.^[45] The cell was heated up with heating cartridges to $80\text{ }^\circ\text{C}$ and purged with air for 5 min on the cathode. The next step consisted of heating the cell to a temperature of $120\text{ }^\circ\text{C}$, while the anode was purged with nitrogen for 1 min. When hydrogen and air were present, the cell was heated up to the operating temperature of $160\text{ }^\circ\text{C}$. At this temperature, the cell voltage at a current density of 0.50 A cm^{-2} was recorded and fixed for 4 h. In the shut-down period, the current density was decreased to 0.25 A cm^{-2} while cooling the cell to $120\text{ }^\circ\text{C}$ by switching off the heating cartridges. Current was switched off and the anode was purged with nitrogen. Afterwards, the cell was cooled to room temperature and this procedure was repeated for several cycles.

Degradation at long term operation under constant load

Long term operation under constant load was conducted at a current density of 0.2 A cm^{-2} at 160°C . On the anode side, the single cell was fed with pure hydrogen whereas the stack was fuelled with reformed methanol (stoichiometry 1.4), on the cathode side always air was supplied (stoichiometry 2.0). Due to a different test equipment for the degradation tests a different gas composition was used compared to the polarization measurements. The gas composition, determined by gas chromatographic measurements, was 21.0% CO_2 , 64.0% H_2 , 14.5% H_2O and 0.5% CO . No methanol was detected.

8.3 Results and Discussion

8.3.1 Structural Analysis

8.3.1.1 Morphology and elemental composition

To study the redistribution of elements in an MEA during fuel cell operation we analyzed the elemental distribution of the components of our MEA before and after different modes of operation (see Table 8.1). The SEM micrograph in Figure 8.1 shows a cross-section of the ready-to-use MEA (sample MEA I). The cathode is located on the left side, in the middle is the proton exchange membrane and to the right the anode. Via EDS elemental mapping the distribution of the elements C, O, P, W and Pt was analyzed.

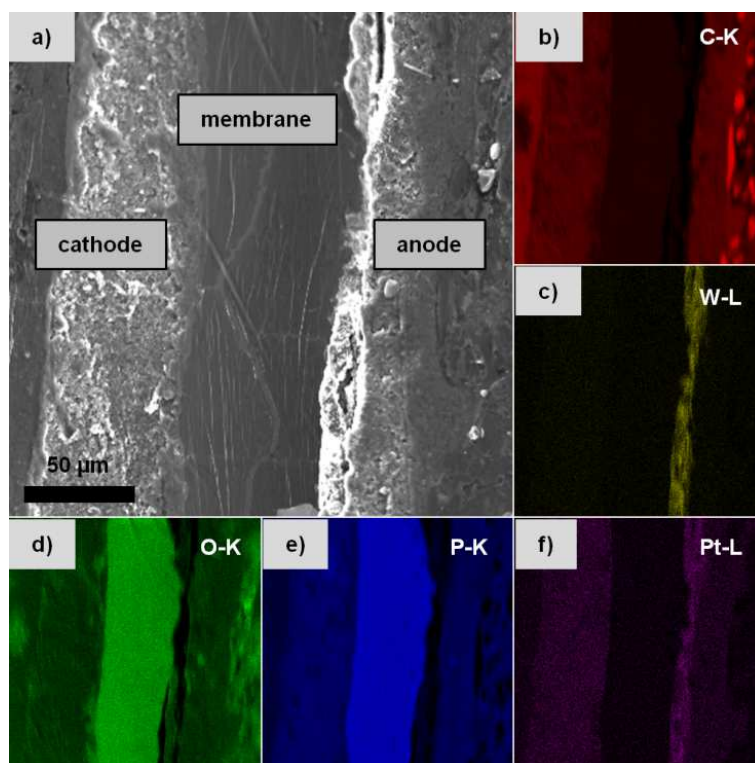


Figure 8.1: Cross-sectional SEM micrograph of a ready-to-use MEA (sample MEA I). The corresponding elemental maps obtained by EDS are also shown.

As can be seen in Figure 8.1b), a high amount of C is detected at the cathode electrode and the adjacent micro porous layers which is due to the presences of HSAC based catalyst supports in the cathode and pure carbon in the micro porous layers, respectively. Since the incorporated proton exchange membrane is a PBI based membrane, C can also be found in this region. On the anode side a band with a thickness of about 20 μm where mostly W can be detected is found which corresponds to the WO_{3-x} based catalyst support material. The detected amount of O in this region is very small. This can be explained by the absorption of low energy X-rays in this high density material. That is why the signal of most of the X-rays of the light elements like C, O and P is low at this region. This circumstance is also present in the EDS line scans shown later (Figure 8.2). During the MEA fabrication the electrodes were doped with phosphoric acid and finally hot pressed with the membrane. In this process the phosphoric acid is absorbed by the proton exchange membrane which leads to a strong increase in its proton conductivity. Therefore P and O are mainly detected in the membrane region which has a thickness of about $65 \pm 2 \mu\text{m}$, as can be seen in Figure 8.1 d) and e). Pt is present in both electrode areas (Figure 8.1 f)). On the cathode the Pt is distributed

homogeneously over the whole electrode. However, at the anode side the concentration of Pt is highest directly at the area which contains WO_{3-x} .

After studying the elemental distribution in the ready-to-use MEA, we compared the elemental distribution of the differently operated and the ready-to-use MEA via EDS line scans. Several measurements have been performed from which one line scan of each MEA is shown exemplarily (Figure 8.2). These measurements have revealed that the W rich areas have an inhomogeneous thickness within each sample which varies between 14 μm and 36 μm . However, related to the total length of the electrodes all W rich areas have an average width of $22 \pm 7 \mu\text{m}$ which is not markedly changing during operation. In Figure 8.2 only the X-rays associated with Pt-L, W-L and P-K are shown. Since the fluorescence yield for light elements is low and X-rays of C-K and O-K can be easily absorbed in the sample these data are omitted.

The EDS line scan of the ready-to-use MEA I (Figure 8.2 a)) exhibits the same elemental distribution as already described in the EDS map in Figure 8.1. The membrane of MEA I, located between the electrodes, contains a high amount of P, but no Pt. P is stemming from the doping with phosphoric acid which guarantees proton conductivity during fuel cell operation. The concentration of P within the MEA is constant in the center of the membrane and has a maximum value at the interfaces of the membrane and the electrodes. In all EDS line scans the P concentration is lowest at the location of the WO_{3-x} based anode (Figure 8.2). Again, the dense WO_{3-x} can absorb the X-ray signals emitted by the lighter P, explaining this phenomenon. A rather high amount of P is observed in the HSAC and the C-based regions of both electrodes. This is related to the fabrication process described above. The detected amount of Pt (ten times magnified) in the cathode (left) of MEA I is larger than the amount of Pt in the anode (right) (Figure 8.2). This is reasonable and done deliberately in the manufacturing process of the MEA since the water which is produced during fuel cell operation at the cathode side might wash out a part of the Pt catalyst.

In Figure 8.2 b) the EDS line scan of MEA II which was operated continuously for nominal 600 h is shown. Via the distribution of P the membrane can easily be located. Here, the membrane has a reduced thickness of about $46 \pm 2 \mu\text{m}$ which might be due to the assembly into a test fuel cell or due to degradation of the PBI. In the electrodes the P

distribution shows some variation that might be attributed to the preparation method of the SEM cross-section. During the wet grinding the introduced phosphoric acid can be washed out of the MEA. Nevertheless, this can happen for all discussed samples. The Pt loading of the cathode shows a broader distribution compared to the one of the ready-to-use MEA I. This indicates that part of the Pt moved towards the gas diffusion electrode. A small amount of Pt can also be found in the membrane area directly next to the cathode and is therefore lost for the catalytic reaction. On the anode side small amounts of Pt also diffuse away from the membrane electrode interface into the electrode. Nevertheless, it can be observed that most of the contained Pt is still located at the W rich region.

The distribution of the elements for MEA III is presented in Figure 8.2 c). After nominal 2000 h of continuous operation the membrane shows a thickness of about $46 \pm 2 \mu\text{m}$ and thus has not decreased in thickness any further. The diffusion of Pt from the cathode into the membrane is stronger than it was observed for MEA II. On both electrodes a higher loss of Pt compared to sample MEA II was found. When comparing the standard carbon cathode with the WO_{3-x} based anode, the Pt concentration at the membrane electrode interface is higher at the anode, even after nominal 2000 h of operation.

Figure 8.2 d) displays the elemental distribution in MEA IV, which was operated for 300 h in start-stop cycles. The abrupt temperature changes in the system strongly induce mechanical stress in the MEA. Due to high cathode potentials, which occur during this test protocol, the amount of Pt, which diffused from the electrode into the membrane, is higher than for sample MEA II and MEA III. As in all samples so far, this effect is stronger at the cathode side rather than at the anode side in agreement to literature results. The thickness of the membrane did not change compared to MEA II and MEA III. In the shown EDS line scan two separated regions at the anode, containing W can be seen. Most likely the anode was damaged during the SEM sample preparation. Nevertheless, this measurement demonstrates the correlation of the elements Pt and W, showing that Pt is strongly bound to the WO_{3-x} support.

The distribution of C and O (not shown here) strongly correlates in the three operated MEAs. This indicates a partial oxidation of the carbon present in the electrodes during the fuel cell operation. Our EDS analyses indicate that the Pt binds more strongly to

tungsten oxide compared to C based materials even after different modes of operation. The W rich regions in all MEAs reveal a high value of Pt and only a relatively weak Pt diffusion from this area into the membrane is detected. In contrast, on the cathode side a high amount of Pt is observed in the adjacent membrane after fuel cell operation.

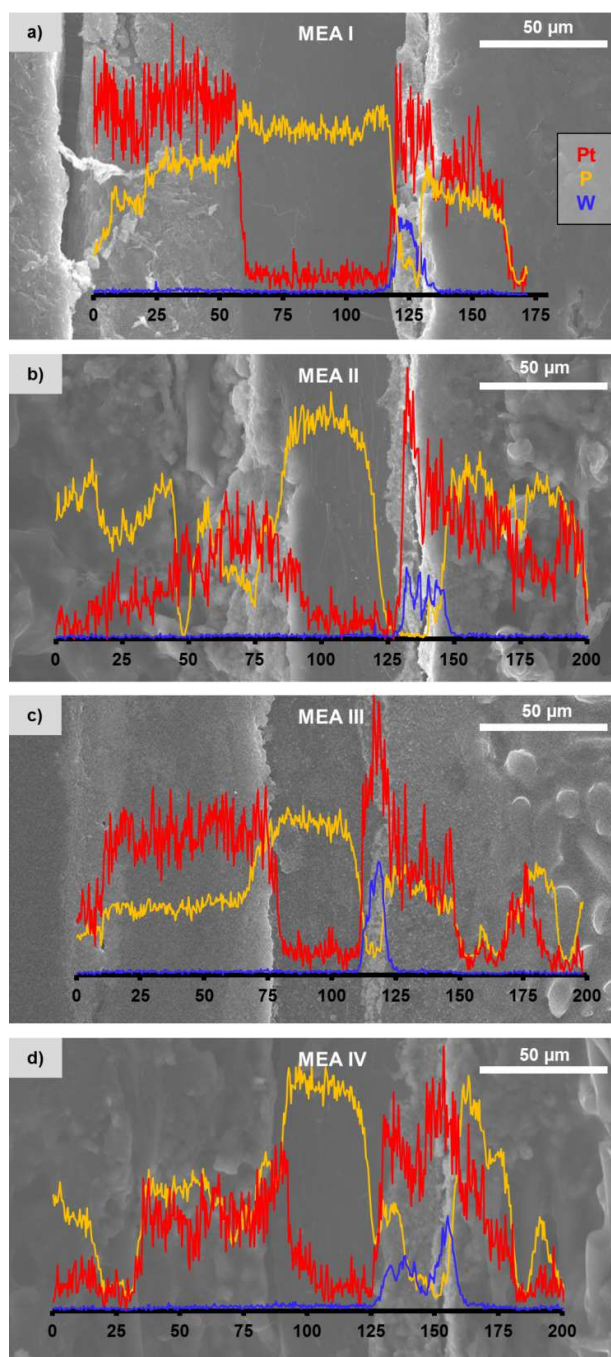


Figure 8.2: SE images and correlated EDS line scans of the four MEA samples. The elemental distribution of the elements Pt (red, magnified ten times), P (orange) and W (blue) are shown for the ready-to-use MEA (a), after continuous operation for nominal 600 h (b), after continuous operation for nominal 2000 h (c) and after start-stop operation (d).

The WO_{3-x} based anode was also analyzed separately in the SEM before it was used for MEA fabrication. Figure 8.3 shows a representative SEM top view micrograph of the ready-to-use anode surface. The rough surface observed in Figure 8.3 a) consists of WO_{3-x} grains which are covered homogeneously with bright octahedral features. The size of the WO_{3-x} grains is between $0.2\text{ }\mu\text{m}$ and $1.0\text{ }\mu\text{m}$ while the octahedrons have a size of about $1.1 \pm 0.3\text{ }\mu\text{m}$. One of the bright octahedrons is shown in detail in Figure 8.3 b), which reveals a porous morphology but also defined, planar surfaces, edges and corners. Via EDS measurements these structures were proven to be pure Pt. The presence of these Pt structures, tightly bound to the WO_{3-x} surface, explains the Pt distribution behavior observed in the EDS line scans. The superordinate Pt structures are only formed on the surface of the tungsten oxide based anode while deeper inside the anode there is not enough space provided to form these several micrometer large structures. During the subsequent production process of the MEAs the anode is pressed with the surface first to the membrane, so the superordinate structures are located at the interface between anode and membrane. Since a considerable amount of Pt is present in these superordinate structures the Pt distribution curves of the EDS line scans exhibit a high value at the aforementioned interface.

Usually the desired morphology of the introduced catalyst in HT-PEMFC is in the form of nanoparticles with sizes of only few nanometers. Due to their small size, the nanoparticles have a highly favorable surface to volume ratio and exhibit therefore a large catalytic active surface area. As can be seen later, the MEAs with the WO_{3-x} based anode containing Pt octahedrons still perform reasonably well. Due to the porous morphology the free-standing surface area of the Pt octahedrons, consisting of nanorods, seems to be large enough so that the majority of the Pt can be utilized in the catalytic process. The formation of these Pt structures is not part of the present study and will be addressed in a future work.

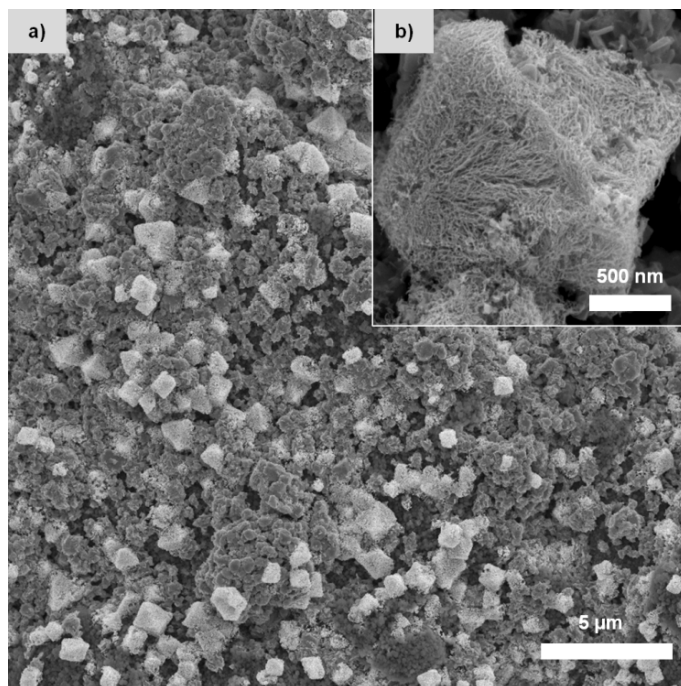


Figure 8.3: SEM top view image of the ready-to-use WO_{3-x} anode. a) The electrode surface consisting of WO_{3-x} crystals is homogeneously covered with bright octahedral features. b) Detailed view at one bright feature which is built of a porous network of Pt nanorods.

8.3.1.2 Crystallinity analysis

The differently operated MEAs were further analyzed using XRD. The XRD patterns of the ready-to-use MEA I, the nominal 600 h operated MEA II, the nominal 2000 h operated MEA III and the start-stop cycle operated MEA IV are given in Figure 8.4. The 2θ Bragg reflexes at about 46.7° , 54.5° , 80.5° , 98.6° and 104.8° correspond to the reflections of face-centered cubic Pt(111), Pt(200), Pt(220), Pt(311) and Pt(222), respectively.^[49] In addition the reflexes of the contained WO_{3-x} are observed. The d -values correspond to several monoclinic phases with a stoichiometry varying between WO_3 and $\text{W}_{18}\text{O}_{49}$. Due to this and the fact that our electrode is conductive we chose as chemical formula WO_{3-x} throughout the manuscript.

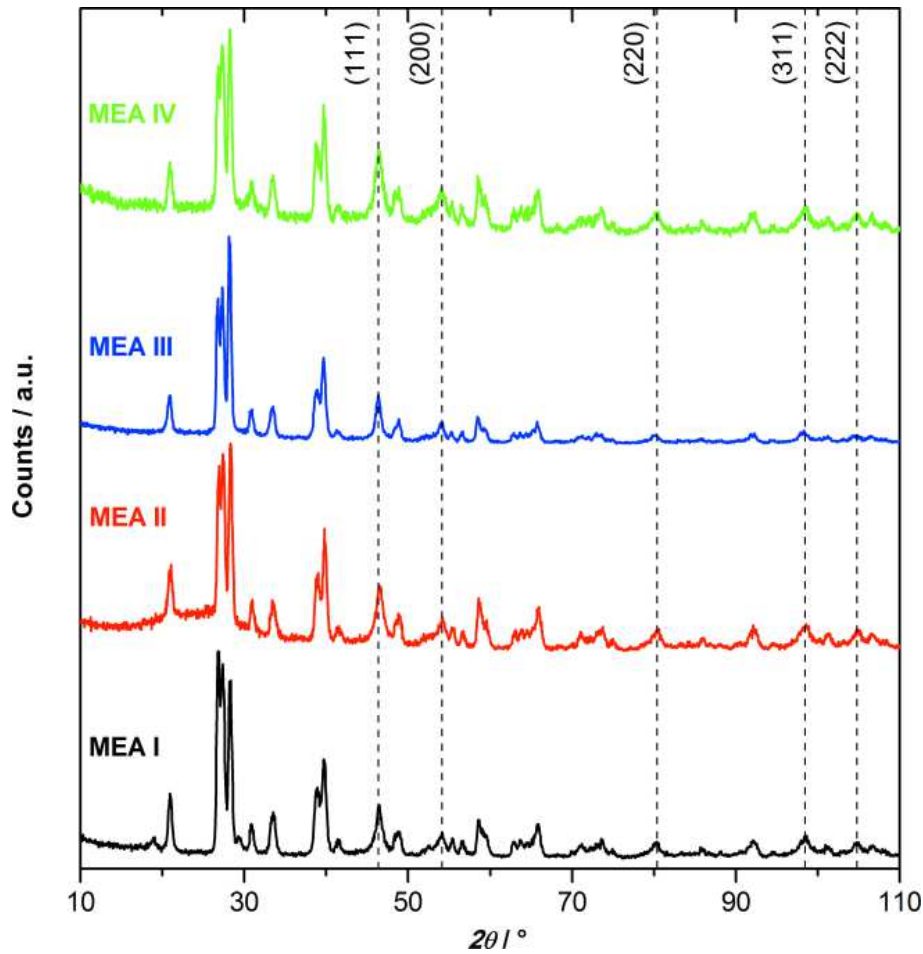


Figure 8.4: Comparison of the X-ray diffractograms of the investigated MEAs. The face-centered cubic reflections of Pt are marked with dashed lines. The remaining reflexes originate from WO_{3-x} .

By using the Scherrer equation the average size of the crystalline Pt catalyst particles was determined assuming a spherical shape.^[48] The experimental error of $\Delta 2\theta$ was 0.1° . The obtained crystallite sizes are presented in Table 8.2 and compared to the Pt catalyst sizes determined by TEM analysis. For the ready-to-use MEA I an average Pt particle size of about 10.5 ± 1.1 nm was calculated. In the course of continuous fuel cell operation the overall crystallite particle size usually increases. During operation the particles tend to grow together via coalescence or an Ostwald ripening process.^[50] This was indeed observed for MEA III after nominal 2000 h of operation where Pt particles with a mean diameter of 13.3 ± 1.7 nm occur. However in the nominal 600 h operated MEA II the catalyst exhibits particle sizes in the range of 9.5 ± 0.9 nm. This decrease is unexpected but was also observed in the TEM analysis (see below). It seems that the Pt octahedra partly dissolve in the first hundred hours of operation. The crystallite size of 9.1 ± 0.8 nm for the start-stop cycle operated MEA IV is about the same as for the

nominal 600 h operated MEA II, thus also smaller than expected. Nevertheless, one has to consider that by applying the Scherrer equation for X-ray measurements only average values of the size of the diffracting crystals can be obtained. As can be seen in the TEM micrographs shown later, the Pt catalyst exhibits different morphologies in the MEAs operated for different times or modes. Therefore the XRD results only give a trend about the development of the Pt catalyst size in the course of operation.

Table 8.2: Summary of the Pt catalyst particle size obtained by XRD and by TEM. The sign “-” stands for not detected, the sign “*” for data which did not allow a quantitative size determination.

Sample	Average crystallite size of Pt catalyst particles determined by XRD / nm	Average width and length of Pt rods determined by TEM / nm	Average size of spherical Pt particles on C based material determined by TEM / nm	Average size of spherical Pt particles in the membrane determined by TEM / nm
MEA I	10.5 ± 1.1	7.3 ± 1.5 // 36.0 ± 9.2	-	-
MEA II	9.5 ± 0.9	5.1 ± 0.8 // 24.5 ± 6.3	10.0 ± 3.4	5.4 ± 0.7
MEA III	13.3 ± 1.7	8.5 ± 1.7 // 25.0 ± 6.2	12.5 ± 3.8	2.9 ± 0.5
MEA IV	9.1 ± 0.8	*	7.1 ± 1.9 and agglomerates	3.7 ± 0.5

8.3.1.3 In-depth TEM investigation

TEM measurements were performed to obtain information on degradation processes that take place during fuel cell operation at the nanoscale. As mentioned above, the focus of the TEM investigation was laid on the anode as well as the membrane side. We investigated in detail the WO_{3-x} and C based areas and the Pt particles located in the anode as well as the membrane before and after the different types of fuel cell operation. Figure 8.5 shows exemplarily one of the FIB lamellae that were investigated. The micrograph was taken in HAADF STEM mode. In this mode of operation the measured intensity is proportional to Z², the square of the atomic number of each element in the sample. The colored squares in Figure 8.5 highlight the MEA components of interest. The anode is built up of a C based micro porous layer (MPL, area marked by a green square) and WO_{3-x} (blue square) which is used as support material for the Pt catalyst (red square). The membrane (yellow square) is composed of PBI and impregnated with

phosphoric acid. These different areas will be separately described for the four different MEAs.

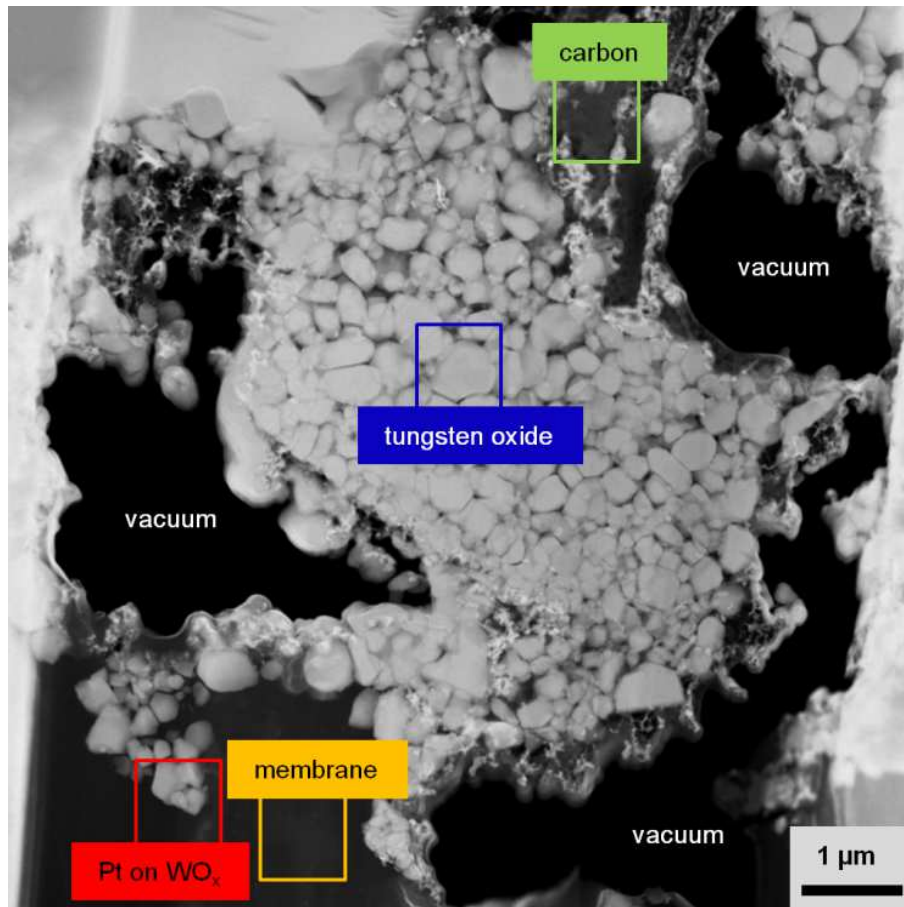


Figure 8.5: Overview STEM micrograph of the anode area of one of the FIB lamellae that were investigated via TEM (sample MEA I). The colored squares highlight a carbon based area (green), WO_{3-x} grains (blue), a Pt catalyst structure (red) and the membrane (yellow). The areas labeled “vacuum” are regions where material was completely removed or broke off during FIB sectioning.

Figure 8.6 shows micrographs of WO_{3-x} based areas of MEA I (a), MEA II (b), MEA III (c) and MEA IV (d). As already seen in the SEM measurements, the WO_{3-x} forms grains with sizes of up to 1 μm. Before fuel cell operation two morphologies of these grains were observed: in some areas WO_{3-x} forms loosely arranged, rounded grains, in other sections densely packed, faceted grains could be found (Figure 8.6 a)). After fuel cell operation only loosely arranged assemblies of rounded WO_{3-x} grains were observed (Figure 8.6 b) – d)). Since hydrogen spill over and good electrical connection between Pt and WO_{3-x} are attributes of the used anode and catalyst material, a high contact area between Pt and the support material WO_{3-x} is crucial. Besides in the octahedral Pt structures

described above, further Pt catalyst material could be found between loosely arranged grains (Figure 8.6 b)-d)). No Pt was detected between the mosaic-like assemblies, probably because there is not enough space provided.

ED measurements reveal that the WO_{3-x} grains are single crystalline. On the bottom right corner of Figure 8.6 a) an ED pattern is displayed which was taken in $[-2-32]$ zone axis.

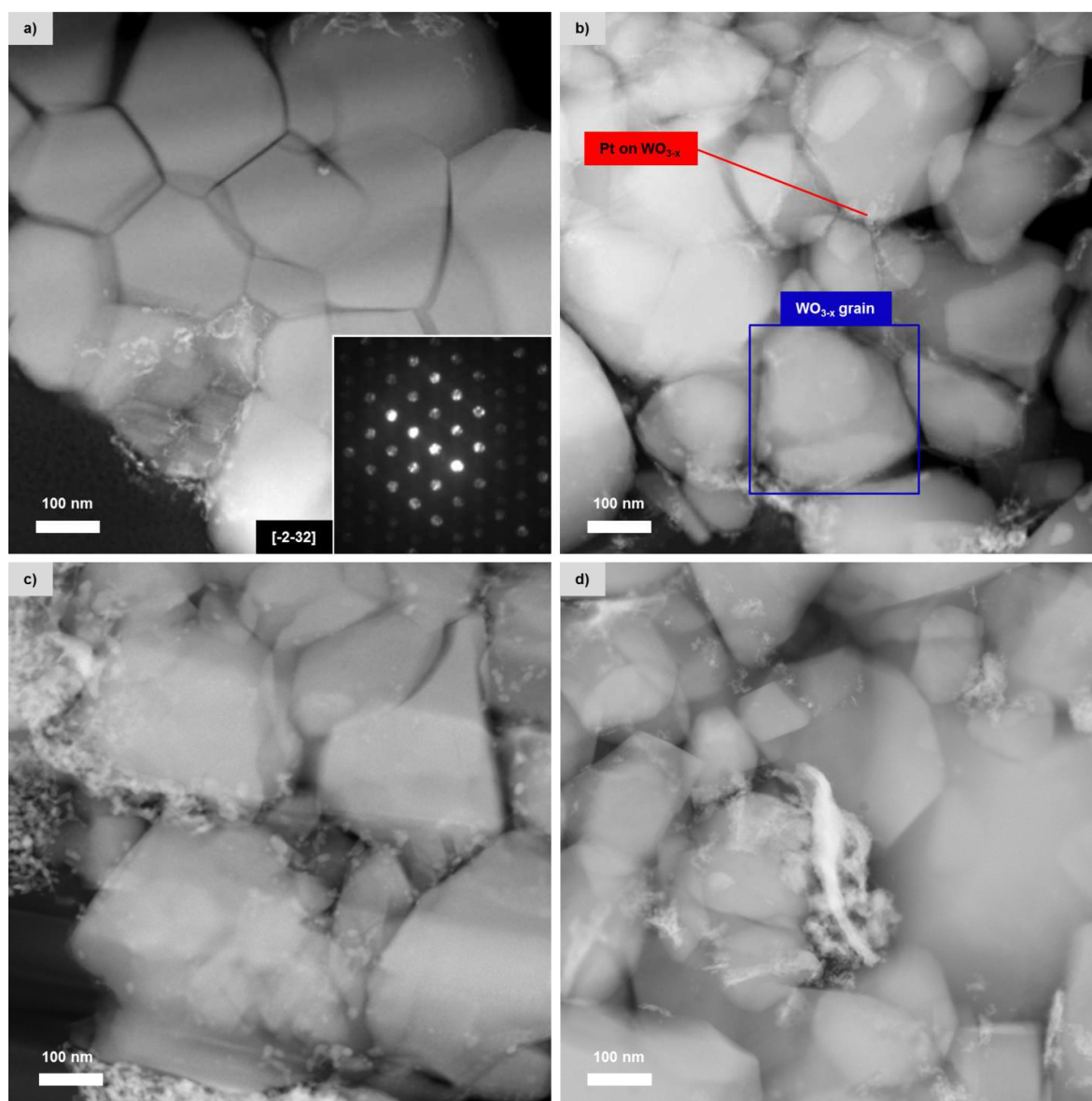


Figure 8.6: STEM images of WO_{3-x} based areas of: a) MEA I, b) MEA II, c) MEA III, d) MEA IV. In a) in addition an ED pattern of one grain is given.

EELS measurements of the WO_{3-x} grains were performed to examine a possible change of the oxidation state of W due to oxidation during fuel cell operation. This information

can be obtained by analyzing the oxygen K edges at 532 eV which are shown for the four investigated MEAs in Figure 8.7. The data were acquired in the center of the grains.

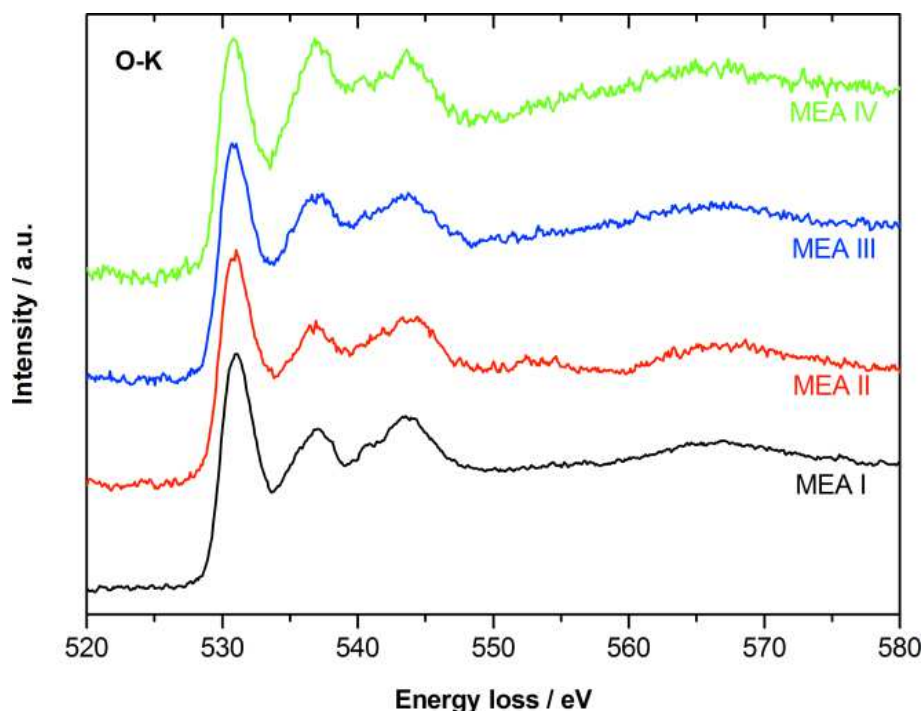


Figure 8.7: O-K EELS spectra of MEA I, MEA II, MEA III and MEA IV, taken in the interior of the WO_{3-x} grains.

All four EELS spectra have an onset of 529 eV followed by a first main peak at 531 eV and two other features at around 537 eV and 545 eV, which is in good agreement with literature.^[51] All EELS spectra exhibit the same features at identical energy loss. This indicates that in all investigated MEAs O and W have the same coordination and most likely oxidation state in the interior of the grain. Since our EELS measurements cover a large internal area of WO_{3-x} it is possible that only the surface of the WO_{3-x} grains change their oxidation state during fuel cell operation. In order to prove this, additional EELS measurements using a monochromator have to be performed, which will be done in future studies. The $M_{4,5}$ ionization edges of W occur at 1872 eV and 1809 eV. The measurement of such large energy losses is difficult since the intensity ratio of characteristic edge and background decreases rapidly with increasing eV. A minor ionization edge of W $N_{4,5}$ appears at energy losses of 245 eV and overlaps with the C-K edge at 284 eV making the analysis more difficult. Therefore, these data are not shown here.

The Pt catalyst octahedrons that have already been discussed in the foregoing SEM investigation were also analyzed via HAADF STEM. In Figure 8.8 one section of these features of each MEA is displayed. These features are only present on WO_{3-x} grains and are exclusively located at the interface between anode and membrane. The elemental composition of these features is pure Pt as was further proven via local EDS measurements in STEM. Having a closer look at the features it can be seen that they are built of elongated, cross-linked Pt crystals. In the upper right corner of Figure 8.8 a) an ED pattern is shown which was acquired at the displayed superordinate catalyst structure. The ED experiments confirmed the presence of polycrystalline, cubic Pt in all MEAs.

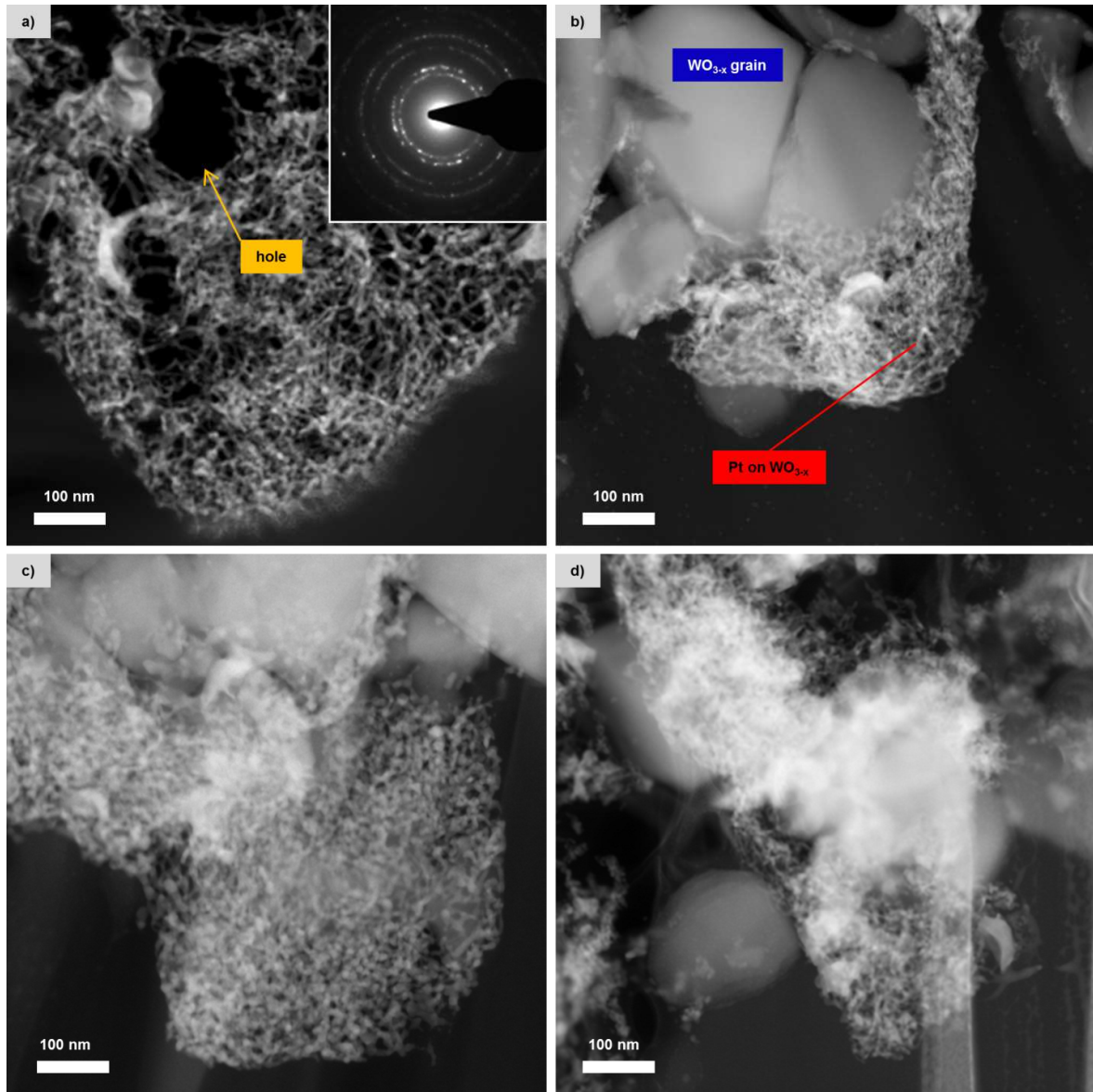


Figure 8.8: Pt catalyst structures at the interface region between anode and membrane of a) MEA I, b) MEA II, c) MEA III, d) MEA IV.

Before operation of the fuel cell system the observed octahedral Pt morphologies are formed by crystalline Pt rods with a diameter in the range of 7.3 ± 1.5 nm and a length of about 36.0 ± 9.2 nm (Figure 8.8 a)). Some holes are visible in the network which might partly originate from the FIB sample preparation (see arrow Figure 8.8 a)). After an operation time of nominal 600 h and even more after nominal 2000 h the Pt octahedrons are more closely packed. Similar observations were made for MEA IV. Also in MEA IV (Figure 8.8 d)), the edges of the catalyst structure are not smooth anymore which can be caused by disintegration of the Pt network due to the stressful potential

changes. Furthermore after a continuous operation of nominal 600 h the Pt crystals were found to have a reduced width (5.1 ± 0.8 nm) and length (24.5 ± 6.3 nm) compared to MEA I, but with an ongoing operation time (MEA III, nominal 2000 h) they become even thicker than at the beginning (8.5 ± 1.7) while the length remains nearly constant (25.0 ± 6.2 nm) (Table 8.2). The medium width and length of single Pt rods in the catalyst structures of MEA IV could not be measured due to their strongly condensed, interconnected architecture after start-stop cycling which makes it difficult to identify the individual rods. Nevertheless the changes in the width and length of the Pt rods in MEA I – MEA III match the results of the XRD measurements shown earlier. The different values obtained by XRD compared to the TEM results can be explained by the assumption of using spherical particles in the Scherrer equation. In addition, the XRD data are averaging over all catalyst particles – the rods on the tungsten oxide as well as spherical particles on the HSAC – while in TEM we analyzed them separately. Further investigations of the catalyst structures are still subject to ongoing work.

C based areas in the anode are also exposed to degradation during fuel cell operation. In Figure 8.9 C based areas of the four investigated MEAs are displayed. Since these areas were visualized by applying conventional TEM a different contrast compared to measurements in the HAADF STEM mode is obtained. Having a closer look at the series that is displayed in Figure 8.9 C based areas with Pt particles can be seen. The C material exhibits holes. Presumably these holes mark areas where WO_{3-x} grains have been located before they were removed during the preparation of the FIB lamellae. The dark areas are Pt particles. Before fuel cell operation large areas of C are free of Pt and only areas in close vicinity to WO_{3-x} are loaded with the catalyst (Figure 8.9 a)). Before operation Pt is mostly present in form of elongated crystals like the ones that form the three dimensional network, as discussed above. In contrast to MEA I the C based areas of MEA II, MEA III and MEA IV are increasingly covered with Pt. Here Pt is present in the form of individual nanoparticles possessing a spherical shape. After an operation time of nominal 600 h these nanoparticles exhibit an average diameter of 10.0 ± 3.4 nm. With an ongoing fuel cell operation the nanoparticles still grow to a size of 12.5 ± 3.8 nm after a working period of nominal 2000 h. The comparatively large standard deviations of the size of the Pt nanoparticles in MEA II and MEA III illustrate the wide particle size distribution. The operation mode of periodically repeated start-up and shut-down cycles

of the investigated fuel cell system (MEA IV) leads to the formation of large agglomerates in the range of up to several 100 nm (Figure 8.9 d)). In addition individual small spherical nanoparticles with an average diameter of 7.1 ± 1.9 nm are also present. Different Pt degradation mechanisms on C material during fuel cell operation have been studied elsewhere in literature^[52] and are only minor subject to the work in hand. Nevertheless it seems that part of the Pt, which is in the beginning located in the superordinate structures, is diffusing onto the contained C during operation.

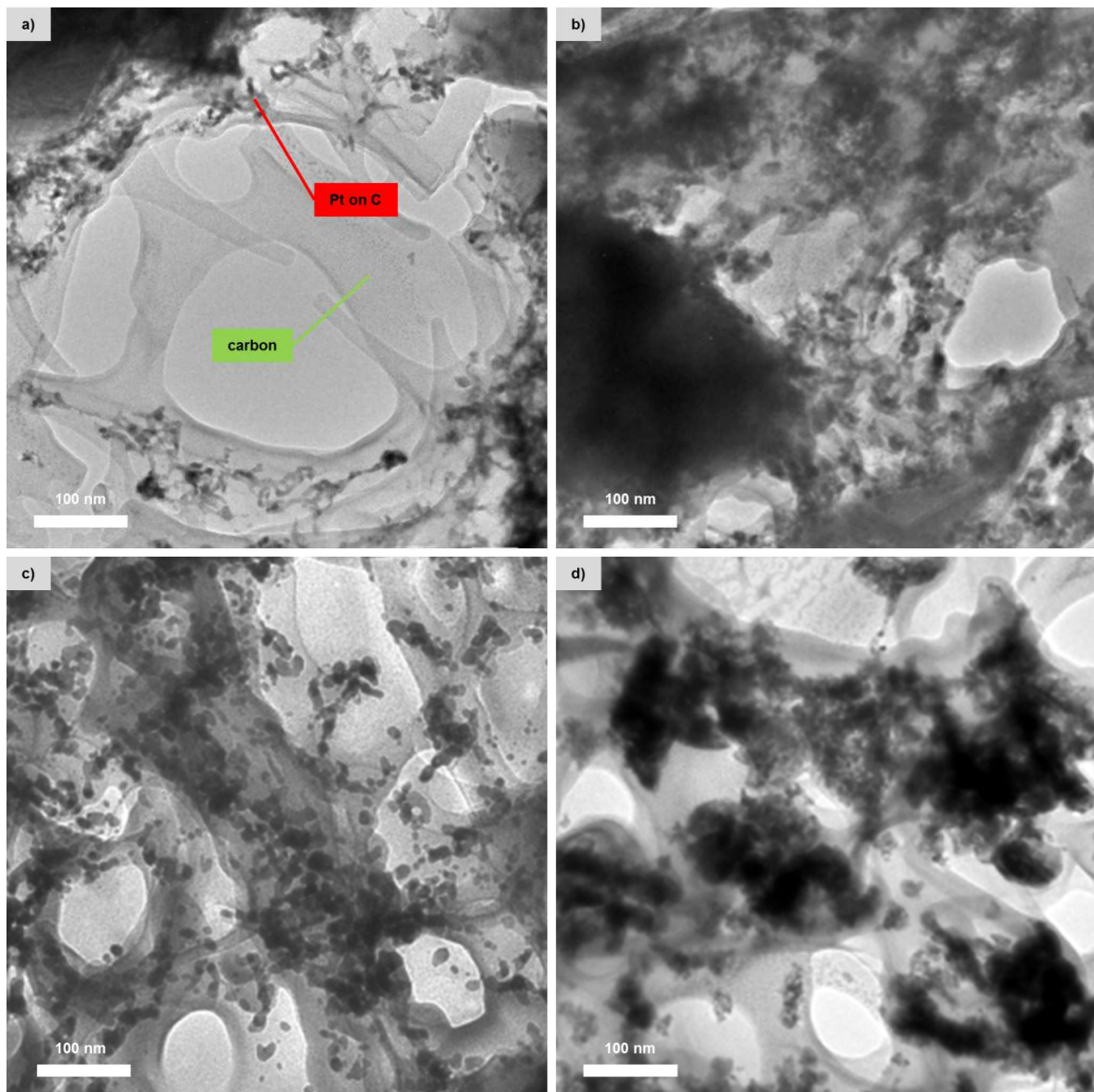


Figure 8.9: Carbon based areas in the anode of a) MEA I, b) MEA II, c) MEA III, d) MEA IV.

Another important fuel cell component which is subjected to degradation in the course of operation is the proton exchange membrane. In Figure 8.10 areas of the membrane

before (a) and after (b)-d)) fuel cell operation are displayed. All shown HAADF micrographs were recorded at positions having about the same distances from the membrane anode interface. The absolute penetration depth of Pt into the membrane could not be determined, since the FIB lamellae are thin enough for TEM analysis only for a finite length. The PBI based membrane itself is amorphous and therefore shows constant contrast in the TEM images.^[53] The bright area in the upper part of Figure 8.10 a) is WO_{3-x} which is located close to the membrane. The dark spot in Figure 8.10 d) is a hole in the membrane that was caused by electron beam damage. As discussed above in the SEM investigations, Pt can be found in the membrane material after fuel cell operation. The bright spots in Figure 8.10 b) – Figure 8.10 d) are Pt nanoparticles. This was proven via high resolution TEM and EDS measurements as well as ED. The inset in Figure 8.10 b) shows a higher magnification high resolution TEM (HRTEM) image of a Pt particle. The distances of the visible atomic planes are $2.24 \pm 0.03 \text{ \AA}$ and match (111) hkl values of cubic Pt.^[49] Diffraction experiments reveal diffraction patterns equivalent to the one that is shown in Figure 8.8 a). Furthermore the diameter of the Pt nanoparticles within the membrane was measured. After an operation time of nominal 600 h (MEA II) the nanoparticles exhibit an average diameter of $5.4 \pm 0.7 \text{ nm}$ which decreases in size with ongoing fuel cell operation. After nominal 2000 h (MEA III) Pt particles in the range of $2.9 \pm 0.5 \text{ nm}$ can be found. The decrease in size of the nanoparticles can be explained by a periodical dissolution and precipitation of the catalyst in the course of redox reactions within the PBI membrane. In 2005 Xie et al.^[24] postulated an oxidation of Pt to form PtO due to the presence of water, which is then dissolved in the acidic solution of the cell. Periodically repeated start-up and shut-down cycles result in nanoparticles with an average size of $3.7 \pm 0.5 \text{ nm}$. The result of the TEM particle size determination is summarized in Table 8.2. Comparing the total amount of Pt diffused into the membrane it is highest in MEA IV (Figure 8.10 d)). This type of accelerated lifetime test seems to put the highest stress on the Pt catalyst.

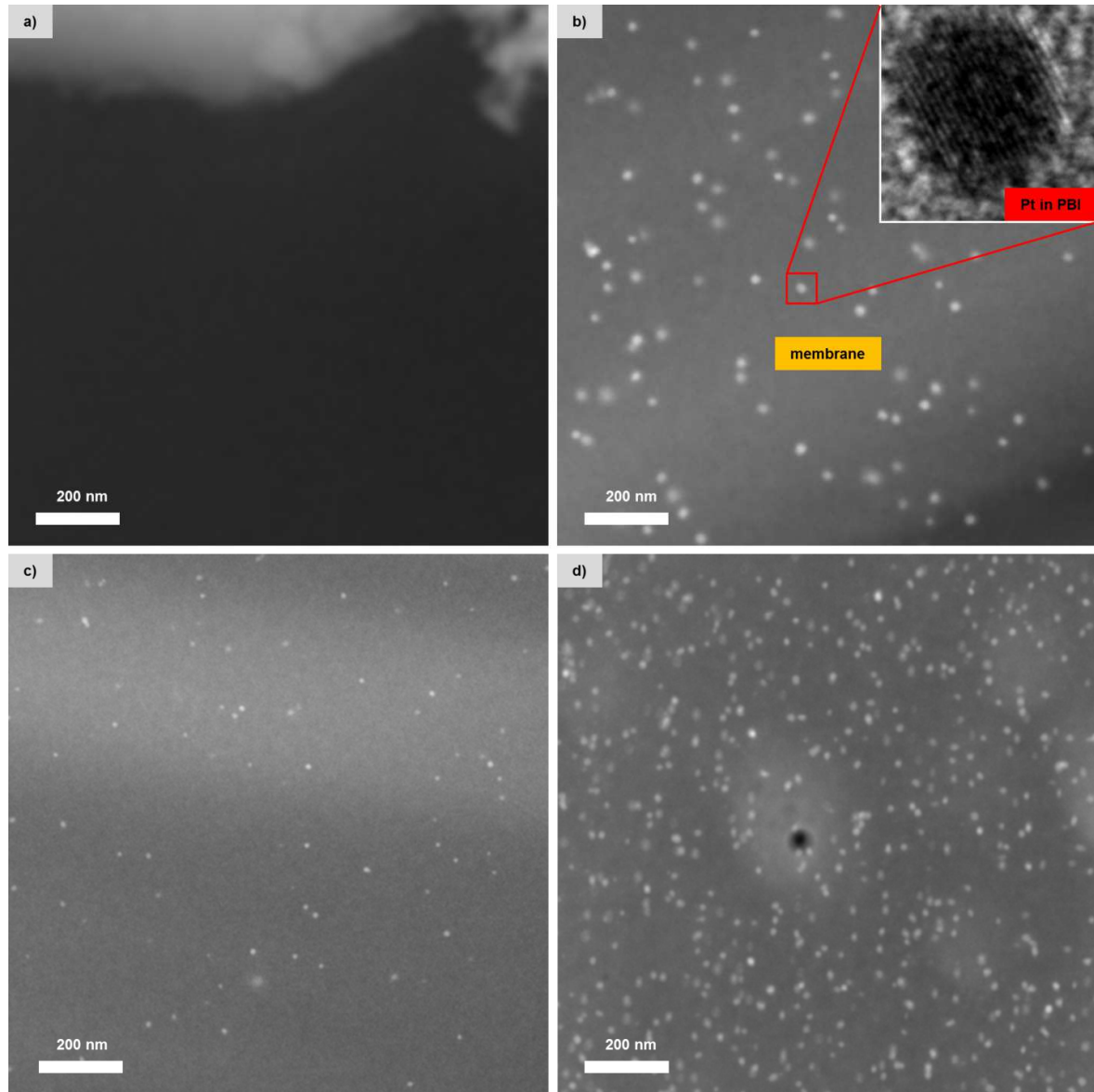


Figure 8.10: STEM HAADF micrographs of the proton exchange membrane of: a) MEA I, b) MEA II, c) MEA III, d) MEA IV. The inset in b) shows a HRTEM image of an individual Pt particle.

8.3.2 *In-situ* MEA properties

8.3.2.1 Polarization curves

The polarization curves in Figure 8.11 show the voltage of the four investigated MEAs as well as a standard HSAC based MEA in dependency of current density. The performance tests were done with synthetic reformat on the anode with a CO content of 1.2%. This leads to an anode overvoltage of approximately 20 mV. An equivalent ideal phosphoric acid doping level was determined for all samples. Even though the open-circuit voltage (OCV) indicate that no short circuits and electrical losses are present, the performance of

MEA I is 10 mV lower compared to the HSAC based reference MEA. This can be explained by a slightly higher ohmic resistance of MEA I due to the use of WO_{3-x} . For MEA IV the OCV is lowered due to the start-stop cycling from 910 to 890 mV. Regarding the polarization curve of MEA II the cell voltage at 20% of the maximum current density shows a decrease from 590 to 570 mV, compared to MEA I. This correlates to the cell voltage behaviour during the long term test (Figure 8.12). After the nominal 2000 h stack test (MEA III), the corresponding polarization curve shows an increase in the slope in the ohmic region. The increase of the ohmic resistance at the anode side of the WO_{3-x} based MEAs is one reason for the lowering of the overall cell performance.

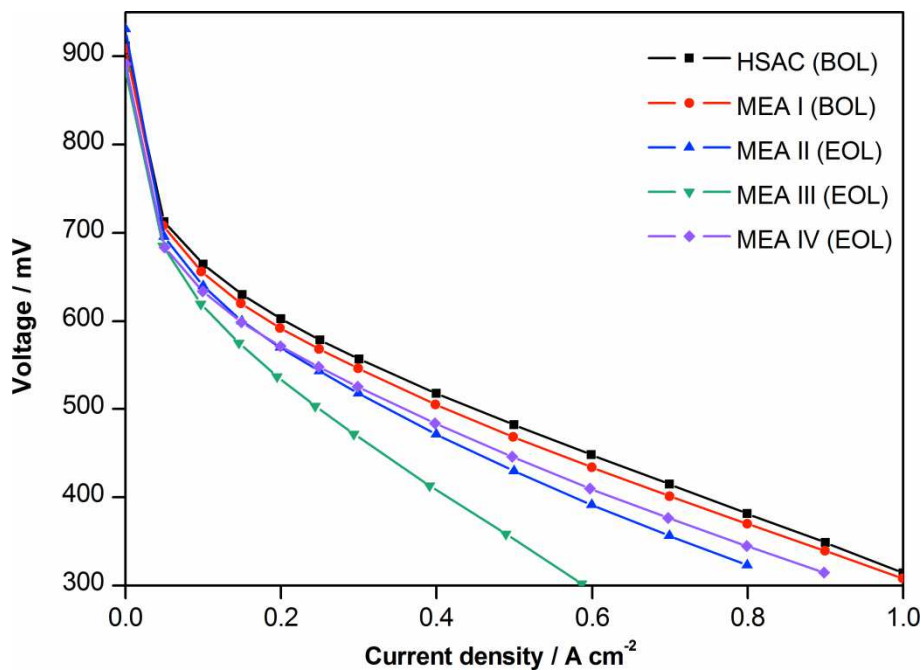


Figure 8.11: Polarization curves with synthetic reformat of MEAs with WO_{3-x} as catalyst support material on the anode after different fuel cell tests and in comparison to a HSAC based MEA.

8.3.2.2 Start-stop cycling

Accelerated stress tests of the WO_{3-x} based MEA were done via start-stop cycling under fuel cell conditions over nominal 300 h for 35 start-stop cycles (MEA IV). During the shutdown of the cell, only air was used on the cathode. Hydrogen was allowed to diffuse out of the cell and was replaced with air. This leads to a long lasting hydrogen air mixing time on the anode and in consequence to a long exposure of the cathode and anode to high potentials. There were no countermeasures in the operation strategy to reduce the humidity on the cathode side. The air supply was switched off only a few seconds after

switching off the current. The degradation rate of MEA IV is 1.1 mV per cycle. In comparison, the calculated cycle degradation rate for the standard HSAC based MEA is 2.3 mV. By using WO_{3-x} the cycle loss was reduced by 48% compared to standard HSAC.

8.3.2.3 Long-term fuel cell operation

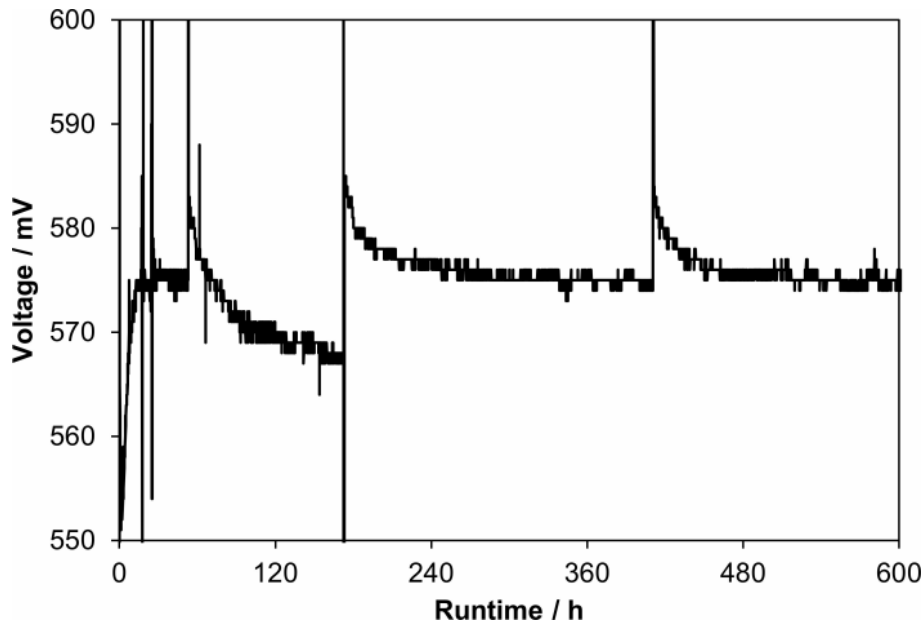


Figure 8.12: MEA II: nominal 600 h test at constant current density in a 50 cm² single cell with pure hydrogen.

In Figure 8.12 a nominal 600 h single cell test with pure hydrogen is shown. A large cell voltage increase was gained at the shutdown at 170 h, which is currently under investigation. A reason for this increase could be a partly incorporation of Pt into the WO_{3-x} layer as was observed by the TEM investigations. After running up the system again a 50 h lasting conditioning time occurs. Afterwards the cell voltage stabilizes at 574 mV and no further pronounced degradation is visible. Compared to a stack test with a standard HSAC based MEA the here investigated MEA containing WO_{3-x} shows a slightly lower performance. The difference in the corresponding cell voltages is in the range of 10 mV.

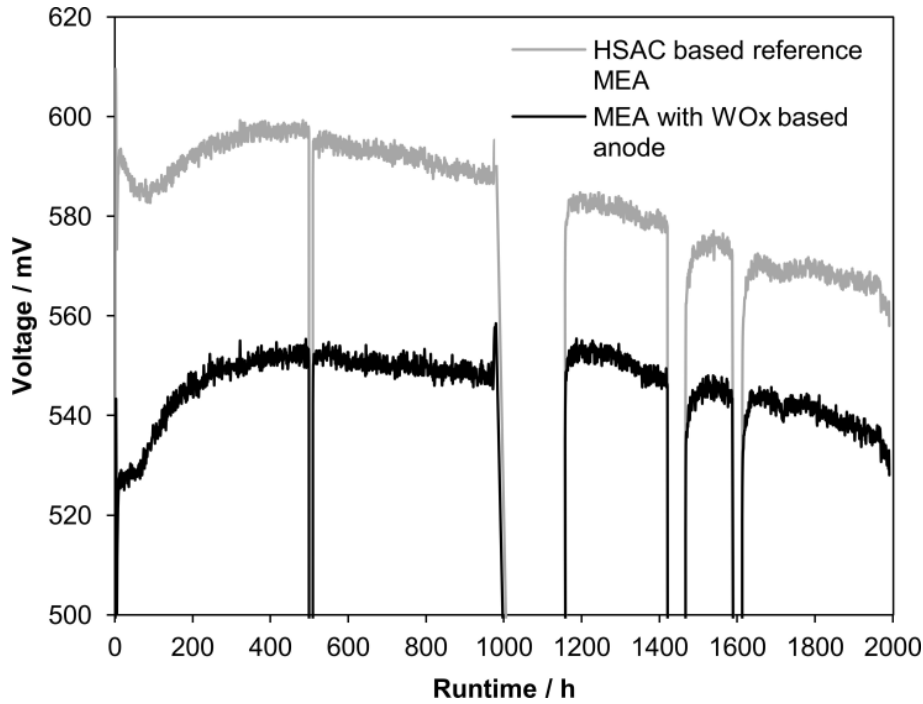


Figure 8.13: Cell voltage during a nominal 2000 h stack test of MEAs with WO_{3-x} based anodes and HSAC based reference MEAs.

In Figure 8.13 the cell voltages during the nominal 2000 h stack test of WO_{3-x} containing MEAs (MEA III) in comparison to HSAC based MEAs are shown. The lower performance of the WO_{3-x} containing MEAs can be explained by the fact that reformed methanol was used for the stack test instead of pure hydrogen. Compared to the single cell test (Figure 8.12) the performance of WO_{3-x} containing MEAs in the stack test was reduced. At the peak power after 450 h a voltage difference of 40 mV between HSAC based MEAs and WO_{3-x} containing MEAs occurred. Nevertheless this difference decreased to 30 mV after nominal 2000 h of stack operation, including four test rig related shutdowns. The reduced slope indicates that the degradation rate of WO_{3-x} based MEAs is slightly lower compared to the standard HSAC based MEAs. We expect that for longer operation times and a high number of start-stop cycles the WO_{3-x} based MEA outperforms the standard HSAC based MEAs.

8.4 Summary and Conclusion

In this paper the morphology, the elemental distribution and the performance of Pt loaded WO_{3-x} based anodes for HT-PEMFCs were analyzed after different operation

modes and times. HT-PEMFCs with WO_{3-x} as catalyst support material on the anode, a standard HSAC based cathode and a PBI based membrane were manufactured and studied *ex-situ* via several electron microscopy based methods like SEM, STEM, EDS, ED and EELS. The MEAs were investigated before operation, after nominal 600 h of continuous operation in a single cell test, after nominal 2000 h of continuous operation in a fuel cell stack test and after nominal 300 h of start-stop cycle operation. The variation of the elemental distribution in the MEAs was analyzed via EDS line scans in the SEM. The diffusion of Pt into the membrane and away from the electrodes was observed. Furthermore the crystallinity of the components in the MEAs' anodes was analyzed via XRD. The development of the size of the crystalline Pt catalyst particles was revealed by applying the Scherrer equation and compared to the sizes obtained by TEM measurements. In contrast to conventional HT-PEMFC electrodes where the Pt catalyst forms spherical particles in the size of only few nanometers, here the Pt forms up to about 1 μm large, three dimensional networks of few nanometer thin, crystalline Pt rods on the WO_{3-x} grains. The thickness of the Pt rods building this network changes with ongoing operation time and Pt diffuses onto the C based areas of the anode. The WO_{3-x} grains are single crystalline and form mosaic-like assemblies which get more rounded and show small Pt incorporations after operation. EELS measurements in the interior of the grains revealed that the oxidation state of the W does not change due to the different operation modes in the center of the grain. In the PBI based membrane adjacent to the anode few nanometer small Pt particles were found after operation. The highest amount of Pt in the membrane was found after the start-stop cycling. In addition, *in-situ* measurements like polarization curves, start-stop cycling and long-term fuel cell tests were performed. The performance of the WO_{3-x} based MEAs was found to be slightly below the standard HSAC MEAs due to the higher ohmic resistance of the WO_{3-x} layer compared to HSAC. Nevertheless the degradation due to start-stop cycling of the WO_{3-x} based MEAs is better than the standard HSAC MEAs. Also the nominal 2000 h long-term fuel cell tests showed that the degradation rate of the WO_{3-x} based MEAs is superior and therefore it is supposed that they should outperform the standard HSAC based MEAs with ongoing operation.

8.5 Chapter references

- [1] Nakicenovic, N.; Jefferson, J. M. *International Institute for Applied Systems Analysis* **1995**.
- [2] Carpetis, C. *Deutsches Zentrum für Luft und Raumfahrt (DLR-ITT)* **2000**, STB-Bericht Nr. 22.
- [3] Carrette, L.; Friedrich, K. A.; Stimming, U. *ChemPhysChem* **2000**, *1*, 162.
- [4] Carrette, L.; Friedrich, K. A.; Stimming, U. *Fuel Cells* **2001**, *1*, 5.
- [5] Gang, X.; Qingfeng, L.; Hjuler, H. A.; Bjerrum, N. J. *J. Electrochem. Soc.* **1995**, *142*, 2890.
- [6] Knights, S. D.; Colbow, K. M.; St-Pierre, J.; Wilkinson, D. P. *J. Power Sources* **2004**, *127*, 127.
- [7] Blurton, K. F.; Greenberg, P.; Oswin, H. G.; Rutt, D. R. *J. Electrochem. Soc.* **1972**, *119*, 559.
- [8] Li, Y. M.; Hibino, M.; Miyayania, M.; Kudo, T. *Solid State Ionics* **2000**, *134*, 271.
- [9] Chandan, A.; Hattenberger, M.; El-kharouf, A.; Du, S.; Dhir, A. et al. *J. Power Sources* **2013**, *231*, 264.
- [10] Kinoshita, K. *J. Electrochem. Soc.* **1990**, *137*, 845.
- [11] Li, Q.; He, R.; Jensen, J. O.; Bjerrum, N. J. *Chem. Mater.* **2003**, *15*, 4896.
- [12] Winter, M.; Brodd, R. J. *Chem. Rev.* **2004**, *104*, 4245.
- [13] Meier, J. C.; Galeano, C.; Katsounaros, I.; Topalov, A. A.; Kostka, A. et al. *ACS Catalysis* **2012**, *2*, 832.
- [14] Shao, Y.; Yin, G.; Gao, Y. *J. Power Sources* **2007**, *171*, 558.
- [15] Shao, Y.; Wang, J.; Kou, R.; Engelhard, M.; Liu, J. et al. *Electrochim. Acta* **2009**, *54*, 3109.
- [16] Oh, H.-S.; Lee, J.-H.; Kim, H. *Int. J. Hydrogen Energy* **2012**, *37*, 10844.
- [17] Matthew, M.; Emin Caglan, K.; Veziroglu, N. T. *Polymer Electrolyte Fuel Cell Degradation*; Academic Press: Boston, **2012**.
- [18] Ferreira, P. J.; la O', G. J.; Shao-Horn, Y.; Morgan, D.; Makharia, R. et al. *J. Electrochem. Soc.* **2005**, *152*, A2256.
- [19] Bi, W.; Gray, G. E.; Fuller, T. F. *Electrochem. Solid-State Lett.* **2007**, *10*, B101.
- [20] Péron, J.; Nedellec, Y.; Jones, D. J.; Rozière, J. *J. Power Sources* **2008**, *185*, 1209.
- [21] Aragane, J.; Murahashi, T.; Odaka, T. *J. Electrochem. Soc.* **1988**, *135*, 844.
- [22] Aragane, J.; Urushibata, H.; Murahashi, T. *J. Appl. Electrochem.* **1996**, *26*, 147.
- [23] Shao-Horn, Y.; Ferreira, P.; la O', G. J.; Morgan, D.; Gasteiger, H. A. et al. *ECS Trans.* **2006**, *1*, 185.
- [24] Xie, J.; Wood, D. L.; More, K. L.; Atanassov, P.; Borup, R. L. *J. Electrochem. Soc.* **2005**, *152*, A1011.

- [25] Inzelt, G.; Berkes, B.; Kriston, Á. *Electrochim. Acta* **2010**, 55, 4742.
- [26] Voorhees, P. W. *J Stat Phys* **1985**, 38, 231.
- [27] Wagner, C. *Zeitschrift für Elektrochemie, Berichte der Bunsengesellschaft für physikalische Chemie* **1961**, 65, 581.
- [28] Lifshitz, I. M.; Slyozov, V. V. *J. Phys. Chem. Solids* **1961**, 19, 35.
- [29] Maillard, F.; Schreier, S.; Hanzlik, M.; Savinova, E. R.; Weinkauf, S. et al. *Phys. Chem. Chem. Phys.* **2005**, 7, 385.
- [30] Cherstiouk, O. V.; Simonov, P. A.; Savinova, E. R. *Electrochim. Acta* **2003**, 48, 3851.
- [31] Shao, Y.; Kou, R.; Wang, J.; Viswanathan, V. V.; Kwak, J. H. et al. *J. Power Sources* **2008**, 185, 280.
- [32] Mayrhofer, K. J. J.; Ashton, S. J.; Meier, J. C.; Wiberg, G. K. H.; Hanzlik, M. et al. *J. Power Sources* **2008**, 185, 734.
- [33] Zheng, H.; Ou, J. Z.; Strano, M. S.; Kaner, R. B.; Mitchell, A. et al. *Adv. Funct. Mater.* **2011**, 21, 2175.
- [34] Maillard, F.; Peyrelade, E.; Soldo-Olivier, Y.; Chatenet, M.; Chaînet, E. et al. *Electrochim. Acta* **2007**, 52, 1958.
- [35] Viswanathan, K.; Brandt, K.; Salje, E. *J. Solid State Chem.* **1981**, 36, 45.
- [36] Butler, M. A. *J. Appl. Phys.* **1977**, 48, 1914.
- [37] Wöhler, F. *Annalen der Physik* **1824**, 78, 345.
- [38] Nalbadjan, V. B.; Trubnikov, I. L.; Bukun, N. G.; Medvedev, B. S. *Inorganic Mater* **1986**, 22, 836
- [39] Antolini, E.; Gonzalez, E. R. *Appl. Catal. B* **2010**, 96, 245.
- [40] Crandall, R. S.; Faughnan, B. W. *Physical Review Letters* **1977**, 39, 232.
- [41] Perchthaler, M.; Ossiander, T.; Juhart, V.; Mitzel, J.; Heinzl, C. et al. *J. Power Sources* **2013**, 243, 472.
- [42] Shao-Horn, Y.; Sheng, W. C.; Chen, S.; Ferreira, P. J.; Holby, E. F. et al. *Top. Catal.* **2007**, 46, 285.
- [43] Hartl, K.; Hanzlik, M.; Arenz, M. *Energy Environ. Sci.* **2011**, 4, 234.
- [44] Meier, J. C.; Katsounaros, I.; Galeano, C.; Bongard, H. J.; Topalov, A. A. et al. *Energy Environ. Sci.* **2012**, 5, 9319.
- [45] Reiser, C. A.; Bregoli, L.; Patterson, T. W.; Yi, J. S.; Yang, J. D. et al. *Electrochemical and Solid-State Letters* **2005**, 8, A273.
- [46] Wu, F.; Liu, Y.; Wu, C. *J. Mater. Sci. Technol.* **2010**, 26, 705.
- [47] Ossiander, T.; Perchthaler, M.; Heinzl, C.; Scheu, C. *J. Power Sources* **2014**, 267, 323.
- [48] Scherrer, P. *Nachrichten von der Gesellschaft der Wissenschaften zu Göttingen, Mathematisch-Physikalische Klasse* **1918**, 1918, 98.

- [49] Wyckoff, R. W. G. *The Structure of Crystals. 2nd ed*; Interscience Publishers: New York, **1963**; Vol. 1.
- [50] Zhang, S.; Yuan, X.-Z.; Hin, J. N. C.; Wang, H.; Friedrich, K. A.et al. *J. Power Sources* **2009**, *194*, 588.
- [51] Kielwein, M.; Saiki, K.; Roth, G.; Fink, J.; Paasch, G.et al. *Phys. Rev. B* **1995**, *51*, 10320.
- [52] Meier, J. C.; Galeano, C.; Katsounaros, I.; Witte, J.; Bongard, H. J.et al. *Beilstein Journal of Nanotechnology* **2014**, *5*, 44.
- [53] Ossiander, T.; Heinzl, C.; Gleich, S.; Schönberger, F.; Völk, P.et al. *J. Membr. Sci.* **2014**, *454*, 12.

9 Conclusion

The main focus of this thesis was the investigation of membranes and electrodes for fuel cell applications. Sample preparation strategies were developed for both types of materials. In the case of polymer electrolyte membranes a conventional cross-section sample preparation was modified to meet the requirements of an organic material. The fabrication of artifact-free TEM samples of membranes strengthened by inorganic nanofillers was successfully performed by using gentle grinding and ion beam thinning conditions. Considering the electrode materials, different sample preparation methods were applied. For basic investigations material was scratched off, ultra-sonicated in solvents and dropped on a carbon-coated copper grid. For more detailed analysis of specific sample areas, two cross-section sample preparation strategies using FIB were applied. The preparation of FIB lamellae for TEM also allowed the investigation of anodes after fuel cell operation, as the area of interest could be cut out of the whole MEA. Stable, electron transparent and artifact-free samples with lengths of up to 20 μm were achieved in this way.

The materials for fuel cell application were analyzed regarding their morphology, crystallinity and chemical composition. For this purpose, different analytical methods, most of them based on electron microscopy, were used. SEM was applied to investigate the morphology and general microstructure of electrodes and membranes and EDS measurements in the SEM were used to determine the average chemical composition of the samples. Conventional TEM, HRTEM, STEM and ED were performed for in-depth studies of the morphology, particle size, particle distribution and crystallinity. EDS and EELS in the STEM mode were applied for the chemical analyses and bonding behavior analyses of electrode and membrane materials at the nanometer scale. In addition, the overall crystallinity of all components present in electrodes and membranes was determined with XRD measurements. The results were correlated to *in-situ* and *ex-situ* fuel cell performance tests.

As described in chapter 5, PBI-based membranes with different amounts of silica nanoparticles were synthesized by an *in-situ* sol-gel reaction. The amount of the precursor TEOS was varied between 40, 80 and 120 wt% of the polymer PBI and the resulting silica nanoparticles were bound to the polymer via a cross-linker. The size,

shape and distribution of the silica nanoparticles were determined by STEM HAADF measurements and analyzed in detail by a statistical particle evaluation. Only in HAADF imaging the silica nanoparticles could be distinguished well enough from the organic background. In the sample with 40% TEOS elongated, larger silica particles were found. The other two membranes contained smaller, round particles. The average particle size decreased with increasing concentrations of TEOS from $293 \pm 201 \text{ nm}^2$ (40% TEOS) over $162 \pm 107 \text{ nm}^2$ (80% TEOS) to $56 \pm 56 \text{ nm}^2$ (120% TEOS). In all samples the particles were well dispersed and via EDS measurements it was proven that they consist of Si and O only. EDS measurements of large areas also showed that a higher amount of silica is incorporated into the membrane when a higher amount of TEOS was used in synthesis. Phosphorus, which is present in each of the membranes in equal quantity as well as in uniform distribution as a softener, was used as the reference quantity. XRD experiments of the three membranes showed a broad signal for the amorphous PBI and no signal of crystalline silica was found. In addition, the FWHM of the broad PBI diffraction peaks was measured. It was shown that all samples with incorporated silica particles had a larger FWHM than a pure PBI membrane without any inorganic nanofillers. This is indicative of the incorporation of silica nanoparticles leading to increasing disorder of the polymer matrix. The mechanical stability of the 40% and 80% TEOS membranes was increased compared to a pure PBI membrane. The sample with 120% TEOS was too brittle for operation and thus not analyzed in more detail. In a 360 h start-stop cycling test the sample with 40% TEOS outperformed the 80% TEOS sample. Hence, the 40% TEOS sample was tested in long-term fuel cell operation and compared to a pure PBI membrane. The membrane containing silica nanoparticles exhibited a higher voltage and a lower degradation rate. This study showed that the incorporation of the larger, fibrous silica particles enhanced the durability and performance of HT-PEMFCs.

The influence of an additional heating step before membrane casting on the size, distribution and composition of the embedded silica particles was investigated in chapter 6. Since the implementation of 40% TEOS in PBI-based membranes turned out to give the best properties, the same amount was used here. The membrane which was heated to 70 °C (M I) before casting showed a higher yield stress of 160 MPa in stress-strain measurements and exhibited a higher liquid uptake than the membrane synthesized without additional heating (M II). Nevertheless, the performance of the

membrane prepared at a higher temperature was lower than the one prepared at room temperature, as shown by polarization curves, start-stop cycling and long-term testing. The reason for this behavior was investigated by TEM measurements. The focus in this study was set on a detailed investigation of the distribution of elements in the membranes via analytical measurements in the TEM such as EDS and EELS. The silica particles were visualized by STEM HAADF imaging. In membrane M II the typical elongated, fibrous silica nanostructures were found. Membrane M I on the other hand comprised several large, ellipsoidal particles which had sizes of up to few hundred nanometers in diameter. The large particles were elongated in the membrane pulling direction and homogeneously dispersed. In addition to the large silica structures, the same elongated particles as in M II were found in M I. Due to the higher temperature applied in the case of membrane M I the formation of larger silica particles was favored. The results indicated that for this membrane, small silica particles congregated in some regions and/or that TEOS which did not form silica particles so far started to react. XRD measurements showed no differences between the two amorphous membranes. Further TEM investigation on the silica reinforced membranes focused on elemental composition analysis with a high spatial resolution. EDS line scans and maps revealed that all types of silica particles had a homogeneous elemental composition and were free of any kind of contamination. No enrichment of other elements such as P or Cl was found at the interface between the particles and the polymer matrix. EELS measurements of the Si-L_{2,3} and the O-K edge on all types of silica particles also proved the homogeneity of the particles and confirmed their amorphous character. The results of this study showed that very large silica particles in PBI membranes are not beneficial for the fuel cell performance, possibly because large particles hinder the formation of proton channels through the membrane.

In chapter 7 WO_x synthesized by the project partner, commercial WC and commercial WO_x were evaluated as alternatives for the conventionally used catalyst support material HSAC. It was shown that WO_x was formed on the surface of WC due to high electrochemical potentials during testing. This can lead to mechanical detachment of catalyst material which is a main degradation factor in fuel cell electrodes. Therefore, WC is not a suitable catalyst support material. Furthermore it was shown that the non-commercial WO_x did not lose as much electro-catalytically active surface area as HSAC after 3600 cycle scans. Via XRD and ED in the TEM the high crystallinity of the WO_x was

determined. A loading of 13 wt% of Pt on WO_x was confirmed by EDS measurements. The Pt catalyst nanoparticles had sizes of about 3–4 nm and were randomly distributed. The study revealed by several performance and degradation tests that WO_x has a higher electrochemical stability than HSAC and is an appropriate catalyst support material in the anode of HT-PEMFCs.

A detailed degradation analysis of Pt loaded WO_{3-x} based anodes for HT-PEMFCs is described in chapter 8. At first, the assembled MEA was investigated via SEM and EDS measurements to determine the morphology and the overall distribution of elements in the MEA. It was shown that Pt forms up to 1 μm large, three dimensional networks of few nanometer thin, crystalline Pt rods on WO_{3-x} grains. This is in contrast to conventional HT-PEMFC electrodes where the Pt catalyst forms particles of a few nanometers only. Afterwards, the same MEA was operated for different time spans and in different operation modes. FIB was used to prepare TEM samples of the operated MEAs. EDS line scans perpendicular to the MEA interface revealed diverse behavior regarding the redistribution of e.g. Pt after different operation times/modes. Pt was preferably present at sample locations where a high amount of W was detected, indicating that Pt is tightly bound to the WO_{3-x} anode. With ongoing operation times the Pt diffused into the membrane from both electrodes and was lost for the catalytic reaction. XRD measurements were applied to analyze the changes in crystallinity in dependence of operation times and modes. Via the Scherrer equation changes in the average crystallite size of Pt catalyst particles were calculated and correlated to the measured particle sizes in TEM. STEM HAADF imaging was used to investigate four different areas of each anode after different operation times/modes. The tungsten oxide structure changed with time and the tightly packed grains found in the beginning formed loosely arranged, rounded grains with Pt catalyst material between them. EELS measurements of the O-K edge at 532 eV of WO_{3-x} showed no change in oxidation state. The large Pt catalyst networks consisting of elongated, cross-linked Pt crystals were deformed by operation. Also, the thickness of the Pt rods forming the network changed. During operation Pt, which was in the beginning located in the superordinate structures, partly diffused onto carbon based areas in the anode. In addition, it diffused into the polymer electrolyte membrane. The fuel cell performance of the WO_{3-x} based MEAs was slightly below the standard HSAC but the degradation rate due to start-stop cycling of the investigated WO_{3-x} based MEAs was lower than for the standard HSAC MEAs. The

WO_{3-x} based MEAs also showed better results in a 2000 h long-term fuel cell test compared to the standard carbon material. This study proofed that WO_{3-x} based anodes are superior to HSAC electrodes regarding degradation.

In summary, this thesis shows that combining different electron microscopic and spectroscopic methods allows for an in-depth characterization of fuel cell components. The obtained results further the understanding of the processes and degradation phenomena happening during the operation of the fuel cell and should be taken into consideration when designing future fuel cell generations.

10 Appendix

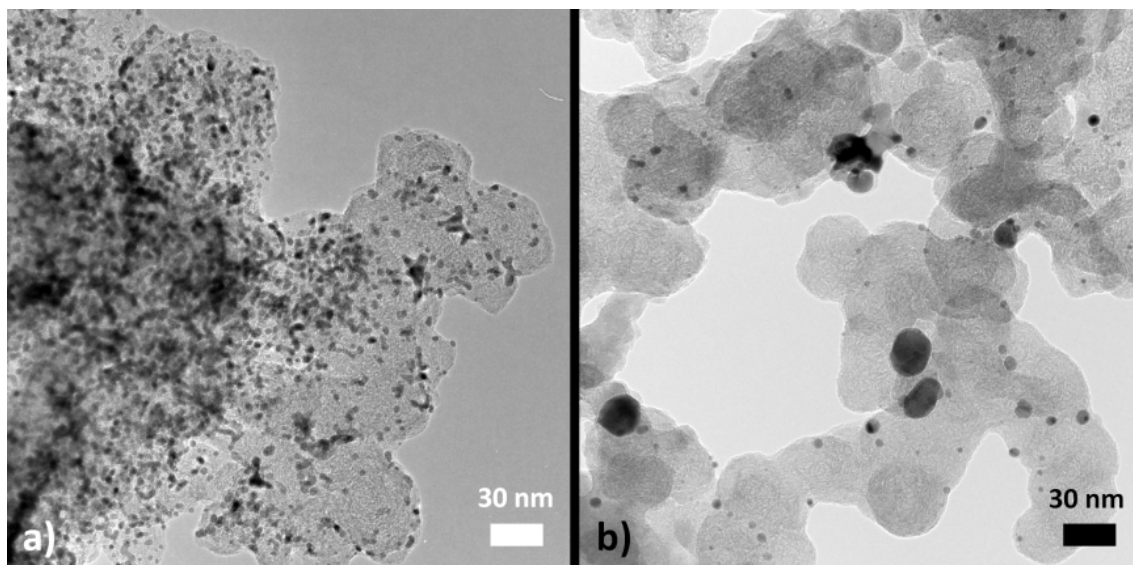


Figure 10.1: TEM micrographs of a C based electrode before operation (a) and after 2000 h of operation (b).

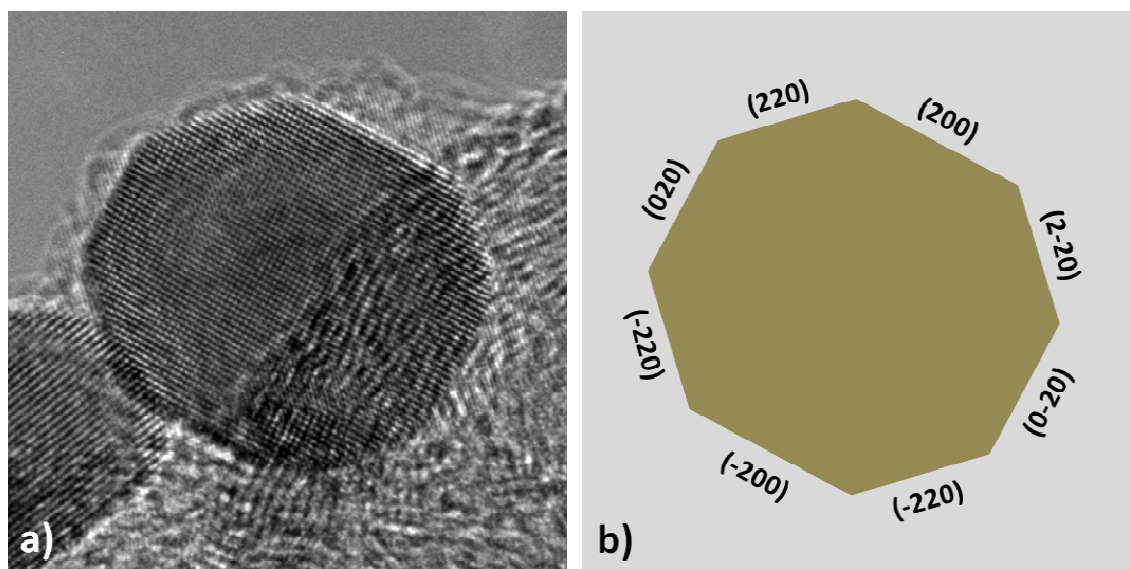


Figure 10.2: a) HRTEM micrograph of a Pt particle; b) schematic drawing of the particle with indexed facets (right).

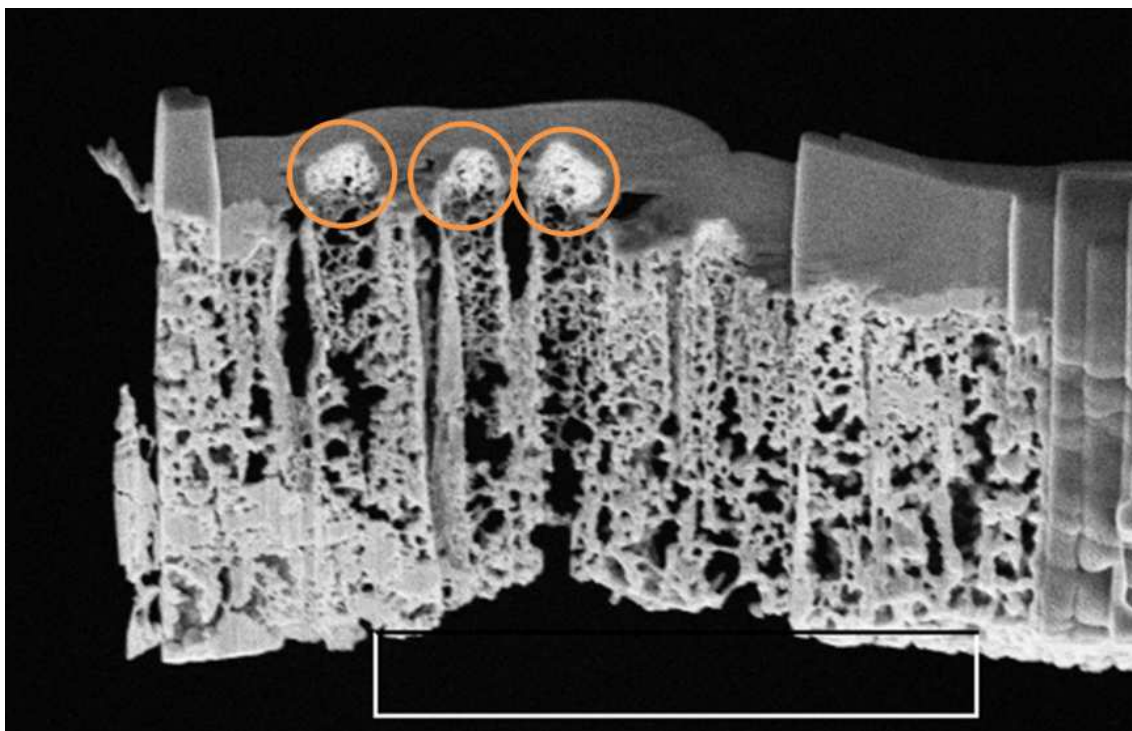


Figure 10.3: SE image of a thinned FIB lamella. Three Pt octahedrons (marked in orange) were investigated.

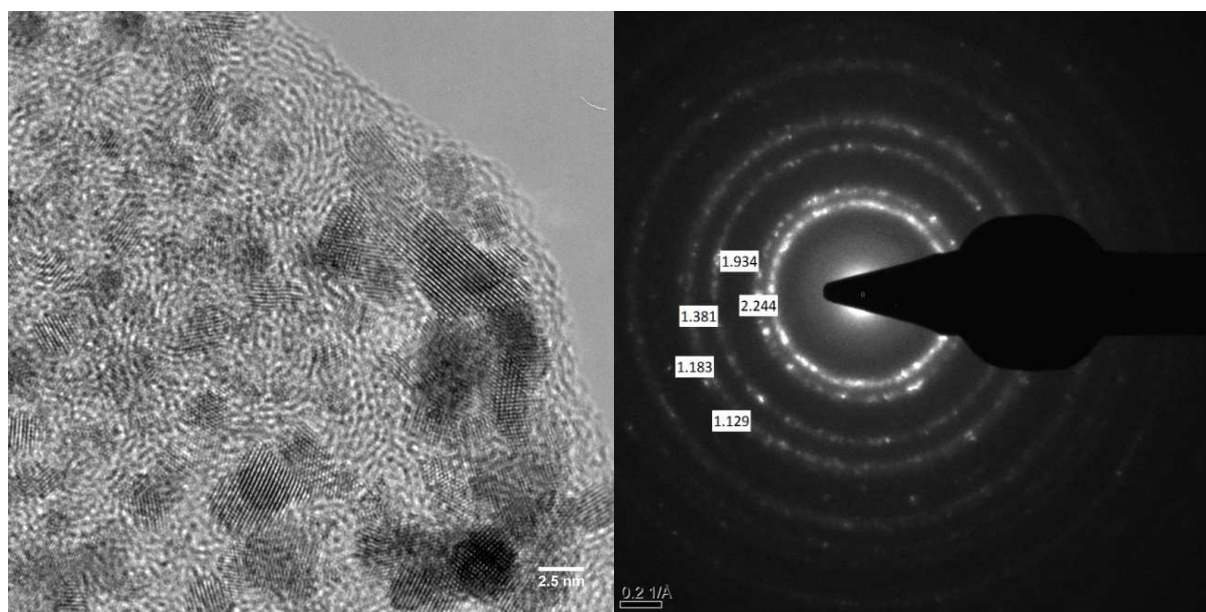


Figure 10.4: HRTEM image of crystalline Pt particles on turbostratic carbon (left). Electron diffraction pattern of this area shows the signals of cubic Pt.

11 Curriculum Vitae

Personal Information

Name: Christoph Heinzl

Nationality: German

Education

04/2011 – 10/2014 PhD studies in physical chemistry, Prof. Dr. Christina Scheu, Ludwig-Maximilians-University, Munich

04/2009 – 03/2011 Studies of chemistry, Ludwig-Maximilians-University, Munich, graduation: Master of Science

10/2005 – 03/2009 Studies of chemistry and biochemistry, Ludwig-Maximilians-University, Munich, graduation: Bachelor of Science

09/1995 – 06/2004 Finsterwalder-Gymnasium, Rosenheim, graduation: Abitur

Work experience

08/2010 – 01/2011 Student research assistant, research group Prof. Dr. Christina Scheu, LMU, Munich

10/2009 – 11/2009 Tutor, introductory chemical practical course, LMU, Munich

06/2009 – 09/2009 Tutor, advanced inorganic practical course, LMU, Munich

07/2007 – 08/2007 Student employee in Automation and Drives, Siemens AG, Munich

02/2006- 03/2006 Student employee in Automation and Drives, Siemens AG, Munich

08/2004 – 05/2005 Community service, hospital Rosenheim, pickup and delivery service

Membership

Graduate Program of the Nanosystems Initiative Munich (NIM)

Center of NanoScience (CeNS)

Honors

Römer Award 2011 for outstanding performance in master studies

Skills

Experiments in chemical synthesis

Autonomous working at Transmission Electron Microscopes (TEM), conventional TEM, electron diffraction, high resolution TEM, High angle annular dark-field imaging, Energy-dispersive X-ray Spectroscopy, Energy Electron Loss Spectroscopy, TEM sample preparation

Autonomous working at Scanning Electron Microscopes

Training and supervising of bachelor students, supervising of practical courses in inorganic and physical chemistry

Languages

German native speaker

English business fluent

French basic

IT-Knowledge

MS Word, MS Excel, MS Powerpoint (frequent use)

Digital Micrograph, TEM Imaging and Analysis, ImageJ (frequent use)

12 List of Publications and Presentations

12.1 Scientific publications

Journals

1. C. Heinzl, K. A. Hengge, M. Perchthaler, V. Hacker, C. Scheu, Insight into the degradation of HT-PEMFCs containing tungsten oxide catalyst support material for the anode, *Journal of The Electrochemical Society* (accepted).
2. C. Heinzl, T. Ossiander, S. Gleich, C. Scheu, Transmission electron microscopy study of silica reinforced polybenzimidazole membranes, *Journal of Membrane Science* (accepted).
3. A. Schenk, C. Grimmer, M. Perchthaler, S. Weinberger, B. Pichler, C. Heinzl, C. Scheu, F.-A. Mautner, B. Bitschnau, V. Hacker, Platinum–cobalt catalysts for the oxygen reduction reaction in high temperature proton exchange membrane fuel cells – Long term behavior under ex-situ and in-situ conditions, *J. Power Sources* **2014**, 266, 313-322.
4. T. Ossiander, M. Perchthaler, C. Heinzl, C. Scheu, Influence of thermal post-curing on the degradation of a cross-linked polybenzimidazole-based membrane for high temperature polymer electrolyte membrane fuel cells, *J. Power Sources* **2014**, 267, 323-328.
5. T. Ossiander *, C. Heinzl *, S. Gleich, F. Schönberger, P. Völk, M. Welsch, C. Scheu, Influence of the size and shape of silica nanoparticles on the properties and degradation of a PBI-based high temperature polymer electrolyte membrane, *J. Membr. Sci.* **2014**, 454, 12-19.

* These authors contributed equally.
6. R. Hoffmann, A. S. Wochnik, C. Heinzl, S. B. Betzler, S. Matich, E. Griesshaber, H. Schulz, M. Kučera, J. R. Young, C. Scheu, W. W. Schmahl, Nanoprobe crystallographic orientation studies of isolated shield elements of the coccolithophore species *Emiliania huxleyi*, *Eur. J. Mineral.* **2014**, 26, 473-483.

7. M. Perchthaler, T. Ossiander, V. Juhart, J. Mitzel, C. Heinzl, C. Scheu, V. Hacker, Tungsten materials as durable catalyst supports for fuel cell electrodes, *J. Power Sources* **2013**, 243, 472-480.
8. A. S. Wochnik, A. Frank, C. Heinzl, J. Häusler, J. Schneider, R. Hoffmann, S. Matich, C. Scheu, Insight into the core-shell structures of Cu-In-S microspheres, *Solid State Sci.* **2013**, 26, 23-30.
9. A. S. Wochnik, C. Heinzl, F. Auras, T. Bein, C. Scheu, Synthesis and characterization of CuInS₂ thin film structures, *J. Mater. Sci.* **2011**, 47, 1669-1676.
10. M. M. Reichvilser, C. Heinzl, P. Klüfers, Boronic acid mono- and diesters of the aldopentoses, *Carbohydr. Res.* **2010**, 345, 498-502.

Conference Proceedings

1. A. Wochnik, D. Durach, C. Heinzl, F. Auras, T. Bein, C. Scheu. *Electron Microscopy Characterization of TiO₂ and CuInS₂ used in Solar Cells. Microscopy Conference MC 2011, Kiel, Germany, 28.08. - 02.09.2011, Materials Science, M1: Materials for Energy Technology, M1.P510 (CD) 2011.*
2. A. Wochnik, C. Heinzl, A. Frank, J. Häusler, R. Hoffmann, S. Matich, C. Scheu. *TEM investigation of the growth of CuInS₂ nanospheres. 15th European Microscopy Congress EMC 2012, Manchester, England, 16.09. - 21.09.2012, Towards Sustainable Energy and Environmental Protection, PS1.8 (CD) 2012.*

12.2 Conference contributions

Oral presentation

1. *Analysis and optimization of high-temperature polymer electrolyte membrane fuel cell components regarding lifetime performance*, E-MRS Spring meeting 2014, Lille, France.
2. *Microscopical insight into degradation phenomena in high-temperature polymer electrolyte membrane fuel cells*, Mechanics meets energy II 2014, Winterberg, Germany.

3. *Improving energy conversion efficiencies - HTPEM fuel cells in the spotlight of electron microscopy*, Mechanics meets energy 2013, MPIE Düsseldorf, Germany.

Poster presentation

1. *Characterization of high-temperature proton exchange membrane fuel cells by electron microscopy (II)*, EMAT Workshop on transmission electron microscopy 2013, Antwerp, Belgium.
2. *Characterization of high-temperature proton exchange membrane fuel cells by electron microscopy (I)*, NIM winter school 2013, Kirchberg, Austria.
3. *Investigation of the growth of CuInS_2 microspheres*, EMC 2012, Manchester, UK.
4. *Synthesis and electron microscopy characterization of CuInS_2 films for photovoltaic application*, CENS summer school 2011, Venice, Italy.

Danksagung

Ganz besonders danken möchte ich Frau Prof. Dr. Christina Scheu, die mich im Laufe meines Studiums und meiner Promotion betreut und unterstützt hat. Durch ihre stets gut gelaunte und positive Art stand sie mir immer hilfreich mit Rat und Tat zur Seite und hat mir einen tiefen Einblick in die faszinierende Welt der Elektronenmikroskopie ermöglicht.

Herrn Prof. Dr. Konstantin Karaghiosoff danke ich für seine stets nette und hilfsbereite Unterstützung und für die spontane Übernahme der Zweitkorrektur meiner Arbeit.

Tanja Ossiander und Markus Perchthaler von ELCOMAX GmbH möchte ich für die großartige und wunderbar unkomplizierte Zusammenarbeit danken. Wann immer ich Fragen zu unserem gemeinsamen Projekt hatte, habt ihr euch die Zeit genommen, um mir zu helfen. Danke dafür!

Herrn Dr. Markus Döblinger möchte ich für die vielen Stunden danken, in denen er mir die Bedienung der Mikroskope näher gebracht hat. Auch dafür, dass seine Türe immer offen stand, wenn ich Hilfe brauchte oder Fragen hatte.

Des Weiteren danke ich Steffen Schmidt für die vielen kleinen Tipps und Tricks, die er mir am Mikroskop beibrachte und für die hervorragenden REM Messungen zu Beginn meiner Arbeit.

Für die zahlreichen XRD Messungen geht mein Dank an Tina Reuther und Benjamin Breitbach. Außerdem bedanke ich mich bei Sonja Matich und Ramona Hoffmann für den riesigen Aufwand, den sie für die Präparation der TEM Lamellen auf sich genommen haben.

Regina Huber und Alena Vock danke ich für ihre nette Hilfe bei Verwaltungsangelegenheiten und sonstigen organisatorischen Belangen.

Ganz besonders danke ich meinen fleißigen und top motivierten Praktikanten und Masteranden Stefan Hieke, Lukas Neudert, Stephan Gleich und Katharina Hengge: Ihr habt maßgeblich zum Erfolg meiner Doktorarbeit beigetragen!

Außerdem danke ich dem gesamten Arbeitskreis Scheu für den großartigen Zusammenhalt und die fantastische Arbeitsatmosphäre. Egal ob bei wissenschaftlichen Diskussion, Praktika, auf Konferenzen oder bei freizeitlichen Aktivitäten, es hat immer großen Spaß mit euch gemacht. Angela Wochnik, die mich als F-Praktikanten und Masteranden in den Arbeitskreis aufgenommen hat, danke ich für ihre immerwährende Unterstützung und die hilfreichen und motivierenden Gespräche zwischendurch. Sophia, Katha und Stephan danke ich für die super Atmosphäre in unserem kleinen „Schlauchbüro“. Besonders Sophia danke ich für die moralische Unterstützung am Ende meiner Promotion: Die Qualifikation zur „psychologischen Betreuung“ hast du dir in deinem Lebenslauf redlich verdient ☺. Ein weiterer Dank geht an die fleißigen und gründlichen Korrekturleser meiner Dissertation: Tanja, Stephan, Katha, Alex und Sophia. Auch meinen anderen Kollegen Andi, Ramona, Teresa, Anna, Alena, Sriram, Michi und Chris danke ich für die unvergessliche Zeit. Unsere gemeinsamen Jahre im Arbeitskreis werden mir immer in guter Erinnerung bleiben!

Meinen Eltern und meiner Schwester danke ich für ihre unermüdliche Unterstützung und Ermutigung während meines Studiums und meiner Promotion.

Besonders danke ich Caroline Müller, die mich während meiner Zeit an der Uni immer unterstützt und aufgemuntert hat und immer für mich da war.